2023

Dose Analysis of CT and SPECT Medical Imaging Systems using Monte Carlo techniques.

Doctoral Dissertation

NIKOLAOS CHATZISAVVAS
UNIVERSITY OF WEST ATTICA

© Copyright by Nikolaos Chatzisavvas 2023
This work is licensed under Attribution-NonCommercial 4.0 International

University of West Attica

School of Engineering

Department of Industrial Design and Production Engineering

Doctoral Dissertation

Dose Analysis of CT and SPECT Medical Imaging Systems using Monte Carlo techniques.

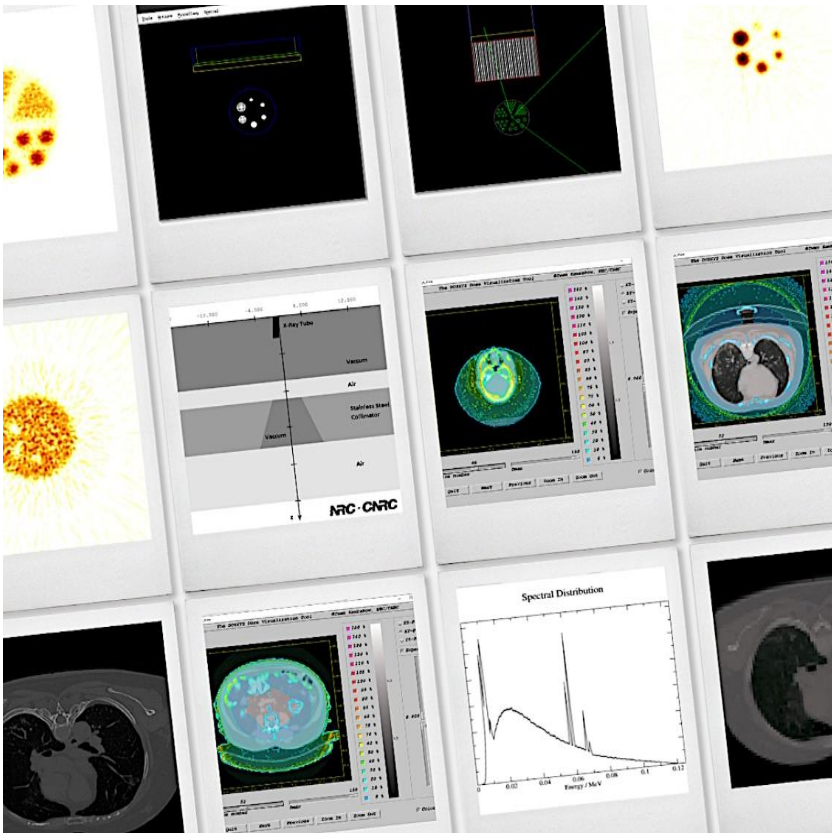

Nikolaos Chatzisavvas: PHD19389034

AIGALEO

DECEMBER 2023

Πανεπιστήμιο Δυτικής Αττικής

Σχολή Μηχανικών

Τμήμα Μηχανικών Βιομηχανικής Σχεδίασης και Παραγωγής

Διδακτορική Διατριβή

Ανάλυση δόσεων συστημάτων ιατρικής απεικόνισης CT και SPECT με χρήση τεχνικών Μόντε Κάρλο.

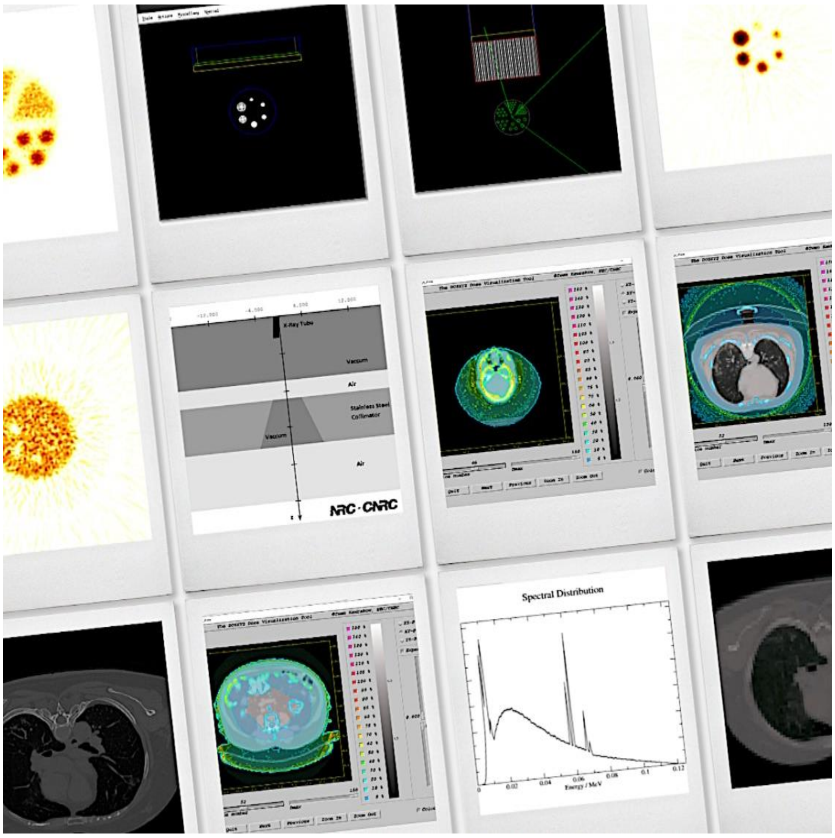

Νικόλαος Χατζησάββας: PHD19389034

ΑΙΓΑΛΕΩ

ΔΕΚΕΜΒΡΙΟΣ 2023

Μέλη Τριμελούς Συμβουλευτικής Επιτροπής συμπεριλαμβανομένου και του Επιβλέποντα.

Α/Α	ΟΝΟΜΑ ΕΠΩΝΥΜΟ	ΒΑΘΜΙΔΑ/ΙΔΙΟΤΗΤΑ/ΤΜΗΜΑ	ΨΗΦΙΑΚΗ ΥΠΟΓΡΑΦΗ
1	Δημήτριος Νικολόπουλος	Καθηγητής Α’ βαθμίδας, Επιβλέπων, Τμήμα Μηχανικών Βιομηχανικής Σχεδίασης και Παραγωγής ΠαΔΑ	Dimitrios Nikolopoulos Digitally signed by Dimitrios Nikolopoulos Date: 2023.12.20 15:09:47 +02'00'
2	Γεώργιος Πρινιωτάκης	Καθηγητής Α’ βαθμίδας, Τμήμα Μηχανικών Βιομηχανικής Σχεδίασης και Παραγωγής ΠαΔΑ	Digitally signed by Georgios Priniotakis Date: 2023.12.20 17:01:29 +02'00'
3	Ιωάννης Βαλαής	Καθηγητής Α’ βαθμίδας, Τμήμα Μηχανικών Βιοϊατρικής ΠαΔΑ	Ioannis Valais Digitally signed by Ioannis Valais Date: 2023.12.20 17:17:47 +02'00'

Μέλη Επταμελούς Εξεταστικής Επιτροπής

Α/Α	ΟΝΟΜΑ ΕΠΩΝΥΜΟ	ΒΑΘΜΙΔΑ/ΙΔΙΟΤΗΤΑ/ΤΜΗΜΑ/ΠΑΝΕΠΙΣΤΗΜΙΟ
1	Δημήτριος Νικολόπουλος	Καθηγητής Α’ βαθμίδας, Επιβλέπων, Τμήμα Μηχανικών Βιομηχανικής Σχεδίασης και Παραγωγής ΠαΔΑ
2	Γεώργιος Πρινιωτάκης	Καθηγητής Α’ βαθμίδας, Τμήμα Μηχανικών Βιομηχανικής Σχεδίασης και Παραγωγής ΠαΔΑ
3	Ιωάννης Βαλαής	Καθηγητής Α’ βαθμίδας, Τμήμα Μηχανικών Βιοϊατρικής ΠαΔΑ
4	Παναγιώτης Γιαννακόπουλος	Καθηγητής Α’ βαθμίδας, Τμήμα Μηχανικών Πληροφορικής και Υπολογιστών ΠαΔΑ
5	Γεώργιος Πρεζεράκος	Καθηγητής Α’ βαθμίδας, Τμήμα Μηχανικών Πληροφορικής και Υπολογιστών ΠαΔΑ
6	Χρήστος Μιχαήλ	Επίκουρος Καθηγητής, Τμήμα Μηχανικών Βιοϊατρικής ΠαΔΑ
7	Γεώργιος Φούντος	Καθηγητής Α’ βαθμίδας, Τμήμα Μηχανικών Βιοϊατρικής ΠαΔΑ

Ημερομηνία εξέτασης: 20/12/2023

Η έγκριση της διδακτορικής διατριβής από το Τμήμα Μηχανικών Βιομηχανικής Σχεδίασης και Παραγωγής του Πανεπιστημίου Δυτικής Αττικής δεν υποδηλοί αποδοχή των γνωμών του συγγραφέα (Ν. 5343/32, Άρθρο 202).

ΔΗΛΩΣΗ ΣΥΓΓΡΑΦΕΑ ΔΙΔΑΚΤΟΡΙΚΗΣ ΔΙΑΤΡΙΒΗΣ

Ο κάτωθι υπογεγραμμένος Νικόλαος Χατζησάββας υποψήφιος διδάκτορας του Τμήματος Μηχανικών Βιομηχανικής Σχεδίασης και Παραγωγής της Σχολής Μηχανικών του Πανεπιστημίου Δυτικής Αττικής, δηλώνω ότι:

«Είμαι συγγραφέας και δικαιούχος των πνευματικών δικαιωμάτων επί της διατριβής και δεν προσβάλω τα πνευματικά δικαιώματα τρίτων. Για τη συγγραφή της διδακτορικής μου διατριβής δεν χρησιμοποίησα ολόκληρο ή μέρος έργου άλλου δημιουργού ή τις ιδέες και αντιλήψεις άλλου δημιουργού χωρίς να γίνεται αναφορά στην πηγή προέλευσης (βιβλίο, άρθρο από εφημερίδα ή περιοδικό, ιστοσελίδα κ.λπ.). Επίσης, βεβαιώνω ότι αυτή η εργασία έχει συγγραφεί από μένα αποκλειστικά και αποτελεί προϊόν πνευματικής ιδιοκτησίας τόσο δικής μου, όσο και του Ιδρύματος.

Παράβαση της ανωτέρω ακαδημαϊκής μου ευθύνης αποτελεί ουσιώδη λόγο για την ανάκληση του διδακτορικού διπλώματός μου.

……………………

Νικόλαος Χατζησάββας

Life is a piece of Act.

-Anonymous

Acknowledgments

Many thanks to my supervisor, Dr. Dimitrios Nikolopoulos for his valuable observations, guidance and ability to stir me in a direction towards fruitful results. Ii is an honor to be a student of Dimitrios from my bachelors' years up until now. An enormous thanks Dr. Ioannis Valais for his continuous support and feedback for all these years during my PhD. Special thanks to Dr. Georgios Priniotakis for the encouragement and guidance all these years. Additional thanks goes to Dr. Georgios Karpetas for his valuable contribution of knowledge on image reconstruction and technical support. Also many thanks Mr. Athanasios Koustas for his valuable help.

Another huge thanks goes to the Special Account for Research Funds of ELKE/PADA more specifically, Dr. Ioanni Kaldelli, Vice Rector for Research and Lifelong Education and Mrs Sideri Dimitra for the financial support, without them my journey would be much more difficult and those people lift a weight of my shoulder.

The help and support from the communities of EGSnrc, OpenGATE collaboration, STIR, Topas, Kaggle and Zenodo needs to be acknowledged. Many thanks to Dr. Wamied Ahdel-Rahman for his YouTube series on utilizing EGSnrc routines. Special thanks to Dr. David Sarrut for his valuable help on utilizing GATE routines to do SPECT simulations.

This work would not have been possible without the help of PhD Candidate Matthew Strugari, from the Dalhousie University of Canada and Dr. Han Gyu Kang, from the National Institute of Radiological Sciences in Japan. Also a huge thank you to Dr. Joseph Perl of the Topas community.

Last but not least a huge thank you to my parents, my family, my friends and colleagues that helped me with various ways, under different circumstances.

Table of Contents

List of Figures **10**

List of Tables **15**

List of Abbreviations **16**

Abstract **18**

Research's Preface **20**
General Remainder **20**
Publications **23**
International scientific journals with peer review: 23
National scientific conference proceedings with referees: 24
Financial Support **24**

Chapter A. Theoretical background **25**
General Introduction **25**

General Aims **26**

1 Charged Particle Interaction with matter **27**
1.1 Introduction **27**
1.2 Heavy charged particles interactions **27**
1.3 Electron & Positron interactions **28**
1.4 Conclusions **34**

2 Photon Interaction with matter **35**
2.1 Introduction **35**
2.2 Cross-section definition **35**
2.3 Differential Cross-section **37**
2.4 Photon Scattering **38**
2.5 Photoelectric effect **44**
2.6 Pair and Triplet production **47**
2.7 Conclusions **51**

3 Radiation Dosimetry **52**
3.1 Introduction **52**
3.2 Fluence **52**
3.3 KERMA - CEMA **54**
3.4 Absorbed Dose **55**
3.5 Conclusions **56**

4 Computed Tomography Radiology **57**
4.1 Introduction **57**
4.2 Fundamental of Computed Tomography **57**
4.3 X-ray source **61**
4.4 Conclusions **63**

5 Nuclear Imaging SPECT **65**
5.1 Introduction **65**
5.2 Basic SPECT concepts **66**
5.3 Basic principles for reconstructing projections to image **69**
5.4 Back projection and Filtered Back projection **73**

5.5 Image reconstruction via iteration methods 75
5.6 Conclusions 77

6 Monte Carlo Computational Techniques 79
6.1 Introduction 79
6.2 Random Variables 83
6.3 Random number Generators RNGs 84
6.4 Modelling Particle Trajectories – Tracks 87
6.5 Modelling Particle Tallies 89
6.6 Simulation optimization 91
6.6.1 Variance reduction 91
6.6.2 Other Optimization methods 93
6.7 Conclusions 95

Chapter B. Research Part 96

General Targets 96

7. Materials and Methods 97
7.1 Introduction 97
7.2 Basic Software configuration 98
7.2.1 Hardware 98
7.2.2 Linux OS shell & Package Manager 99
7.2.3 Builders – Compilers 100
7.2.4 Extra Resources 101
7.3 EGSnrc environment 102
7.3.1 Compiling and Installing EGSnrc 103
7.3.2 Getting started 104
7.3.3 CT x-ray source optimization and simulation 106
7.3.4 CT dose simulation and case studies 112
7.4 GATE environment 121
7.4.1 Building and configuring GATE 122
7.4.2 AnyScan S based SPECT head simulation with GATE. 127
7.4.3 Custom small animal SPECT head simulation with GATE. 130
7.5 Tomographic Reconstruction with STIR 132
7.6 Conclusions 134

8. Results and Discussions 135
8.1 Introduction 135
8.2 CT Beams quality assurance 136
8.2.1 AU target - Spectral and Energy Fluence Distributions 30-150keV. 136
8.2.2 W target - Spectral and Energy Fluence Distributions 30-150keV. 141
8.3 CT irradiation – Dosimetric map slices. 147
8.3.1 Abdomen phantom dosimetric maps. 147
8.3.2 Brain phantom dosimetric maps. 148
8.3.3 Chest phantom dosimetric maps. 149
8.4 Organ dose profiles. 151
8.4.1 Abdomen 151
8.4.2 Brain 152
8.4.3 Heart 153
8.4.4 Lung 154
8.4.5 Skin 155
8.4.5 Spine 156

8.5 AnyScan based SPECT-head Simulation. **157**
8.5.1 OSMAPOSL Comparison for optimal subset and iteration combination. 160
8.5.2 Hot spheres Jaszczak phantom OSMAPOSL vs FBP Comparison. 162
8.5.3 COLD spheres Jaszczak phantom OSMAPOSL vs FBP Comparison. 164
8.5.4 Comparison for various Crystal substances for AnyScan S based SPECT-head. 165
8.6 Custom Small Animal SPECT-head Simulation. **169**
8.6.1 OSMAPOSL Comparison for optimal subset and iteration combination. 172
8.6.2 Comparison of collimator’s hole size for small animal SPECT. 174
8.7 Conclusions **177**

9. General Conclusions **179**

10. Future work **183**

References **184**

Appendix1: CT simulation results **203**

Appendix2: Compilation and Installation Technical Report **204**

Appendix3: SPECT-heads simulations Results. **218**

Appendix4: Source Code. **219**

Author's Curriculum Vitae **220**

List of Figures

Figure 1 Ion interaction with a nucleus, three types of collisions. [7] 29

Figure 2 Ionization and Excitation processes [8]. 31

Figure 3 Visual representation of the bremsstrahlung process [11]. 34

Figure 4 Photon scatter trajectory [15]. 37

Figure 5 Compton Scattering effect visualization [17]. 40

Figure 6 Thomson scattering visualization [18]. 42

Figure 7 Photoelectric effect visualization [20]. 45

Figure 8 Total photoelectric absorption cross-section for lead [22]. 46

Figure 9 Pair and Triplet production visualization[25]. 48

Figure 10 Total and partial cross-sections for Carbon and Lead [28]. 50

Figure 11 Photon Fluence and energy fluence for an x-ray source with W target, Be+Al+Cu filtration at 250keV [29]. 54

Figure 12 X-ray CT configurations. a) Gantry based system, b) Cone beam system, c) Parallel beam system, d) Slice of an attenuation contrast technique in tomography of a mouse embryo [44]. 59

Figure 13 Basic X-ray tube visualization [6]. 62

Figure 14 AnyScan S Flex system, with dual head detectors. 67

Figure 15 Basic assembly of a typical SPECT detector [61]. 67

Figure 16 Visualization for various types of SPECT detector collimators [61]. 68

Figure 17 LOR example in two dimensions [53]. 70

Figure 18 Visualizing the integration of f(x,y) to form $p(x_r,\varphi)$ [53]. 71

Figure 19 Visualization of the relationship between a (x_0,y_0) point integrated into a sinogram [53]. 72

Figure 20Visualization of the central section theorem [53]. 73

Figure 21 Visualization of the MLEM algorithm workflow [70]. 76

Figure 22 Geometrical pi estimation (500 points), a) Plot of points, b) end result estimator [91]. 82

Figure 23 Geometrical pi estimation (50,000 points), a) Plot of points, b) end result estimator [91]. 82

Figure 24 Ubuntu application gedit execution via WSL 2.0 with GWSL inside Windows 10. 99

Figure 25 EGS_gui Main Menu Panel. 104

Figure 26 Pegs Data Creation by the graphical user interface. 105

Figure 27 Pegs Data Selection Option for compound or element. 105

Figure 28 BEAMnrc gui Main Panel. 106

Figure 29 BEAMnrc New Accelerator creation by adding Component Modules. 107

Figure 30 BEAMnrc Geometry Visualization of X-ray Source [137]. 108

Figure 31 BEAMnrc simulation parameters example. 110

Figure 32 BEAMDP gui parameters selection and execution example. 111

Figure 33 Example of the BEAMDP output opening an xmgrace session. 111

Figure 34 Text file with the full path of all anonymous dicom slice files. 112

Figure 35 CTCREATE program interface. 113

Figure 36 CTCREATE - CT volume subset selection. 114

Figure 37 CTCREATE – new dimensions and voxel size for egsphantom. 115

Figure 38 Finalizing the creation of the chest egs-phantom. 117

Figure 39 DOSxyznrc gui Main Menu Panel. 117

Figure 40 DOSxyznrc ISOURCE 8 visualization [141]. 118

Figure 41 DOSxyznrc Inputs and Parameters Panels. 119

Figure 42 Dosxyz_show example - Visualization of the dosimetric map on the phantom. 120

Figure 43 STATDOSE - Program execution in cli environment. 120

Figure 44 Example of the STATDOSE plot command opening an xmgrace session. 121

Figure 45 GATE cli session. 123

Figure 46 GATE session with OpenGL graphics panel enabled. 123

Figure 47 GATE session with QT graphics panel enabled. 124

Figure 48 GATE code example. 125

Figure 49 ROOT output file opened in a root browser for further processing. 126

Figure 50 ROOT leaf opening on canvas – Energy Distribution example. 127

Figure 51 AnyScan S Dual-Head Flex Mediso SPECT system, with torso phantom. 128

Figure 52 AnyScan SPECT system, taking projection and monitoring the procedures. 128

Figure 53 AnyScan SPECT-head and Jaszczak spheres phantom – front view. 129

Figure 54 Custom-SmallAnimal SPECT-head and Jaszczak rods phantom – front view. 131

Figure 55 STIR - FBP2D script execution via cli. 132

Figure 56 Amide - Importing new raw tomographic data, example. 133

Figure 57 Amide - Main Panel. 134

Figure 58 AU target 30keV Spectral Distribution. 136

Figure 59 AU target 30keV Energy Fluence Distribution. 136

Figure 60 AU target 60keV Spectral Distribution. 137

Figure 61 AU target 60keV Energy Fluence Distribution. 137

Figure 62 AU target 90keV Spectral Distribution. 138

Figure 63 AU target 90keV Energy Fluence Distribution. 138

Figure 64 AU target 120keV Spectral Distribution. 139

Figure 65 AU target 120keV Energy Fluence Distribution. 139

Figure 66 AU target 150keV Spectral Distribution. 140

Figure 67 AU target 150keV Energy Fluence Distribution. 140

Figure 68 W target 30keV Spectral Distribution. 141

Figure 69 W target 30keV Energy Fluence Distribution. 142

Figure 70 W target 60keV Spectral Distribution. 142

Figure 71 W target 60keV Energy Fluence Distribution. 143

Figure 72 W target 90keV Spectral Distribution. 143

Figure 73 W target 90keV Energy Fluence Distribution. 144

Figure 74 W target 120keV Spectral Distribution. 144

Figure 75 W target 120keV Energy Fluence Distribution. 145

Figure 76 W target 150keV Spectral Distribution.. 145

Figure 77 W target 150keV Energy Fluence Distribution. 146

Figure 78 Abdomen AU target Beam - Dosimetric map30-150keV................................. 147

Figure 79 Abdomen W target Beam - Dosimetric map30-150keV................................... 147

Figure 80 Brain AU target Beam - Dosimetric map30-150keV. 148

Figure 81 Brain W target Beam - Dosimetric map30-150keV. 148

Figure 82Chest AU target Beam - Dosimetric map30-150keV. 149

Figure 83 Chest W target Beam - Dosimetric map30-150keV 149

Figure 84 Abdomen Dose Comparison Profile - AU target... 151

Figure 85 Abdomen Dose Comparison Profile - W target.. 151

Figure 86 Brain Dose Comparison Profile - AU target.. 152

Figure 87 Brain Dose Comparison Profile - W target.. 152

Figure 88Heart Dose Comparison Profile - AU target... 153

Figure 89 Heart Dose Comparison Profile - W target.. 153

Figure 90 Lung Dose Comparison Profile - AU target. 154

Figure 91 Lung Dose Comparison Profile - W target. 154

Figure 92 Skin Dose Comparison Profile - AU target. 155

Figure 93 Skin Dose Comparison Profile - W target. 155

Figure 94 Spine Dose Comparison Profile - AU target.. 156

Figure 95 Spine Dose Comparison Profile - W target.. 156

Figure 96 AnyScan NaI Crystal, Hot spheres Jaszczak Phantom Sinogram Visualization. 157

Figure 97 AnyScan NaI Crystal, Hot spheres Jaszczak Phantom - Singles Energy Distribution.. 157

Figure 98 AnyScan NaI Crystal, Hot spheres Jaszczak Phantom - Singles Spatial Distribution Position X.. 158

Figure 99 AnyScan NaI Crystal, Hot spheres Jaszczak Phantom - Singles Spatial Distribution Position Y.. 158

Figure 100 AnyScan NaI Crystal, Hot spheres Jaszczak Phantom - Singles Spatial Distribution Position Z. 159

Figure 101 Custom Small Animal NaI Crystal, Hot rods Jaszczak Phantom Sinogram Visualization..169

Figure 102Custom Small Animal NaI Crystal, Hot rods Jaszczak Phantom, Singles - Energy Distribution. 170

Figure 103 Custom Small Animal NaI Crystal, Hot rods Jaszczak Phantom, Singles - Spatial Distribution Position X...170

Figure 104 Custom Small Animal NaI Crystal, Hot rods Jaszczak Phantom, Singles - Spatial Distribution Position Y...171

Figure 105 Custom Small Animal NaI Crystal, Hot rods Jaszczak Phantom, Singles - Spatial Distribution Position Z. 171

List of Tables

Table 1 Main computational units characteristics. 98

Table 2 Dicom (a) - Egsphantom (b) slices for abdomen, brain and chest phantoms........ 116

Table 3 OSMAPOSL reconstructions for various subset and iteration options. 160

Table 4 OSMAPOSL Volume Rendering for various subset and iteration options........... 161

Table 5 FBP - OSMAPOSL Jaszczak hot spheres phantom. 163

Table 6 FBP - OSMAPOSL Jaszczak cold spheres phantom. 164

Table 7 Sinograms for different crystal substances.. 165

Table 8 Singles - Energy distributions for different crystal substances. 166

Table 9 FBP reconstructions and volume renderings for different crystal substances. 167

Table 10 OSMAPOSL reconstructions and volume renderings for different crystal substances. 168

Table 11 OSMAPOSL reconstructions for various subset and iteration options. 172

Table 12 OSMAPOSL Volume renderings for various subset and iteration options. 173

Table 13 Singles - Energy distribution for different diameters of collimator’s hole sizes. 174

Table 14 FBP reconstructions and volume renderings for different diameters of collimator’s hole sizes. 175

Table 15 OSMAPOSL reconstructions and volume renderings for different diameters of collimator’s hole sizes. 176

List of Abbreviations

2D	Two Dimensional
3D	Three Dimensional
AI	Artificial Intelligence
AU	Gold
BGO	Bismuth germanium oxide
CEMA	Converted Energy per unit MAss
CERN	Conseil Européen pour la Recherche Nucléaire
CLI	Command-Line Interface
CPU	Central Processing Unit
CT	Computed Tomography
DBS	Directional bremmstraulung Splitting
DICOM	Digital Imaging and Communications in Medicine
DOI	Digital Object Identifier
ECT	Emission Computed Tomography
EGSNRC	Electron Gamma Shower, National Research Council of Canada
EM	Expectation Maximization
FBP	Filtered Back Projection
FOV	Field Of View
FWHM	Full Width at Half Maximum
GAGG	Gadolinium Aluminium Gallium Garnet
GATE	Geant4 Application for Tomographic Emission
GEANT	GEometry ANd Tracking
GSO	Gadolinium Orthosilicate
GUI	Graphical User Interface
HU	Hounsfield Unit

ICRU	International Commission on Radiation Units and Measurements
KERMA	Kinetic Energy Released per unit MAss
LINAC	LINear ACcelerator
LOR	Lines Of Response
LSO	Lutetium oxyorthosilicate
MC	Monte Carlo
ML	Maximum Likelihood
ML	Machine Learning
MLE	Maximum Likelihood Estimate
NaI	Sodium iodide
OS	Operating System
OSEM	Ordered Subsets Expectation Maximization
OSMAPOSL	Ordered Subsets Maximum A Posteriori One Step Late
PET	Positron Emission Tomography
PMT	PhotoMutliplier Tube
PRNG	Pseudo Random Number Generator
PRNs	Pseudo-Random Numbers
RN	Random Numbers
RNG	Random Number Generators
SPECT	Single Photon Emission Tomography
STIR	Software for Tomographic Image Reconstruction
UCSF	University of California, San Francisco
VM	Virtual Machine
W	Tungsten
WSL	Windows Subsystem for Linux
Z	Atomic Number
eV	electron Volt

Abstract

An addressing of questions about the methodologies, strategies, optimizations, and approaches used to assess dosimetric data in Computed Tomography (CT) and Single Photon Emission Computed Tomography (SPECT) systems was primarily the purpose of this thesis. The key task throughout the study time was to evaluate the two dissimilar systems, understand their principles of operation, and eventually apply Monte Carlo software to imitate them and monitor outcomes from the standpoint of dosages. All trials were composed, validated, and explored using cutting-edge, primarily open-source Monte Carlo software.

The software packages Geant4, GATE, and EGSNRC, as well as auxiliary scripts to assess, transform, and analyze simulated inputs and outputs were successfully configured and built in most cases from source code. The correct configuration and installation of all packages in an Ubuntu 20.04 environment was a difficult task, owing to the involvement of several programming languages, including Fortran, C/C++, Java, and Python, as well as the fact that most software packages were built from source code, requiring the use of numerous packages, compilers, and builders. An extensive installation instruction for configuring, building and installing all software packages utilized are given in Appendix2.

The CT system was configured by simulating various x-ray sources, creating personalized phantoms from patient-specific examinations (DICOM format), and scoring doses on those phantoms by simulating x-ray source irradiation circularly from all angles (360^{O}). Tungsten (W) and gold (Au) anode target materials were used, and each anode target material was simulated in the energy range of 30 keV–150 keV with a step of 5 keV. Overall, 50 beams (25 for W and 25 for Au) were simulated once the x-ray source characteristics were determined. The EGSnrc software was used to execute the simulations, and the output files for each beam simulation were saved in binary phase space file format.

Many elements of the x-ray source also have a substantial influence on the quality of the beam and thus the dosage received by such a complicated piece of equipment.

For the SPECT system, a new approach was employed. Since the source (radiopharmaceutical-isotope) is injected directly into the patient and is irradiated from within the body as it travels within the patient, it was difficult to simulate such an operation in the same way as the CT. Following the injection, the patient is placed on the SPECT bed where the imaging system takes shots- projections, circularly from all angles, and a sinogram is created as an output. Finally, specialized algorithms reconstruct the raw data, sinogram, into a 3D picture which provides valuable information to the doctors. The approach was to simulate a whole SPECT system, in which different SPECT system factors impacting the image's quality as well as the characteristics of the reconstruction processes producing the image were explored. The open-source program GATE was used in collaboration with STIR to reconstruct the image from the raw output data provided by GATE simulation. The filtered back projection (FBP) and iterative approach of Ordered Subsets Maximum A Posteriori One Step Late (OSMAPOSL) algorithms were supplied by STIR.

Keywords

Medical Imaging, Monte Carlo, GATE, Geant4, EGSnrc, STIR, Linux, Image Reconstruction, Dose

Research's Preface

General Remainder

The study begins with the quest for appropriate software tools that employ Monte Carlo techniques and methods to approach medical physics experiments from a dose perspective. The fundamental idea was to observe the two distinct systems of CT and SPECT, understand their operating principles, examine how to generate scenarios based on those principles, and finally replicate solutions. The guiding premise was to determine which software, in our opinion, is most suited for which simulation setting.

The open-source software packages EGSNRC, Geant4, ROOT, GATE, and STIR were able to be build, mostly from source code, after extensive investigation. The first challenge was to figure out how to properly build and install them with all of their dependencies. Plethora of operating systems and computer environments were there to choose from so the need to utilize every machine possible regardless of the characteristics was essential. The decision was that building, installing mainly on Ubuntu Linux native environment and Ubuntu on Windows environment via VirtualBox, and Windows WSL2.0 was possible, and essentially the same instructions were used.

After extensive testing on various versions of Ubuntu Linux and other Linux distributions such as Fedora and Arch Linux, the decision was made to utilize Ubuntu. Specifically Ubuntu version 20.04.03, was very stable and during compilation with various compilers such as gcc, g++, gfortran, etc. In addition, the particular operating system could handle the use of building tools such as cmake and was going very smoothly with minimal errors when compiling. The correct configuration and installation of all packages was a difficult task, due to the involvement of several programming languages, including Fortran, C/C++, Java, and Python, as well as the fact that most software packages were built from source code and required many packages at specific versions.

Given the complexity of building from source code lead to develop Appendix 2 with more detailed installation instructions for all packages involved, as well as certain code fixtures for libraries necessitating GATE installation. As a commitment to open-source partnerships and communities video instructions for installing Geant4, ROOT, GATE 9.0, and EGSNRC were produced.

The initial concern was how to approach the CT system, so it was divided it into three components. A general CT system consists of an x-ray source, which creates the photon beam, a detector and a patient, both of which may move and capture projections around the patient. The scenario was to simulate photon beam production, assess the quality, and then irradiate a personalized phantom, built from real examination patient data, from all directions circularly and score dosage values for distinct photon beams. That scenario was possible by utilizing EGSNRC; by leveraging BEAMnrc, x-rays could be created, and the output files produced by BEAMnrc were phase-space binary files with the ending egsphsp.

That BEAMnrc output file described a photon beam and may be used as input to the DOSXYZnrc program, coupled with a phantom built from examination data. DOSXYZnrc provided the capability to simulate the irradiation of that photon beam on a phantom-dose scorer and observe how the energy, collimation, angle of the anode, beam's field of view (FOV) and other parameters of the x-ray source affect a patient on the level of absorbed dose. Anode target materials of tungsten (W) and gold (Au) were employed, and each anode target material was simulated in the energy range of 30 keV-150 keV with a step of 5 keV. Once the x-ray source properties were identified, 50 beams (25 for W and 25 for Au) were simulated.

For the SPECT system, a new technique was employed. It was difficult to approach such an operation in the same way as the CT, due to the source (radiopharmaceutical-isotope) which is injected directly into the patient and is irradiated from within the body as it travels within the patient. Following the injection, the patient is placed on the SPECT bed, and the imaging system takes circular pictures from all angles, producing a sinogram as an output. Finally, specialized algorithms recreate the raw data, sinogram, into a 3D picture. All of these extra steps, from positioning the patient on the bed up until the final exam 3d picture is produced, are not seen both by the patient and the doctors. The SPECT system is difficult to simulate, but with the assistance of GATE and STIR it became possible.

The technique was to mimic a SPECT head system and attempt to optimize the SPECT head and reconstruction procedures. The open-source program GATE was utilized in collaboration with STIR to rebuild the image from the raw output data provided by the GATE simulation. The filtered back projection (FBP) and iterative technique of maximum likelihood estimation (MLE-OSMAPOSL) algorithms provided by STIR. Two distinct SPECT head scenarios were simulated: one with an AnyScan S FLEX system SPECT head and one with a custom small animal SPECT head.

In the instance of the AnyScan system, the Jaszczak spheres phantom for both hot and cold spheres modes were utilized. In both cases, hot and cold, the rebuilt of the sinograms with FBP and OSMAPOSL was necessary in order to evaluate how the reconstructed pictures differed and if there is a benefit to use one over the other. For the case of the small animal SPECT head the Jaszczak hot rod phantom was used, but with very small dimensions to test the distinctive ability of such a system and the limitations of GATE to simulate. In the instance of OSMAPOSL, an investigation was carried out in order to determine the best settings between the number of iterations and the subsets required to provide the greatest picture quality, for both the AnyScan and the custom small animal SPECT head. For the AnyScan also the performance of the whole SPECT system when the crystal material changes from NaI to BGO, LSO, and GSO was analyzed. On the SPECT head for the small animal, an evaluation was being carried out in order to measure the effect that the collimator’s hole diameter has on reconstructed pictures.

Publications

International scientific journals with peer review:

1. Nikolaos Chatzisavvas, Georgios Priniotakis, Michael Papoutsidakis, Dimitrios Nikolopoulos, Ioannis Valais and Georgios Karpetas, (2021) **Monte Carlo Computational Software and Methods in Radiation Dosimetry**, *Annals of Emerging Technologies in Computing (AETiC)*, IF:1.73.
2. Nikolaos Chatzisavvas, Thanasis Koustas, Georgios Karpetas, Ioannis Valais, Georgios Priniotakis, Dimitrios Nikolopoulos, (2022) **Simulating Medical Imaging x-ray tubes with various parameters using BEAMnrc Monte Carlo Software**, *Open Journal of Radiology,* IF:0.33.
3. Nikolaos Chatzisavvas, Dimitrios Nikolopoulos, Georgios Priniotakis, Thanasis Koustas, Georgios Karpetas, Ioannis Valais, (2022) **Generating CT x-rays and score dosimetric quantities on DICOM-based phantom utilizing Open Source Monte Carlo Software**, *International Journal of Computer Engineering and Sciences Research.*
4. Nikolaos Chatzisavvas, Dimitrios Nikolopoulos, Georgios Priniotakis, Ioannis Valais, Thanasis Koustas, Georgios Karpetas, (2023) **Monte Carlo Simulation of**

Cone x-ray Beam and Dose Scoring on Voxel Phantom with Open Source Software EGSnrcmp, *Annals of Emerging Technologies in Computing (AETiC)*, IF:1.73.

National scientific conference proceedings with referees:

1. Nikolaos Chatzisavvas, Thanasis Koustas, Georgios Karpetas, Ioannis Valais, Georgios Priniotakis, Dimitrios Nikolopoulos, **Investigation of x-ray tube target material, anode angle and filter at 120keV and 30keV using Monte Carlo**, (poster) *1st Panhellenic Congress of Medical Physics*, Athens, 23-25 September, 2022.
2. Nikolaos Chatzisavvas, Thanasis Koustas, Georgios Karpetas, Ioannis Valais, Georgios Priniotakis, Dimitrios Nikolopoulos, (2022) **Investigation of x-ray tube target material, anode angle and filter at 120keV and 30keV using Monte Carlo(Abstract)**, *Abstracts/Physica Medica.*

Financial Support

This doctoral dissertation was supported by The Special Account for Research Funds of ELKE/PADA of the University of West Attica.

Chapter A. Theoretical background

General Introduction

This part of the doctoral dissertation contains all of the pertinent material on physical processes and Monte Carlo modeling for the sort of experimentation that needs to be conducted. To clarify what a particle is, what are the physical events that occur when kinetic energy is given to particles, how they interact with matter and which are the physical phenomena observed by other scientists over the course of the years, in a few remarks. The Physics Processes and Monte Carlo Computational Techniques are the two main chapters in this section.

In the first chapter, ions were introduced, particularly their interaction with matter, their energy loss mechanisms and how they collide with other particles. In addition, a closer look at photons, how they interact with physical matter, what kinds of effects have been observed over the years and what information can be used to model such phenomena is being described. Following that, the question what radiation dosimetry is and what are the quantities that can be calculated is being addressed. Because x-ray tubes are the most fundamental component in CT scanning systems, a few words on the generation and quality of photons generated are necessary. In addition, it would be helpful to know how a CT scanner and a SPECT scanner work from the ground up. The next step is to learn how to model complex systems, or at the absolute least, how to model a single experiment and extract meaningful data from it. Also, a closer look at the various protocols utilized in modern medicine was presented. The last chapter is devoted to Monte Carlo methodology, in which an explanation of the fundamental principles was being provided, as well as an overview of how to approach stochastic approaches by utilizing complex algorithms for solving deterministic problems. The case of particle physics simulation is complex so in order to plan such computation several parts needs to be addressed.

General Aims

In this subchapter, the fundamental principles of radiation transport through matter and the fundamentals of the operating principles of SPECT and CT are presented.

Additionally, the principles of Monte Carlo techniques are also taught, to give the framework and basis to comprehend the how the simulations are happening on the computing device.

1 Charged Particle Interaction with matter

1.1 Introduction

The idea of matter as empty space occupied by tiny invisible bits was suggested as early as few centuries BC, most notably by Democritus of Greece [1]. However, the most conclusive proof of matter structure was disclosed with the discovery of radioactivity in 1896 by Henri Becquerel [2]. The definition of a heavy particle is one having a value of Z between 26-1. A significantly charged particle passing through media has an impact on the electromagnetic force acting on the atomic electron. The nucleus is ionized and stimulated, which causes the particle to give up energy [3]. The mass-based impact-stopping power calculation for heavy charged particles developed by H.A. Bethe using modern quantum mechanics is presented in eq. 1.1:

$$\frac{1}{\rho}\left(\frac{dE}{dx}\right)_{col}=\frac{S_{col}}{\rho}=\frac{4\pi r_e{}^2 mc^2 z^2 ZN_A}{\beta^2\alpha}\ln\frac{2mc^2\beta^2}{I\left(1-\beta^2\right)}-\beta^2 \quad (1.1)$$

in which β=V/c is the proportion of the particle's speed over the speed of light, $r_e = e^2/mc^2$ is the fundamental electron radius, I is the average excitation energy of the media that the particle is passing through and z is the charge of the heavy ion.

1.2 Heavy charged particles interactions

It was determined that Bethe's formula was accurate when compared to experimental evidence. This nonetheless is unable to replicate the experimental findings in the low-energy region below a few hundred keV. When rapid ions slow down close to the Bragg peak, events featuring electron capture and loss by traveling ions get a growing crucial part of the energy loss mechanism. By including the effective charge as a parameter, the impact of charge exchanges is lessened. ICRU Report 49 [4] recommends that additional adjustment parameters be included to the algorithm. If the stopping power of one particle has been determined, it can be used to approximate the stopping power of another particle moving at an identical speed.

It is impossible to ignore the energy loss resulting from the elastic scattering of heavy ions with a nucleus less energetic than 10 keV. Nuclear stopping powers are the term used to describe the discharge energy of the target nucleus as an outcome of the kinematical relationship between them. The differential cross section for elastic scattering, $d\sigma_{el}/d\Omega$, is used to represent the mass nuclear-stopping power S_{nuc}/ρ.

$$\frac{1}{\rho}\left(\frac{dE}{dx}\right)_{nuc}=\frac{S_{nuc}}{\rho}=\frac{2\pi N_A}{A}\int_0^{\pi}\frac{d\sigma_{el}}{d\Omega}\,W(\theta,E_K)\sin\theta d\theta \quad (1.2)$$

with $W(\theta, E_K)$ representing the rebound energy, which is affected by the scattering angle θ and the ion particle's kinetic energy E_K. The total stopping power is equal to the sum of the nuclear loss and impact loss since the radiative stopping power of heavy ions may be disregarded [5].

$$\left(\frac{dE}{dx}\right)_{tot}=\left(\frac{dE}{dx}\right)_{col}+\left(\frac{dE}{dx}\right)_{nuc}\ \text{or}\ \frac{S_{tot}}{\rho}=\frac{S_{col}}{\rho}+\frac{S_{nuc}}{\rho}\quad (1.3)$$

The proportion of the output of nuclear-stopping power to total stopping power is negligible at energies greater than 10 keV, but it increases when the energy is lessened. This is equivalent to around 30% at 1 keV.

1.3 Electron & Positron interactions

Charged particles have a significant role in radiation therapy. Despite the fact that the main radiation is a photon beam, the biological effect, such as cell death or other changes that might result in cancer, is produced by charged particles, frequently described as secondary radiation. In actuality, photons (and neutrons) are known as indirectly ionizing radiation, while ions are generally referred to as ionizing radiation [6].

The ion's Coulomb electric force field engages with each atomic unit it encounters, causing collision losses and radiative losses with electrons in orbit and nuclei, respectively. This happens when the charged particle encounters a substance medium. The particle must contact with a vast array of other particles until its kinetic energy wears out. Since the energy transfer from the ion to the material matter in every single atomic collision is generally minimal. Stopping power is a term used to indicate how much energy a charged particle loses when it passes through an absorbing substance.

The two different kinds of stopping power are radiative stopping power and collision stopping power, which results from charged particle interactions with the media of absorption orbital electrons. Coulomb interactions take place when an ion travels through an absorbing medium and comes into contact with the nuclei of atoms and orbital electrons [3].

These events may be divided into three groups based on how much the classical impact parameter b differs from the classical atomic radius a:

I. For b<<a, Bremsstrahlung photon creation.
II. For b≈a, Hard Collision.
III. For b>>a, Soft Collision.

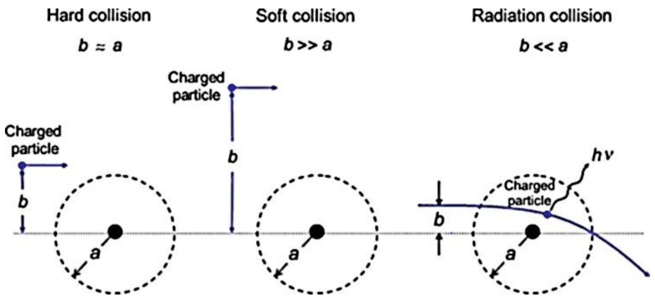

Figure 1 Ion interaction with a nucleus, three types of collisions. [7]

The electron often experiences a large number of encounters before its kinetic energy is depleted. The charged particle's path may be altered by elastic or inelastic scattering, and it might give up some of its motion energy, which is transferred to the medium during each impact or to photons, radiative loss. The rate of diminished energy per unit of route length experienced by ions in a medium is known as the linear stopping power (dE/dx). The mass stopping power S, being equivalent to the linear stopping power divided by the density of the receiving media, is the typical unit of measurement for stopping power, which is represented in $MeVcm^2/g$. The substance's capability to inhibit charged particles from moving through it is one of its properties [4].

Stopping powers come in two different varieties:

a) radiative stopping power produced by Coulomb interactions with the targets media atom. These events, also called bremsstrahlung interactions, where only electron and positrons significantly lose energy.

b) Collision (ionization) stopping power, brought on by interactions between charged particles and the orbital electrons of the absorber. When both large and small ions collide, energy is transferred from the ion to orbital electrons, which leads to the stimulation and ionization of the target media's nuclei.

The combination of the radiative and collision stopping powers for a charged particle of energy EK moving into an atomic number Z material is known as the total stopping power S_{tot}.

$$S_{tot}=S_{rad}+S_{col} \quad (1.4)$$

The Coulomb force, which occurs when an ion interacts with an orbiting electron in an absorbing material, allows for the exchange of energy that can either excite the electron into a higher orbital shell or release it from the atom, ionization. It is important to note that an immediate collision is not necessary for the incident ion to cause an electron in the target material to move. The incident ion may engage with several orbital electrons in the matter at once because the Coulomb force has an infinite range. The ion does not deviate significantly from its starting status since only a small quantity of energy is transferred upon excitation. The atom becomes not stable when one electron is moved to a higher orbit. In addition, this will cause the electron to finally return to its steady place and emit a distinctive x-ray [7]. Ionization is the conversion of an atom into a positively charged ion as a result of an exchange of energy from an incoming ion to a nucleus electron.

The electron's kinetic energy will be what differs between the binding energy and the transmitted energy. The term "delta-ray" is used to describe an electron that has sufficient energy to produce secondary ionization and excitation. Recognizing these secondary ionizations is essential to the scheduling and validation of radiotherapy treatments since they must be taken into consideration when determining a patient's radiation dosage. Due to the greater amount of energy conveyed during ionization compared to excitation, the ions are deflected more significantly off their intended destination.

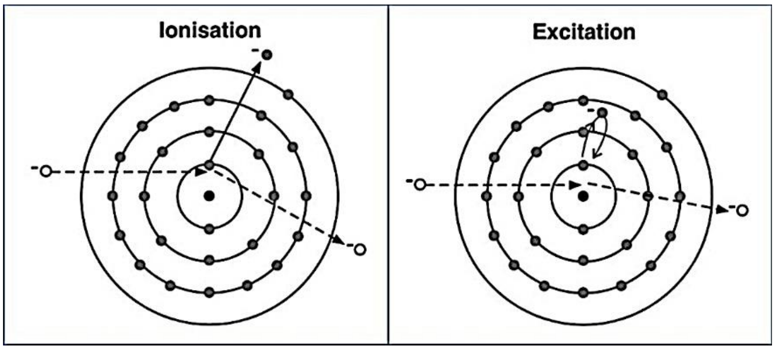

Figure 2 Ionization and Excitation processes [8].

It can be demonstrated that the energy transfer Q can be calculated using Newton's second equation for the force involving charged particles and the classical, non-relativistic collision model, as Bohr did a while ago.

$$Q=\frac{2k^2z^2e^4}{mb^2v^2} \quad (1.5)$$

where b is the impact variable, m is the electron's mass, v is the main particle's speed, and z is the charge on the main particle. The k is a constant, which appears in the Coulomb-force model and has value equal to $8.9875\times10^9\ \mathrm{N\cdot m^2\cdot C^{-2}}$.The differential cross-section per electron in the energy transfer Q, provides the following classical equation:

$$\frac{d\sigma}{dQ}=\frac{2\pi z^2e^4k^2}{mv^2}\frac{1}{Q^2} \quad (1.6)$$

The principle of stopping power, which can be expressed as the mean amount of energy loss (dE) per unit of space (dx) across the path of any ion in the matter, comes straight from the presence of incredibly frequent, small energy losses. The mass collision stopping power $(1/\rho)(dE/dx)_{col}$ or $S_{col}/$ is a common representation of this and is calculated from:

$$\frac{1}{\rho}\left(\frac{dE}{dx}\right)_{col}=N_A\left\langle\frac{Z}{A}\right\rangle\int_{Q_{min}}^{Q_{max}}Q\frac{d\sigma}{dQ}dQ \quad (1.7)$$

Z is the element's atomic number, NA is its Avogadro number, and A is the target element's relative atomic mass. The emission of bremsstrahlung radiation, also known as radiative energy loss, can occur when high-energy ions reach the kernel's Coulomb field due to the possibility that they could decelerate and experience a significant deflection [9]. Throughout this process, energy passes on from the ions to a continuous spectrum of bremsstrahlung photons that can either be recycled or exit from the substance in question.

These losses are also more probable for charged particles that are energetically interacting in a high-Z receiving material. Therefore, for the kinds of substances and energies of ions used in nuclear medicine, radiation energy loss is far less significant than collisional energy loss.

Bremsstrahlung is produced when very light electrons are accelerated in the core's powerful electric field [10]. The nuclear charge of a moving particle, Z, has a relation to its mass, m, divided by this charge. The magnitude of the radiation that results is related to $(Z/m)^2$. In low-Z materials, this energy loss mechanism is rather minor, and it has no effect at all on heavy-charged particles. The cross-section of this fully non-classical process, σ_{rad}, is very complicated. It may be roughly calculated as follows:

$$\frac{d\sigma_{rad}}{dh\nu} \infty \frac{1}{h\nu} \quad (1.8)$$

Similar to how collision losses were described in the paragraph before, a radiative stopping power, $(dE/dx)_{rad}$ or S_{rad}, in addition to a mass-based radiation stopping power (S_{rad}/ρ), can be determined. The mass radiative stopping power in high energy roughly resembles the following:

$$\frac{1}{\rho}\left(\frac{dE}{dx}\right)_{rad} \infty \frac{Z^2}{A} EB \quad (1.9)$$

where B is a function of E and Z that changes extremely slowly. For increasing Z, the Z^2/A variable leads to a rise in rad/r. Equation 2.36 demonstrates that as kinetic energy grows the radiative stopping power climbs about linearly.

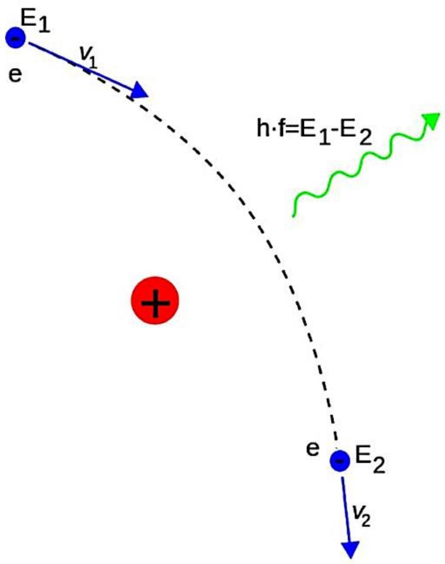

Figure 3 Visual representation of the bremsstrahlung process [11].

1.4 Conclusions

This chapter covered the principles of understanding charged particles, including what they are, how they differ between light (electron-positron) and heavy (proton) charged particles, and how they interact with matter. Concepts including the bremsstrahlung process, ionization and excitation processes, as well as the stopping power of charged particles, both radiative and collisional, were discussed. The mathematical basis with cross-section concepts used in particle physics was taught along with a rudimentary explanation of the mathematics behind those physical processes.

2 Photon Interaction with matter

2.1 Introduction

Electromagnetic waves consist of both electric and magnetic fields travelling via matter perpendicular to each other. Such waves can be recognized by a few highly distinctive properties, such as wavelength (λ), their transmission medium is vacuum and they travel at the speed of light. Now, it is simple to determine the cycles per unit of time (frequency) v=c/λ. If the electromagnetic waves can ionize molecules and particles within the atomic structure, then it is defined as ionizing. Once the electromagnetic ionizing radiation passes via matter, then the best model to describe such interactions would be to think of electromagnetic waves as particles called photons. Each photon has an energy equal to h*v, where h is Planck's constant and v is the frequency. Unlike electrons [12], photons might have some, one or none events of encountering other particles as this phenomenon is by nature stochastic. Each encounter results in the production of secondary ionizing particles, which could or could not be charged. While secondary photons may travel a great distance before meeting, charged particles contribute to local energy deposition by depositing their energies close to the point of the encounter. The introduction of interaction coefficients that assess this energy transfer will highlight the significance of the transmission of energy to charged particles in dosimetry. Because of how they interact and produce secondary electrons, secondary photons are important. As a result, they affect dose as well as the photon fluence within and around a treated body.

2.2 Cross-section definition

Photons interact with atomic electrons, the nucleus, atomic particles, and molecular structures. The probability of interacting with a target item is depicted using the cross-section σ. The likelihood of contact may be calculated using this information, which can be thought of as the target's cross-sectional area in the plane normal to the incident photon direction. Considering a beam that randomly impinges one photon onto an absorber that has one target entity for every unit p of space measured in the photon direction. Assume that if the photon crosses across the target's cross-sectional area, it will interact. The probability of contact, p [13], is dependent on how much of the unit area is filled by the target region. In terms of numbers, this is the same as σ the cross-section. Photon beams interactions can be explained via absorption and scattering mechanisms. The energy from the incoming photon is sent to the target entity once it completely absorbs all of its energy. Secondary particles are emitted either during or following the impact. The direction of motion, energy, and momentum of the object of interest may be changed because of the interaction between an incoming photon and the target object during the full scattering process.

On the other hand, if the photon particle is not absorbed, the laws of classical kinematics govern changes in energy and momentum. The three main absorption methods are pair production, triplet production, and photoelectric absorption. The two main scattering processes are coherent and incoherent. The nuclear photo-effect is an absorption mechanism that takes place close to the electric field of the nucleus. Equation 1.10 may be used to demonstrate that no matter which process occurs, the cross-section for all interactions is equal to the total of the cross-sections for the various processes.

$$\sigma=\sigma_{pe}+\sigma_{coh}+\sigma_{incoh}+\sigma_{pair}+\sigma_{trip}+\sigma_{phn} \quad (1.10)$$

An atomic electron, a nucleus, an atomic particle, or a molecule structure are a few examples of the aiming object. It's crucial to differentiate between these groupings. Where appropriate, an index σ is added to in the following to indicate the kind of interaction target. As a result, ${}_{e}\sigma$ and ${}_{\alpha}\sigma$ are used to represent the cross-sections per electron and per atom, respectively. This relationship between the cross-sections is shown by equation 1.11. The cross-section units are measured in m^2, as well as the non-SI unit called a Barn, where 1 barn equals 10^{-28} m^2. [14]

$${}_{\alpha}\sigma = Z\ {}_{e}\sigma \quad (1.11)$$

2.3 Differential Cross-section

Most times when photons particles are being scatter the amount of particles after scattering are distributed anisotropic and not isotropic in relation to the direction and the polarization of the original particle. In order to estimate these kind of events the cross-section is defined and observed as a function of the angle Ω in the path of the scattered particle, in our case photon. The differential cross-section $d\sigma/d\Omega$ is being needed in our case and it is calculated in an identical manner as the total cross-section, with $(d\sigma/d\Omega)d\Omega$ representing the probability of a photon to scatter in an angle $d\Omega$.

$$\sigma = \int_{4\pi} \frac{d\sigma(\theta,\varphi)}{d\Omega} d\Omega \quad (1.12)$$

Where $d\Omega = d(\cos\theta)d\varphi = \sin\theta d\theta d\varphi$ (1.13)

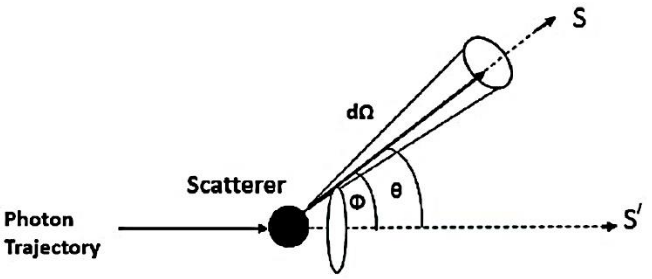

Figure 4 Photon scatter trajectory [15].

Once a photon beam is passing through a medium all particles may have a number of ways it can interact with the medium's atoms, that kind of interactions could involve the nuclei of the material, the orbiting electrons and the free electrons. It could be direct photon with particles (proton, neutron) interaction or interactions with the nucleus' electromagnetic realm [12]. Photons collisions with electrons occupying particular orbits could be with a weakly bound electron, also known as free electron, resulting to Thomson scattering, triplet formation and Compton effect or it could be with a tightly bound electron resulting in photoelectric effect.

2.4 Photon Scattering

An electron, which has strong connection to the nucleus, has a binding energy E_B that is relatively low to the energy of photon hv, for the interaction between those two to happen the E_B energy must be close to the energy of the photon but slightly lower than it. If the interaction of the photon occurs with a tightly bonded electron, then it is possible to state that the photon engaged with the complete atom.

When photons contact with an atom, one of two things can happen:

i) the photon disappears and some of its energy is transformed to negative or positive charged particles, electron-positron, or

ii) the photon is dispersed. In this instance, one of the following things may occur:

a) The resulting particle has the same energy as the initial photon, and no charged particle is formed.

b) The dispersed photon has less energy than the incident photon; the energy surplus is delivered to a charged particle.

The energy of the charged particles that are produced in the media because of photon interactions is deposited there by Coulomb interactions with the orbital electrons of the particular media. In the event that they have sufficient kinetic energy, they can irradiate it by interacting with the nuclei of this media via Coulomb interactions [16].

Throughout a scattering event, the photon changes its trajectory of motion. When the energy of the scattered photon decreases, incoherent scattering takes place. When there is little or no energy loss throughout the scattering process, coherent scattering takes place. Other names for this phenomenon are elastic scattering and Rayleigh scattering. The target electron must be free and at rest at the time of the collision in order to adequately describe the motion of the scattering process. This hypothesis is only valid if the photon beam energy is much higher than the atomic electron's binding energies.

At lesser energies of photons, the nucleus electrons' binding energies must be taken into account. After that time, the particle might scatter either from a single bound electron, incoherent scattering, or from every bound electron at once, phase-coherent scattering. In the latter case, the entire atom takes part in the process to maintain momentum [6].

A portion of the photon's energy is transferred to an electron in the atom's structure that undergoes incoherent scattering and is ejected from the atomic shell. This mechanism was initially explained by Compton, who presupposed that the electron was freely and at rest when it collided. The angle θ, angle of scattering, distributes the energy hv of the entering photon. The dispersed photon's energy, hv', is determined by the Compton equation.

$$h\nu' = \frac{h\nu}{1+\alpha(1-\cos\Theta)} \quad (1.14)$$

where $\alpha = h\nu/(m_0c^2)$ and m_0 is the mass of the electron at rest.

According to the equation, a photon loses no energy when it is scattered forward (θ=0). The dispersion of light at an angle of 180 degrees, or reverse scattering, causes the photon to lose the most energy. The percentage of scattering back photons reaches a limit of $m_0c^2/2$ =256 keV, at high photon energies and $m_0c^2/2$= 511 keV, is the comparable limit threshold for 90° scattering.

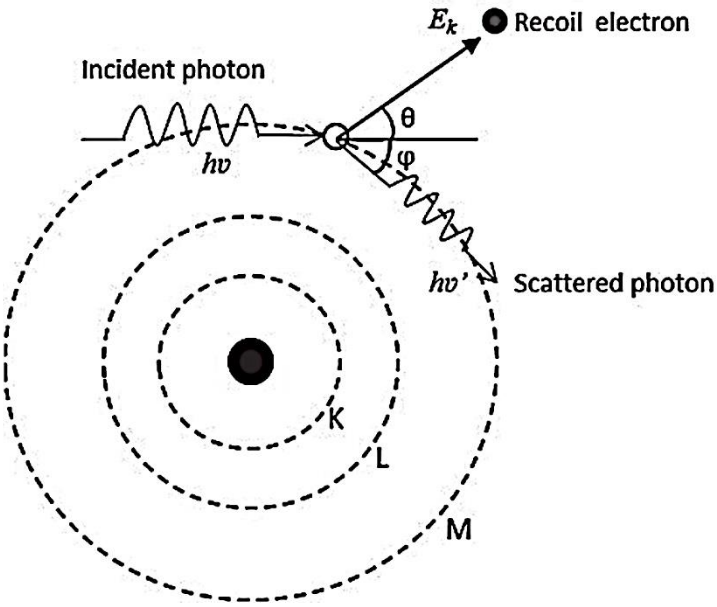

Figure 5 Compton Scattering effect visualization [17].

E_e=hv - hv' gives the electron energy to move. This energy becomes nothing when a photon scatters in front, and it gets its maximum value when a photon scatters behind, with $E_{e,max}$=(hv2α)/(1+2α).

Klein and Nishina, who created the initial formula to determine the value of the Compton scattering cross-section, received credit for giving it a name. the cross-section of the per-electron differential is:

$$\frac{d_e\sigma_{KN}(\theta)}{d\Omega}=\frac{r_e^2}{2}\left(\frac{h\nu}{h\nu'}\right)^2\left[\frac{h\nu'}{h\nu}+\frac{h\nu}{h\nu'}-\sin^2\theta\right] (1.15)$$

with r_e (2.818 fm) is the electron's fundamental radius.

Equation 1.15 may be used to replace hv' in Equation 1.14 to calculate the overall Klein-Nishina cross-section of each electron. The outcome is:

$$ {}_e\sigma_{KN}=2\pi r_e^2\left[\frac{1+a}{a^2}\left(\frac{2(1+a)}{1+2a}-\frac{\ln(1+2a)}{a}\right)+\frac{\ln(1+2a)}{2a}-\frac{1+3a}{(1+2a)^2}\right] \quad (1.16)$$

Each atom has an overall cross-section of:

$$ {}_{a}\sigma_{KN}=Z_{e}\sigma_{KN} \quad (1.17) $$

The secondary photon will go much further than the Compton electron, but the energy delivered to the Compton electron will be deposited at the point of contact. It is significant to separate the total cross-section into the amount of absorption (σ_a) and the amount of scatter (σ_s) components.

$$ \sigma=\sigma_a+\sigma_s \quad (1.18) $$

where $\sigma_a=\langle\frac{E_e}{h\nu}\rangle\,\sigma$ and $\sigma_s=\langle\frac{h\nu'}{h\nu}\rangle\,\sigma$

The incoherent scattering function S(x,Z) is often used to quantify the impact of electron attachment on the incoherent scattering cross-section. The differential cross-section for incoherent scattering per atom can be calculated by:

$$ \frac{d_a\sigma_{incoh}(\theta)}{d\Omega}=\frac{d_e\sigma_{KN}(\theta)}{d\Omega}S(x,Z) \quad (1.19) $$

Normally, it is thought that the incoherent scattering function is a function of the movement of momentum and the atomic number, Z. The incoherent scattering function is related to the probability that the electron will be released from the atomic shell as a result of the movement of momentum x to the nucleus. Its lowest value is at =0, where S(x,Z)=0. As x gets closer to infinity, it increases monotonically and becomes closer to Z, or the number of electrons in an atom. The free electron cross-section is then used to represent the cross-section. At high photon energies, the cross-section for Compton scattering becomes apparent from all reflecting angles [12].

Low energies (hv -> 0) lead to a reduction of equation 1.15 to:

$$ \frac{d_e\sigma_{Th}(\theta)}{d\Omega}=\frac{r_e^2}{2}(1+\cos^2\theta) \quad (1.20) $$

A free electron shifts in Thomson scattering in response to an electromagnetic wave's electric vector. This type of scattering is significant at low energy. The incident wave's frequency matches that of the shifting electron's emission. In this procedure, no energy is lost. Only the angle of displacement is changed during an impact. Quantum physics shows that Thomson scattering is an instance of Compton scattering when the input photon energy is zero. According to Joseph J. Thomson, the photon that enters the beam causes an atom's sort of semi-electron to enter a harmonic vibration. Then, applying the traditional approach, the cross-section for the re-emission of electromagnetic (EM) radiation due to the generated dipole vibration of the electrons was estimated. This type of photon elastic scattering is known as Thomson scattering. [4]

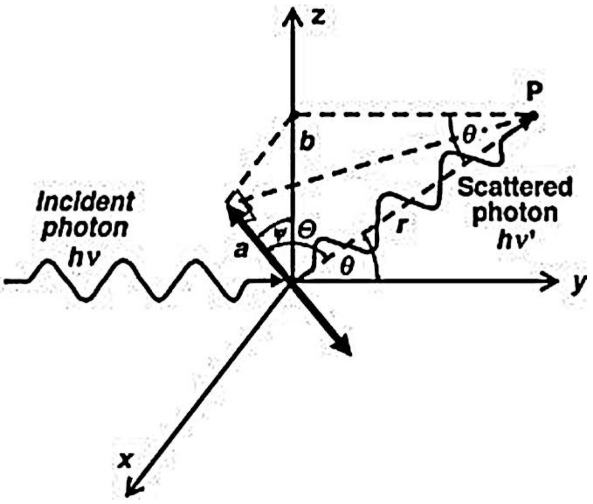

Figure 6 Thomson scattering visualization [18].

Likewise, the total Thomson scattering cross-section for eq. 1.16 is:

$$_{e}\sigma_{Th}=\frac{8\pi}{3}r_e^2=0.655\text{ b}\ (1.21)$$

This observation is crucial since it does not contain any energy-dependent components. It asserts that the electromagnetic waves' energy won't alter when they're reemitted. The Thomson classical cross-section, denoted by the notation $_{e}\sigma_{Th}$, has the same value (0.665 b) for all incoming photons [18]. The atomic cross section ${}_{a}\sigma_{Th}$ is as follows when compared to the electronic cross section ${}_{e}\sigma_{Th}$:

$$ {}_{a}\sigma_{Th}=Z_{e}\sigma_{Th} \quad (1.22)$$

Atomic electrons in coherent scattering symmetrically scatter the photon. The photon essentially loses no energy as it imparts momentum x to the atom while being scattered over the angle q. The pattern of interference typical of the atom's atomic number controls the angular deflection that results from the different electrons scattering in phase. The differential cross-section for coherent scattering is produced by multiplying the differential cross-section for Thomson scattering by the atomic structure factor F squared.

$$\frac{d_{e}\sigma_{coh}(\theta)}{d\Omega}=\frac{d_{e}\sigma_{Th}(\theta)}{d\Omega}\ F^{2}(x,Z) \quad (1.23)$$

Similar to the incoherent scattering function, the atomic shape factor is a generic function of x. The front direction (θ=0), where F(0,Z)=Z, is where the form factor achieves its maximum value. It gets harder and harder for all electrons to scatter in phase without taking energy as x increases. On the flip side, for a given momentum exchange, the normalized shape factor F/Z grows with larger atomic numbers. For low photon energy, x is nearly zero at all refraction angles, and the total cross-section for coherent scattering is as follows:

$$ {}_{a}\sigma_{coh}\cong{}_{e}\sigma_{Th}Z^{2} \quad (1.24)$$

For a large portion of the energy range, x gets larger as energy gets larger while F stays small. Then, when the energy level increases, the cross-section falls roughly this way:

$$\sigma_{coh}\infty\ (h\nu)^{-2} \quad (1.25)$$

Coherent scattering, or Rayleigh scattering, is a process whereby bound atomic electrons deflect photons. The contact causes the confined electrons to revert to their initial condition, and the atom is neither excited nor ionized. The transmitted momentum is absorbed by the entire atom, its rebound energy is insignificant, and the dispersed photon has almost the same energy as the original photon. The scattering angles are minimal because the atom's recoil cannot generate atomic excitation or ionization. The term "Rayleigh scattering" honors scientist John W. Rayleigh, who in 1900 developed a standard model for the dispersion of electromagnetic radiation by atoms [19]. The effect is most apparent for absorption with a high atomic number Z and low photon energies hv, in the amount of energy region where electron binding effects considerably lower, Compton Klein-Nishina cross sections. Due to a coherent contribution from all electrons in the nucleus to the Rayleigh (i.e., coherent) atomic cross-section, the Rayleigh cross-section outperforms the Compton cross-section in the aforementioned energy level [4].

2.5 Photoelectric effect

A photon particle is photoelectrically consumed when it encounters an atom. An atomic electron is ejected from one of the atomic rings with kinetic energy E_e. This is how its kinetic energy is determined:

$$E_e = hv - E_B \quad (1.26)$$

where E_B is the binding force of the nucleus electron and hv is the energy of the colliding photon. The process is impossible when there is a free electron because momentum maintenance requires the atom's activity. Due to the nucleus' enormous bulk, the amount of energy that is communicated to the atom is minimal.

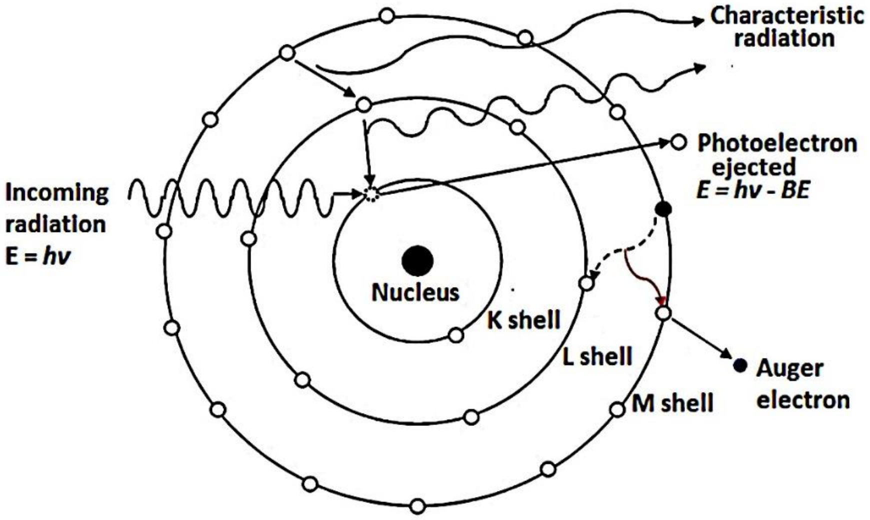

Figure 7 Photoelectric effect visualization [20].

The diagram in Figure 8 demonstrates that when photon energy declines, the cross-section σ_{pe} for photoelectric absorption increases significantly. At energies that match the forces that bind the electrons in the atomic shells, a series of disruptions may be visible in the cross-section. At energies equivalent to the fundamental energies of the target material, these breaks appear [21]. A photon's energy is insufficient to free an electron from its shell below the absorption limit. The photon has sufficient energy to release the electron at just over-the-edge energies. The cross-section increases quickly as a result of more electrons that might potentially take part in the absorption task. When the cross-section increases near the absorption edge, the binding energy increases proportionately. The target material's atomic number has a big impact on the cross-section of photoelectric absorption. As a function of photon energy and atomic number, the cross-section per atom above the K absorption edge is depicted in eq. 1.27:

$$ {}_{a}\sigma_{ph} \cong Z^4/(h\nu)^3 \quad (1.27) $$

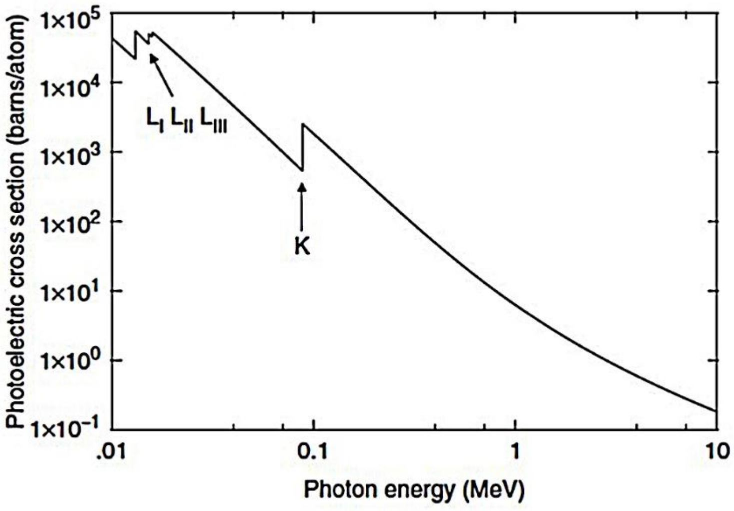

Figure 8 Total photoelectric absorption cross-section for lead [22].

The cross-section rises with the increasing atomic number because of their exponential to the fourth power relationship and inverse exponential connection to the photon energy to the third power. This suggests that this process, particularly at high atomic numbers, has a major impact at low photon energy. It also clarifies the reasons why bones exhibit a large beam attenuation during soft tissue radiography. As the photon energy rises, the photoelectrons' angular distribution starts to be forward-directed, peaking at angles of π/2 to the forward-facing direction at low photon energies. After photoelectric absorption, a hole is left in the atomic shell. In order to fill the empty space, an electron from an outer shell is subsequently employed. The energy released is equivalent to the difference between an electron's binding energies in its two shells [22]. To remove the released energy, either a photon or an electron are expelled. The photon is referred to as a typical x-ray because of its fixed energy determined by the atomic number of the atom and the involved shells. Isotropically emitted x-rays have a distinctive spectrum.

At energies slightly higher than the absorption edge, they could transfer a substantial part of the input photon energy. They are going to have a lesser photoelectric cross-section than the initial photon since their energy is lower compared to that of the absorption edge.

Electrons that are released after an electrical rearrangement are known as auger electrons. The Auger effect, which occurs spontaneously, is a phenomenon in atomic physics where an atom with an electron hole in the deepest (K) shell resets to a state of stability by releasing one or more electrons instead of producing a single x-ray photon.

All atoms are composed of a positively charged nucleus and quantized electron shells. Through the use of electron bombardment, absorbing into the nucleus, or any other technique, if an electron from one of the inner shells is removed, an electron from another shell will move into the empty spot, letting go of energy that is swiftly lost by either producing an x-ray or by the Auger effect [23]. One electron is removed from one of the shells by the Auger effect's potential energy, causing the remaining atom with two electron holes.

As soon as new holes get filled, the procedure will be repeated, emitting x-rays continuously. The possibility of an Auger electron being emitted is known as the Auger yield associated with that shell. The Auger yield drops as the atomic number lowers and the likelihood of generating Auger electrons and x-rays from the inner shell is roughly similar. When the photon energy hv reaches at least $2m_ec^2 = 1.022$ MeV, pair production—the process by which the photon is turned into a pair of electron-positron becomes energetically feasible in conjunction with complete photon absorption [24].

2.6 Pair and Triplet production

For the effect to happen, energy, charge, and momentum must all be preserved. Pair creation occurs in the field of atomic electrons for photon energy greater than $4mc^2$, but the possibility is incredibly slim. This process is called triplet pair generation because it results in the creation of a second recoiled electron. In the production of photon-nucleus pairs, the stumbled energy of a heavy nucleus is negligible. Energy and charge may be kept even if pair creation takes place in free air for hν > $2m_ec^2$. However, the effect must take place in the Coulomb field of a collision particle that can effectively absorb a significant portion of the photon's momentum in order to preserve linear momentum. The photon energy hν is thus changed into:

$$h\nu=2m_ec^2+E_{K+}-E_{K-} \quad (1.28)$$

where E_{K+} and E_{K-} are the kinetic energies of positrons and electrons, respectively. The electron and positron energy distributions fluctuate between 0 and hν - $2m_ec^2$.

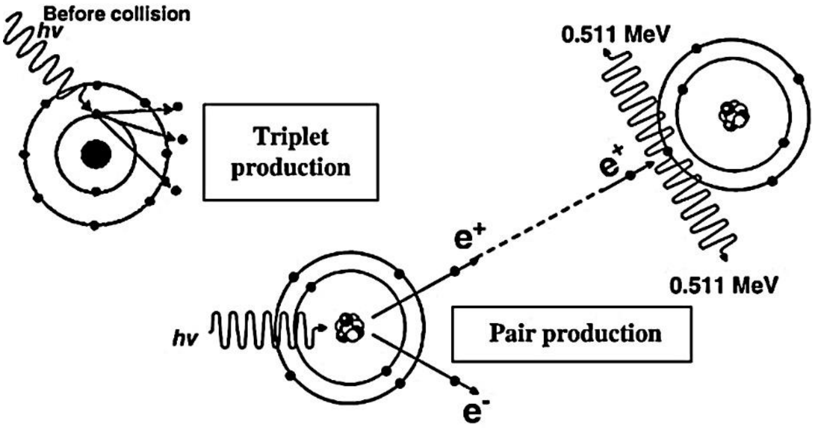

Figure 9 Pair and Triplet production visualization[25].

Just like in photoelectric absorption, the nucleus has to maintain momentum. The electron-positron pair splits its accessible kinetic energy almost equally on average. The likelihood of either particle absorbing most of the energy is low [26]. Both electrons are ejected in different directions. For energies greater than the limit of energy, the average angle θ of divergence from the photon direction is substantially bigger.

$$\bar{\theta}\approx\frac{m_0c^2}{\bar{E}_K} \quad (1.29)$$

where

$$\bar{E}_K=\frac{1}{2}(h\nu\text{-}1{,}022\ \text{MeV}) \quad (1.30)$$

The decay of an electron-positron pair produces photons in an opposite process. By decreasing its velocity, a positron pulls an electron. Then a positron atom, which resembles a hydrogen atom, is formed. The annihilation yields two photons with a total energy of 511 keV [27]. When photons are emitted, they go in opposing directions. The likelihood of annihilation in-flight is smaller than ten percent.

The cross-section for pair generation in the nuclear field is zero below the threshold. It then quickly rises as the energy grows, until it varies about as the square of the nuclear charge Z, i.e.

$$_{a}\sigma_{Pair} \infty Z^{2} \quad (1.31)$$

The cross-section for triplet production varies approximately as Z at energy over the point of threshold.

$$_{a}\sigma_{Tr} \infty Z \quad (1.32)$$

In hydrogen, triplet generation is as important as pair generation, although it loses significance in comparison to pair formation as the atomic number rises. The Z dependence of these processes is being reduced because, in high atomic number structures, the target objects' electric fields are filtered by the atomic electrons nearby.

In a nuclear reaction, photons with energies larger than the nucleon's binding energy can be consumed. The reaction results in the expulsion of one or more nucleons. The fact that the nuclear photo-effect cross-section depends on the atomic number, Z, and the atomic mass, A, and consequently on the isotopic abundance in a sample of a particular element, complicates matters. Due to these discrepancies, it is difficult to find them in a table form. In contrast to the photoelectric effect, Compton scattering, and pair formation, the chance of a photonuclear reaction is much smaller [12]. Still, this reaction is important in terms of radiation protection since it generates neutrons. Additionally, the procedure frequently leaves behind an unstable atom. These factors make this reaction essential in the field of high-energy electron accelerators.

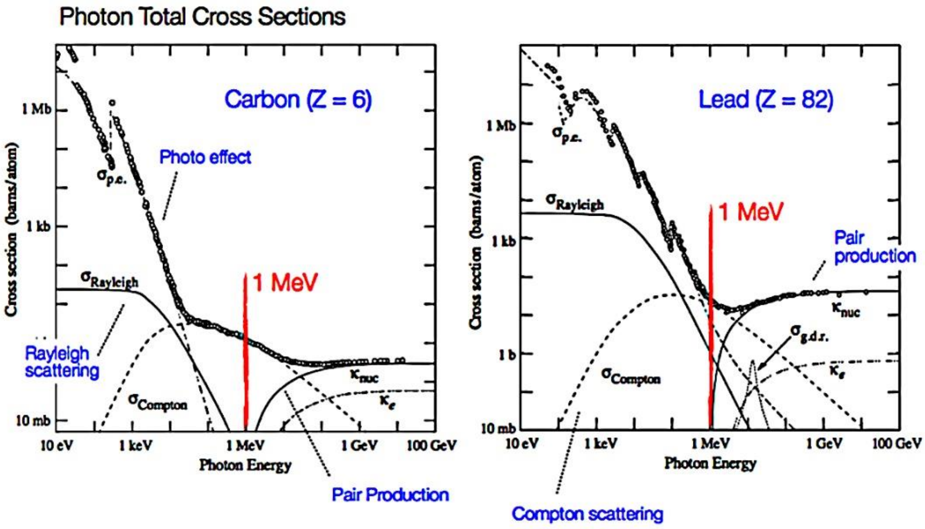

Figure 10 Total and partial cross-sections for Carbon and Lead [28].

In a wide range of energies, from 100 keV to 20 MeV, this phenomenon is particularly significant in a low atomic number material like carbon. Lead's 800 keV to 5 MeV energy range is the only one in which incoherent scattering predominates in high atomic number materials. This is due to the process' considerable atomic number dependence and the fact that pair production starts at energies higher than 1.02 MeV. The pair production cross-section for both components approaches a fixed value of around 100 MeV.

The proportionate contribution of triplet production increases as the atomic number decreases. The nuclear photo effect significantly increases the total cross-section in a narrow energy window near the massive resonance peak. The nuclear photo effect takes place in carbon at photon energy greater than 10 MeV, but it occurs in lead at lower photon energies. Coherent scattering is usually never the main event. At low energies, it is of greater significance than incoherent scattering; nonetheless, photoelectric absorption is by far the most important process [6].

2.7 Conclusions

The electromagnetic waves were classified in this chapter based on their wavelength (λ), transmission medium (vacuum), and travelling with the speed of light. It is referred to as ionizing if such waves may ionize molecules and particles inside atomic structures. Three primary absorption processes, pair generation, triplet production, and photoelectric absorption, are used by photons in their stochastic interactions with other particles. When photons alter their travel trajectory, scattering processes known as coherent and incoherent scattering take place. Coherent scattering happens when there is little energy loss, but incoherent scattering happens when there is energy loss. Rayleigh scattering, Compton scattering, and Thomson scattering are further forms of scattering discussed in this chapter as well.

3 Radiation Dosimetry

3.1 Introduction

Radiation studies and research on radiation implications demand diverse radiation field characteristics at the place of interest as such. Radiation dosimetry is concerned with methods for quantifying the energy deposited in a particular material by either direct or indirect ionizing radiations [29]. A variety of parameters and units have been developed to describe the radiation beam, and the most regularly utilized dosimetric values and their units are listed here.

3.2 Fluence

A beam that consists of ions and thus carrying ionizing radiation, is explained better by a number of quantities such as: fluence of the particle, energy fluence, planar fluence rate, etc. These parameters are commonly used for analyzing particle beams more precisely photon beams but they could also be employed to address ion beams as well. The particle fluence Φ is defined as the ratio of dN by dA, where dN is the number of particles impacting a sphere with a cross-sectional space of dA:

$$\Phi=\frac{dN}{dA} \quad (1.33)$$

The particle fluence metric is m^{-2}. The usage of a sphere with a cross-sectional space dA conveys in the most basic manner that an area dA crosswise to the trajectory of each particle is considered, and hence particle fluence has no effect on the incidence angle of the radiation.

Planar particle fluence is the total amount of particles passing the surface of a plane per unit area and is thus affected by the particle beam's degree of occurrence. The energy fluence Ψ is defined as the ratio of dE by dA, where dE is the amount of radiant energy received on a sphere with a cross-sectional region of dA:

$$\Psi=\frac{dE}{dA} \quad (1.34)$$

J/m^2 is the metric measure of energy fluence. The following relationship may be used to derive energy fluence from particle fluence:

$$\Psi=\frac{dN}{dA}E=\Phi E \quad (1.35)$$

at which E is the particle's energy and dN is the total amount of particles having energy E. Nearly all practical photon or particle beams contain multiple energies, a whole spectrum of energies, and the ideas stated previously must be applied to such beams. Particle fluence spectrum and energy fluence spectrum are notions that replace particle fluence and energy fluence, respectively. They can be calculated as follows:

$$\Phi_E(E)=\frac{d\Phi}{dE}(E) \quad (1.36)$$

And

$$\Psi_E(E)=\frac{d\Psi}{dE}(E)=\frac{d\Phi}{dE}(E)E \quad (1.37)$$

where $\Phi_E(E)$ and $\Psi_E(E)$ denote the particle fluence spectrum and energy fluence spectrum partial differential in energy E, accordingly.

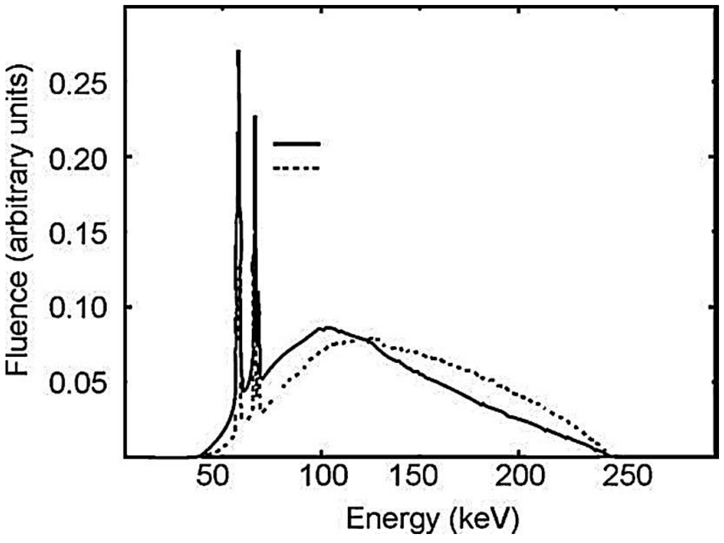

Figure 11 Photon Fluence and energy fluence for an x-ray source with W target, Be+Al+Cu filtration at 250keV [29].

Figure 11 illustrates photon and energy fluence spectrums produced by a 250 kVp orthovoltage x-ray source with additional filtration of 1mm Al and 1.8mm Cu, target material tungsten W, and built-in filtration of 2mm Be. The two separate spikes overlaid across the continuous bremsstrahlung spectrum showed the tungsten target's distinctive x-ray lines, K_a and K_b.

3.3 KERMA - CEMA

Kerma is an abbreviation for the amount of Kinetic Energy Released per unit Mass. It is a proven number that applies to ionizing radiations that are emitted indirectly, such as photons and neutrons. It calculates the mean value of energy converted from indirectly to directly ionizing radiation, without consideration for what happens because of this transfer [30]. In the following discussion, only photons will be considered. The energy of photons is transferred to matter in two stages. Photon radiation transmits energy to secondary charged particles like electrons at the first stage via numerous photon interactions, the photoelectric effect, the Compton Effect, pair production, etc. The ion transmits energy to the material in the second stage via atomic excitations and ionizations.

The kerma can be explained in this regard, as the average energy passed from indirectly ionizing radiation to charged particles like electrons in the material $d\overline{E}_{tr}$ per unit mass dm:

$$K=\frac{d\overline{E}_{tr}}{dm} \quad (1.38)$$

Kerma is measured in joules per kilogram (J/kg). The gray (Gy) is the unit of kerma, with 1 Gy equaling 1 J/kg.

Cema is an abbreviation for converted energy per unit mass. It is a real number that applies to directly ionizing radiations like electrons and protons. The cema C is the ratio of dE_c by dm, where dE_c is the energy loss by ions in collisions with a substance of mass dm:

$$C=\frac{dE_c}{dm} \quad (1.39)$$

Cema is measured in joules per kilogram (J/kg). The gray (Gy) is the term given as the cema unit.

3.4 Absorbed Dose

The absorbed dose is a measured amount that may be used to both indirectly and directly ionize radiations. Energy is transferred to physical matter in two steps for indirectly ionizing radiations. In the first stage, resulting in kerma, indirectly ionizing radiation transfers energy to secondary ions as kinetic energy. In the second stage, these charged particles lose some of their energy as radiative losses and send some of their kinetic energy to the material, resulting in absorbed dosage [31]. The absorbed dosage is proportional to the random amount of energy delivered. The mean energy $\bar{\varepsilon}$ staged by ionizing radiation to a substance of mass m in a certain amount V is expressed as the absorbed dosage by:

$$D=\frac{d\bar{\varepsilon}}{dm} \quad (1.40)$$

The total energy entering and leaving the volume of interest, while accounting for any mass-to-energy conversion occurring within the volume, equals the total energy $\overline{\varepsilon}$ staged by ionizing radiation. For example, pair formation reduces energy by 1.022 MeV, but electron-positron annihilation enhances energy in roughly the same proportion. Because electrons flow across the medium and place energy along their paths, energy absorption does not occur at the same point as the energy transfer represented by kerma. The absorbed dosage is measured in joules per kilogram (J/kg). The gray (Gy) is a term given to the unit of absorbed dose.

3.5 Conclusions

Some fundamental information on radiation dosimetry was provided in this chapter, including the fact that metrics like particle fluence, energy fluence, and planar fluence, among others, are better able to describe ion beams transporting ionizing radiation. Kerma is a known quantity for kinetic energy released per unit mass, while Cema is a valid figure for converted energy per unit mass. Lastly the absorbed dose has been introduced as the measurement used for both indirectly and directly ionizing radiations. Ionizing radiation transfers energy to secondary ions as kinetic energy known as kerma, and charged particles lose some of their energy as radiative losses and send some of their kinetic energy to the material in the known as absorbed dosage.

4 Computed Tomography Radiology

4.1 Introduction

X-ray computed tomography (CT) can give unparalleled information on the interior blueprint of substances at length scales ranging from meters to tens of nanometers. It uses the piercing impact of x-rays to create a sequence of two-dimensional pictures of the item from various angles. This procedure is also known as a CT scan. These two-dimensional projections of the object are then employed by a calculated reconstruction technique to build a stack of divided slices. Through this procedure, the underlying structure of the item is represented digitally in a three-dimensional gray-scale image called a tomogram. The three-dimensional morphology may be seen by mathematically analyzing it, visually slicing it in any direction, digitally color-coding, or making translucent certain elements [79].

The fact that x-ray CT imaging is not damaging over other methods is one of its key benefits. This is crucial when looking at sensitive samples that are unable to be easily divided, like frozen edible substances [32], samples that shouldn't be harmed, like cultural artifacts [33], or samples where the stability of a science and technology component needs to be ensured before it becomes operational, like a generator's blade. This has contributed to the broad acceptance of CT as a medical diagnostic tool, as has the ability of contemporary CT equipment to work at x-ray levels that represent a comparatively minimal danger to people's well-being [34].

4.2 Fundamental of Computed Tomography

The harmless element also makes continuous investigations of how things change in a three-dimensional structure possible, such as the development of a cancerous tumor under therapy [35], the production and assembly of goods [36], or the deterioration of goods in usage [37]. In this regard, CT scanning can be done either regularly in real-time, such as to follow the progression of fluid within rock [39], fractures throughout the breakage of a specimen [40], or the disastrous thermally driven malfunction of a lithium-ion battery [41], or frequently in a time-lapse way like as to comply with the transformation of an embryo [38].

Every projection's measured contrast depends on how the substance interacts with x-rays. Therefore, a variety of contrast settings are feasible to accommodate various scanning tasks. The intensity and phase shift of an electromagnetic x-ray pulse as it travels inside a solid substance depends on the refractive index, n:

$$n=1-\delta+i\beta \quad (1.41)$$

with the real portion (δ) regulating the amount of phase shift and the imaginary part (β) affects the attenuation absorption, of the x-rays as they travel via the substance. While the actual component is used to get phase contrast, the former is used to create attenuation contrast. The x-ray absorption as it passes through the medium is expressed by the linear attenuation coefficient, μ, which is equal to $4\pi\beta/\lambda$, with λ being the x-ray wavelength [42].

The three fundamental operational elements of a CT machine are the specimen the platform, the x-ray detection device, and the x-ray source. The creation and usage of CT systems are governed by the engineering idea "form follows function" [43]. The function may be seen from two associated but slightly dissimilar angles: one governed by the items being seen and the other specified by the structure of the source of x-rays and detection device.

For example, if the purpose is to scan an individual or an experimental pet, the shape will depend on how immobile the patient and their organs must be. Since the x-ray source and detector spin around the resting patient, the shape is a scanner that is housed in a hospital or laboratory. When imaging in centimeter or millimeter scaled size specimens, it is ideal to keep the x-ray source and detection system fixed as the object turns.

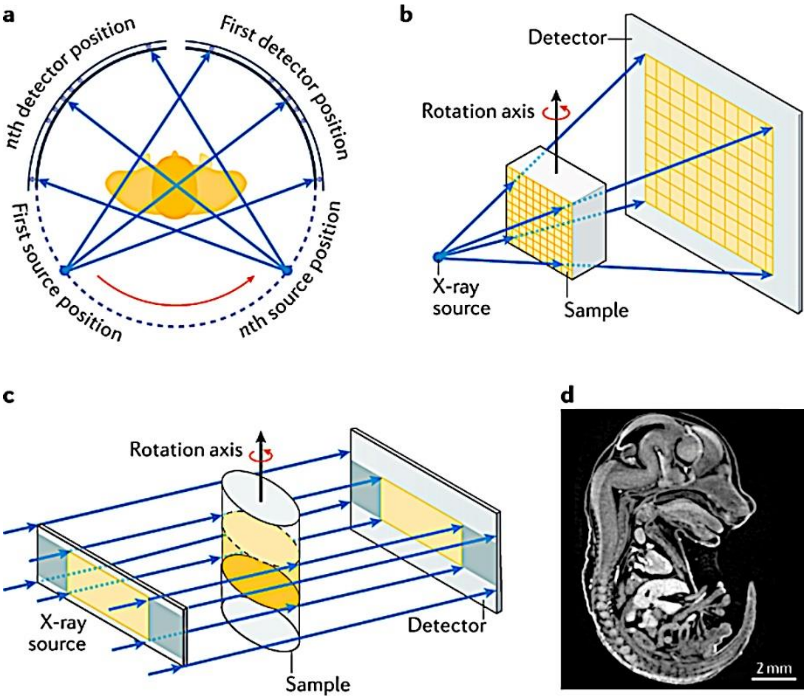

Figure 12 X-ray CT configurations. a) Gantry based system, b) Cone beam system, c) Parallel beam system, d) Slice of an attenuation contrast technique in tomography of a mouse embryo [44].

Realistic scanner types are determined by the x-ray source and the x-ray detector from the viewpoint of equipment operation. Usually, an x-ray tube or a synchrotron storage ring serves as the source in the majority of cases. Both times, the swift acceleration of electrons results in the production of x-rays. While there are only a few synchrotron facilities globally, each of which has hundreds of research workstations, x-ray tubes are somewhat easy to manufacture, plentiful, and affordable components that power laboratory and clinical CT machines. Each approach beams differ in terms of x-ray movement, source shape, and x-ray energy range [45], as explained below.

A variety of x-ray energy is released by tube sources in the form of a cone-shaped, broad polychromatic beam that is typically white and has strong peaks that are specific to the target substance. The electron boosting voltage determines the peak energy of this x-ray energy spectra. Tube source micro CT equipment [46] commonly uses the cone beam architecture to utilize as many photons as feasible that come from where they originate.

A substantial sample volume is illuminated by the x-ray cone's uniform angle. Placing fewer samples toward the source and further away from the detector, will enhance the physical amplification of the picture by expanding the projection of the image across more detector pixels. This geometric magnification reduces the effective size that each voxel represents. Based on the needed resolution, scan timeframes generally range from minutes to hours.

The Hounsfield scale is represented in relation to the linear attenuation coefficient of water at room temperature (μ_{water}) in the ct picture, and the matrix of reconstructed linear attenuation coefficients ($\mu_{material}$) is translated into a corresponding matrix of Hounsfield units ($HU_{material}$) [47]:

$$HU_{material}=\frac{\mu_{material}-\mu_{water}}{\mu_{water}}*1000 \quad (1.42)$$

As can be observed, HU_{air} = -1000 ($\mu_{material} = 0$), HU_{water} = 0 ($\mu_{material} = \mu_{water}$), and HU = 1 is related to the linear attenuation coefficient of water at about 0.1 percent. It derives from the explanation of the HU that, for any material other than water and air, the HU values change when they are calculated at various tube voltages. The explanation is that different materials display the non-linear connection between their linear attenuation coefficient and that of water as an expression of the energies of the photons. This effect is especially noticeable in substances with a large effective atomic number, like bone and blood. The lowest bit depth that needs to be allocated to a pixel is 12, allowing for the development of a typical Hounsfield scale ranging from [-1024, +3071] HU, encompassing the majority of clinically significant cells.

4.3 X-ray source

X-rays are created by bombarding a dense object with accelerating electrons. These electrons experience a constant cycle of collisions and scattering processes as they slow down, producing bremsstrahlung and characteristic radiation. However, the majority of the electron's momentum turns into thermal energy in the target, and very little of it is transformed into x-ray photons. The x-ray generating mechanism determines the energy spectrum's structure. It's important to remember that the energy spectra depict the radiation's strength over the entire beam's energy band [80].

The emission of distinctive x-rays is caused by coulomb reactions that occur between incoming electrons and the atom's electron cloud of the target material. The electron gets thrown out when a rapidly moving electron collides with an electron in a nucleus's distinctive shell and its kinetic energy is greater than the binding energy of the electron in that shell. In the internal K shell, the binding energy is greatest, and it diminishes in the outer shells [48]. Since the energy of the photon released in this process is characteristic of each individual atomic structure, the binding energies for the shells of various substances differ [49].

Characteristic radiation is released for electron transitions to the K and L shells. The position of the electron filling the vacancy is indicated by the suffixes (a, b, g, etc.), where *a* indicates the move from the outermost shell immediately following it, *b* to the outer shell after that, and so forth. K_a radiation is produced by L-to-K shell transitions, K_b radiation is produced by M-to-K shell transitions, and so on [6].

Bremsstrahlung, which translates to braking radiation in German, is an appropriate word to describe this phenomenon. When light-charged particles such as electrons and positrons, interact with heavier charged particles, such as those particles which can be found in atomic nuclei, they lose kinetic energy, which converts to electromagnetic radiation known as bremsstrahlung radiation. The supply of the electron's kinetic energy, the target's width, and its atomic number Z all play a role in the formation of the bremsstrahlung spectrum in an x-ray source [50].

The x-ray tube, which is illustrated in Figure 13 requires three key elements in order to function properly and generate bremsstrahlung and distinctive radiation. The fundamental parts of an x-ray tube are, a source of electrons from a hot tungsten filament with a narrowing cup acting as the tube cathode, an anode or target, and a tube enclosure that preserves the inner vacuum. The electrical current that flows from the cathode to the anode is controlled by an electrical current that heats the filament by regulating the thermal release of electrons. The acceleration potential variation between the cathode and anode controls both x-ray energy and yield. The two main systems that operate throughout the x-ray tube are the filament circuit and the tube voltage circuit.

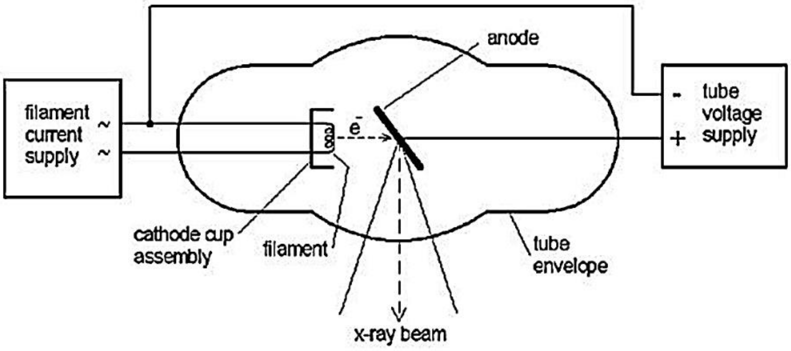

Figure 13 Basic X-ray tube visualization [6].

An electric field is created by the combination of the cathode filament, concentrating cup, anode terrain, and tube electricity, which drives electrons in the direction of the anode's concentrated location. In x-ray tubes with a pair of focal points, two separate filament/cup systems are frequently utilized. The level of focus is controlled by the possibility of variations or biased voltage between the filament and the centering electrode. As the adverse bias voltage at the concentrating cup rises, the focus will get smaller and finally, the current of electrons will stop flowing.

For conventional radiographic purposes, the anode has to have a high bremsstrahlung yield, which necessitates the use of substances with high atomic numbers (Z) [51]. The thermal parameters must also be set so that the highest practicable heat, such as is established by high melting point, vapor pressure, heat transmission, heat concentration, and density, is taken into account due to the poor effectiveness of x-ray production. Tungsten (Z = 74) is the finest material in this situation. The x-ray field's center ray is parallel to the tube axis, and the anode is inclined toward it. Wherever the electrons reach the anode in the electrically powered focus depends on the cathode filament's height.

Contrary to its intended use, diagnostic tubes' anode angles can range from 6° to 22°, with 10° to 16° representing the most typical. The peripheral dimension of the focus size is determined by the filament coil thickness and the intensity of the focusing cup activity. The ability to reduce anode angles and achieve smaller effective focus sizes is constrained by the size of the anode's field of view required to shut off the x-ray beam [52].

4.4 Conclusions

This chapter introduces computed tomography (CT) using x-ray beams. The basic working concept of the computed tomography system is presented, along with an abstract idea of the system's components, such as the specimen platform, x-ray detecting device, and x-ray source. The Hounsfield scale is also shown since output reconstructed CT image files are saved in that scale. Additionally, it is stated how x-ray beams are produced by the bremsstrahlung process and distinctive radiation. Additionally, the basic components of an x-ray tube are described.

5 Nuclear Imaging SPECT

5.1 Introduction

The healthcare imaging method known as single-photon emission computed tomography, SPECT, is often utilized in clinics for treatment checking and diagnostic procedures. They are frequently referred to as nuclear medicine imaging or molecular imaging techniques, alongside positron emission tomography, PET [53]. The true SPECT system wasn't made practicable until 1957, at that time when Hal Anger created the idea of the planar still gamma camera [54], commonly referred to as the Anger camera. That was the beginning so that the first SPECT system would be built, however without the technologies of PET and CT systems it would not be possible for the SPECT to mature from separate images [55] scanning to tomographic scanning. For Emission Computed Tomography (ECT) systems to advance and become helpful in clinics, another ten years were required [56]. Many unique systems were developed in the late 1960s and early 1970s for a variety of specialized uses, including heart and brain imaging [57]. Due to their adaptability, twin or triple camera for general-purpose SPECT scanners dominated the clinic by the middle and end of the 1980s [58].

The first SPECT/CT system was shown in 1992 by a team at the University of California, San Francisco, UCSF [59]. The 2002 release of the GE Hawkeye system marked the beginning of commercially viable SPECT/CT. SPECT/CT can significantly increase the precision of diagnosis by integrating the benefits of the functional information from SPECT with the anatomical data from CT. SPECT systems have progressed steadily during the last 30 years. With the advancement of better technology for computers, better sensors, probabilistic iterative reconstruction methods, and radiation treatments, contemporary SPECT is now a significant tool for both evaluation and treatment in individualized precision healthcare [60].

5.2 Basic SPECT concepts

SPECT imaging has made use of a variety of radioactive substances. During radioactive decay, these substances release gamma photons with distinct energies, known as photo peaks. The gamma-ray release can come from a variety of decay modes, including beta emission (β^-, γ), numerous transitions and conversions as well as a lot of types of electron capture. Among these are radionuclides that decay via β^-, γ mode, which generates electrons that can be employed in treatment to destroy cancer cells when linked to the appropriate medicines [81].

A SPECT structure's primary elements are the gamma ray detector or head, the gantry, and the acquisition computational system. The detector’s heads are positioned on a gantry, which includes the machinery for moving and rotating the detector arrangement around a bed. An acquisition console system controls the whole arrangement, which may autonomously do the whole procedure. Figure 14 depicts a modern SPECT/CT from different angles; this system is from the University hospital of Larissa, Greece. The model name is AnyScan S Flex system, with dual head detectors.

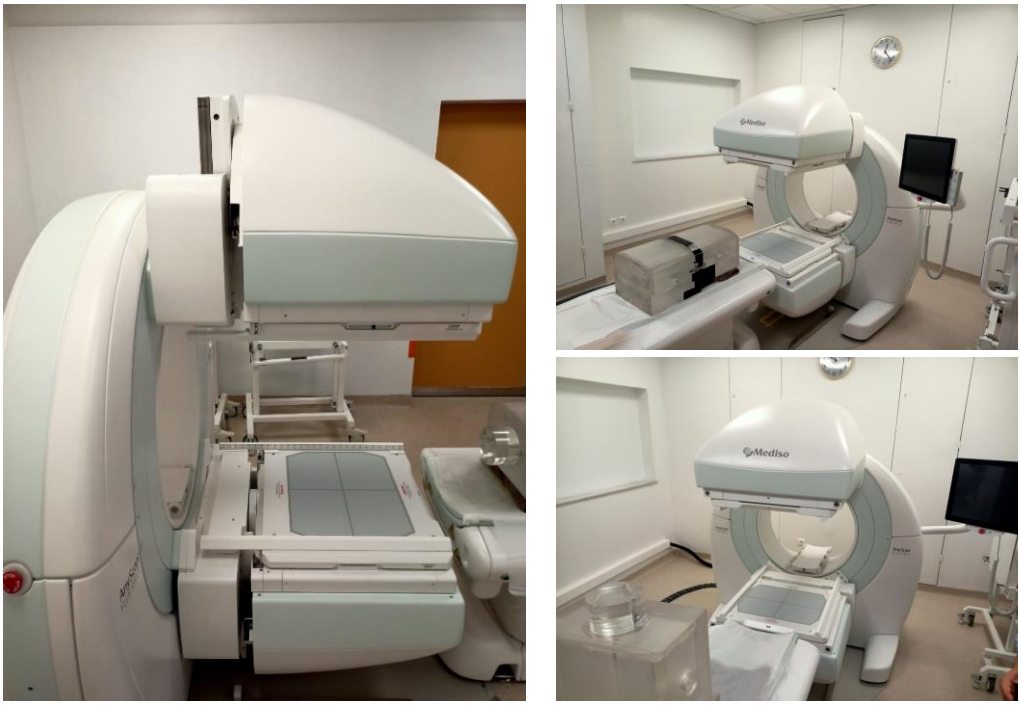

Figure 14 AnyScan S Flex system, with dual head detectors.

A photon detectors catch arriving photons and transforms their energy into electrical signals that processors can analyze. A detector Head has four basic components: the collimator, the light guide, the scintillation crystal and an array of photomultiplier tubes, as it can be observed in Figure 15. When photons arrive at the detector's head, they first contact the collimator. The collimator functions similarly to a filter, because it allows only parallel photons to reach the light guide and the other parts of the detector's head. The collimator is an arrangement of small openings composed of high-density absorbing metals such as lead. Only photon particles moving in the exact same direction as the collimator holes will be able to pass by and hit the scintillation crystal. All other particles will be collected in the collimator, but there will always be a small angle that photons will pass through depending on the collimator's type.

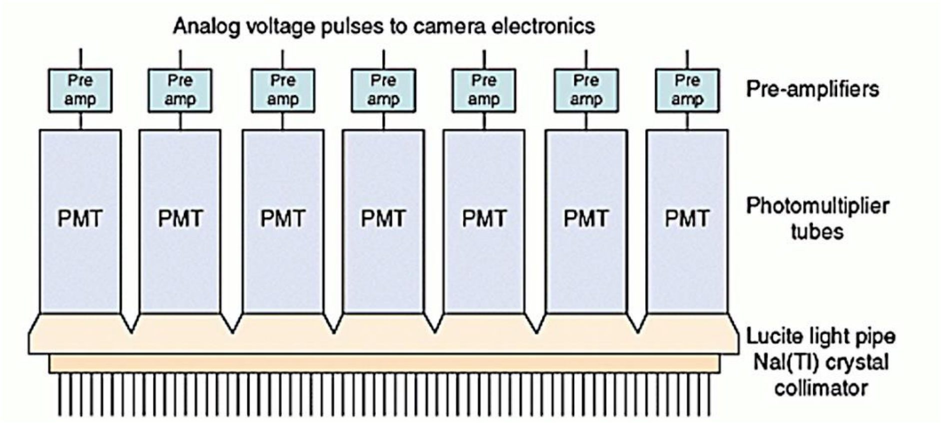

Figure 15 Basic assembly of a typical SPECT detector [61].

In tomographic imaging there are a lot of different collimators for different use cases. There are parallel hole collimators, converging holes' collimators, diverging holes' collimators and pinhole collimators as it can be seen in Figure 16. Most clinical uses can be done with parallel hole collimator, however pinhole and converging collimators are used in special cases such as brain scanning, tiny organ scanning, animal scanning, preclinical scanning [62]. Divergent collimators are rarely used in hospitals because of their low spatial resolution and effectiveness.

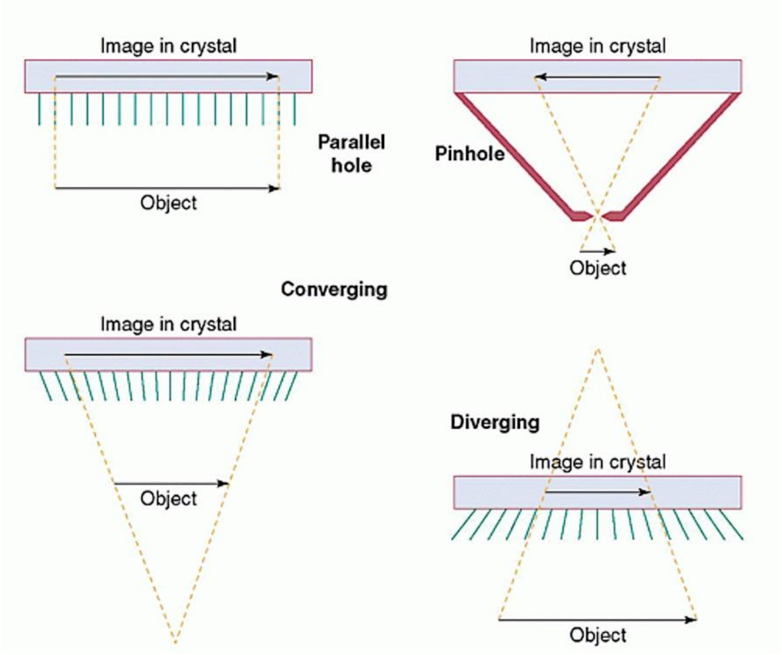

Figure 16 Visualization for various types of SPECT detector collimators [61].

The pinhole collimator has a high spatial resolution but low effectiveness, especially in regions remote from the pinhole. As a result, the field of view is restricted to the immediate local area of the pinhole. Multiple pinholes can be employed to boost performance. A pinhole collimator is useful for imaging tiny organs like the thyroid that may be placed close to the collimator. It is also often employed in preclinical methods for imaging tiny animals like mice, where great spatial resolution is required [63].

The majority of photons going through the collimator will be caught by the scintillation crystal. The energy released in the crystal is transformed into light that is visible by scintillation, which is then detected by an array of PMTs combined to the out of the crystal and generates an electrical current pulse equivalent to the amount of input light photons, which subsequently, in turn, has a relation to the energy of the gamma photon. The sodium iodide (NaI) crystal is one of the most often utilized scintillation crystals in

SPECT. They have strong stopping power, an excellent photon yield, and are quite affordable to produce [82].

5.3 Basic principles for reconstructing projections to image

The goal of tomographic image reconstruction aims to produce a cross-sectional picture of the movement of radiotracer emission from the scanner's recorded data. The various techniques used for tomographic reconstruction can be classified as analytical or iterative. Analytical reconstruction approaches provide a quick and straightforward mathematical solution to the image's problems without attempting to represent the stochastic character of the gamma-ray calculating operation [64]. A more thorough overview of the imaging process provides the foundation for statistically significant iterative approaches, which leads to a more challenging mathematical solution and several phases to produce the desired image [65].

Tomographic images produced from SPECT most of the times follow two-dimensional imaging set up by considering lines of response, LORs, lying within a predetermined plane. Figure 17 has a visualization of the image that is being scanned and the collection of a two dimensional function f(x,y). Each point of data for the projections can be described as a mathematical expression $p(x_r,f)$ [66], for all distances x_r that are collected at an angle φ which can take values between [0,2π]. All x_r values have a relationship with all original coordinates as follows:

$$\begin{bmatrix} x \\ y \end{bmatrix} = \begin{bmatrix} \cos\varphi & -\sin\varphi \\ \sin\varphi & \cos\varphi \end{bmatrix} \begin{bmatrix} x_r \\ y_r \end{bmatrix} \quad (1.43)$$

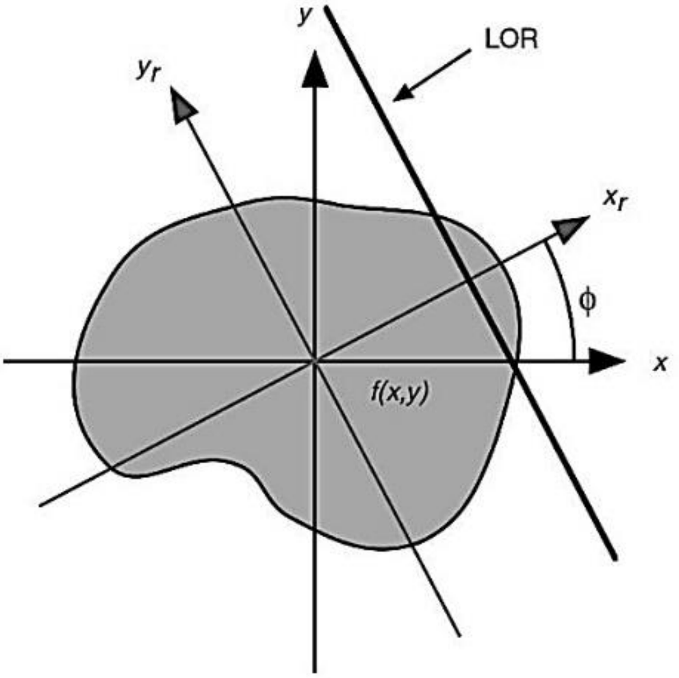

Figure 17 LOR example in two dimensions [53].

As it can be observed in Figure 18 the visualization of the process of collecting projections at a certain angle f. The equivalent to the Radon function [67] is the integral transformation of f(x,y) → p(x_r,φ):

$$T_R[f(x,y)]=p(x_r,\varphi)=\int_{-\infty}^{\infty} f(x,y)\,dy_r \quad (1.44)$$

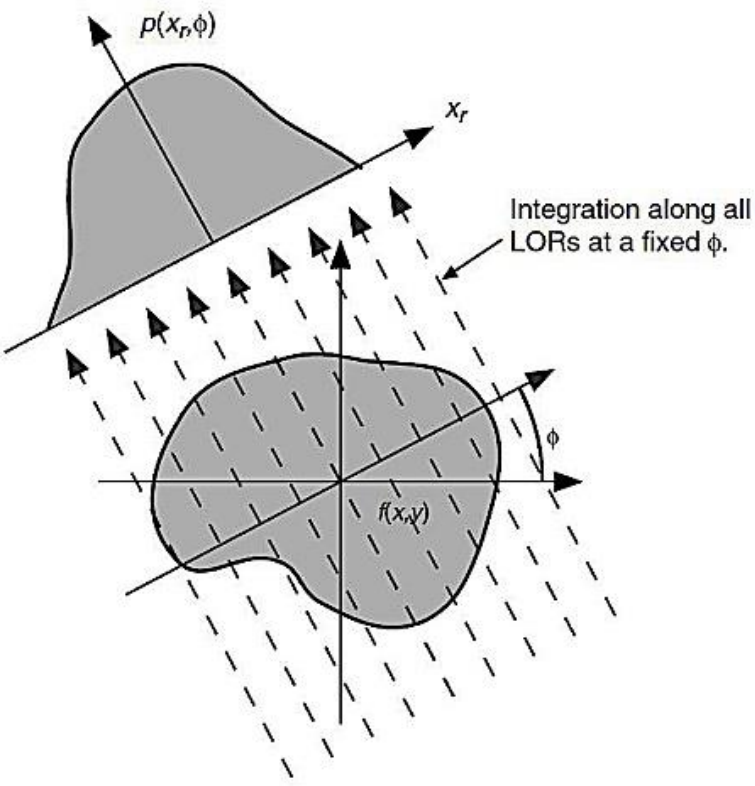

Figure 18 Visualizing the integration of f(x,y) to form p(x_r,φ) [53].

The function p(x_r,φ) is often referred to as the sinogram because a stationary point in the picture follows a sinusoidal pattern in the projection space, as it can be observed in Figure 19. In few words, a sinogram for a generic object is the combination of all sinusoids matching to the scanned item's points of activity.

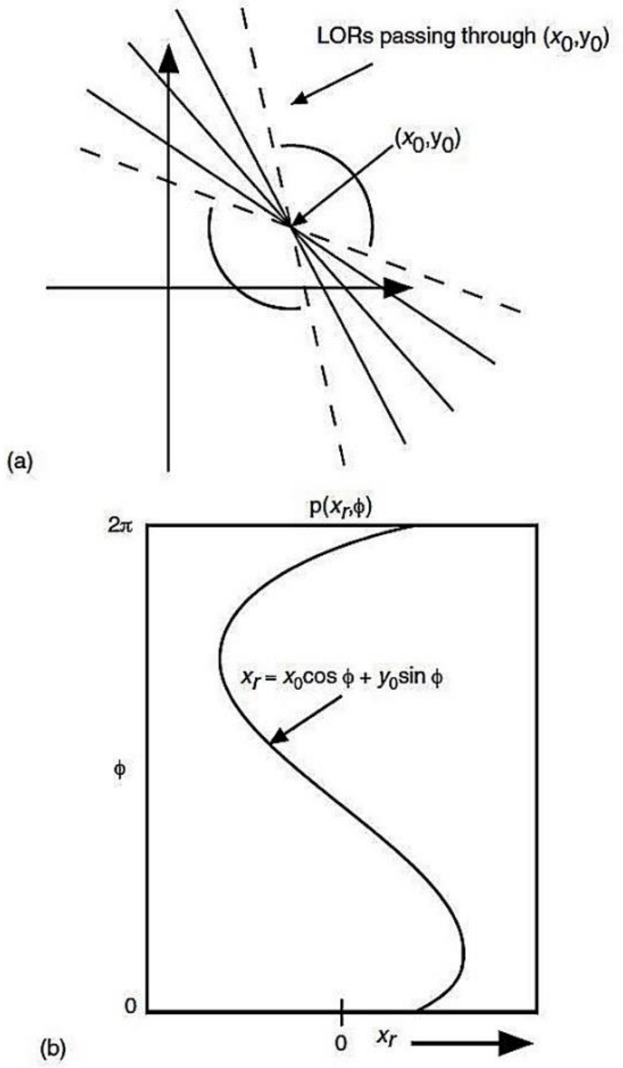
LORs passing through (x_0,y_0)
(x_0,y_0)
(a)
$p(x_r,\phi)$
2π
$x_r = x_0\cos\phi + y_0\sin\phi$
ϕ
0
0
x_r
(b)

Figure 19 Visualization of the relationship between a (x_0,y_0) point integrated into a sinogram [53].

The determination of the inverse Radon Transform T_R^{-1} is essential for the reconstruction of an undefined distribution. The essential connection in analytical reconstruction is the central section theorem. According to this theorem, an area taken through the center of an item's two-dimensional Fourier transform at a certain angle is identical to the Fourier transform of a first-dimensional projection [68]:

$$P(u_{xr},\varphi)=F(v_x,v_y)|u_{yr}=0 \quad (1.45)$$

Where $F_1\{p(x_r,\varphi)\}=P(u_{xr},\varphi)$ refers to the first dimensional Fourier transform of a projection set, the $F_2\{f(x,y)\}=F(v_x,v_y)$ is the Fourier transform of the original item.

With few words the central section theorem suggest that if $P(u_{xr},\varphi)$ is identified at all angles $[0,\pi]$, then the identification of the function $F(v_x, v_y)$ is an easy job. By applying the inverse Fourier on the function $F(v_x, v_y)$ then the unknown item $f(x, y)$ becomes known.

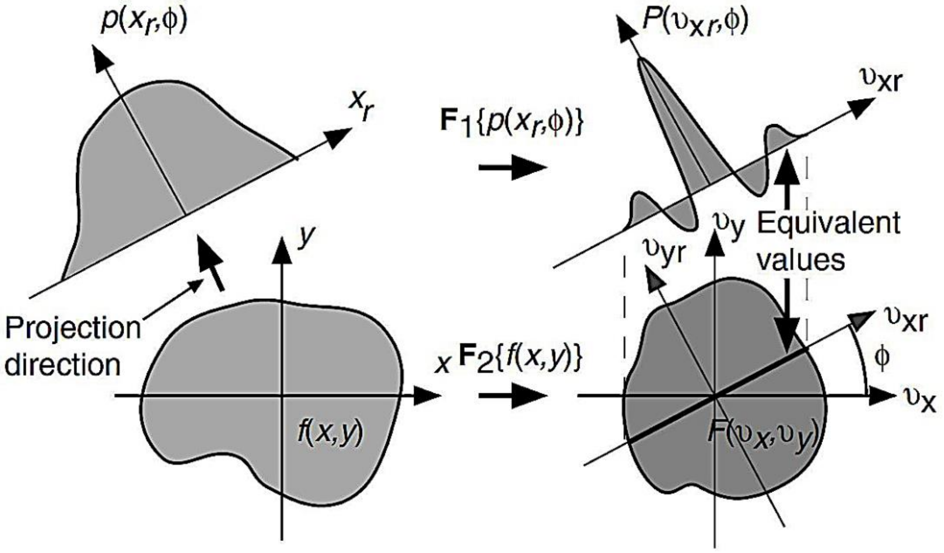

Figure 20Visualization of the central section theorem [53].

5.4 Back projection and Filtered Back projection.

Before doing reconstruction a crucial step is to calculate the back-projection b(x, y), which can be said that is a method of identifying an picture array back from the function $p(x_r, \varphi)$ utilizing the particular LOR and the angle φ.

$$b(x,y)=\int_0^{\pi} p(x_r,\varphi)d\varphi \quad (1.45)$$

Since the projection stage disguised the source of the values, an equal amount will be applied to each element across the LOR. The picture will not be returned by a direct back-projection of all the gathered projections due to oversampling in the Fourier transform's central region. The Fourier space is filled in by each projection, which causes oversampling in the middle and under sampling at the edges. For the contributions to be distributed equally across the field of view FOV, this oversampling has to be reweighted. In theory, the two-dimensional cone filter $u=\sqrt{u_x^2+u_y^2}$, which emphasizes values at the borders of the Fourier space and mask values at the center of the Fourier space, must be used to filter the Fourier transform of the back-projected picture. Here's how this operation is summed up:

$$F\left(u_x,u_y\right)=uB\left(u_x,\ u_y\right)\ (1.46)$$

Where the $B\left(u_x,\ u_y\right)$ is the Fourier transformation of the back-projected picture and $F\left(u_x,u_y\right)$ is the Fourier transform of the back-projected and filtered picture. If the inverse Fourier to $F\left(u_x,u_y\right)$ is applied then the original image f(x,y) will be returned. This method also has the name back-projection-filtering image reconstruction (BPF).

Filtered back-projection (FBP) is also a very common method just like BPF with the difference that the function is filtered and afterwards back-projected.

$$f(x,y)=\int_0^\pi p^F(x_r,\varphi)d\varphi\ \ (1.47)$$

Where the $p^F(x_r,\varphi)$ is calculated as follows:

$$p^F(x_r,\varphi)=F_1^{-1}\left\{|u_{xr}|F_1\{p(x_r,\varphi)\}\right\}\ (1.48)$$

In this case the oversampling of the Fourier transform is being corrected before using the inverse Fourier. The term $|u_{xr}|$ is a part of simple symmetry to the cone filter $u=\sqrt{u_x^2+u_y^2}$. By nature the process of FBP is unstable due to the fact that small changes on the data $p^F(x_r,\varphi)$ can direct an unprecedented outcome of the estimate to f(x,y). Because in most cases the detection of particles is a stochastic function it is hard to bound the solution's space in order to have natural values that can represent stochastic physical phenomena. Utilizing a plain smoothing technique can bring us a picture reconstruction solution that can be regulated and evaluated. So the calculation of the FBP solution is as follows:

$$f(x,y) \approx \tilde{f}(x,y) = \int_0^{\pi} F_1^{-1}\{W(u_{xr})|u_{xr}|F^1\{p(x_r,\varphi)\}\} \quad (1.49)$$

Here the observation is that $\tilde{f}(x,y)$ is the solution estimate for f(x,y), the function $W(u_{xr})$ is the key to smooth and bound the final result. There is a great deal of effort to properly determine the function $W(u_{xr})$, because a correct shape in this function can bring low noise to signal ratio and also determine the resolution of the final picture.

5.5 Image reconstruction via iteration methods

Fast calculation of tomographic pictures is often possible using analytical reconstruction techniques like FBP. The generated pictures can show considerable flaws since the FBP model does not accurately reflect real obtained SPECT data. Iterative methodologies, as opposed to analytical techniques, can simulate the translation from source to detector without directly calculating a line-integral. Additionally, statistical representations of noise and attenuation processes are included in iterative reconstruction methods during the imaging process. These enhancements come at the expense of a more challenging mathematical issue than the calculation of the inverse Radon transformation function. They're either not offering a straight analytical answer or the processing power at hand prevents finding one. Therefore, these accurate solutions are frequently solved with techniques that continuously enhance the predicted picture. Accuracy against efficiency is the main sacrifice between iterative approaches and FBP. Each iterative approach calls for a particular amount of back-projection and projection processing to be performed. As a result, they require much more computing time than FBP. The computing load of iterative approaches has been reduced because of improvements in calculation speed and more efficient algorithms, which has led to a rise in overall clinical adoption.

Iterative techniques typically include five parts. A model of the image makes up the first part. For two-dimensional visual components, this is generally a separation of the image area into N separate pixels, whereas, for three-dimensional visual components, this is a separation of the image area into voxels. Other models, such as spherical parts [69] with overflowing borders, have been suggested.

A system model that connects the picture to the data within it is the second part. The imaging system is characterized by the system model or system matrix (SM), wherein one element, A_{ij}, stands for the likelihood that signal from pixel j would be observed in projection i.

A framework for the data, which is the third part, defines the correlation between the measured value and the predicted value of the analysis in statistical approaches. This model describes the deviations from the projected mean values of the metrics. The majority of techniques use a Poisson model because photon detection has a Poisson distribution [70]. Despite the Poisson model accurately describing SPECT imaging, the results cease to exhibit Poisson statistics once random, scatter and attenuation adjustments have been made. To increase model accuracy, other models have been suggested, including Gaussian models, displaced Poisson models [71], and estimates of the Poisson model [72].

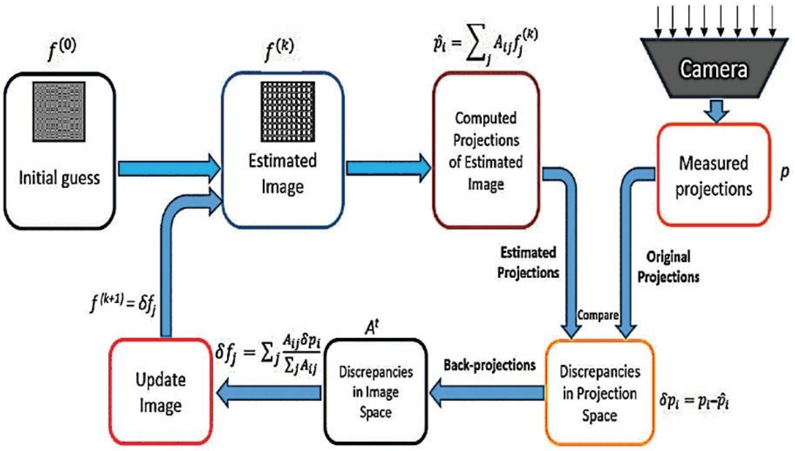
$f^{(0)}$
Initial guess
$f^{(k)}$
Estimated Image
$\hat{p}_i = \sum_j A_{ij} f_j^{(k)}$
Computed Projections of Estimated Image
Camera
Measured projections
p
Estimated Projections
Original Projections
Compare
$f^{(k+1)} = \delta f_j$
A^t
$\delta f_j = \Sigma_j \frac{A_{ij}\delta p_i}{\Sigma_j A_{ij}}$
Update Image
Discrepancies in Image Space
Back-projections
Discrepancies in Projection Space
$\delta p_i = p_i - \hat{p}_i$

Figure 21 Visualization of the MLEM algorithm workflow [70].

With the picture definition, the metrics, and the system that connects the two, the fourth part must be what determines the best image. In mathematics, the controlling rule is frequently represented as a cost or objective function. The Maximum Likelihood (ML) procedure, a widely known statistical estimating technique, is the most often utilized premise in iterative reconstruction [73]. Because ML estimators are simultaneously unbiased that is, the estimates grow accurate as the number of events increases, they are favorable. Additionally, it has been demonstrated that these estimators offer the smallest variance of all conceivable unbiased estimation tools, producing a result with lower noise than other unbiased estimation methods [74].

An algorithm that gets the best image approximation or improves the cost function makes up the last part of iterative approaches. Numerous techniques, including the most popular expectation maximization (EM) algorithm initially published in 1977 [75] and gradient-based algorithms [76], have been suggested in the available research. A numerical approach for arriving at a maximum likelihood estimate (MLE) is provided by the EM algorithm. Since its debut in 1982 [77], the ML-EM algorithm has served as a base for many additional approaches as well as the most well-liked statistical reconstruction techniques. In 1994, a modification of the ML-EM method was published to address the issue of delayed convergence [78]. For each picture update, the ordered subsets expectation maximization (OSEM) algorithm employs subsets of the full data set, as the name implies. The OSEM algorithm becomes the ML-EM algorithm whenever just one subset is utilized.

5.6 Conclusions

The nuclear imaging SPECT technology is discussed in this chapter. The fundamental operating principles for the SPECT tomographic system are covered and introduced. In addition, the gantry, source, and head of the SPECT are discussed. Additionally, the two-dimensional image reconstruction approach has been analyzed for systems like SPECT and CT which utilize projections. Lastly iterative and back projection techniques are presented.

6 Monte Carlo Computational Techniques

6.1 Introduction

With the use of statistical and continuous random sampling, the fundamental goal of Monte Carlo was to accurately represent an actual stochastic phenomenon. The Monte Carlo (MC) technique for calculation, which employs statistical sampling techniques to get a probabilistic approximation to the solution of a mathematical problem or model, was created in the 1940s [83]. Researchers at the Los Alamos National Laboratory were the very first to employ Monte Carlo simulation to imitate the random distribution of neutrons. The scientist who created this modeling method titled it "Monte Carlo" from the town of Monaco and its numerous casinos [84]. MC simulations are employed in a variety of fields, including physics, economics, earthquake forecasting, and aeronautical engineering. Statistical methods are used in the Monte Carlo analysis to model actual stochastic systems. Prior to using Monte Carlo simulation, it is necessary to specify the statistical distribution of the event that will be depicted. In addition to testing with the model to draw conclusions about it, MC simulation provides a flexible tool for researching and assessing complicated stochastic systems [85].

A second, distinct set of random numbers won't yield exactly the same results as the initial set, but they will give results that are between the boundaries of statistical uncertainty of the results of the first run. Monte Carlo methods may be used to study a huge diversity of physical events [86]. Examining models that can be approximatively or spontaneously divided. The subsequent steps [87] are frequently employed for a Monte Carlo computation of a real-world event:

i) Creation of an abstract model.

ii) Recognition of input statistics.

iii) Generation of random variables.

iv) Evaluation and decision-making.

i) Creation of an abstract model: Each Monte Carlo experiment starts by building a model with predictable behavior that closely resembles the system in the actual world. In this predictable model, the input parameters are employed at their most probable value or default scenario. In order to transform the outcomes of the given input data into the required output, mathematical connections, mostly statistical are utilized.

ii) Recognition of input statistics: Following the satisfaction of the probabilistic model, risk-associated elements are added to the simulation. The identification of the basic distributions that affect the input variables are a difficult task due to the risks caused by the random nature of the variables being used. This stage needs previous information for the input values.

iii) Generation of random parameters: After the finding of the underlying values of the input parameters, a set of random numbers is generated based on these distributions. One value will be produced for each of the input parameters in the deterministic model, from a collection of fifty random integers to produce a single set of results. After then, the process is repeated by producing more random number sets, each for every input distribution, and assembling several collections of potential results. This part is the core of the Monte Carlo simulation.

iv) Evaluation and decision-making: After the collection of an instance of simulated outcomes, a statistical evaluation is performed on the data. This stage provides statistical support for any conclusions drawn after the computerized model completed its run.

Two well-known fields where Monte Carlo is employed include stochastic mechanics and continuous particle transport theories. A very particular sampling strategy contains the first type of calculations, which are not further detailed. The second field is based on a computational model of a number of exciting unpredictable scenarios and covers issues such as transport of neutrons, shielding, nuclear reactor's physics, cosmic radiation etc.

The three problem types of optimization, solving numerical integration, and producing selections from a probability distribution [88] are where Monte Carlo techniques are most frequently applied. Monte Carlo techniques may simulate systems with numerous connected levels of autonomy, including liquids, unstable materials, highly interconnected solids, and structures in cells, in physics-related issues. Additional cases involve simulating input-dependent processes, such as calculating risk in business and simulating multi-dimensional specific integrals having intricate limit conditions in calculus. When applied to technological challenges, Monte Carlo-based forecasts of malfunction, excess costs, and unexpected delays are typically better than human judgment or other approaches [89].

In theory, every issue with a probabilistic approach may be solved using Monte Carlo techniques. The practical mean from separate samples of the parameter can be used to approach integrals that are characterized by a predicted value for a particular random variable according to the law of large numbers. Let’s see a practical example and one of the most known simple example of Monte Carlo usage [90], the geometrical estimation of pi.

Utilizing a simple algorithm, with simple steps, the estimation of the value of pi is possible.

1. Create points inside a square.
2. Identify the points that are inside the circle.
3. Plot the points.
4. Plot the estimated value of pi.

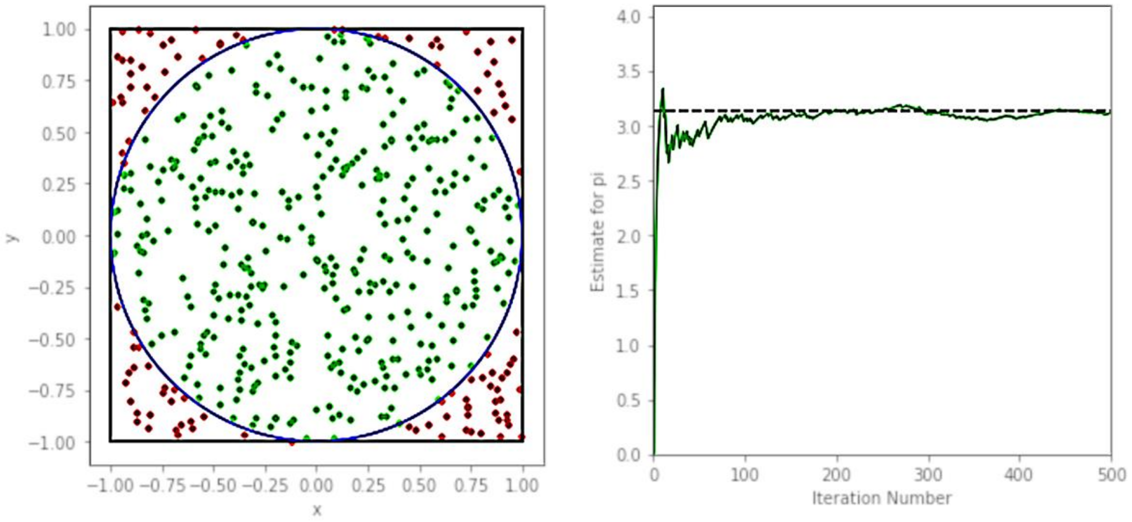

a

b

Figure 22 Geometrical pi estimation (500 points), a) Plot of points, b) end result estimator [91].

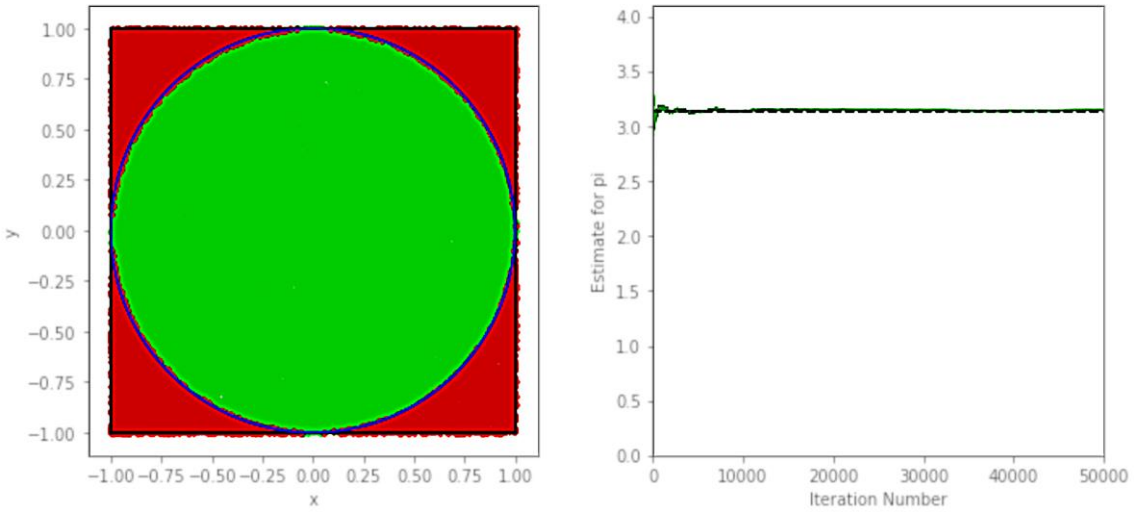

a

b

Figure 23 Geometrical pi estimation (50,000 points), a) Plot of points, b) end result estimator [91].

From Cartesian geometry the area of the circle divided by the area of the square is equal to pi/4.

$$\frac{\pi}{4}=\frac{A_{\text{circle}}}{A_{\text{square}}} \quad (2.1)$$

Where A_{circle} is the area of the circle and A_{square} is the area of the square. Utilizing a uniform random number generator, the Monte Carlo method would generate points in that square including areas that the circle overlap. Now the value of pi can be approximated by:

$$\pi \approx 4 \frac{N_{circle}}{N_{total}} \quad (2.2)$$

Where N_{circle} is the number of points inside the circle area and N_{total} is the total number of points generated inside the square area. As seen in Figures 22 and 23 as the number of points increases the Monte Carlo method converges faster and the estimation error drops in satisfactory levels.

6.2 Random Variables

Typically, results are assigned values in numbers so as to be mathematically handled. These numerical values are referred to as random variables. A random variable, like a result, can be discrete or continuous. A discrete random variable may symbolize the end result of a rolling dice throw, whereas a continuous random variable may describe the duration among electrons produced by a radioactive material. Two functions have been established for any random variable (x): the probability density function (pdf) and the cumulative distribution function (cdf).

A random variable that is discrete has a probability density function that expresses the likelihood that the end result of a random process will be x_n. It should be noted that the pdf must be normalized to ensure the chance of receiving any of those potential events is precisely one. The cumulative distribution function cdf(x) expresses the likelihood that the random process's output has a value less than x_n. Assume a continuous random variable (x) with a range of values {a, b}. The probability density function pdf(x) represents the likelihood that the random variable x will take a value between x and x + some small value dx. It is worth noting that p(x) is defined in such a way that the chance of receiving any amount of x in the range [a, b] is the same as one. The cumulative distribution function cdf(x) shows the likelihood of a random variable is going to have a number less than or equal to x. The pdf and cdf must have a few key features for Monte Carlo, including

1. The pdf must constantly be positive.
2. The cdf is a non-decreasing, constant-value function of its random parameter.
3. The pdf is normalized so that the cdf that corresponds to it ranges from {0,1}.

6.3 Random number Generators RNGs

Random numbers, also known as RNs, are a critical component of any kind of Monte Carlo modeling. The reliability of the random numbers utilized determines the degree of accuracy of any Monte Carlo simulation. If the generated numbers form a uniform distribution, a significant amount of unpredictability is attained. As a result, researchers must create methods for producing random number series that have a long duration before going over and don't need a great deal of money to manufacture. Random number generators were first utilized on computing devices by John von Neumann [92], who used them to conduct Monte Carlo simulation [93]. Several methods [94] for the production of random numbers have been proposed since then [95]. The standard technology consumer [96] believes that the issue of computer-generated uniform unpredictability numbers has been answered [97]. Despite substantial advances in the production of fruitful generators, yet remain unacceptable or unfit generators that produce unpleasant effects. As a result, each Monte Carlo participant must be conscious of the difficulties and restrictions. There are basically two ways for producing random numbers. Algorithmic and experimental [91].

An experiment, or physical procedure, is used to create a series of random numbers which are kept in records within a computer system. For instance, the total amount of a radioactive substance breakdowns [98] during a specific time span.

Algorithmic: To create random numbers, an algorithm is utilized. Due to its predictable character, this technique is known as a pseudo-random number generator or PRNG, and the numbers related to this can be described as pseudo-random numbers or PRNs. Every technique has benefits as well as drawbacks that influence its utilization.

The following are crucial considerations while choosing the best approach:

a) Randomness: Every number ought to be truly random, with a uniform distribution. Randomness is obtained in the experimentation approach if the setup maintains a uniform distribution. The resultant sequence must pass numerous statistical criteria in the algorithmic technique.

b) Reproducibility: In order to evaluate a simulation technique, the random number series must be reproducible.

c) Length of the generated random number series: Numerous millions of random numbers are required to execute a Monte Carlo experiment for genuine scientific issues; hence, the generator must be capable of producing a significant amount of random numbers.

d) System memory: The generator ought to avoid using an excessive amount of computer memory.

e) Production time: The quantity of duration required to produce an arrangement of random numbers shouldn't be significant, like days.

f) Computer time: the volume of cpu time required to create the numbers ought to be much less than the time required to run the simulation.

In fact, the algorithmic technique is the favored option since the order of operations is repeatable and needs very little effort. It is required to execute a series of randomness trials and to observe and measure the moment at which the generator repeats its sequence and losses it's unpredictability, when employing any algorithmic unit. The parts that follow go through several algorithmic pseudo-random number generators and randomness testing methodologies. A decent PRNG must provide a series of consistently dispersed random numbers in the (0, 1) region. It ought to have a lengthy term and satisfy a variety of randomization evaluations. Congruential [94] and multiple recursive [99] generators are the most widely employed.

If a pseudo random generator of numbers satisfies a variety of randomness evaluations, only then it is accepted. Numerous randomness investigations [92] have been developed that examine a variety of factors in order to determine the independence and uniformity of a random number series. There are several trials that look at random numbers both as an entire number and as a sequence of digits [100]. Instances include the x^2-test [101], which calculates the difference between the sample and the presumptive probability distribution. The randomness generated by a certain generator may also be tested using a number of other tests [90], such as the likelihood ratio test, the gap test, the poker test, the moment test, the serial correlation test, and the serial test through charting, to mention a few.

Monte Carlo simulation can effectively simulate a physical phenomenon by randomly sample pdf or cdf functions. A simulation may be done in order to approximate the distribution of a target function; to approach some statistical quantities of the particular distribution by simulation or optimizing the solution by minimize or maximize a target’s function [102]. The purpose of the computation is often a calculation of an integral of a continuous distribution or the calculation of a sum of a discrete distribution, therefore it is computationally challenging. Numerous factors, including the number of random variables, the unpredictability of the field, the degree of noise in the data, the dearth of evaluations, and others, might make the computation unattainable. Frequently, through direct or indirect means through a computational simulation, it is likely to determine or approximate the probability distributions of the crucial random variables in these kinds of situations. Sampling is able to be utilized rather than determining the value exactly. From the probability distribution, samples could be chosen at random and utilized to get close to the target amount. The foundational idea of Monte Carlo refers to this broad category of methods for randomly picking samples from a probability distribution.

6.4 Modelling Particle Trajectories – Tracks

Planning an abstract model for physics particle Monte Carlo simulation would consists of the following parts:

a) Particle source: A source function specifies the probability distributions for all the variables of every particle that was generated. These variables contain phase coordinates and internal dimensions of autonomy, as well as the specific kind of particles.

b) Time dynamic modelling: In certain circumstances, system characteristics alter over time as a result of radiation. Typically, changes in shape and material qualities occur.

c) Geometry and Materials: While choosing the geometry, it's crucial to consider the size of the simulation volume and which items should be included in the simulations. Also an important part of the simulation is the identification of materials to different types of objects with various geometries and associate that geometry with the material that an item consists.

d) Physics definition: In order to plan Monte Carlo simulations, it is necessary to identify the solutions to a number of significant physics-related questions.

e) Selecting tallies: Another topic that must be answered is how and what quantities are computed. Also a determination of what is the outcome of the simulation is determined in this section of the planning.

f) Simulation time optimizations: Monte carlo optimization almost all the time means variance reduction. The phrase variance reduction, refers to a collection of techniques that lessen statistical uncertainty without skewing the outcome or adding systematic mistakes ideally.

Since neutral particle movement simulation is considerably simpler to model than charged particle movement, a good starting point is to analyze the neutral particle trajectory model. The trajectory is created once a particle departs the source until it is either absorbed, escapes the computational region, or has energy under the tracking cut-off. Secondary and higher-generation produced particles are treated in the same way [103]. The known as phase space source is one kind of significant source. The phase vectors of all particles reaching the scoring surface are recorded in a phase space file during the initial computation, which also defines a scoring field. Particle paths begin at this scoring field in all future operations, with the initial coordinates received from a file. This approach is meant for issues where a specific section of the system, closest to the source, remains constant between computations while other parts of the system vary. Significant processing time may be saved in this instance since no more simulation of the initial stage of the system is required for each new configuration of the variable components of other parts of that system.

In other words, the same general algorithm is used for charged particles and neutral particles. The drawback of this approach is the slowness of the algorithms due to the interaction cross sections being typically orders of magnitude larger for charged particles than for neutral particles. The drawback of this approach is the slowness of the algorithms due to the interaction cross sections being typically orders of magnitude larger for charged particles than for neutral particles. In a nutshell, charged particles and neutral particles both follow the same basic method. The disadvantage of this method is the speed of the algorithms since ion interaction cross sections are often orders of magnitude bigger than neutral particle interaction cross sections [104]. Charged particles approaches for faster calculations involves better approximations of the Boltzmann equation and other approaches for problem specific scenarios.

6.5 Modelling Particle Tallies

Another point that must be addressed is how and what quantities are computed. There are two aspects of addressing radiation mobility issues with Monte Carlo simulations: creating particle paths and gathering data from particle tracks to determine quantities of importance. The second stage is known as tallying. In the broadest sense, it is the computation of a detector value J(x), such as dosage or fluence at a specific location, as well as more commonly, their spatial distributions. Tallying is the procedure of obtaining data from created particle trajectories in order to compute a measurement J(x), and tallies serve as the estimation tools used in that procedure. There are several tallies that may be utilized for calculating the same quantity, hence a choice must be taken regarding which tallies to apply to the given situation. The geometry resolution for a dose matrix is a crucial factor for computing a 3-D dosage distribution. It requires a longer computation to achieve reduced statistical uncertainty with a sharper resolution. On the contrary hand, a rough matrix may distort some of the more intricate details of the dosage distribution. Particle trajectories are difficult to produce, as it was already noted, calculations, however, are rarely done for the sake of trajectories alone. Some basic tallies that are used for medical applications namely are:

a) Surface Crossing Tally: Estimating fluence or other values on a surface.
b) Boundary Crossing Tally: The boundary crossing tally is used to compute quantities averaged over a limited, typically small, volume. Calculations of dosage or energy deposition benefit greatly by boundary crossing tally.
c) Collision Tally: Very helpful when there are ion collisions or if it's necessary to estimate amounts in a limited volume based on electron, positron and ion collisions.
d) Track End Tally: When particle paths come to an end, this tally is called. These kinds of tallies only have a few uses, they are mostly used in dosage calculations and ion implantation profiles.
e) Path Length Tally: This kind of tally is employed on ions, particularly when plenty of routes need to be estimated in a tiny space.
f) Voxel Tally: This method divides the computing domain into tiny cubes known as voxels. It is necessary to determine the material for every single voxel. A voxel in a heterogeneous media could include many materials, and its density might not be uniform. An excellent resource for calculations including patient dosage, dose maps, patient specific, etc.
g) Mesh Tallies: The material’s topology and tallies are established on two usually distinct grids in the mesh tally approach. Neither grid needs to be square. For example, a dosage counting mesh might be elliptical or spherical. Surface and area tally classes can both be defined using a mesh tally. The disadvantage of utilizing mesh tallies for dose estimates is that the total weight of material for every region determined by the mesh tally must be known, but since materials are specified on a

distinct space grid, a volume described by the mesh tally may include multiple various substances.

6.6 Simulation optimization

6.6.1 Variance reduction

Variance reduction is the name given to a series of techniques that lower statistical uncertainty without skewing the outcome by including systematic mistakes. The specific approaches for variance reduction that will be applied must be decided. The latter involves deciding on the best settings for the procedures that have been chosen. A related issue is estimating and presenting statistical uncertainty. A concise strategy that details how statistical uncertainty will be computed and communicated is essential. Additionally, it is important to anticipate the amount of statistical uncertainty that may be attained as well as the computational time and resources that would be needed. For the majority of the moment, the result of t*Var{x}, where t is the CPU time and Var{x} is the variance of the random variable, has to be reduced. Var{x} is often unknown, but the variance of the sample s^2 can be utilized in its stead. In a perfect world, both t and Var{x} could be reduced, realistically most of the times huge improvements are accomplished by reducing the variance. In actuality, the goal is to significantly reduce Var{x} while maintaining the same calculating speed. What information will be contained in the output files and how frequently they will be transferred to disk are other factors to take into account. Monte Carlo computations may take several hours or days to complete. Because of that, it is customary to routinely store intermediate findings on the drive. In the event that the code is restarted and the computations are continued, whether unintentionally or on purpose, these stored files ought to contain all the data required to do so. The most basic and important concepts are:

a) Particle Splitting: In comparison to the actual process, the quantity of secondary particles produced by an interaction between a particle and a number of additional particles is intentionally enhanced by a factor of n. Every new secondary particle, which is drawn from the same distribution as the others, has a unique unpredictable motion. Each particle has an n=1 weight to account for the bias on the total quantity of secondary particles. For instance, an electron impacting a tungsten target in an X-ray tube results in the production of bremsstrahlung photons. The dosage is given by these photons. In a Monte Carlo technique, for instance could produce three photons, each having a weight of 1/3, but in an impact, the electron generates just one photon. The advantage is that more photons are generated per incoming electron. Since the modeling of electron tracks takes a while, this reduces the load on the CPU. However, photons are primarily responsible for delivering the radiation dose to the person receiving it. In a variant of this approach, every single one of the bremsstrahlung photons would have been carrying the same momentum. By only sampling the photon momentum once, as opposed to three times, simulation time is saved. The three photons' paths are linked, especially close to the place of origin, which is a disadvantage.

b) Russian Roulette: The Russian roulette method might be thought of as the antithesis of particle splitting. Its function is to exclude particles that are not likely to affect detector readings, which obviously reduces computation time. Russian roulette may be performed, identically to particle splitting, during the time of impact, whenever secondary particles are created, or as a particle reaches an area.

c) Weight window: Weights are constrained to a customized user range or window, from w_{min} to w_{max} via a method termed weight window. By performing Russian roulette, particles with weights less than w_{min} are obliterated. A low-weight particle under this scenario either perishes or, if it still exists, gains weight. Likewise, particles with weights more than w_{max} are divided, resulting in a weight decrease.

d) Importance sampling: Importance sampling (IS) is a set of algorithms that approximate a mathematical prediction with regard to a target distribution using a weighted average of random samples from another distribution. Those kind of techniques comes in handy when computing integrals.

e) Forced Collisions: Intentionally boost interaction in cross sections inside volume V if enhancement of the average number of interactions is needed there, and then utilize statistical weights to correct the bias. An alternate strategy is the forced interactions method. With this method, a particle that enters the volume interacts with it at least once, with the probability that the user specifies.

6.6.2 Other Optimization methods

In Monte Carlo software, algorithms to accelerate the calculations are widely used. In fact, it happens to be quite rare for software package not to employ a minimum of one of the approaches described in this subsection. Since these methods contribute to systematic mistakes, they can't be referred to as variance reduction methods. Typically, these mistakes may be reduced to the minimum size required for a given issue, the basic of these techniques utilized in medical applications are:

a) Range Rejection: Typically, this method is applied to electrons. Once an electron gets generated within a voxelized geometry, its maximum range is computed. The previous history is ended if its length is less than a certain distance to the closest voxel border. Since the electron's path ended prior to forming a bremsstrahlung photon, it adds a systematic error. Additionally, because the electron range is unpredictable, there is a chance that the real range will occasionally surpass the predicted maximum range. This approach can additionally be employed when the geometry is not made of voxels. If the original particle or one of its offspring is unable to get to the detector's surface or doesn't make any contribution to the detector signal, the electron path has ended in this scenario.

b) Transport Cut-Offs and Generation Thresholds: Since the paths in some situations are basically limitless, the correct settings cannot be avoided in algorithms for the transport of ions. For instance, when an electron is involved in inelastic collisions, it loses energy yet is neither entirely stopped nor absorbed. The efficiency of electron transport cut-offs and production thresholds has a significant impact on the effectiveness of procedures for dose estimations from photon and electron sources. There are lots of low-energy electrons created when secondary electrons are formed since the cross sections are so favorable. But measurements are greatly slowed down if the cut-off and threshold values are configured too low because a cloud of low-energy electrons is created, which do not contribute to the calculated variable at all.

c) Kerma Approximation: The energy which neutral particles transmit to physical matter in this scenario is thought to be made regionally, at the point of contact, and the absorbed dosage is set as kerma. With regard to photon beams used in radiotherapy MeV energy range, this approximation is often not relevant. But photon beams utilized in tomographic images and therapeutic cases, comprise a substantial low-energy component, in keV energy range, are poly energetic. The secondary electrons generated by low-energy photons may thus be calculated using the kerma approximation rather than having to model them.

d) Condensed history algorithms: For the purpose of addressing issues involving charged particles, these kinds of algorithms are particularly very efficient.

6.7 Conclusions

The fundamental approach of Monte Carlo for medical physics was discussed in this chapter. It was shown how to estimate the value of pi by producing random geometrical points with a geometrical rule. Following that, several fundamental statistical concepts about random variables were introduced. Quality random number generators (RNGs), particularly pseudo-random generators, are an essential tool for every Monte Carlo technique. Some fundamental aspects of what qualifies an RNG for Monte Carlo simulations were provided. Following that, how to plan a particle simulation and what crucial elements to be aware of, was addressed. Also a method of how to monitor particle trajectories on both neutral and charged particles was addressed. The tallying process, which is the practice of getting data from produced particle paths in order to compute a value of interest, is another component. Another crucial issue is the optimization of the codes in order for them to run considerably quicker. This is where variance reduction plays a very essential part in the nature of the Monte Carlo codes, as such implementation of these approaches makes a code run much faster. Other technologies that are not associated with variance reduction yet play a vital role in computer simulation were also described. In general, a very abstract and fundamental notion of how to approach particle Monte Carlo efficiently and effectively was presented.

Chapter B. Research Part

This section of the doctorate dissertation covers all of the details of the experimental setup for all of the scenarios utilized. To demonstrate each approach for the CT and SPECT systems, an analytical explanation is provided to address issues such as the complexity of the computations performed by the software, the theoretical validation of the findings, the delivery of outputs from simulations as feedback to other processes for further analysis, and finally the presentation of the results.

In the previous section, an introduction was made of the fundamentals of particle transport via matter, principles of operation of CT and SPECT, as well as the fundamental techniques of Monte Carlo to approach cases of particle transport. The continuation in this chapter is to show how to install, configure and operate open source software routines in Windows and Linux operating systems and show how to effectively produce valuable information and approach experimental set ups.

General Targets

Address the complexities of the techniques utilized.

Demonstrate how to run a CT examination simulation using the EGSnrc environment and present the cases that were utilized.

Demonstrate how to use GATE to simulate a SPECT head, analyze the reconstructed tomographic image created by STIR and present all outcomes of the scenarios that were determined.

Present the research's conclusion and future direction.

7. Materials and Methods

7.1 Introduction

This chapter employs and discusses the methods of compiling, building, installing, executing and testing the open-source Monte Carlo software EGSNRC and GATE, as well as additional software packages like STIR and other routines. In addition, all procedures used are given and supported by experimental data and previous research in order to deliver results from contemporary techniques.

More specifically, the CT system was initially configured by simulating different x-ray sources irradiating from all directions, a patient-specific personalized phantom and score doses. The simulations were run using the EGSnrc program, and the result files were stored in binary format. Three personalized phantoms were used, covering the case studies of brain, chest and abdomen. For each irradiation, six profiles were chosen for particular organs from all three phantoms, such as the spine, lung, abdomen, brain, heart and skin.

Considering that the SPECT system's source, radiopharmaceutical-isotope is directly injected into a patient and irradiated from within the body, an alternative approach was employed than the CT system. The GATE software tool was utilized in order to simulate the SPECT head rotating around an irradiating phantom and take projections. The GATE software routine outputs all projections as a binary sinogram file. STIR routines reconstruct the sinogram utilizing filtered back projection (FBP) and iterative approach of Ordered Subsets Maximum A Posteriori One Step Late (OSMAPOSL) algorithms. Two SPECT heads were simulated, a SPECT head based on the AnyScan S FLEX system and a custom SPECT head for small animals.

7.2 Basic Software configuration

7.2.1 Hardware

The majority of simulations were performed on three main dedicated computational units. These units are two laptops and one desktop computer. Because not everyone is familiar with the Open Source operating system Linux, there was a need to discover a mechanism to access all software packages even if the primary operating system was Windows. Table 1 contains some basic characteristics of the main computational units.

Unit Type	Name	CPU	RAM	OS
Laptop	Dell Inspiron	i5 – 6th generation	16Gb	Ubuntu 20.04
Laptop	HP Probook	i7 – 10th generation	16Gb	Windows 10
Desktop	Custom made	i7 – 6th generation	16Gb	Ubuntu 20.04

Table 1 Main computational units characteristics.

After extensive research with various Linux distributions, Ubuntu [105] version 20.04 was decided as the main operating system. The main reason for that decision was the fact that it was easy to install, it had many issues with the package manager and library dependencies resolved and at the time being the version 20.04 was the most stable version with long-term support. In addition, the errors during compilation and installation of the main software were minimal and any issues quickly resolved.

To run Ubuntu 20.04 inside the Windows 10 operating system, a virtualization approach was required. After experimenting with common virtualization technologies such as Oracle's VM Virtual Box 7.0 [106], VMware Workstation Pro 17 [107] virtualization platform, and Microsoft's WSL 2.0 [108], the choice was taken to install Ubuntu 20.04 on Microsoft's WSL 2.0. Mostly because it was part of Microsoft's ecosystem and installation, redistribution and import/export VM images was simple and very well supported and documented. Utilizing the Microsoft Store app that came pre-installed with Windows 10 installation was very simple and without errors. After installing WSL 2.0 on Windows 10, the Microsoft Store app was used to download and install the Ubuntu 20.04 image and GWSL [109] graphics XServer. Without the need for a third-party program, anyone may run Ubuntu Linux graphical apps on Windows 10 utilizing Microsoft's WSL 2.0 and GWSL.

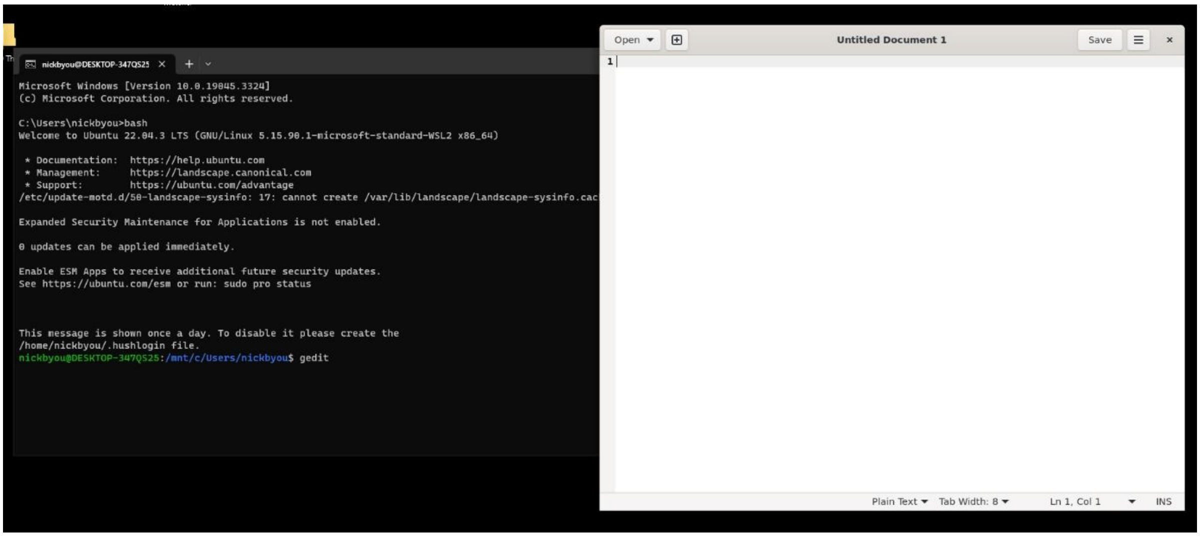

```
Microsoft Windows [Version 10.0.19045.3324]
(c) Microsoft Corporation. All rights reserved.

C:\Users\nickbyou>bash
Welcome to Ubuntu 22.04.3 LTS (GNU/Linux 5.15.90.1-microsoft-standard-WSL2 x86_64)

 * Documentation:  https://help.ubuntu.com
 * Management:     https://landscape.canonical.com
 * Support:        https://ubuntu.com/advantage
/etc/update-motd.d/50-landscape-sysinfo: 17: cannot create /var/lib/landscape/landscape-sysinfo.cac

Expanded Security Maintenance for Applications is not enabled.

0 updates can be applied immediately.

Enable ESM Apps to receive additional future security updates.
See https://ubuntu.com/esm or run: sudo pro status



This message is shown once a day. To disable it please create the
/home/nickbyou/.hushlogin file.
nickbyou@DESKTOP-347QS25:/mnt/c/Users/nickbyou$ gedit
```

Figure 24 Ubuntu application gedit execution via WSL 2.0 with GWSL inside Windows 10.

7.2.2 Linux OS shell & Package Manager

The operating system (OS) [110] is a piece of software that handles every single one of the hardware resources, manages the basic interfaces with those resources and provides available libraries for interaction with the user. One very common approach is to expose a system's services and routines to a human user or other programs via a program called shell. The name shell comes from the description of the program as the outermost layer of an OS.

The bash shell [111] has been utilized in order to provide the infrastructure to run commands on Ubuntu Linux environment and to enable the ability to execute shell scripts for more complex usage. A perfect example is the .bashrc script that is located in the home folder of a fresh Ubuntu installation, in this file the user can modify environmental variables, parameters of the bash session such as the coloring, command aliases, special features etc.

A package management system is essential for installing, maintaining, upgrading, updating, configuring, and removing software. The Advanced Package Tool (APT) [112] package manager is a sophisticated package management application. It simplifies the installation and removal of Linux software packages by utilizing its core libraries. The APT software is dependent on repositories where libraries and software packages may be viewed. The repositories contain pre-compiled packages that can be downloaded and installed on the machine via APT.

7.2.3 Builders – Compilers

One of the most significant computer concept ever created is the compiler. The compiler is a computer program that its primary objective is to translate high-level computer code from a programming language and translate it into low level machine language. Compilers are complex programs mostly because the high-level code that is used, as input needs to be preprocessed, analyzed with various methods, the executable may be generated with optimizations and the compiler needs to support a plethora of options as to the specific machine the executable code will run. Some example of compilers used in this thesis is the gcc compiler, g++ compiler and gfotran compiler.

Besides compilers, some other programming languages are utilizing an interpreter. The interpreter is a program that transforms and then executes systematically the code, an example of such language is python. More specifically python3 played a crucial role in the preprocessing, analyzing and presenting of the results in this thesis.

Cmake [113] a build automation tool allows the automation of building, testing, packaging and installing of software and utilizes a compiler-independent way. Cmake is cross-platform and open source. This piece of software can automate the process of building complicated executable code that depends on many different languages, compilers with various building parameters, compiler instructions for the utilization of multiple libraries with the option to enable or disable them. Cmake reads as input files the so-called makefiles that contains specific instructions on how to compile and build from source code, which defines how the target application is generated.

7.2.4 Extra Resources

Some of the secondary software worth mentioning are Image J [114], the Kaggle [115] online community and the open data repository Zenodo [116]. ImageJ is an image processing application that was designed with Java and follows open architecture. With this application medical dicom image processing, editing and visualization was possible. In addition, ImageJ is extensible with plugins, runs on any device and some binaries for popular distributions as well as the source code are freely available online.

Kaggle is an online platform where people can learn, share and find useful information such as source code, examples as well as data for particular projects and certified datasets for scientific research. Although Kaggle is mostly focused on concepts like Artificial Intelligence (AI) and Machine Learning (ML), still is a very useful resource and a great community that brings together learners, enthusiasts, developers and researchers.

Zenodo is a reputable data repository created to bring open access and open data, one of the main objective of the OpenAIRE project in Europe, operated by CERN it is one of a kind community that has modern capabilities for storing, accessing, managing and presenting data. It is a free, open source data-sharing platform with features including common data extension preview, but most significantly, the data provided by the community is citable, with a digital object identification DOI provided.

7.3 EGSnrc environment

Plenty of Monte Carlo computer programs have been developed, allowing us to conduct experiments in the field of health care using radioactive substances, X-rays, and gamma beams [117]. There is general-purpose software like MCNP [118], EGSnrc [119], Geant4 [120], Topas [121], and application specialized software like GATE [122], Gamos [123], Serpent [124], OpenMC [125] and so on. Some software is open-source and free, while others require a license; some are simple to use, while others require advanced programming abilities.

EGSnrc has the capability to effectively simulate photons, electrons and positrons passing via matter within 1 keV - 10GeV. In addition, it is a software with a lot of history behind it. EGS3 [126] was developed by Stanford Linear Accelerator Center, SLAC in 1978. Afterwards with the collaboration of Nelson, Hirayama and Rogers EGS4 [127] had been updated with an algorithm called PRESTA [128] which provided a solution to step-size reduction inconsistencies.

Kawrakow [129] and Bielajew [130] established advances in multiple scattering processes and created a new electron tracking algorithm PRESTA-II, that at the time provided a breakthrough on particle transport Monte Carlo codes. Over time, lots of updates and new functions were introduced, conclusively leading to the EGS5 [131] and EGSnrc [132]. All the source code of EGSnrc can be found online as well as instructions and code fixtures.

7.3.1 Compiling and Installing EGSnrc

In a technical manner, the EGSnrc is a software toolkit, meaning that it consists from many different source code routines that have some kind of options to configure complicated scenarios that are user defined. Therefore, that software toolkit in order to perform various calculations on a flexible degree of varying and complicated variables has the downside that the compilation procedure is a bit complicated.

Some pre-installed packages needed to be installed before continuing with the procedure of building the software from source code. As a reminder, the operating system utilized is Ubuntu more specifically version 20.04, with that being said the packages required are:

- Compiler gfortran
- Compiler gcc
- Compiler g++
- make (build automation tool)
- Tcl/Tk (Tool Command Language/ graphical user interface ToolKit)
- Grace (graphical interface)
- Open Motif (graphical interface)
- Qt5 (graphical interface)

All the above software packages needed to be installed and configured on the operating system of the calculation machine in order to provide the initial base where the source code building blocks are going to build. More information can be found on the technical report Appendix 2, with analytical instructions for how to perform the compilation steps as well as video tutorial on the YouTube platform [133] for detailed instructions. In addition, the source code that is hosted on the popular platform GitHub

[134] and supported by the National Research Council of Canada (nrc-cnrc) provides detailed instructions for various operating systems.

7.3.2 Getting started

After building and configuring the EGSnrc, good start is to look at the egs_inp, the main menu panel gui to perform basic executions. As shown in figure 25, at the left high there is an options selector which the user can easily navigate in different options to perform basic tasks such as compile a user defined code routine, execute in a specific way a routine, change settings and most importantly the PEGS Data generator routine.

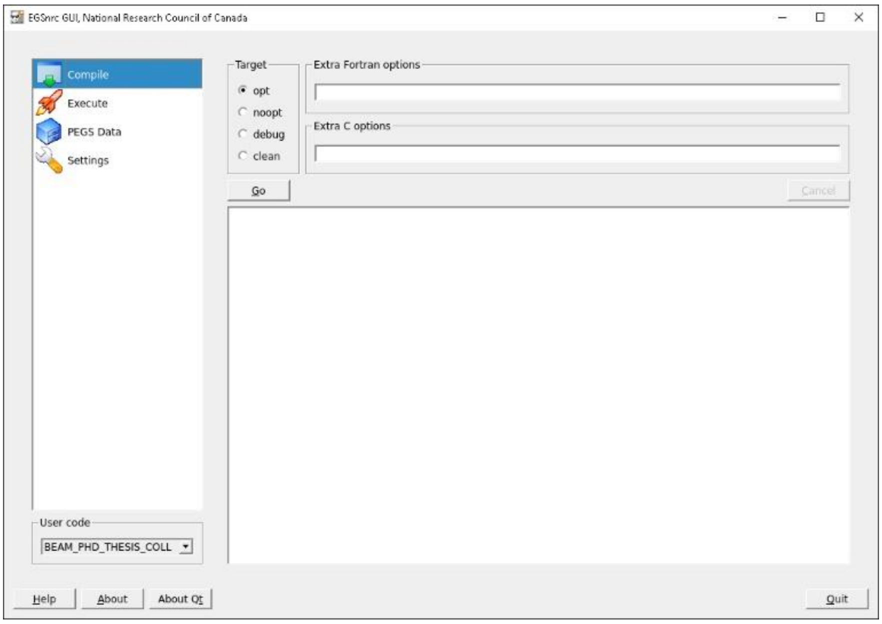

Target
● opt
○ noopt
○ debug
○ clean

User code
BEAM_PHD_THESIS_COLL

Figure 25 EGS_gui Main Menu Panel.

In this routine, as it can be seen in figure 26, the user can create his own pegs4data files. In this data files the user can define materials, which later on can be used in a geometry for a simulation from other EGSnrc routines. The ecosystem of EGSnrc has a pre-processed format the .pegs4data that allows all routines to consume the cross sectional data for the physical phenomena involved in a particular simulation scenario. The importance of those files is that the user defines an upper and lower limit for the photons energy (AP, UP) and the electrons energy (AE, UE) which depending of the range defined a simulation can be faster or slower.

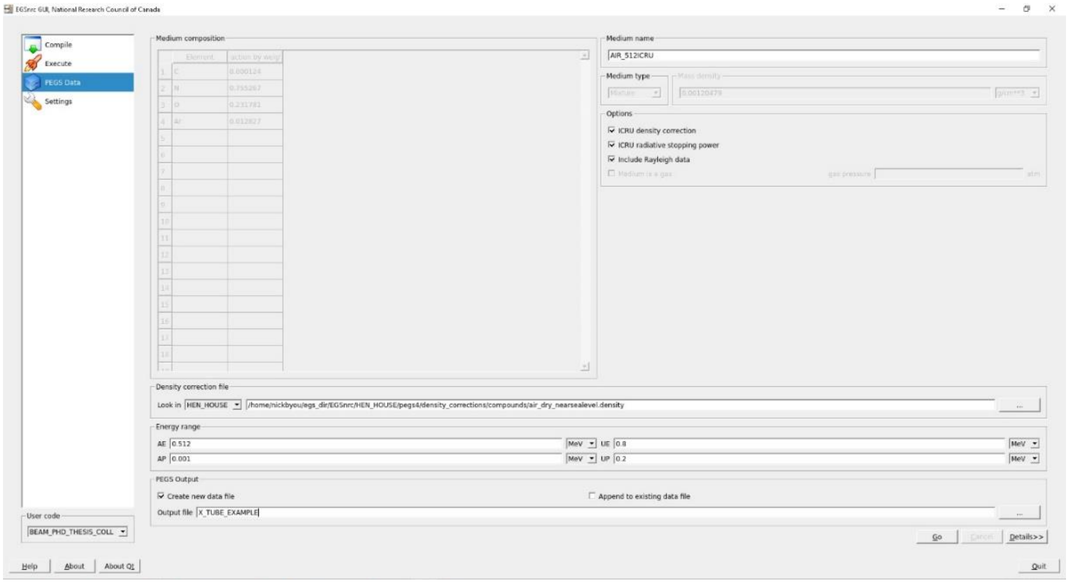

	Element	action by weig
1	C	0.000124
2	N	0.755267
3	O	0.231781
4	Ar	0.012827

Medium name: AIR_512ICRU

Medium type: Mixture; Mass density: 0.00120479 g/cm**3

☑ ICRU density correction
☑ ICRU radiative stopping power
☑ Include Rayleigh data
☐ Medium is a gas — gas pressure — atm

Look in: HEN_HOUSE /home/nickbyou/egs_dir/EGSnrc/HEN_HOUSE/pegs4/density_corrections/compounds/air_dry_nearsealevel.density

AE 0.512 MeV UE 0.8 MeV
AP 0.001 MeV UP 0.2 MeV

☑ Create new data file
☐ Append to existing data file
Output file: X_TUBE_EXAMPLE

User code: BEAM_PHD_THESIS_COLL

Figure 26 Pegs Data Creation by the graphical user interface.

A way to define a material is either to select an element, which represents a material consisting of only one specific element, or to select a compound. A compound represents more complicated materials that consists of multiple elements, contributing with a percentage each. Figure 27 shows how to access the internal folders of EGSnrc where the user can find compounds and elements to choose.

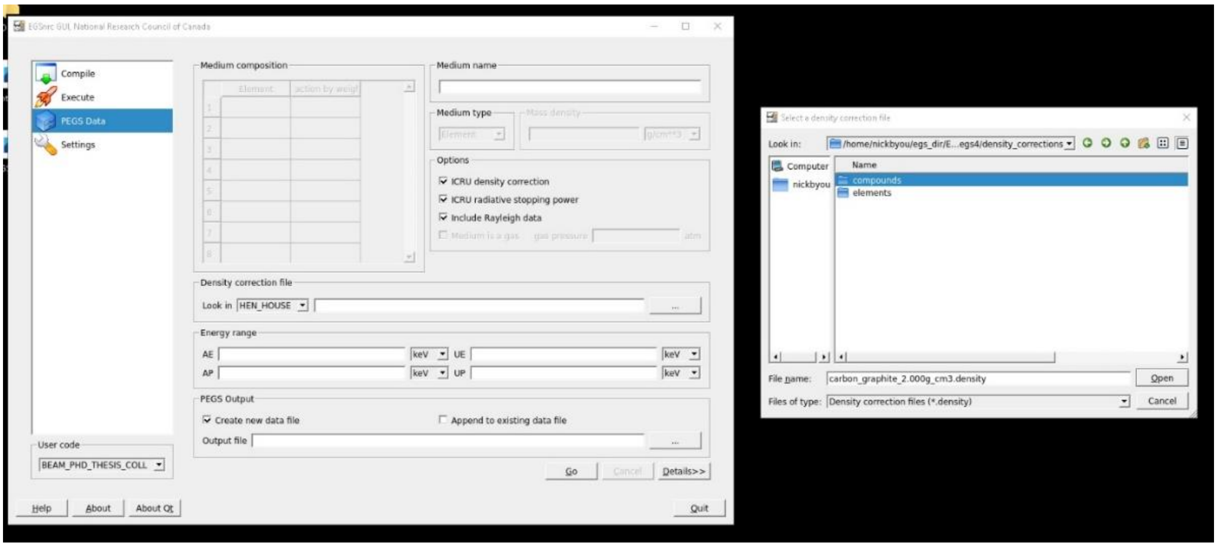

☑ ICRU density correction
☑ ICRU radiative stopping power
☑ Include Rayleigh data
☐ Medium is a gas — gas pressure — atm

Look in: HEN_HOUSE

AE keV UE keV
AP keV UP keV

☑ Create new data file
☐ Append to existing data file
Output file

User code: BEAM_PHD_THESIS_COLL

Look in: /home/nickbyou/egs_dir/E...egs4/density_corrections
File name: carbon_graphite_2.000g_cm3.density
Files of type: Density correction files (*.density)

Figure 27 Pegs Data Selection Option for compound or element.

7.3.3 CT x-ray source optimization and simulation

In order to create an x-ray source the BEAMnrc routines needs to be utilized. By typing beamnrc_gui in the command prompt the main graphical panel now appears, just like in figure 28. This graphical tool is very useful to build beam simulations. In order to create a new beam simulation the geometry of the "accelerator" needs to be defined. BEAMnrc was used to simulate linear accelerators, LINACs, applied in radiotherapy [135], so even if the same code is used for x-ray source for medical imaging as an abstraction to all x-ray sources both for high energies and low energies the term "accelerator" is used by developers.

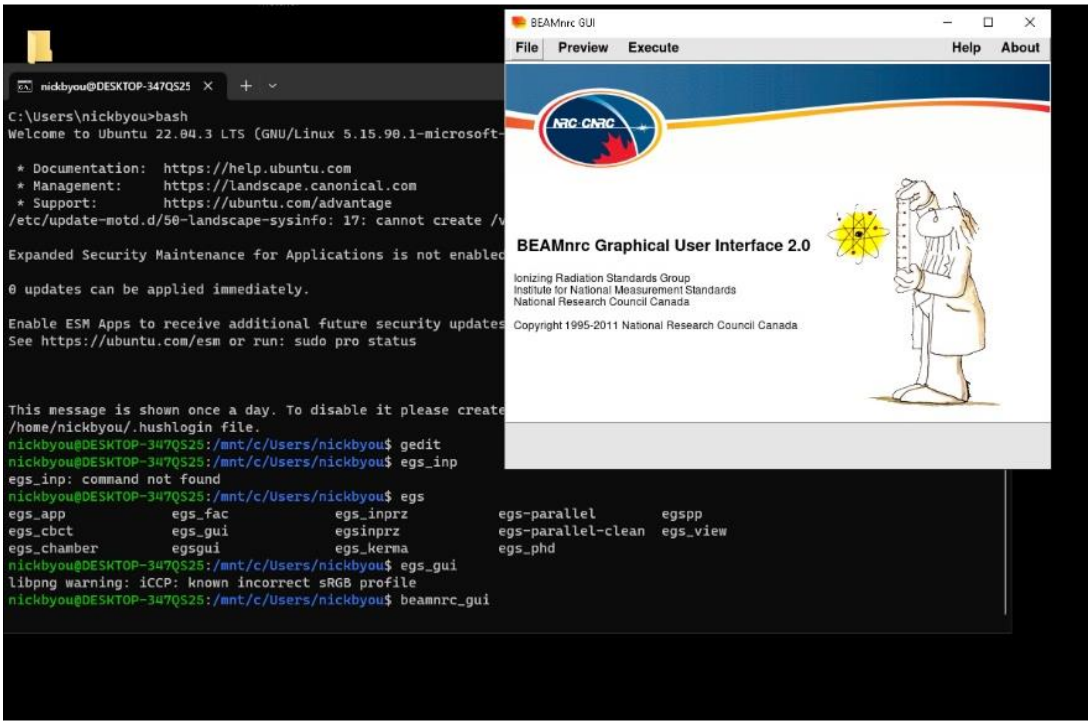

```
C:\Users\nickbyou>bash
Welcome to Ubuntu 22.04.3 LTS (GNU/Linux 5.15.90.1-microsoft-

 * Documentation:  https://help.ubuntu.com
 * Management:     https://landscape.canonical.com
 * Support:        https://ubuntu.com/advantage
/etc/update-motd.d/50-landscape-sysinfo: 17: cannot create /v

Expanded Security Maintenance for Applications is not enabled

0 updates can be applied immediately.

Enable ESM Apps to receive additional future security updates
See https://ubuntu.com/esm or run: sudo pro status


This message is shown once a day. To disable it please create
/home/nickbyou/.hushlogin file.
nickbyou@DESKTOP-347QS25:/mnt/c/Users/nickbyou$ gedit
nickbyou@DESKTOP-347QS25:/mnt/c/Users/nickbyou$ egs_inp
egs_inp: command not found
nickbyou@DESKTOP-347QS25:/mnt/c/Users/nickbyou$ egs
egs_app           egs_fac           egs_inprz         egs-parallel        egspp
egs_cbct          egs_gui           egsinprz          egs-parallel-clean  egs_view
egs_chamber       egsgui            egs_kerma         egs_phd
nickbyou@DESKTOP-347QS25:/mnt/c/Users/nickbyou$ egs_gui
libpng warning: iCCP: known incorrect sRGB profile
nickbyou@DESKTOP-347QS25:/mnt/c/Users/nickbyou$ beamnrc_gui
```

BEAMnrc Graphical User Interface 2.0

Ionizing Radiation Standards Group
Institute for National Measurement Standards
National Research Council Canada

Copyright 1995-2011 National Research Council Canada

Figure 28 BEAMnrc gui Main Panel.

The software here helps the user by providing a graphical environment to create gradually the geometry that will be simulated. For the x-ray source to be created the routine's geometrical components XTUBE, SLABS, CONS3R and SLABS were utilized to fully describe the 3D geometry of the x-ray source . As shown in figure 29 the user systematically can define all those components and assign identifier to them.

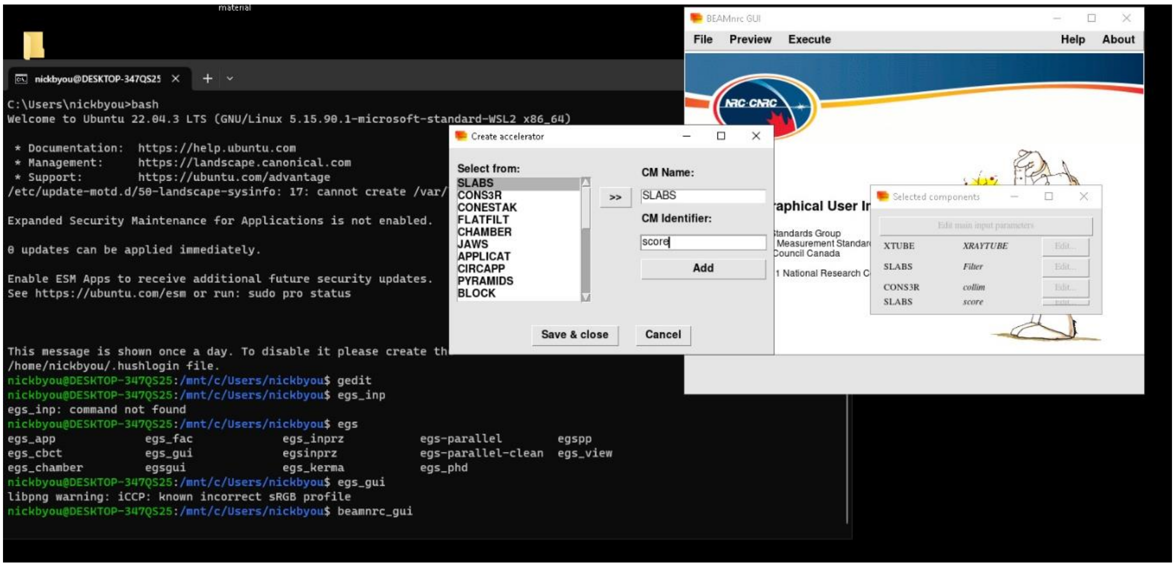

```
C:\Users\nickbyou>bash
Welcome to Ubuntu 22.04.3 LTS (GNU/Linux 5.15.90.1-microsoft-standard-WSL2 x86_64)

 * Documentation:  https://help.ubuntu.com
 * Management:     https://landscape.canonical.com
 * Support:        https://ubuntu.com/advantage
/etc/update-motd.d/50-landscape-sysinfo: 17: cannot create /var/

Expanded Security Maintenance for Applications is not enabled.

0 updates can be applied immediately.

Enable ESM Apps to receive additional future security updates.
See https://ubuntu.com/esm or run: sudo pro status


This message is shown once a day. To disable it please create th
/home/nickbyou/.hushlogin file.
nickbyou@DESKTOP-347QS25:/mnt/c/Users/nickbyou$ gedit
nickbyou@DESKTOP-347QS25:/mnt/c/Users/nickbyou$ egs_inp
egs_inp: command not found
nickbyou@DESKTOP-347QS25:/mnt/c/Users/nickbyou$ egs
egs_app             egs_fac             egs_inprz           egs-parallel        egspp
egs_cbct            egs_gui             egsinprz            egs-parallel-clean  egs_view
egs_chamber         egsgui              egs_kerma           egs_phd
nickbyou@DESKTOP-347QS25:/mnt/c/Users/nickbyou$ egs_gui
libpng warning: iCCP: known incorrect sRGB profile
nickbyou@DESKTOP-347QS25:/mnt/c/Users/nickbyou$ beamnrc_gui
```

Select from:
- SLABS
- CONS3R
- CONESTAK
- FLATFILT
- CHAMBER
- JAWS
- APPLICAT
- CIRCAPP
- PYRAMIDS
- BLOCK

CM Name: SLABS

CM Identifier: score

XTUBE	*XRAYTUBE*
SLABS	*Filter*
CONS3R	*collim*
SLABS	*score*

Figure 29 BEAMnrc New Accelerator creation by adding Component Modules.

The first component XTUBE is used to describe the anode-target of a realistic x-ray tube. The substance of this component is tungsten (W) for half cases and gold (AU) for the other half. The angle of the x-ray tube is defined at 22° [136], as this is the most common angle for a CT x-ray tube anode-target. The electron beam bombarding from the side is simulated by selecting the software's option, “ISOURC 10 – Parallel circular beam incident from the side” and the dimensions are 10, 200, 10 in the x, y, z directions respectively.

The second component utilized is SLABS which can define a simple rectangular geometry like an air gap in this study's case, with dimensions 400,400,10mm in the x,y,z directions respectively.

The CONS3R is a component that describes the collimator that opens the photon beam in order to achieve a 400x400mm field of view (FOV) beam. It consists of cones stack between each other. As shown in figure 30 the cone stack need two radius to be defined, so r1=25mm and r2=55mm were selected, and the material inside the collimator is vacuum and outside is stainless steel. The dimensions of this component is 400,400,50mm in the x,y,z directions respectively.

Lastly an additional air gap is defined as the last component with dimensions 400,400,500mm in the x,y,z directions respectively. After the beam passes the last component and the end, the scoring takes place.

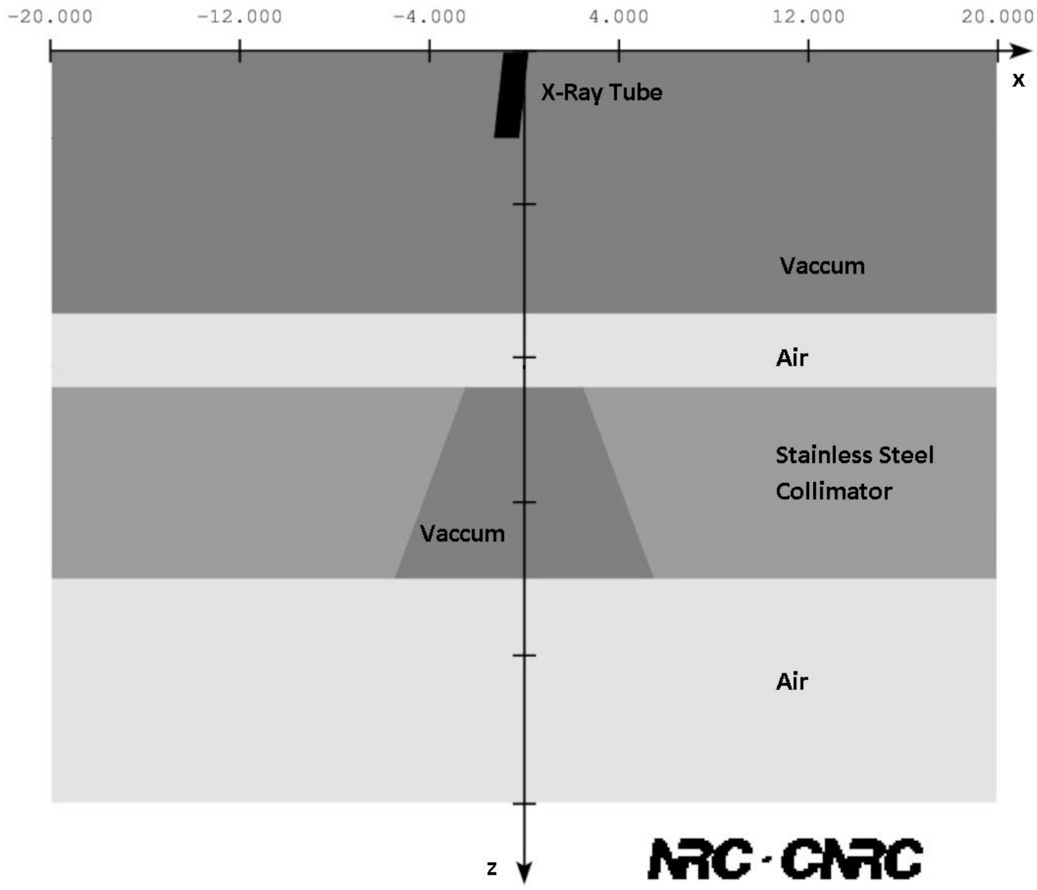

Figure 30 BEAMnrc Geometry Visualization of X-ray Source [137].

In order to make an efficient simulation, minimize the time of execution, and have rich full results, optimization methods were enabled. One such method the DBS (directional bremsstrahlung splitting), which is a variance reduction technique built-in the system of Beamnrc, that was utilized and made the simulation 60 times faster as was expected [138]. Utilizing such techniques enhances the likelihood of the physics phenomena and in this study's case generates more braking radiation in a specific direction.

The downside of utilizing such technique was that the output file was unable to be compressed, due to the statistical weights being stored already compressed inside the binary format. In addition, another downside was that the statistical weights was an overhead and slowed the irradiation simulations.

In order to handle those downsides, the simulation of beam generation had to be cut into two separate simulations. The first simulation, utilized the “ISOURC 10 – Parallel circular beam incident from the side”, and the scoring plane was defined right after the first gap, initially creating an output file with the statistical weights stored for each particle. The second simulation utilized the “ISOURC 21 – Parallel circular beam incident from the side”, utilizing the initially created file as input, those particles were passing via the collimator and scored at the end of the second air gap, but this time without the statistical weights. The built-in routine handling the ISOURC 21 takes into account the statistical weights of the particles used as input. After simulation, the particles scored no longer have statistical weights.

The options selected for beam simulation can be seen in Figure 31. In this figure, besides the Main panel there are also the Component panel, small window on the right, the Main input Panel, bottom down window and the EGSnrc parameters panel, up window. The Beamnrc GUI provides the user with options to choose algorithms such as the crossing boundaries algorithm and the electron-step algorithm. In addition, the user can enable or disable options for atomic relaxations, spin effects, electron impact effects, scattering effects. Additionally the user can choose various methods regarding the sampling techniques for various physics phenomena and choose from what databases the application should consume cross-sectional data regarding the particles utilized in the simulation.

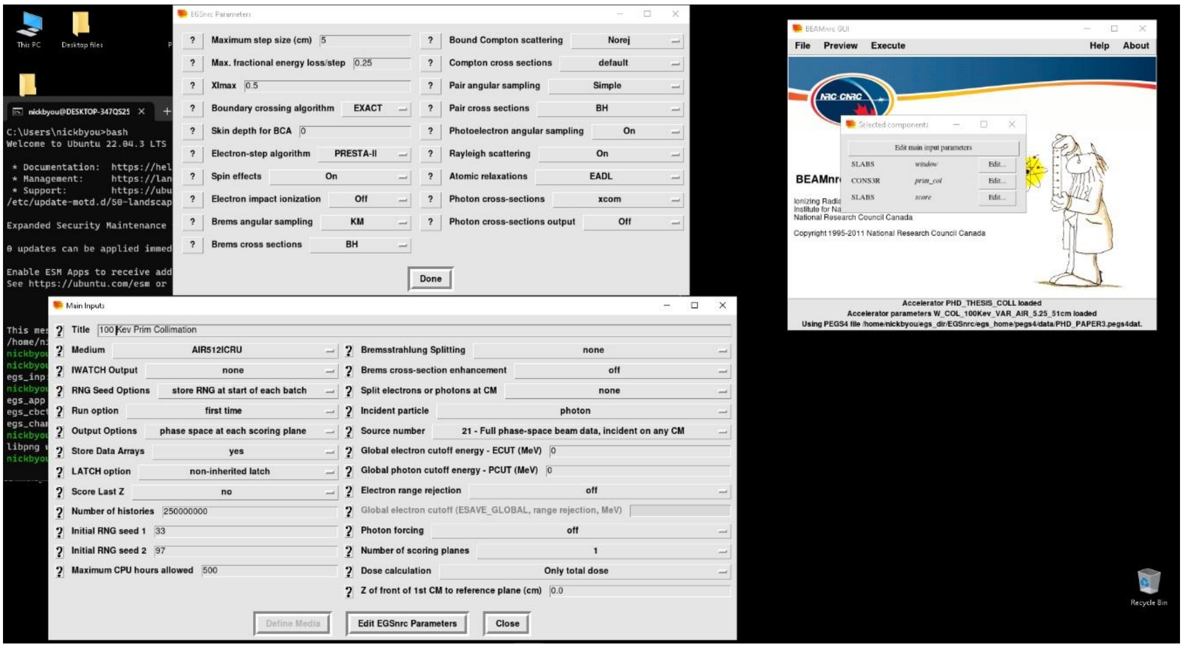

```
nickbyou@DESKTOP-347QS25
C:\Users\nickbyou>bash
Welcome to Ubuntu 22.04.3 LTS

 * Documentation:  https://hel
 * Management:     https://lan
 * Support:        https://ubu
/etc/update-motd.d/50-landscap

Expanded Security Maintenance

0 updates can be applied immed

Enable ESM Apps to receive add
See https://ubuntu.com/esm or


This mes
/home/ni
nickbyou
nickbyou
egs_inp:
nickbyou
egs_app
egs_cbct
egs_char
nickbyou
libpng w
nickbyou
```

EGSnrc Parameters

Maximum step size (cm): 5
Max. fractional energy loss/step: 0.25
XImax: 0.5
Boundary crossing algorithm: EXACT
Skin depth for BCA: 0
Electron-step algorithm: PRESTA-II
Spin effects: On
Electron impact ionization: Off
Brems angular sampling: KM
Brems cross sections: BH
Bound Compton scattering: Norej
Compton cross sections: default
Pair angular sampling: Simple
Pair cross sections: BH
Photoelectron angular sampling: On
Rayleigh scattering: On
Atomic relaxations: EADL
Photon cross-sections: xcom
Photon cross-sections output: Off

Main Inputs

Title: 100 Kev Prim Collimation
Medium: AIR512ICRU
IWATCH Output: none
RNG Seed Options: store RNG at start of each batch
Run option: first time
Output Options: phase space at each scoring plane
Store Data Arrays: yes
LATCH option: non-inherited latch
Score Last Z: no
Number of histories: 250000000
Initial RNG seed 1: 33
Initial RNG seed 2: 97
Maximum CPU hours allowed: 500
Bremsstrahlung Splitting: none
Brems cross-section enhancement: off
Split electrons or photons at CM: none
Incident particle: photon
Source number: 21 - Full phase-space beam data, incident on any CM
Global electron cutoff energy - ECUT (MeV): 0
Global photon cutoff energy - PCUT (MeV): 0
Electron range rejection: off
Global electron cutoff (ESAVE_GLOBAL, range rejection, MeV):
Photon forcing: off
Number of scoring planes: 1
Dose calculation: Only total dose
Z of front of 1st CM to reference plane (cm): 0.0

Selected components

SLABS window
CONS3R prim_col
SLABS score

Accelerator PHD_THESIS_COLL loaded
Accelerator parameters W_COL_100Kev_VAR_AIR_5.25_51cm loaded
Using PEGS4 file /home/nickbyou/egs_dir/EGSnrc/egs_home/pegs4/data/PHD_PAPER3.pegs4dat.

Figure 31 BEAMnrc simulation parameters example.

All simulations had the same options selected for the parameters, what changed was the energy of the electrons bombarding the anode-target ranging from 30keV - 150keV with step 5keV, and the anode material which was either tungsten (W) or gold (AU). All together 50 simulations were carried out, 25 for tungsten and 25 for gold. The initial particles for each beam simulation was 250x10^6 and the scored particles were approximately around 60x10^6. Depending on the geometry, the parameters used and the processing computer system the simulation was carried out, each beam took around 8-12 hours to be generated.

Each simulation produces an output file, an .egsphsp1 file. This file stores data in binary format where information regarding the simulation and the particles are stored. In order to analyze and have a visual representation of the results the user can use the BEAMDP [139] via the command line interface, cli, or the GUI. As shown in Figure 32, by utilizing the beamdp_gui the user can generate from the particles scored, specific plots such as Spectral Distribution, Energy Fluence Distribution, Scatter Plot, etc.

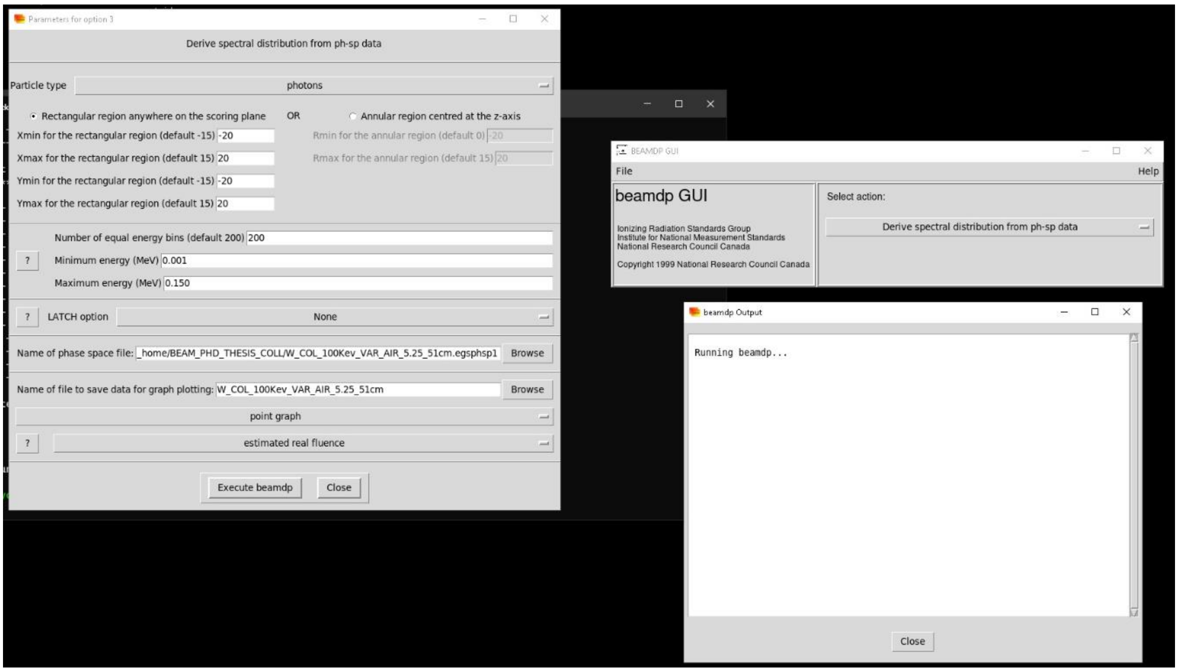

Parameters for option 3

Derive spectral distribution from ph-sp data

Particle type: photons

● Rectangular region anywhere on the scoring plane OR ○ Annular region centred at the z-axis

Xmin for the rectangular region (default -15) -20
Xmax for the rectangular region (default 15) 20
Ymin for the rectangular region (default -15) -20
Ymax for the rectangular region (default 15) 20
Rmin for the annular region (default 0) -20
Rmax for the annular region (default 15) 20

Number of equal energy bins (default 200) 200
Minimum energy (MeV) 0.001
Maximum energy (MeV) 0.150

LATCH option: None

Name of phase space file: _home/BEAM_PHD_THESIS_COLL/W_COL_100Kev_VAR_AIR_5.25_51cm.egsphsp1

Name of file to save data for graph plotting: W_COL_100Kev_VAR_AIR_5.25_51cm

point graph

estimated real fluence

BEAMDP GUI

beamdp GUI

Ionizing Radiation Standards Group
Institute for National Measurement Standards
National Research Council Canada

Copyright 1999 National Research Council Canada

Select action: Derive spectral distribution from ph-sp data

beamdp Output

```
Running beamdp...
```

Figure 32 BEAMDP gui parameters selection and execution example.

After the processing of the .egsphsp1 file has finished the beamdp application opens an xmgrace [140] session. As seen in figure 33, in this xmgrace application session the user can finalize, change, save the plot selected by the user.

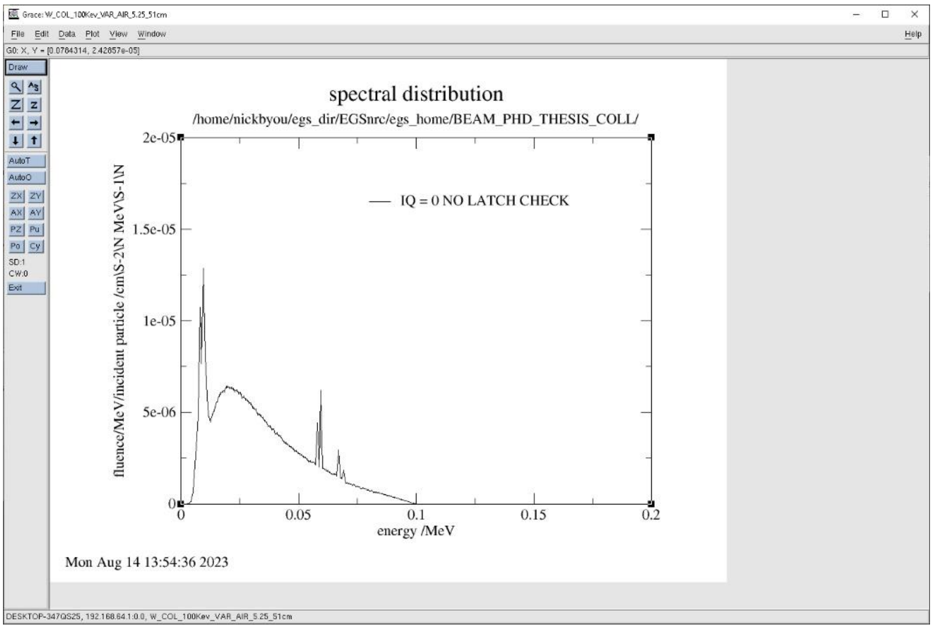

Grace: W_COL_100Kev_VAR_AIR_5.25_51cm

G0: X, Y = [0.0784314, 2.42857e-05]

DESKTOP-347QS25, 192.168.64.1:0.0, W_COL_100Kev_VAR_AIR_5.25_51cm

Figure 33 Example of the BEAMDP output opening an xmgrace session.

7.3.4 CT dose simulation and case studies

After the x-ray beams were ready, another key task was the creation of phantoms to irradiate. One routine namely ctcreate [141], made the creation of phantoms from anonymous dicom images possible. This particular routine creates 3D phantoms based on personalized data from patient specific anonymous dicom files. In the study three phantoms were utilized, a chest phantom based on patient chest [142] examination, a brain phantom based on anonymous patient examination [143] and an abdomen phantom based on patient abdomen examinations [144].

In order to create a phantom via ctcreate, first all images needs to be in a stack of .dcm file format, each slice one file. Afterwards the user needs to create a .txt file with all full path of each .dcm slice just as shown on figure 34.

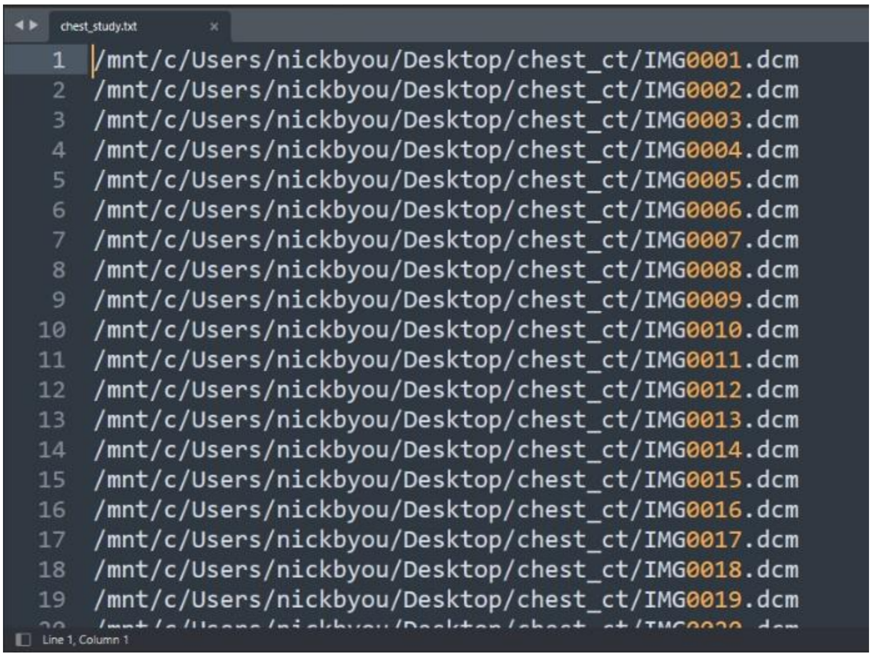

```
/mnt/c/Users/nickbyou/Desktop/chest_ct/IMG0001.dcm
/mnt/c/Users/nickbyou/Desktop/chest_ct/IMG0002.dcm
/mnt/c/Users/nickbyou/Desktop/chest_ct/IMG0003.dcm
/mnt/c/Users/nickbyou/Desktop/chest_ct/IMG0004.dcm
/mnt/c/Users/nickbyou/Desktop/chest_ct/IMG0005.dcm
/mnt/c/Users/nickbyou/Desktop/chest_ct/IMG0006.dcm
/mnt/c/Users/nickbyou/Desktop/chest_ct/IMG0007.dcm
/mnt/c/Users/nickbyou/Desktop/chest_ct/IMG0008.dcm
/mnt/c/Users/nickbyou/Desktop/chest_ct/IMG0009.dcm
/mnt/c/Users/nickbyou/Desktop/chest_ct/IMG0010.dcm
/mnt/c/Users/nickbyou/Desktop/chest_ct/IMG0011.dcm
/mnt/c/Users/nickbyou/Desktop/chest_ct/IMG0012.dcm
/mnt/c/Users/nickbyou/Desktop/chest_ct/IMG0013.dcm
/mnt/c/Users/nickbyou/Desktop/chest_ct/IMG0014.dcm
/mnt/c/Users/nickbyou/Desktop/chest_ct/IMG0015.dcm
/mnt/c/Users/nickbyou/Desktop/chest_ct/IMG0016.dcm
/mnt/c/Users/nickbyou/Desktop/chest_ct/IMG0017.dcm
/mnt/c/Users/nickbyou/Desktop/chest_ct/IMG0018.dcm
/mnt/c/Users/nickbyou/Desktop/chest_ct/IMG0019.dcm
```

Figure 34 Text file with the full path of all anonymous dicom slice files.

By typing in the command prompt the command, “ctcreate” the process of creating the phantom begins. Figure 35 shows that once the process is initiated it requires from the user to select one of the file format supported by the routine. Once the user selects the third option for DICOM format then the process shall ask for the path of the text file containing the full paths of each dicom slices. Ctcreate routine is responsible for the scoring plain of the geometrical components that the phantom consists inside the simulation.

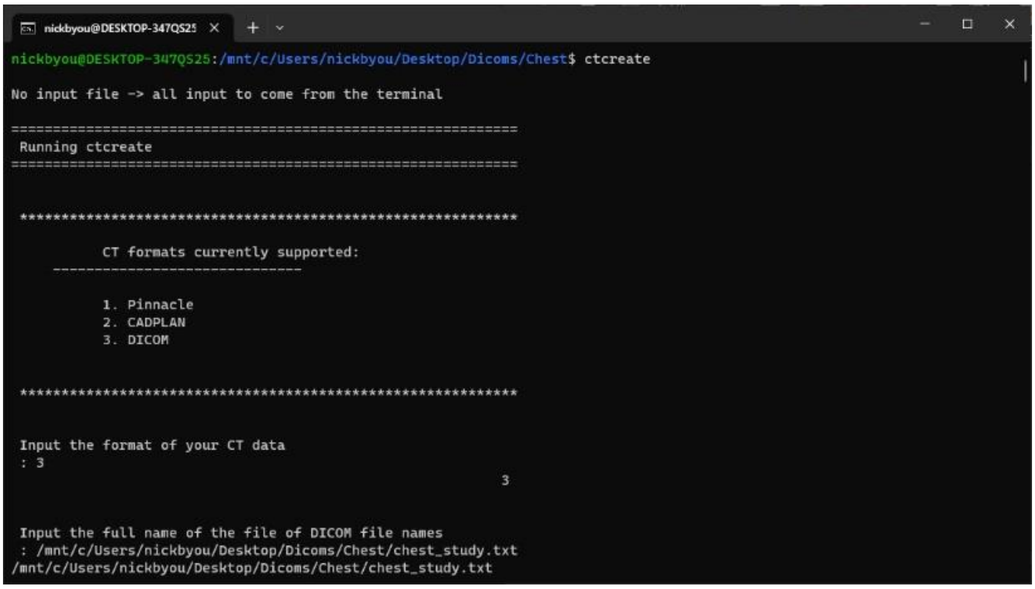

```
nickbyou@DESKTOP-347QS25:/mnt/c/Users/nickbyou/Desktop/Dicoms/Chest$ ctcreate

No input file -> all input to come from the terminal

=============================================================
 Running ctcreate
=============================================================


 ************************************************************

          CT formats currently supported:
     ------------------------------

          1. Pinnacle
          2. CADPLAN
          3. DICOM


 ************************************************************


 Input the format of your CT data
 : 3
                                                           3


 Input the full name of the file of DICOM file names
 : /mnt/c/Users/nickbyou/Desktop/Dicoms/Chest/chest_study.txt
/mnt/c/Users/nickbyou/Desktop/Dicoms/Chest/chest_study.txt
```

Figure 35 CTCREATE program interface.

The ctcreate routine has a limitations of the number of slices it can read, around 269 is the maximum value by default. If all goes well for the user and the routine successfully reads all slices then the routine will identify all dimensions in the x, y, z directions as well as the voxel size in cm from the original, anonymous dicom image. As shown in figure 36 after the image has been read, the user needs to insert the subset dimensions in the x, y, z directions.

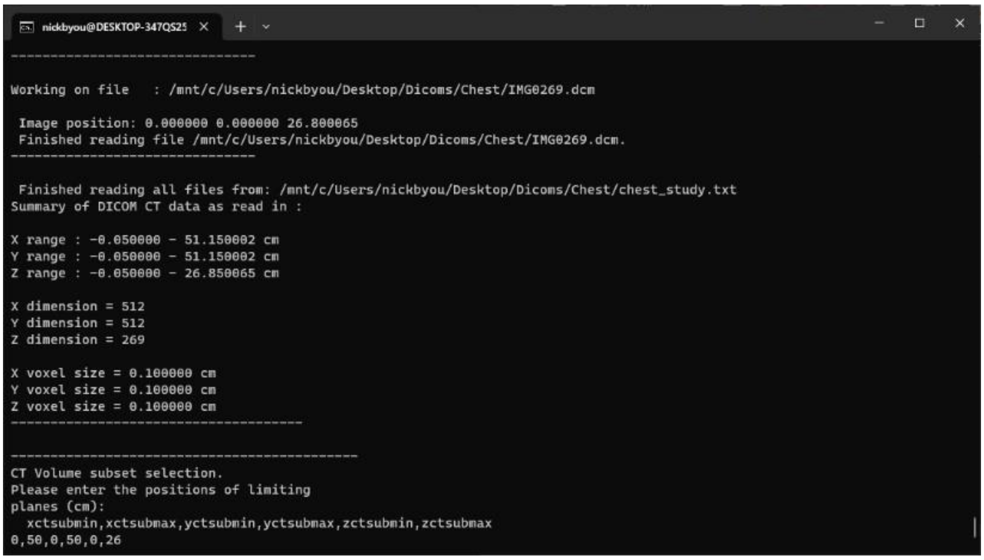

```
-------------------------------

Working on file   : /mnt/c/Users/nickbyou/Desktop/Dicoms/Chest/IMG0269.dcm

 Image position: 0.000000 0.000000 26.800065
 Finished reading file /mnt/c/Users/nickbyou/Desktop/Dicoms/Chest/IMG0269.dcm.
-------------------------------

 Finished reading all files from: /mnt/c/Users/nickbyou/Desktop/Dicoms/Chest/chest_study.txt
Summary of DICOM CT data as read in :

X range : -0.050000 - 51.150002 cm
Y range : -0.050000 - 51.150002 cm
Z range : -0.050000 - 26.850065 cm

X dimension = 512
Y dimension = 512
Z dimension = 269

X voxel size = 0.100000 cm
Y voxel size = 0.100000 cm
Z voxel size = 0.100000 cm
-------------------------------------


--------------------------------------------
CT Volume subset selection.
Please enter the positions of limiting
planes (cm):
  xctsubmin,xctsubmax,yctsubmin,yctsubmax,zctsubmin,zctsubmax
0,50,0,50,0,26
```

Figure 36 CTCREATE - CT volume subset selection.

The phantom that is going to be produced cannot have the same resolution as the original patient image file. As the egs-phantom is going to be the scoring plane for dose simulations with other EGSnrc routines, the developers established some limitations. In figure 36 the number of voxel dimensions in the x, y, z directions are 512, 512, 269 with x, y, z voxel sizes 0.1, 0.1, 0.1 cm respectively, that is the resolution of the anonymous patient dicom image utilized for the chest phantom. However, after the user specified the subset limits, the routine gives the minimum resolution of the egs-phantom. As it can be seen in figure 37 the new dimensions of the chest phantom in the x, y, z directions are 100, 100, 104 with x, y, z voxel sizes 0.5, 0.5, 0.25 cm respectively.

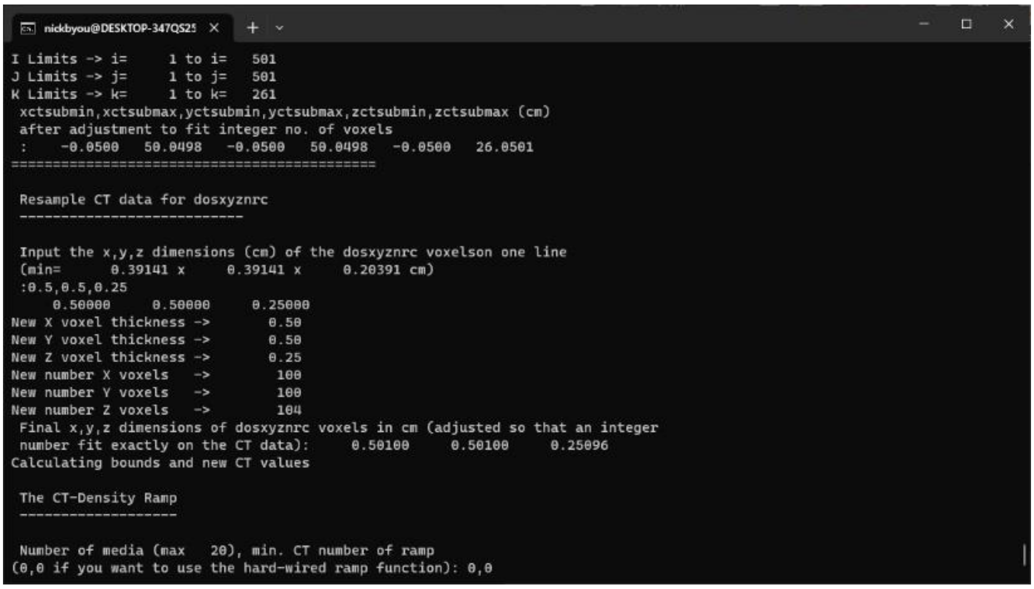

```
I Limits -> i=     1 to i=   501
J Limits -> j=     1 to j=   501
K Limits -> k=     1 to k=   261
 xctsubmin,xctsubmax,yctsubmin,yctsubmax,zctsubmin,zctsubmax (cm)
 after adjustment to fit integer no. of voxels
 :    -0.0500   50.0498   -0.0500   50.0498   -0.0500   26.0501
============================================

 Resample CT data for dosxyznrc
 ---------------------------

 Input the x,y,z dimensions (cm) of the dosxyznrc voxelson one line
 (min=      0.39141 x     0.39141 x     0.20391 cm)
 :0.5,0.5,0.25
     0.50000     0.50000     0.25000
New X voxel thickness ->       0.50
New Y voxel thickness ->       0.50
New Z voxel thickness ->       0.25
New number X voxels   ->        100
New number Y voxels   ->        100
New number Z voxels   ->        104
 Final x,y,z dimensions of dosxyznrc voxels in cm (adjusted so that an integer
 number fit exactly on the CT data):     0.50100     0.50100     0.25096
Calculating bounds and new CT values

 The CT-Density Ramp
 -------------------

 Number of media (max   20), min. CT number of ramp
(0,0 if you want to use the hard-wired ramp function): 0,0
```

Figure 37 CTCREATE – new dimensions and voxel size for egsphantom.

The brain phantom had voxel dimensions 512, 512, 244 in the x, y, z directions with x, y, z voxel sizes 0.1, 0.1, 0.1 cm respectively. The abdomen phantom had voxel dimensions 512, 512, 226 in the x, y, z directions with x, y, z voxel sizes 0.1, 0.1, 0.3 cm respectively. The brain phantom had voxel dimensions 512, 512, 244 in the x, y, z directions with x, y, z voxel sizes 0.1, 0.1, 0.1 cm respectively. The abdomen phantom had voxel dimensions 512, 512, 226 in the x, y, z directions with x, y, z voxel sizes 0.1, 0.1, 0.3 cm respectively. In table 2, slices from the original, anonymous dicom image and slices from the egs-phantom can be observed side by side to compare the difference in resolutions.

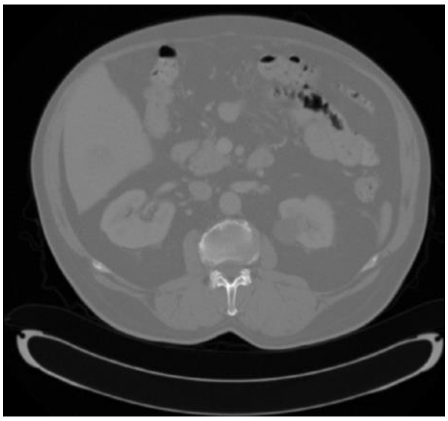	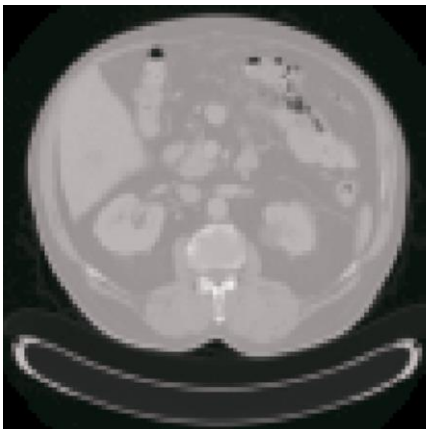

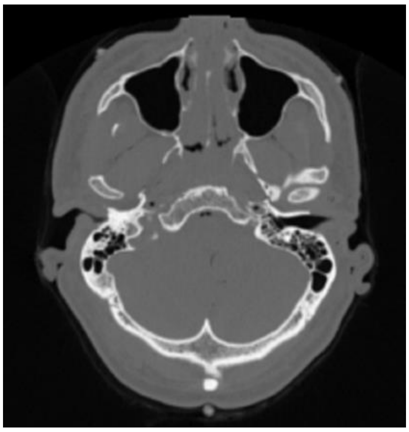	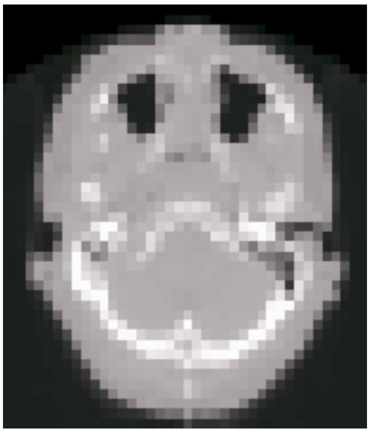
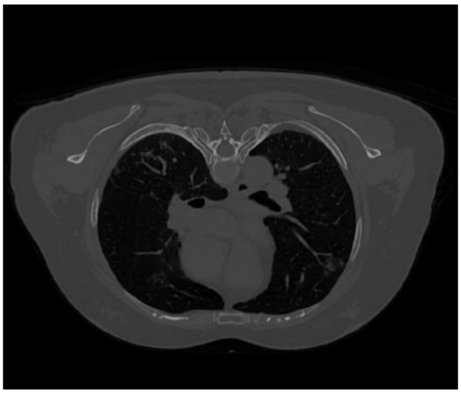	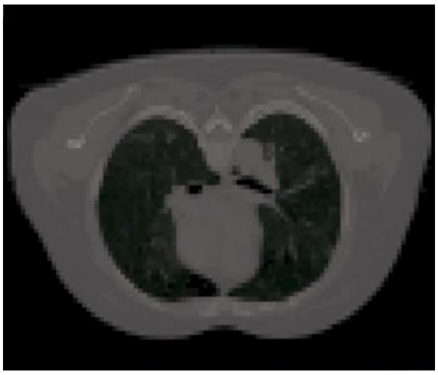
a	b

Table 2 Dicom (a) - Egsphantom (b) slices for abdomen, brain and chest phantoms.

To finalize the egs-phantom creation process and export the options selected via the cli interface of the ctcreate routine, the association of the anonymous dicom image Hounsfield units (HU) value to a material, pegs4data material, and to a value of density (g/cc). Four materials were utilized for the purposes of the study, air, lung, tissue and bone. As it can be seen in figure 38, the default CT ramp function carried out the association of the HU values to material-density values.

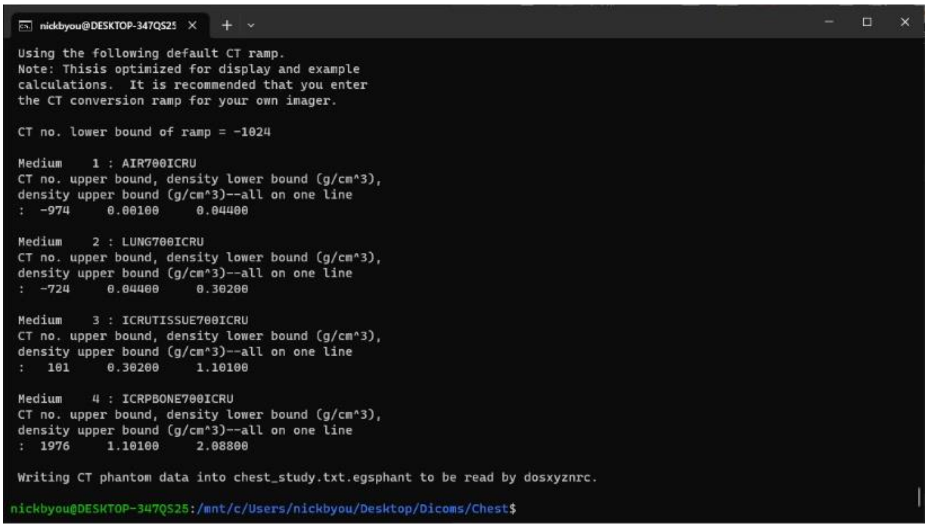

```
Using the following default CT ramp.
Note: Thisis optimized for display and example
calculations.  It is recommended that you enter
the CT conversion ramp for your own imager.

CT no. lower bound of ramp = -1024

Medium    1 : AIR700ICRU
CT no. upper bound, density lower bound (g/cm^3),
density upper bound (g/cm^3)--all on one line
:  -974     0.00100     0.04400

Medium    2 : LUNG700ICRU
CT no. upper bound, density lower bound (g/cm^3),
density upper bound (g/cm^3)--all on one line
:  -724     0.04400     0.30200

Medium    3 : ICRUTISSUE700ICRU
CT no. upper bound, density lower bound (g/cm^3),
density upper bound (g/cm^3)--all on one line
:   101     0.30200     1.10100

Medium    4 : ICRPBONE700ICRU
CT no. upper bound, density lower bound (g/cm^3),
density upper bound (g/cm^3)--all on one line
:  1976     1.10100     2.08800

Writing CT phantom data into chest_study.txt.egsphant to be read by dosxyznrc.

nickbyou@DESKTOP-347QS25:/mnt/c/Users/nickbyou/Desktop/Dicoms/Chest$
```

Figure 38 Finalizing the creation of the chest egs-phantom.

With the beams and the phantoms ready, the next step is to irradiate those phantoms by utilizing the DOSXYZnrc routine, more particular the DOSXYZnrc GUI. By typing dosxyznrc_gui on the command prompt the Main menu panel appear, just like in figure 39.

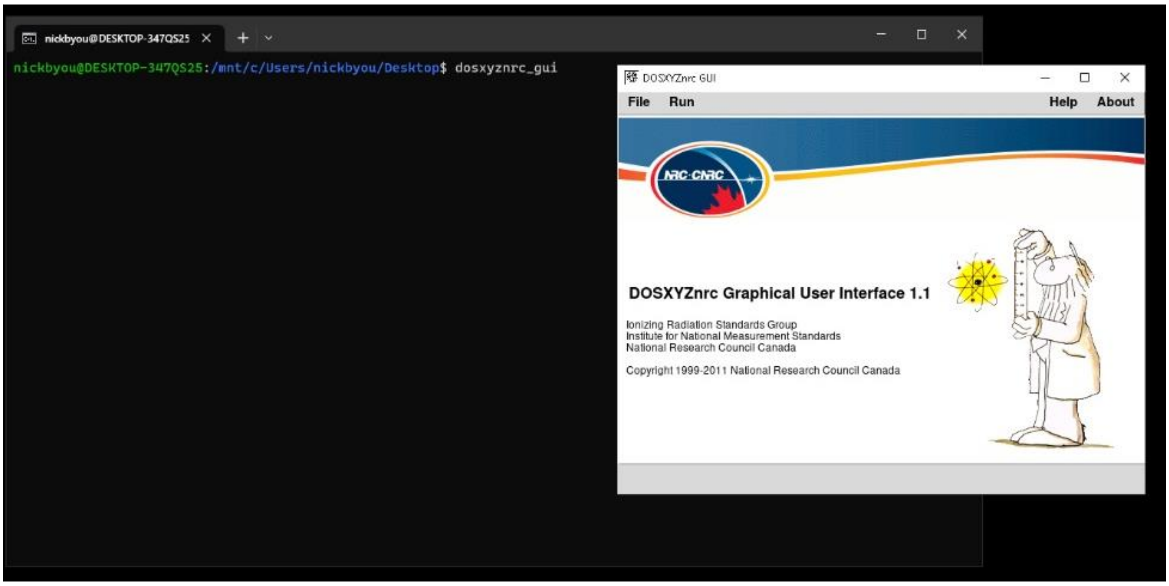

```
nickbyou@DESKTOP-347QS25:/mnt/c/Users/nickbyou/Desktop$ dosxyznrc_gui
```

DOSXYZnrc Graphical User Interface 1.1

Ionizing Radiation Standards Group
Institute for National Measurement Standards
National Research Council Canada

Copyright 1999-2011 National Research Council Canada

Figure 39 DOSxyznrc gui Main Menu Panel.

The scenario here is to simulate an actual CT examination. The patient lays down on the bed, the x-ray source is producing the appropriate beam, and afterwards the x-ray source would irradiate the patient in a circular rotation 360°. The DOSXYZnrc provides the configuration and the functions in order to simulate such procedure and score dosage by utilizing the beams produced previously by the BEAMnrc routines. By selecting the option for the source, provided by the DOSXYZnrc, “ISOURC-8=Phase-space source from multiple direction”, the user can now configure a previously generated .egsphsp file to irradiate circularly from a fixed point, just as shown in figure 40. The number of particles used was 10^9 photons; to achieve this amount, the source turned on the redistribute option; after the procedure reached the final photon within the space phase file, the photons were redistributed once again from the same input .egsphsp file.

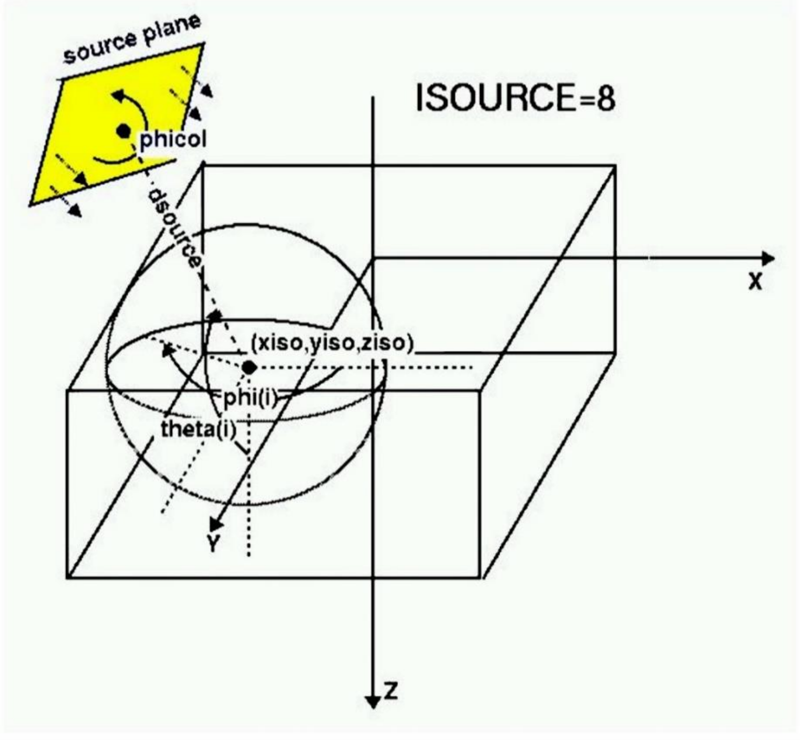

Figure 40 DOSxyznrc ISOURCE 8 visualization [141].

The parameters used for the source would vary from each phantom case. As each phantom takes, the coordinate system from the patient data it was generated from so each of the scenarios utilized had some parameters changed while other parameters were common. For the case of chest phantom the isocenter was x,y,z= 250,250,130mm with dsource=250mm distance, for the case of abdomen phantom the isocenter was x,y,z= 0,-150,0 mm with dsource=220mm distance and for the brain phantom the isocenter was x,y,z= 250,250,1170mm with dsource=70mm distance. For all cases, the angle theta=90° and the varying angle phi from 0-356.6°. The number of projections utilized was 100, with each projection having an angle of 3.6° and an equal probability. Figure 41 shows the parameters utilized for the simulation with DOSXYZnrc.

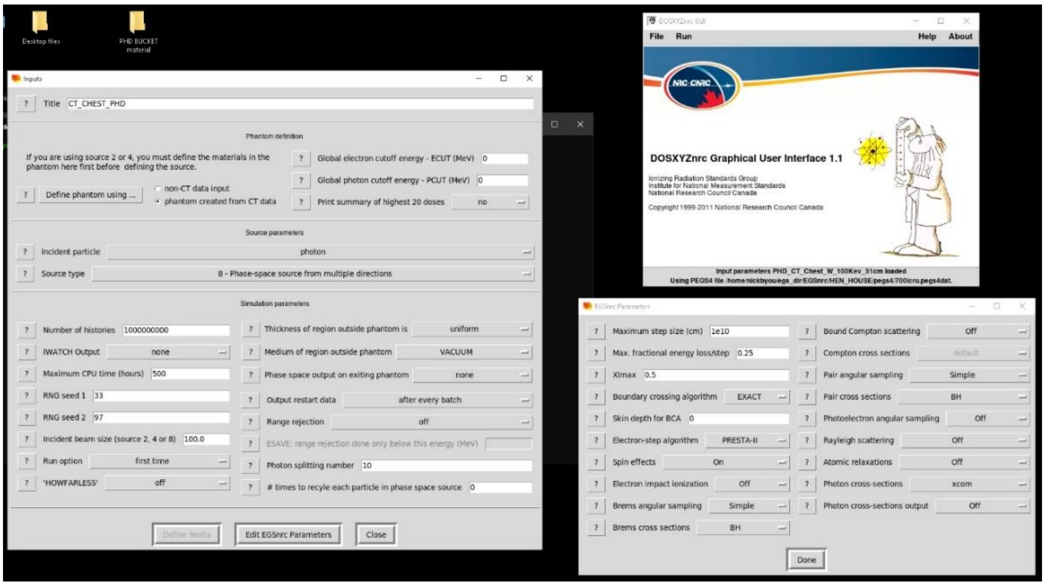

Title CT_CHEST_PHD

If you are using source 2 or 4, you must define the materials in the phantom here first before defining the source.

○ non-CT data input
● phantom created from CT data

Global electron cutoff energy - ECUT (MeV) 0
Global photon cutoff energy - PCUT (MeV) 0
Print summary of highest 20 doses no

Incident particle photon
Source type 8 - Phase-space source from multiple directions

Number of histories 1000000000
IWATCH Output none
Maximum CPU time (hours) 500
RNG seed 1 33
RNG seed 2 97
Incident beam size (source 2, 4 or 8) 100.0
Run option first time
'HOWFARLESS' off
Thickness of region outside phantom is uniform
Medium of region outside phantom VACUUM
Phase space output on exiting phantom none
Output restart data after every batch
Range rejection off
ESAVE: range rejection done only below this energy (MeV)
Photon splitting number 10
# times to recyle each particle in phase space source 0

DOSXYZnrc Graphical User Interface 1.1

Ionizing Radiation Standards Group
Institute for National Measurement Standards
National Research Council Canada

Copyright 1999-2011 National Research Council Canada

Input parameters PHD_CT_Chest_W_100Kev_51cm loaded
Using PEGS4 file /home/nickbyou/egs_dir/EGSnrc/HEN_HOUSE/pegs4/700icru.pegs4dat.

Maximum step size (cm) 1e10
Max. fractional energy loss/step 0.25
Ximax 0.5
Boundary crossing algorithm EXACT
Skin depth for BCA 0
Electron-step algorithm PRESTA-II
Spin effects On
Electron impact ionization Off
Brems angular sampling Simple
Brems cross sections BH
Bound Compton scattering Off
Compton cross sections default
Pair angular sampling Simple
Pair cross sections BH
Photoelectron angular sampling Off
Rayleigh scattering Off
Atomic relaxations Off
Photon cross-sections xcom
Photon cross-sections output Off

Figure 41 DOSxyznrc Inputs and Parameters Panels.

Each simulation produces a .3ddose output file. Inside that file all doses for each voxel of the phantom is stored. The user can access a visual view of the dosimetric map via the routine dosxyz_show [145]. As it can be seen in figure 42, the dosxyz_show routine can take the 3ddose file and visualize it depending on the distribution. In addition, the routine provides some basic image manipulation functions, a 3D phantom rotation between the XZ, XY, and YZ planes.

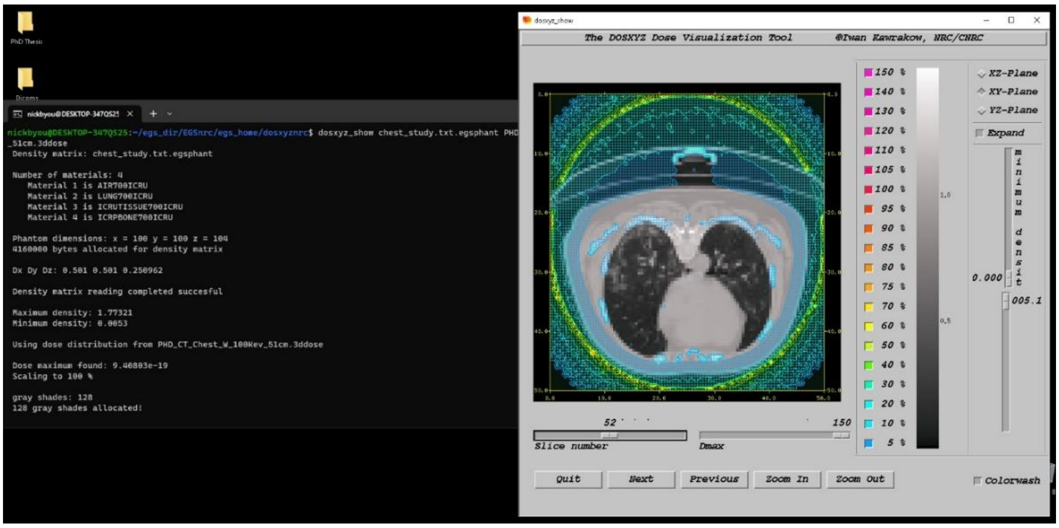

```
nickbyou@DESKTOP-347QS25:~/egs_dir/EGSnrc/egs_home/dosxyznrc$ dosxyz_show chest_study.txt.egsphant PHD
_51cm.3ddose
 Density matrix: chest_study.txt.egsphant

 Number of materials: 4
    Material 1 is AIR700ICRU
    Material 2 is LUNG700ICRU
    Material 3 is ICRUTISSUE700ICRU
    Material 4 is ICRPBONE700ICRU

 Phantom dimensions: x = 100 y = 100 z = 104
 4160000 bytes allocated for density matrix

 Dx Dy Dz: 0.501 0.501 0.250962

 Density matrix reading completed succesful

 Maximum density: 1.77321
 Minimum density: 0.0053

 Using dose distribution from PHD_CT_Chest_W_100Kev_51cm.3ddose

 Dose maximum found: 9.40803e-19
 Scaling to 100 %

 gray shades: 128
 128 gray shades allocated!
```

Figure 42 Dosxyz_show example - Visualization of the dosimetric map on the phantom.

Another very helpful tool is the STATDOSE [146] routine, as it provides functionality to read, analyze, normalize, rebin, plot and save dose distribution produced by the EGSnrc routines like DOSXYZnrc. Figure 43 depicts an example of executing the statdose routine via the command prompt, only the cli is available for the statdose routine, no GUI is available at the moment.

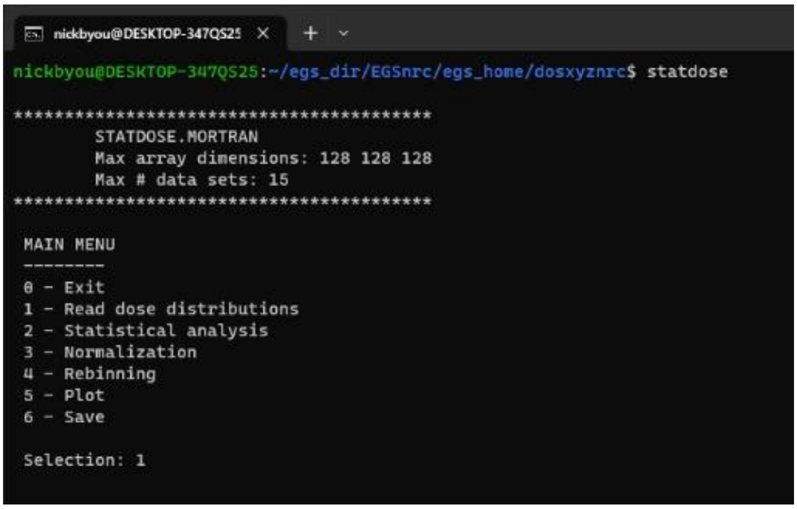

```
nickbyou@DESKTOP-347QS25:~/egs_dir/EGSnrc/egs_home/dosxyznrc$ statdose

*****************************************
        STATDOSE.MORTRAN
        Max array dimensions: 128 128 128
        Max # data sets: 15
*****************************************

 MAIN MENU
 --------
 0 - Exit
 1 - Read dose distributions
 2 - Statistical analysis
 3 - Normalization
 4 - Rebinning
 5 - Plot
 6 - Save

 Selection: 1
```

Figure 43 STATDOSE - Program execution in cli environment.

In addition, statdose opens an xmgrace session for configuring and finalizing the plot, as it can be seen in figure 44.

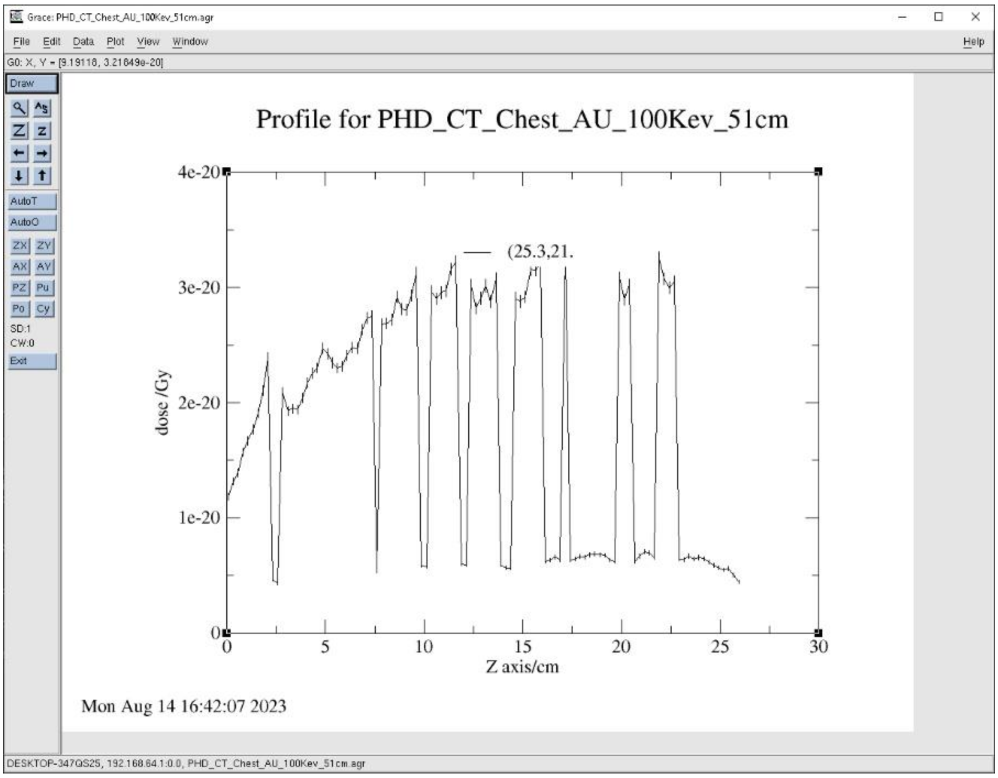
Grace: PHD_CT_Chest_AU_100Kev_51cm.agr
File
Edit
Data
Plot
View
Window
Help
G0: X, Y = [9.19118, 3.21649e-20]
Draw
AutoT
AutoO
ZX
ZY
AX
AY
PZ
Pu
Po
Cy
SD:1
CW:0
Exit
Profile for PHD_CT_Chest_AU_100Kev_51cm
(25.3,21.
dose /Gy
4e-20
3e-20
2e-20
1e-20
0
0
5
10
15
20
25
30
Z axis/cm
Mon Aug 14 16:42:07 2023
DESKTOP-347QS25, 192.168.64.1:0.0, PHD_CT_Chest_AU_100Kev_51cm.agr

Figure 44 Example of the STATDOSE plot command opening an xmgrace session.

7.4 GATE environment

GATE is an open source application, built with the geant4 software toolkit. With GATE, the user can simulate scenarios on emission tomography, dosimetry and radiotherapy [147]. Although GATE was initially created to perform scenarios with Positron Emission Tomography, PET and Single Photon Emission Computed Tomography SPECT [148] soon it was able to move to linear accelerator, LINAC, simulations [149]. In addition, GATE utilizes the data framework ROOT [150] and exports its outputs in a .root format, making the analysis and the plotting procedures easy to use for the user.

The geant4 software toolkit namely, stands for GEometry ANd Tracking, version 4. This particular software toolkit is the most organized and unique project to perform Monte Carlo calculation. Developed in CERN, it utilizes C++ object-oriented techniques and concepts in order to provide users with a plethora of modelling methods for many physics related phenomena regarding particle-matter interactions. Physicists created it with the purpose to meet the needs of the next era of particle physics research. In terms of code size and scope, as well as the number of contributors, Geant4 may be the largest and most sophisticated initiative of its kind. Its applications vary from high-energy physics [151], to space radiation sciences [152] and to medical physics [153].

7.4.1 Building and configuring GATE

GATE is a software the evolved over the years and provided users with extra capabilities. The direct dependencies are Geant4 and ROOT. Other optional dependencies are packages like CLHEP, ITK, ECAT, LMF, libTorch etc. In this work, the GATE version utilized was GATE v9.0, and the packages installed, before the procedure of compilation was:

- Geant4 version 10.06
- ROOT version 6.22.02
- ECAT version 7
- LMF version 3
- ITK version 5.1.1

The operating system in all machine utilized was Ubuntu 20.04, the procedures to compile and install from scratch all the appropriate software, along with fixtures and built on top of them the GATE application, was challenging. All software packages needed to be installed in the correct version and in some cases appropriate compiler flags needed to be turned on. Due to the complexity of the compilation procedure of GATE, there are detailed instruction provided in Appendix 2 and a tutorial video was made and uploaded on the popular platform YouTube [154]. Some fixtures has been provided also in Appendix 2 for the unsupported libraries lmf_v3 and ecat_v7. Extra resources, regarding compilation and installation on various operating systems, and instructions for newer or older versions of GATE can be found on the official Open Gate collaboration website [155].

Once all the steps were followed, the user must be on the way to validate the installation by simply typing the command GATE in the command prompt and the initialization of a GATE session can be started, like showed in figure 45.

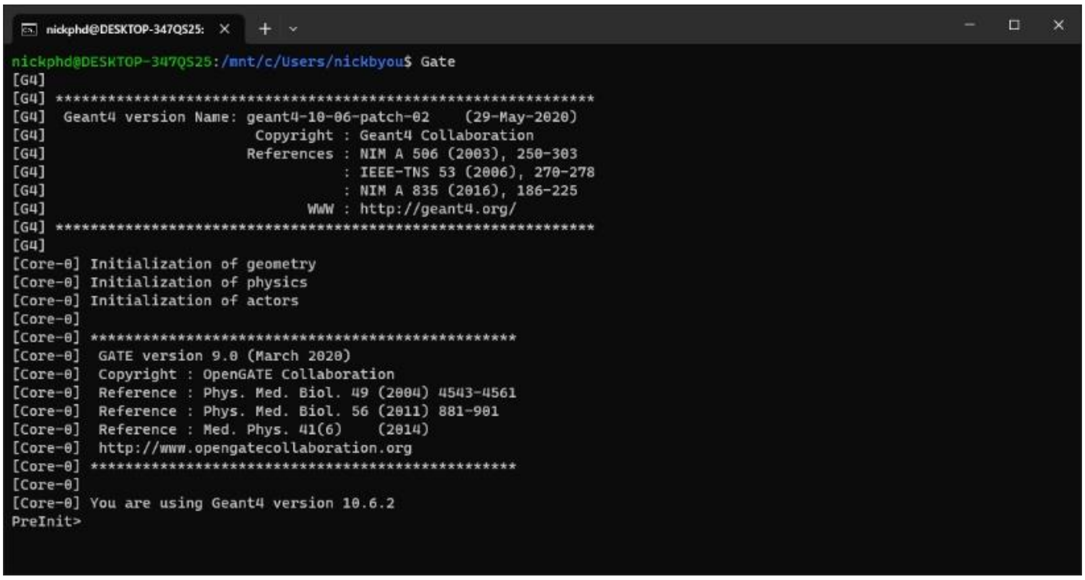

```
nickphd@DESKTOP-347QS25:/mnt/c/Users/nickbyou$ Gate
[G4]
[G4] **************************************************************
[G4]  Geant4 version Name: geant4-10-06-patch-02    (29-May-2020)
[G4]                       Copyright : Geant4 Collaboration
[G4]                      References : NIM A 506 (2003), 250-303
[G4]                                 : IEEE-TNS 53 (2006), 270-278
[G4]                                 : NIM A 835 (2016), 186-225
[G4]                             WWW : http://geant4.org/
[G4] **************************************************************
[G4]
[Core-0] Initialization of geometry
[Core-0] Initialization of physics
[Core-0] Initialization of actors
[Core-0]
[Core-0] *************************************************
[Core-0]  GATE version 9.0 (March 2020)
[Core-0]  Copyright : OpenGATE Collaboration
[Core-0]  Reference : Phys. Med. Biol. 49 (2004) 4543-4561
[Core-0]  Reference : Phys. Med. Biol. 56 (2011) 881-901
[Core-0]  Reference : Med. Phys. 41(6)    (2014)
[Core-0]  http://www.opengatecollaboration.org
[Core-0] *************************************************
[Core-0]
[Core-0] You are using Geant4 version 10.6.2
PreInit>
```

Figure 45 GATE cli session.

GATE also provides sessions with graphics enabled. There the user can visualize the geometry used, monitor kinetic parts that are moving in time and extend or create new geometries. Figure 46 shows a OpenGL graphical GATE session.

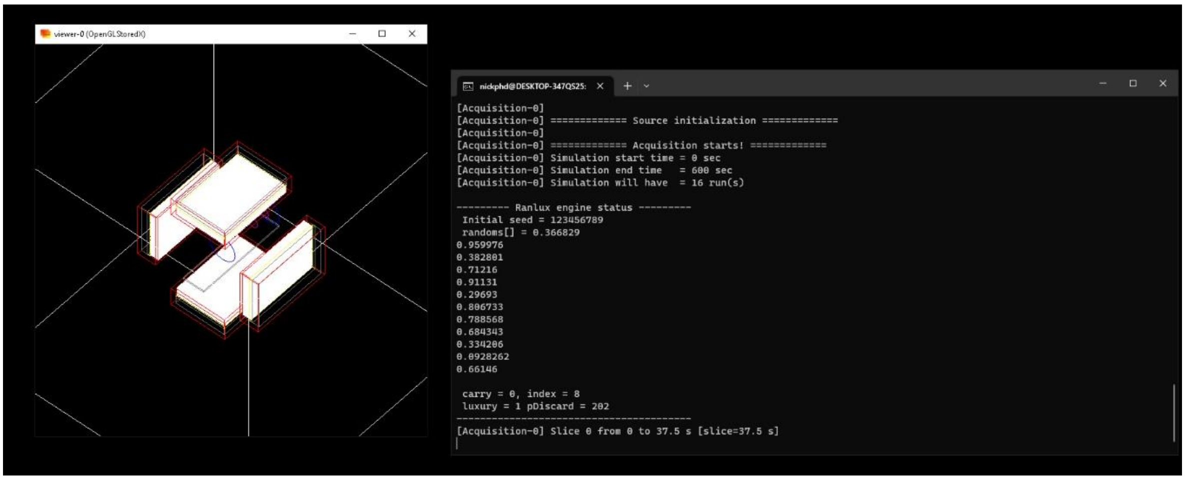

```
[Acquisition-0]
[Acquisition-0] ============= Source initialization =============
[Acquisition-0]
[Acquisition-0] ============= Acquisition starts! =============
[Acquisition-0] Simulation start time = 0 sec
[Acquisition-0] Simulation end time   = 600 sec
[Acquisition-0] Simulation will have  = 16 run(s)

--------- Ranlux engine status ---------
 Initial seed = 123456789
 randoms[] = 0.366829
0.959976
0.382801
0.71216
0.91131
0.29693
0.806733
0.788568
0.684343
0.334206
0.0928262
0.66146

 carry = 0, index = 8
 luxury = 1 pDiscard = 202
----------------------------------------
[Acquisition-0] Slice 0 from 0 to 37.5 s [slice=37.5 s]
|
```

Figure 46 GATE session with OpenGL graphics panel enabled.

Besides OpenGL graphic environment GATE ecosystem provides also QT panel, as shown in Figure 47, that was a feature introduced firstly in geant4. All geometrical components can now be visualized and the user can have a graphical environment containing all the simulation parameters. The downside is that visualization of the geometry in run-time practically works for a couple hundreds of particles, as the number of particles increases the visualization starts to become full of particle lines, so graphics help a lot when building a new geometry and see moving geometrical parts in time, otherwise for speed the visualizations are disabled.

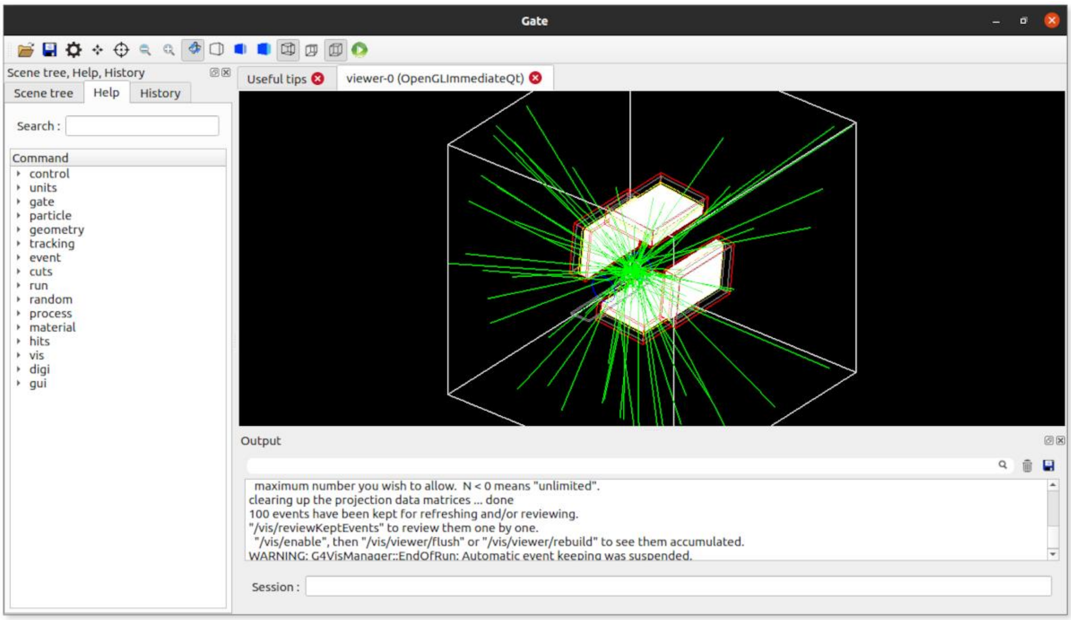

```
 maximum number you wish to allow.  N < 0 means "unlimited".
clearing up the projection data matrices ... done
100 events have been kept for refreshing and/or reviewing.
"/vis/reviewKeptEvents" to review them one by one.
 "/vis/enable", then "/vis/viewer/flush" or "/vis/viewer/rebuild" to see them accumulated.
WARNING: G4VisManager::EndOfRun: Automatic event keeping was suspended.
```

Figure 47 GATE session with QT graphics panel enabled.

The way to assemble a simulation with GATE, for the purpose of the thesis a SPECT simulation scenario, is to understand how GATE works and piece by piece assemble a .mac file where all parts of the simulation can be found. Inside the .mac file. The user has to understand the basic GATE architectural structure of how to code is being executed. There are the GATE pre-init mode, which consists of:

1. Definition of the Geometry.
2. Definition of the behavior.

3. Definition of the system's physics.

In that early stage of code execution in the pre-init mode, GATE is defining a geometry, define its behavior and specify the detector's system physics, all of which with cooperation of geant4. Afterwards the code continues to execute the .mac file with the init mode, which has three parts as follows:

1. Define the sources of the system.
2. Define what output to produce.
3. Start the experiment.

In the init mode, the code proceeds by confirming the various sources in the experimentation set-up. Afterwards the output options needed to be defined. GATE utilizes .ascii output, .root output, .sin output, sinogram projectional data file along with an .hdr and .mhd header files, with information regarding the simulation and the projectional data. A typical GATE code example can be seen in figure 48.

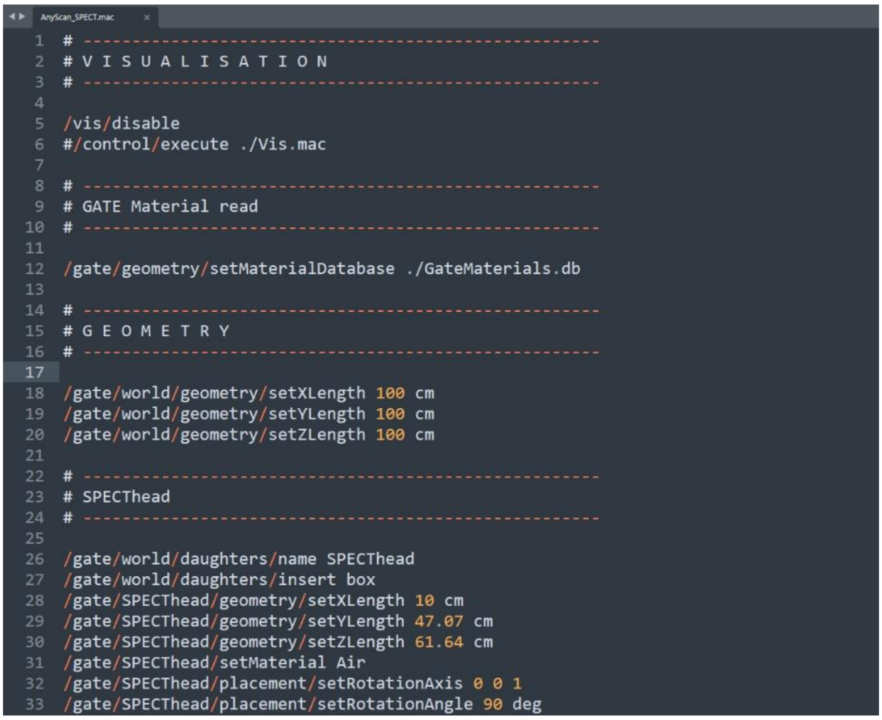

```
# -----------------------------------------------------
# V I S U A L I S A T I O N
# -----------------------------------------------------

/vis/disable
#/control/execute ./Vis.mac

# -----------------------------------------------------
# GATE Material read
# -----------------------------------------------------

/gate/geometry/setMaterialDatabase ./GateMaterials.db

# -----------------------------------------------------
# G E O M E T R Y
# -----------------------------------------------------

/gate/world/geometry/setXLength 100 cm
/gate/world/geometry/setYLength 100 cm
/gate/world/geometry/setZLength 100 cm

# -----------------------------------------------------
# SPECThead
# -----------------------------------------------------

/gate/world/daughters/name SPECThead
/gate/world/daughters/insert box
/gate/SPECThead/geometry/setXLength 10 cm
/gate/SPECThead/geometry/setYLength 47.07 cm
/gate/SPECThead/geometry/setZLength 61.64 cm
/gate/SPECThead/setMaterial Air
/gate/SPECThead/placement/setRotationAxis 0 0 1
/gate/SPECThead/placement/setRotationAngle 90 deg
```

Figure 48 GATE code example.

With the symbol # the user is able to put comments inside the .mac file. After the execution is finished, GATE will produce output files, in the case of any detector GATE produces .root files where data can be accessed via the program ROOT, which is a very convenient and fast way to manipulate and present large datasets with various parameters and variables. All the .mac code files utilized for the entire GATE - SPECT simulations can be found in Appendix 4.

As it can be seen in Figure 49 by typing, a “rootbrowse” command in the prompt along a space and the output name file of the simulation and a root browser is opened the output file unveiling the data stored already in root leafs.

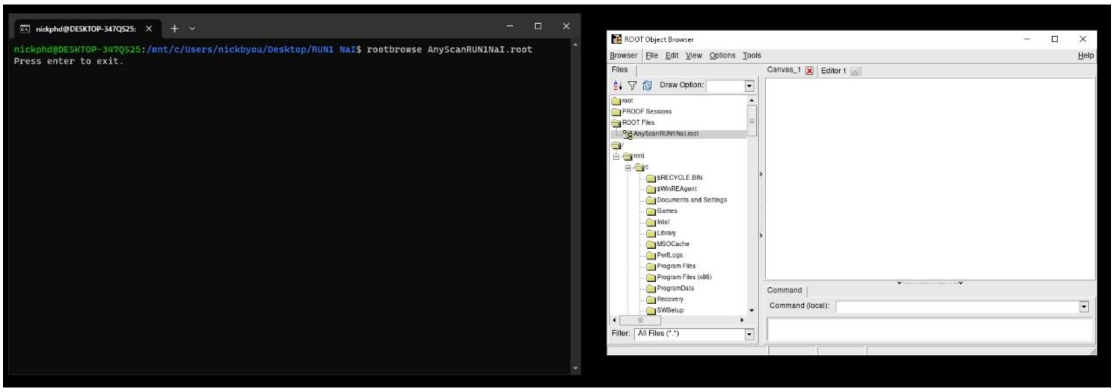

```
nickphd@DESKTOP-347QS25:/mnt/c/Users/nickbyou/Desktop/RUN1 NaI$ rootbrowse AnyScanRUN1NaI.root
Press enter to exit.
```

Figure 49 ROOT output file opened in a root browser for further processing.

By double clicking a leaf, an editor with a new canvas will open with the plot of the quantity stored in that leaf. That way is a very convenient and efficient way to store and distribute large data of output files. As it can be seen in figure 50, a canvas can be seen with a plot inside and some basic statistical information regarding the scored quantity of that particular leaf.

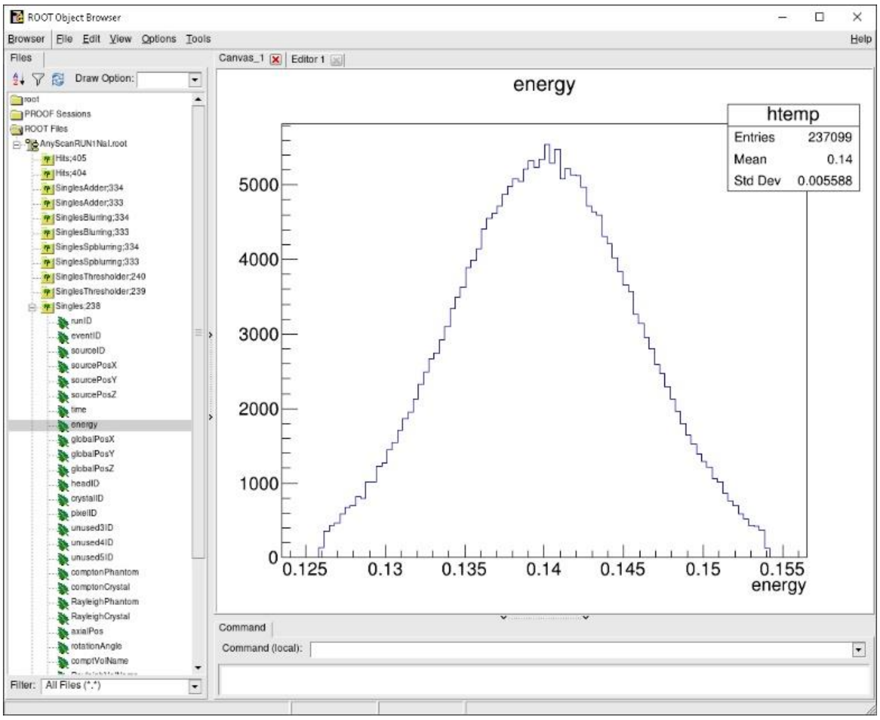

Figure 50 ROOT leaf opening on canvas – Energy Distribution example.

7.4.2 AnyScan S based SPECT head simulation with GATE.

In the University hospital of Thessaly, an experimentation took place where concentration of technetium-99m, ^{99m}Tc was irradiated from within a custom-made torso phantom and the SPECT system AnyScan S Dual-Head Flex took projections and reconstructed the image taken from the scanner. As it can be seen in figure 51, the AnyScan S Dual-Head Flex SPECT system consists of two SPECT heads, the phantom is on the bed and inside it, and there are little cylindrical compartments where the syringe with the concentration of ^{99m}Tc is being placed. From observing the movement and how the SPECT system was manage to take projections in real time, inform the user in all procedures being conducted, as well as reconstruct the final image, a lot of valuable information was produced.

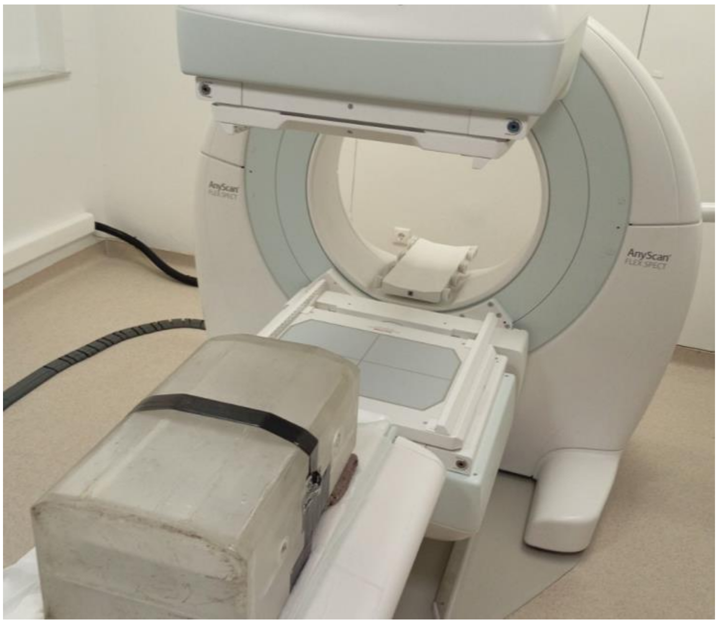

Figure 51 AnyScan S Dual-Head Flex Mediso SPECT system, with torso phantom.

From different setups and various modes of operation on this particular machine, many experimentations took place. As it can be seen in figure 52 the phantom irradiates, the heads are taking projections and a reconstructed image is being displayed in the monitor on the right.

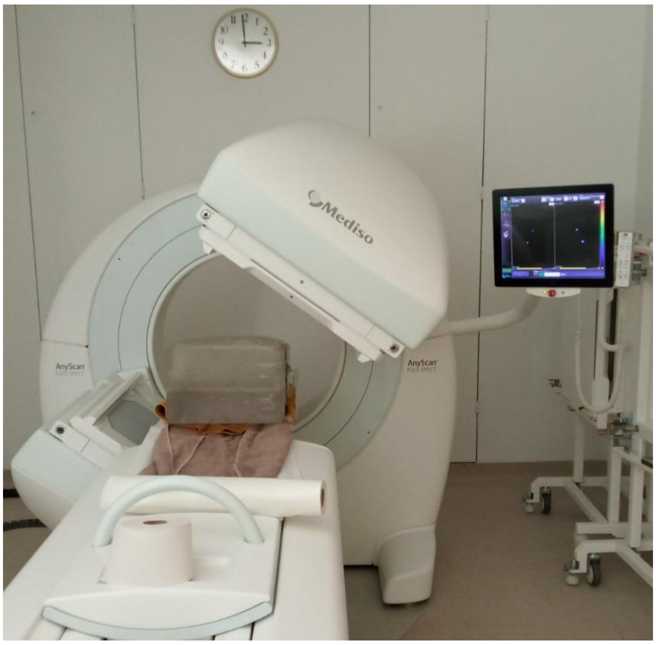

Figure 52 AnyScan SPECT system, taking projection and monitoring the procedures.

The experience was so fruitful that there was a success on building a single head prototype an exact GATE model of the AnyScan S Dual-Head Flex SPECT. By utilizing information of the experimentation conducted with the particular scanner and without revealing valuable and sensitive assembly information to other competitors, the design was possible.

For the purpose of this thesis, a prototype SPECT-head was created, with the software GATEv9.0. As it can be seen in figure 53, on top the SPECT head and on the bottom the Jaszczak [156] phantom, in hot spheres mode.

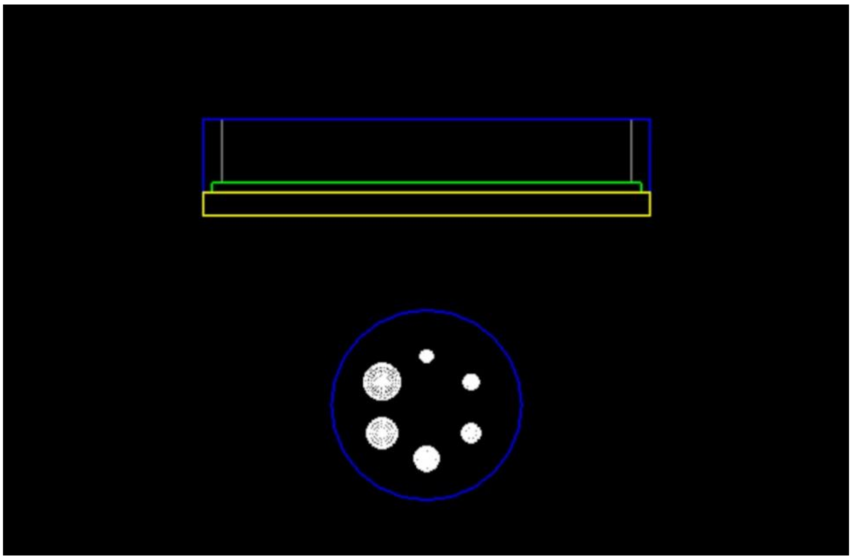

Figure 53 AnyScan SPECT-head and Jaszczak spheres phantom – front view.

The SPECT head consists of the collimator, the crystal, the back compartment with the electronics and the photomultiplier tubes and all together encapsulated in a lead shielding. The collimator has yellow color, consists of lead (Pb), has cylindrical holes with diameter 1.11 mm, 2.4 cm height and 0.16 mm septa, with dimensions 61.64 x 47.07 x 2.4cm in the x, y, z directions. The crystal has green color, consists of NaI, with dimensions 59.64 x 45.04 x 1 cm in the x, y, z directions. The back compartment has grey color with dimensions 57.64 x 43.04 x 6.6cm in the x, y, z directions. With blue color can be seen the lead (Pb), shielding of the SPECT-head with dimensions 61.64 x 47.07 x 10cm in the x, y, z directions.

For each simulation the SPECT-head rotation was 360^o, with 128 projections in each output file, with each projection having pixel size =4.6785 x 4.6785 mm^2. The scan time for a single projection was set to 100 sec with total simulation time 12800 sec. The rotation speed was set to 0.028125 deg/sec, the spatial resolution was set to 4mm (FWHM).

The standard Jaszczak phantom, consists of a 21,6cm radius cylinder and includes 6 spheres with diameters S1=12.7mm, S2=15.9mm, S3=19.1mm, S4=25.4mm, S5=31.8mm, S6=38mm.

Five runs were conducted with this SPECT-head. One run with the Jaszczak phantom hot spheres mode, where the phantom has a ^{99m}Tc concentration of 10Bq/mm^3. Another run with the Jaszczak phantom, cold spheres mode, where the phantom areas that were irradiating before now are cold areas and the hot area is the cylinder in which the spheres are in within, with a ^{99m}Tc concentration of 1 Bq/mm^3. Another three runs were conducted, with each run having each time a different type of crystal inside the SPECT head such as BGO, LSO and GSO crystals.

7.4.3 Custom small animal SPECT head simulation with GATE.

Based on the work of Han Guy Kang et al [157], a custom-made small animal SPECT-head of the exact experimentation was simulated with GATEv9.0. As it can be seen in figure 54 the geometry of the custom-made SPECT-head can be observed. The collimator consists of tungsten (W) material and it can be seen with red color with dimensions 50 x 50 x 30 mm in the x, y, z directions, has square holes with size of 0.8 mm, 30 mm height and 0.1 mm septa. The crystal consists of GAGG, Gadolinium Aluminium Gallium Garnet, material and it can be seen with yellow color, it's dimensions in the x, y, z directions are 49 x 49 x 5 mm. Lastly the PMT (H9500) can be seen with blue color, with dimensions in the x, y, z directions 50 x 50 x 30 mm.

For each simulation the custom made small animal SPECT-head rotation was 360^{o}, with 128 projections in each output file, with each projection having pixel size = 0.3828 x 0.3828 mm^2. The scan time for a single projection was set to 100 sec with total simulation time 12800 sec. The rotation speed was set to 0.028125 deg/sec, the spatial resolution was set to 1mm (FWHM).

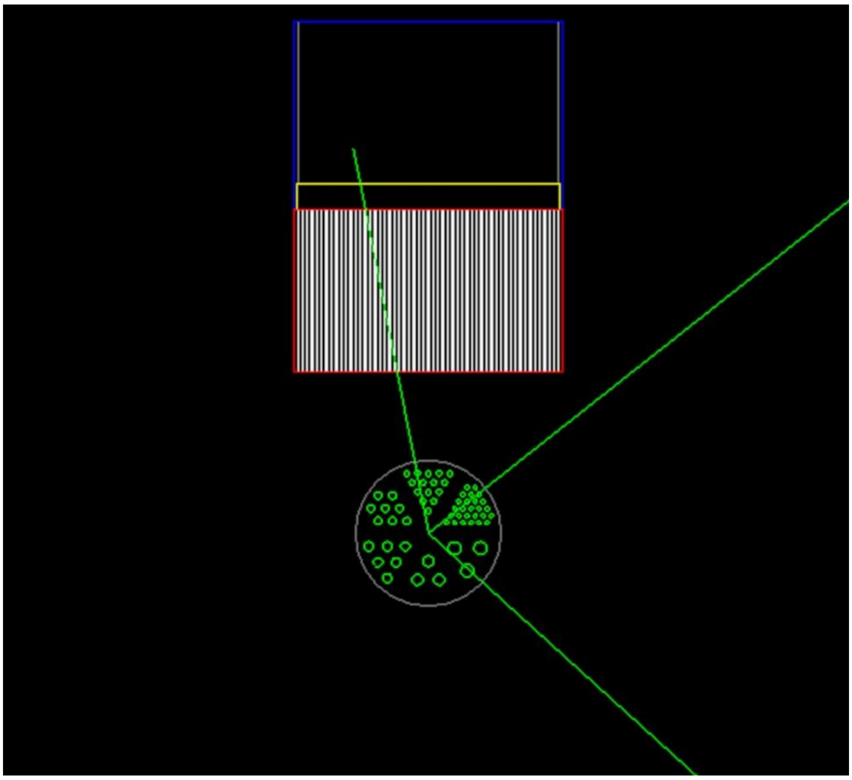

Figure 54 Custom-SmallAnimal SPECT-head and Jaszczak rods phantom – front view.

The Jaszczak phantom consists of a 30 mm radius cylinder and was utilized in rods mode. The rods are categorized in six groups, within each group there are cylinders with various diameters. Group1 has 26 cylinders of radius 0.375 mm. Group2 has 15 cylinders of radius 0.5 mm. Group3 has 8 cylinders of 0.675 mm. Group4 has 6 cylinders of radius 0.85 mm. Group5 has 3 cylinders with radius 1 mm. Group6 has 3 cylinders with radius 1.2 mm.

Three runs were conducted with the small animal custom-made scanner. Each case had different hole size at 0.4, 0.8 and 1.6 mm, while the septa of the collimator are kept at 0.1 mm. The activity of the ^{99m}Tc source was at 1200 Bq/mm^3 for each case utilized.

7.5 Tomographic Reconstruction with STIR

STIR [158] namely, stands for Software for Tomographic Image Reconstruction; this program has utilities to perform 3D PET, 2D SPECT and other imaging systems. This software is open source, contains object oriented c++ code and in a way it is a software toolkit, as it consists of multiple different routines for the user to utilize. In addition, it provides the executables and the api to extend the libraries.

STIR source code can be accessed is hosted in GitHub [159], making it easier to find resources regarding compilation and installation. STIR depends on other libraries and have some prerequisites, cmake is utilized in order to configure and begin the building from source code procedure. Detailed instructions can be found in Appendix 2, as well as some links and fixtures popular libraries like ecat and itk. Once the compilation and installation procedures went well, the validation of the libraries can simply be made by typing the names of the STIR executables like FBP2D, as seen in figure 55.

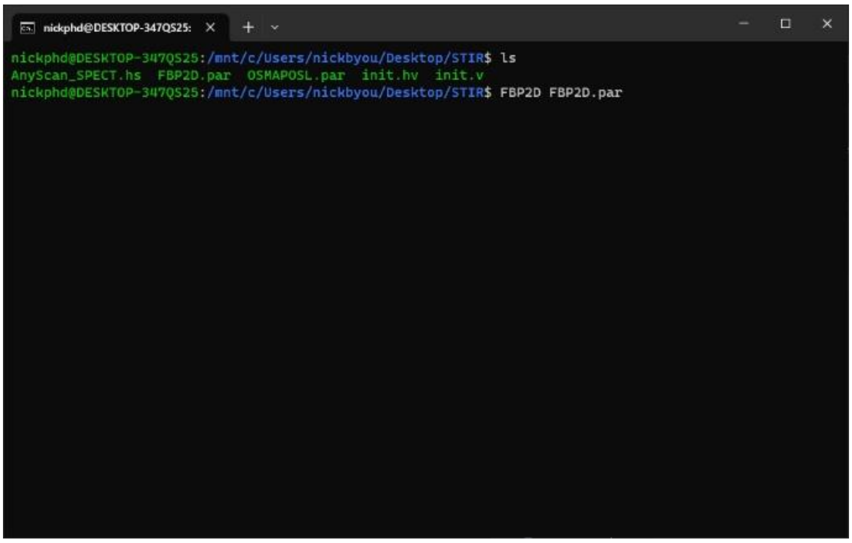

```
nickphd@DESKTOP-347QS25:/mnt/c/Users/nickbyou/Desktop/STIR$ ls
AnyScan_SPECT.hs  FBP2D.par  OSMAPOSL.par  init.hv  init.v
nickphd@DESKTOP-347QS25:/mnt/c/Users/nickbyou/Desktop/STIR$ FBP2D FBP2D.par
```

Figure 55 STIR - FBP2D script execution via cli.

The STIR routines are being executed step by step by calling commands from a script with the extension .par, which the user has prepared. More details can be found in the documentation of the software.

The routines utilized for this thesis are FBP2D and OSMAPOSL. After the routines execute the script code and reconstruct the GATEv9.0 output, .sin file, then the routine produces three files with the extensions .ahv, .hv, .v. The ahv and hv extensions are for interfiles that describe the binary file with the extension .v.

One of the software utilized for opening the reconstructed image was amide [160]. To import the reconstructed image some information needed to be entered to the software, as shown in figure 56. Most of this information required are being stored in the interfiles .ahv and .hv.

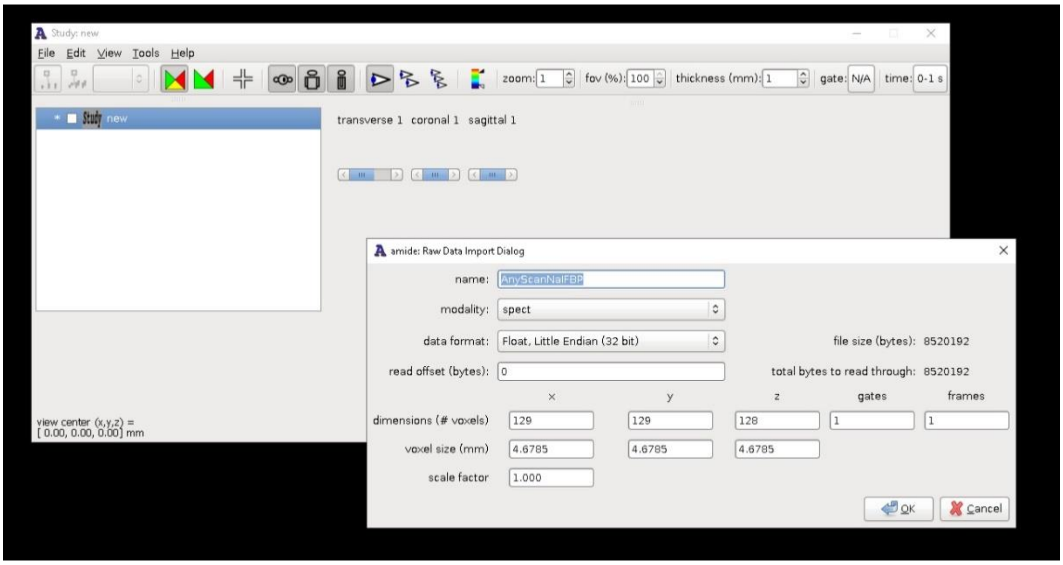

name: AnyScanNaIFBP
modality: spect
data format: Float, Little Endian (32 bit)
read offset (bytes): 0
file size (bytes): 8520192
total bytes to read through: 8520192

	x	y	z	gates	frames
dimensions (# voxels)	129	129	128	1	1
voxel size (mm)	4.6785	4.6785	4.6785		
scale factor	1.000				

Figure 56 Amide - Importing new raw tomographic data, example.

More specifically the program needs to know the data format, the x, y, z dimensions and the voxel size in each dimension. After the image has been imported in to the amide environment, the data analysis can begin. In figure 56 show an example of a slice view of the reconstructed SPECT image, the tomographic image can be viewed simultaneously by the transverse, coronal and sagittal views.

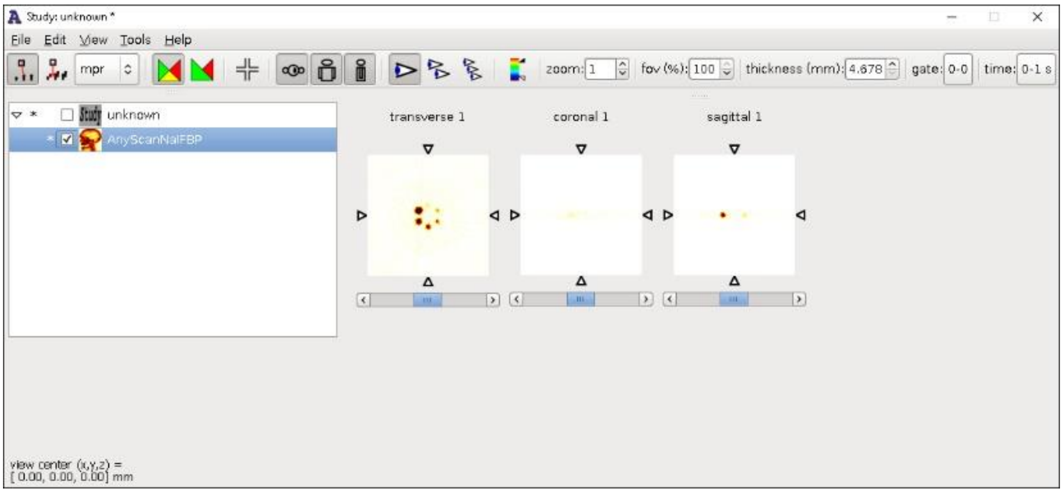

zoom: 1
fov (%): 100
thickness (mm): 4.678
gate: 0-0
time: 0-1 s

view center (x,y,z) =
[0.00, 0.00, 0.00] mm

Figure 57 Amide - Main Panel.

7.6 Conclusions

The hardware and software components were introduced in this chapter. The fundamental software setup was presented, as well as specifics regarding the operating system and the virtualization of a Linux system on a Windows 10 environment using WSL 2.0. The EGSnrc setup, as well as thorough instructions for the methods used, have been explained, along with examples of simulation output and subsequent data processing. The CT examination technique using the EGSnrc environment has been demonstrated. As illustrated, configuring and constructing GATEv9.0 in Ubuntu 20.04 was a difficult effort, but using GATE turned out to be straightforward with utilities that are highly practical and simple. STIR software was also demonstrated and displayed its capabilities. The methodology of the SPECT system employing GATE and STIR has been described in detail.

8. Results and Discussions

8.1 Introduction

This chapter examines and presents the findings from all situations. More precisely, the CT irradiation simulations done with EGSnrc used 25 beams for each of the instances of Au and W target materials ranging in energy from 30keV to 150keV; these beams had to be checked for quality reasons, as described in sub-chapter 8.2. Another challenge was presenting the dosimetric maps for each target material and energy range, as described in sub-chapter 8.3. The organ dosage profiles for each instance are reported in the final chapter of the CT-based simulations 8.4 for six organs: spine, lung, abdomen, brain, heart, and skin.

Sub-chapters 8.5 and 8.6 give the results of the two SPECT-head simulations, the AnyScan-based SPECT-head and the custom-made small animal SPECT-heads. The AnyScan-based simulations outlined in section 8.5 begin with an evaluation of the optimal configuration options for the OSMAPOSL reconstruction method. Following that, the Jaszczak phantom findings for HOT and COLD spheres are provided by comparing the FBP and OSMAPOSL reconstructions. Finally, a comprehensive comparison of the findings when the crystal material is changed to BGO, LSO, and GSO is shown.

Sub-chapter 8.6 begins with an examination for the optimal configuration options for the OSMAPOSL reconstruction approach, much as it does for the AnyScan-based SPECT-head. In the final portion, a more extensive examination into optimizing the resolution depending on collimator hole size is carried out.

8.2 CT Beams quality assurance

8.2.1 AU target - Spectral and Energy Fluence Distributions 30-150keV.

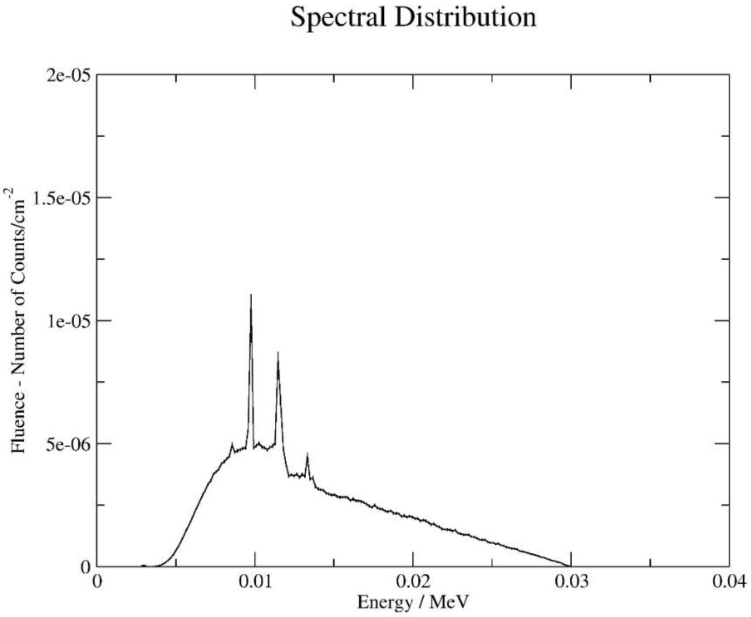

Figure 58 AU target 30keV Spectral Distribution.

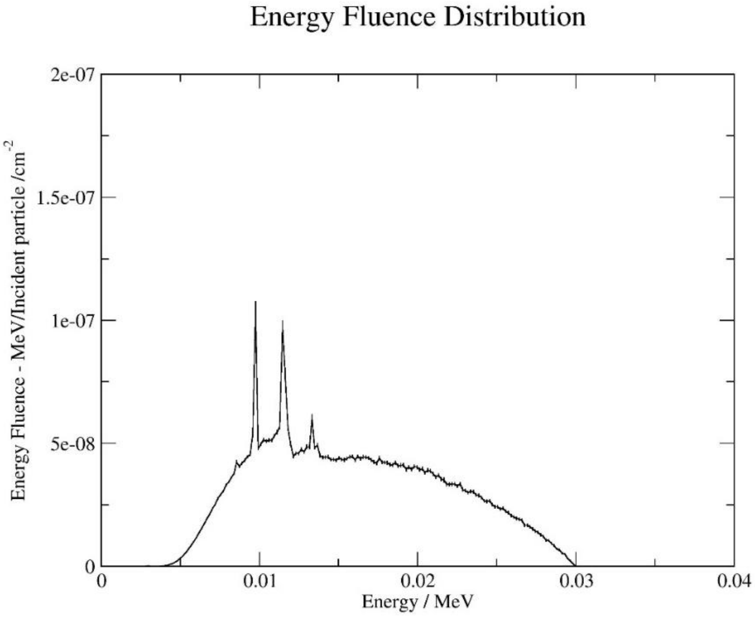

Figure 59 AU target 30keV Energy Fluence Distribution.

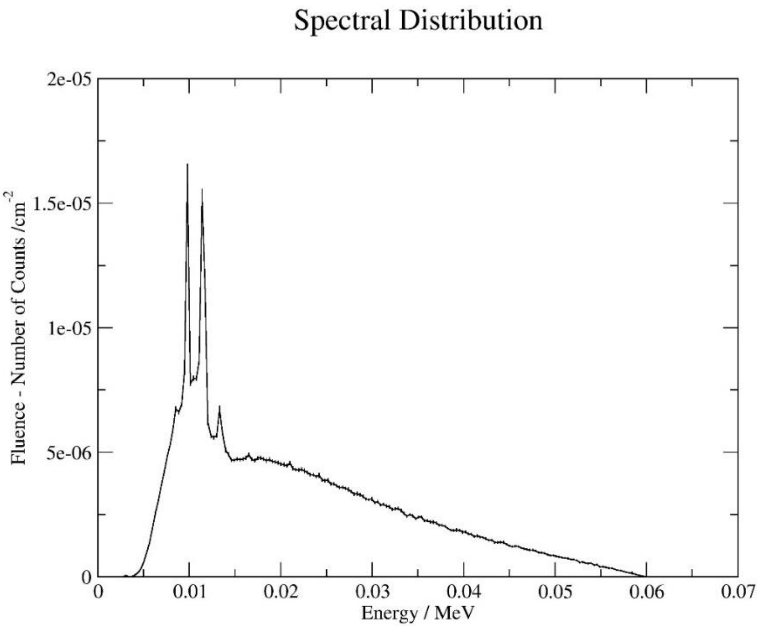

Figure 60 AU target 60keV Spectral Distribution.

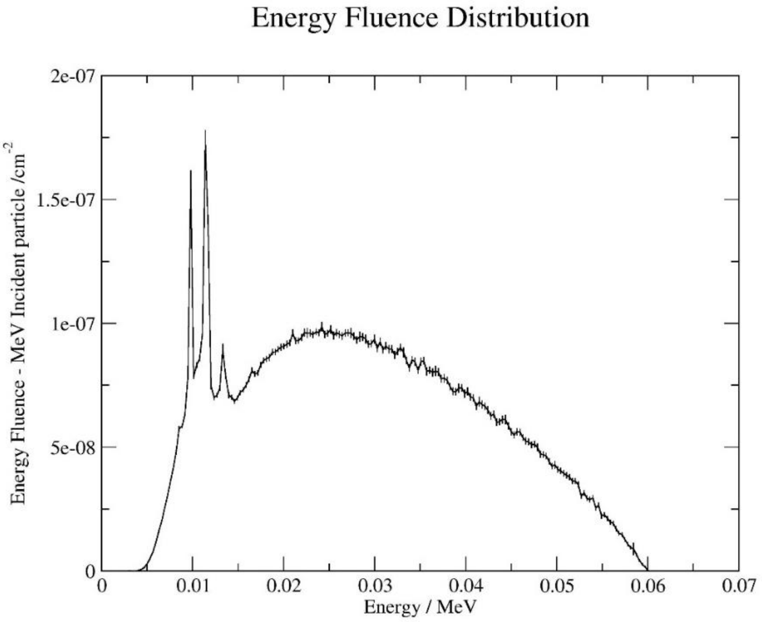

Figure 61 AU target 60keV Energy Fluence Distribution.

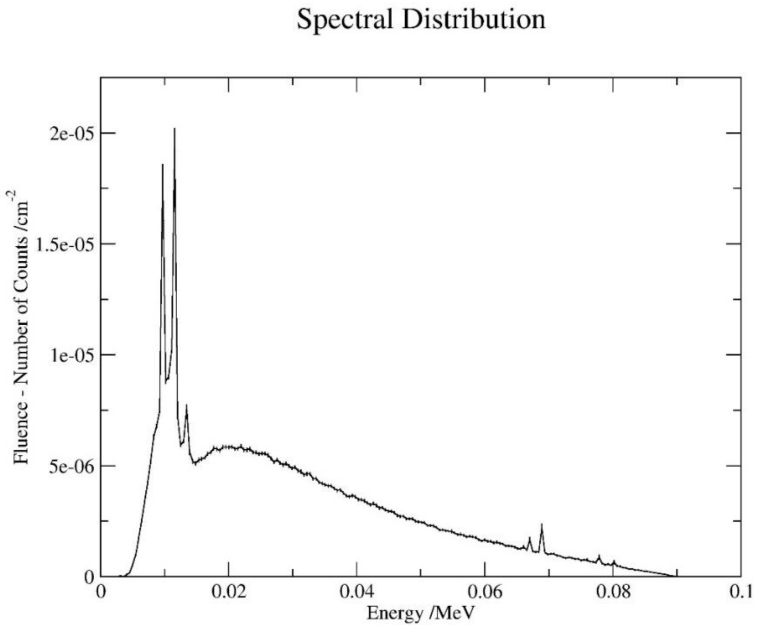

Figure 62 AU target 90keV Spectral Distribution.

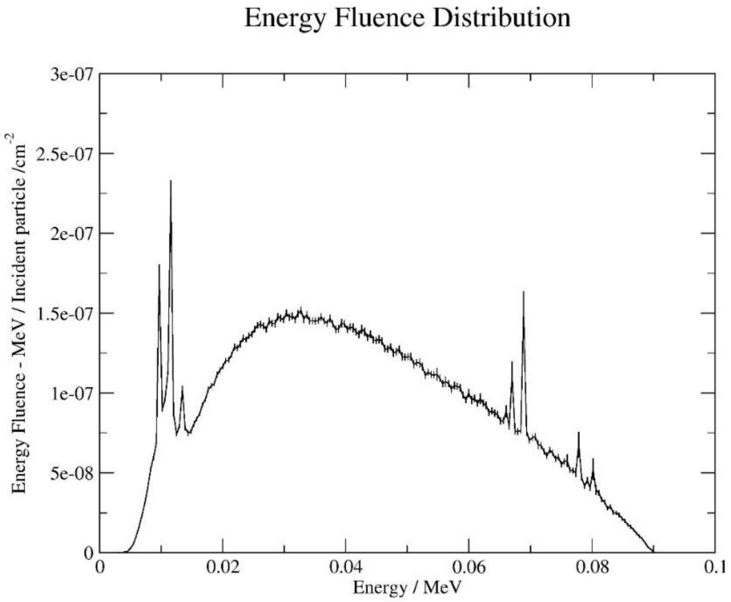

Figure 63 AU target 90keV Energy Fluence Distribution.

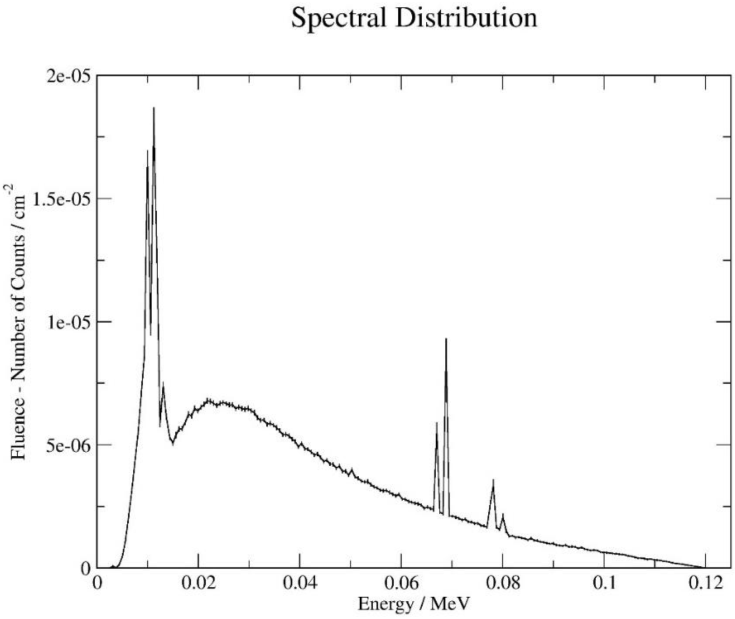

Figure 64 AU target 120keV Spectral Distribution.

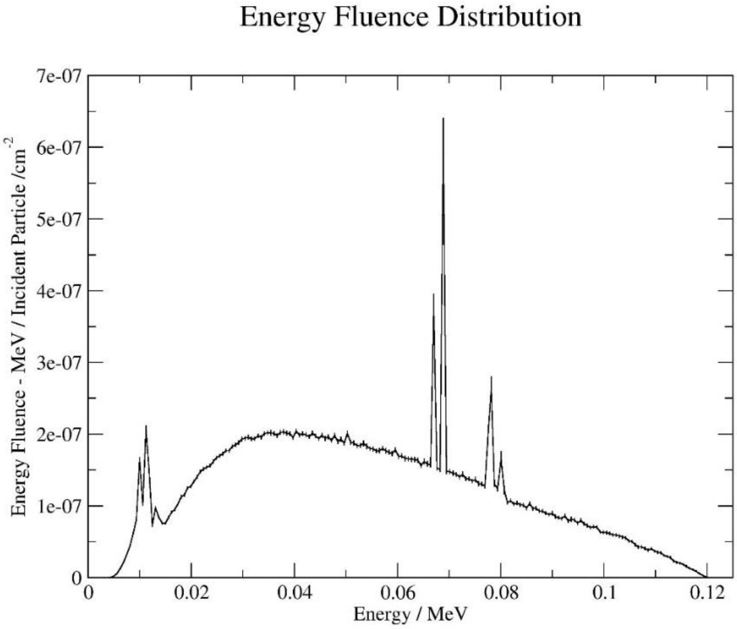

Figure 65 AU target 120keV Energy Fluence Distribution.

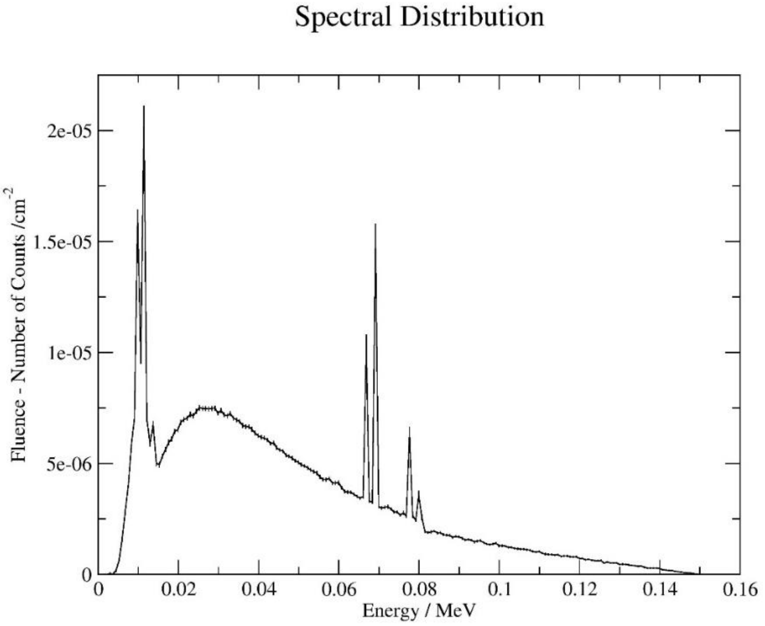

Figure 66 AU target 150keV Spectral Distribution.

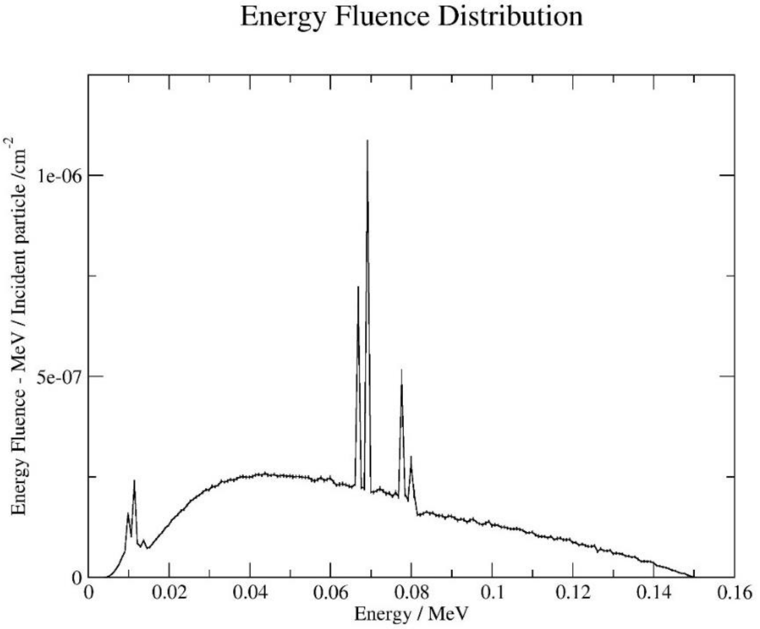

Figure 67 AU target 150keV Energy Fluence Distribution.

From figure 58 - figure 67 the spectral distribution and the energy fluence distribution are being displayed from energy range 30 - 150keV with step 30keV. Addition data in much more detail can be found in Appendix 1 where much more information can be obtained and the energy range is 30 - 150keV with step 5keV.

For Au gold, at the 30keV and 60keV only the L_a = 0.009MeV, L_b = 0.011MeV and L_c = 0.013 MeV characteristics [161] can be observed. As the energy grows at 90keV the characteristics K_{a1} = 0.066MeV, K_{a2} = 0.068MeV, K_{a3} = 0.077MeV [161] starts to show up in the Spectral Distribution with more intense activity in terms of energy fluence. At 120keV and 150keV as it can be seen the K_a characteristics can be seen in the spectral distributions having more counts and in terms of energy fluence, they are leading.

8.2.2 W target - Spectral and Energy Fluence Distributions 30-150keV.

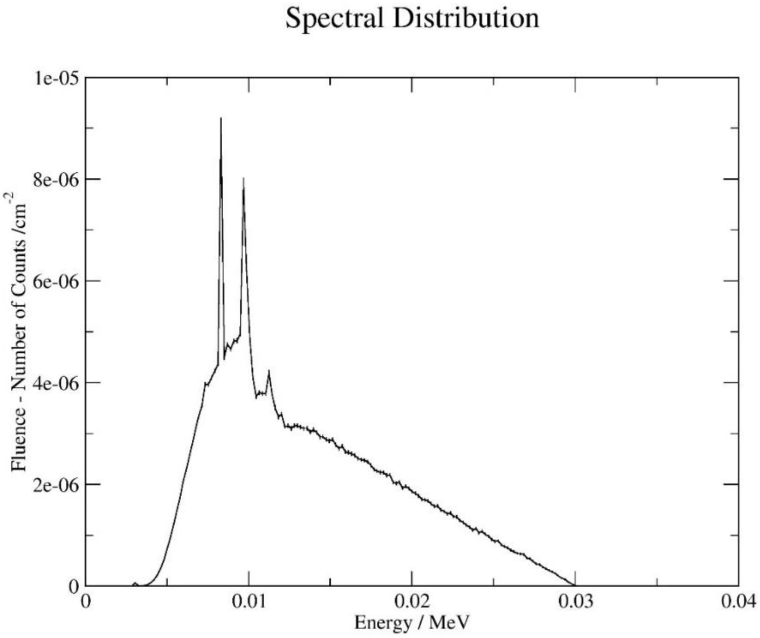

Figure 68 W target 30keV Spectral Distribution.

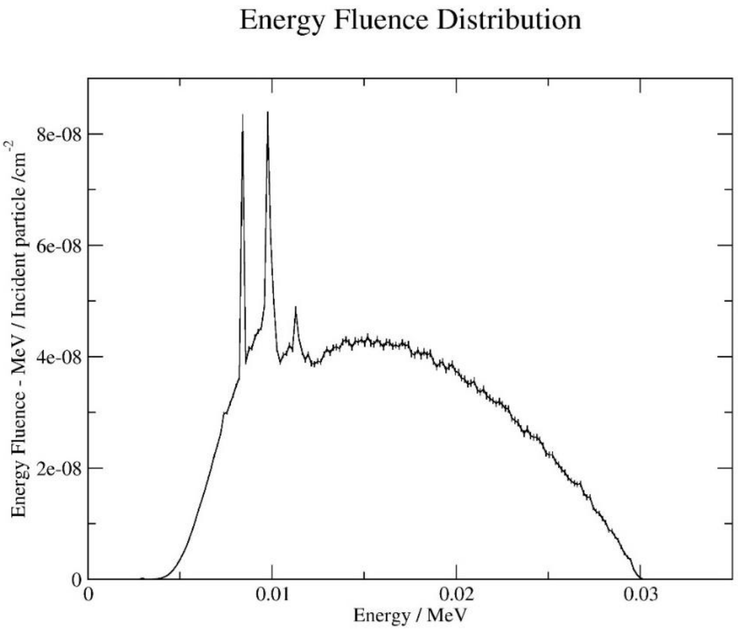

Figure 69 W target 30keV Energy Fluence Distribution.

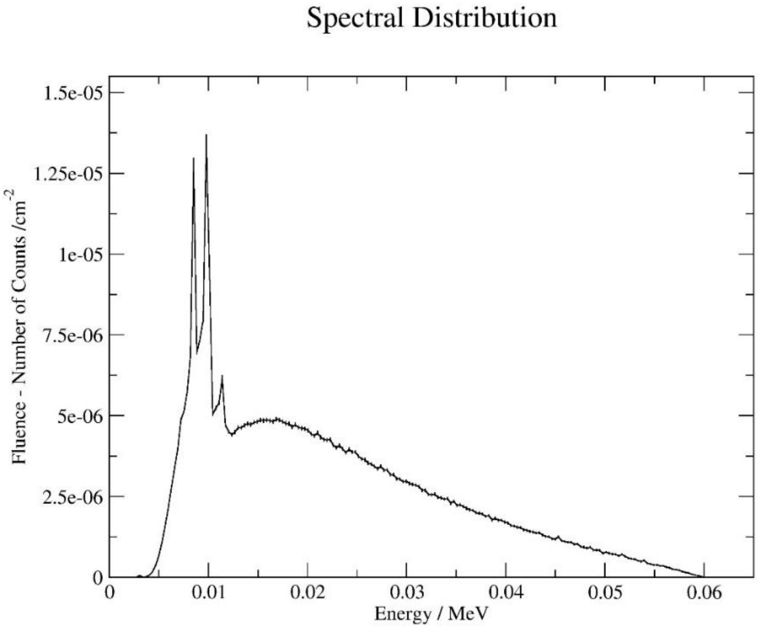

Figure 70 W target 60keV Spectral Distribution.

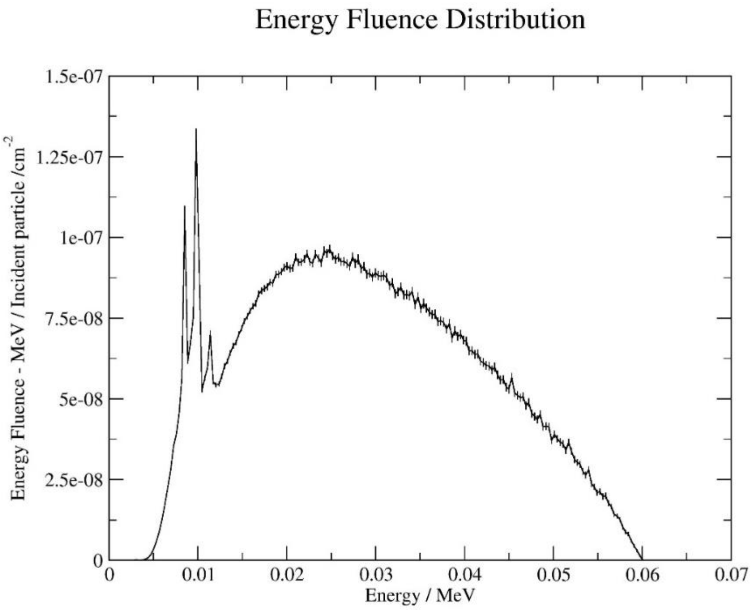

Figure 71 W target 60keV Energy Fluence Distribution.

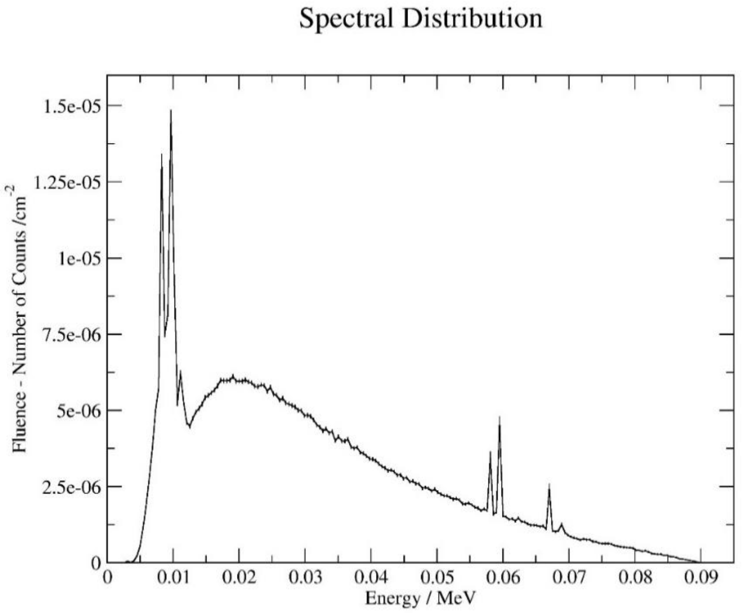

Figure 72 W target 90keV Spectral Distribution.

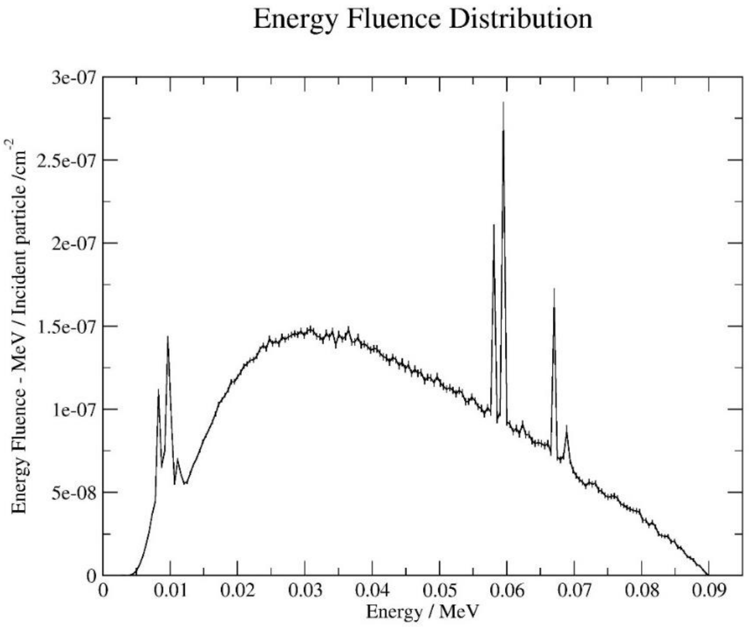

Figure 73 W target 90keV Energy Fluence Distribution.

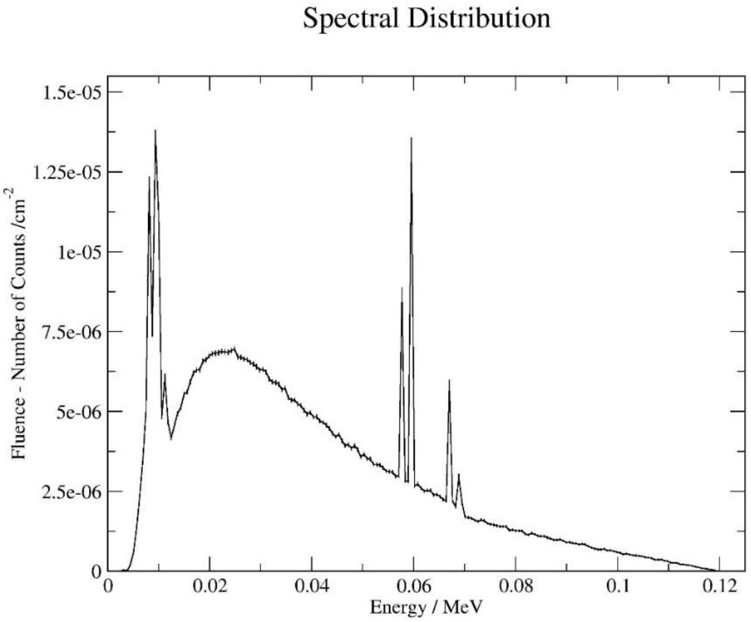

Figure 74 W target 120keV Spectral Distribution.

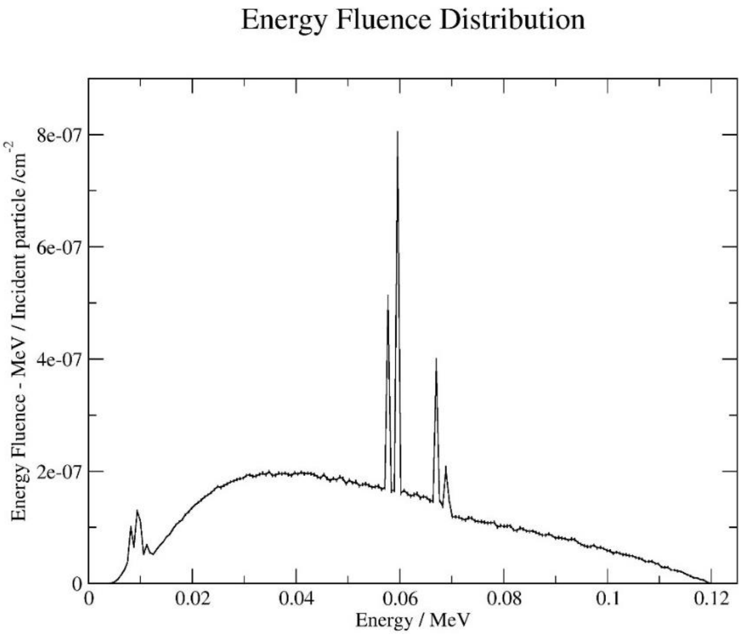

Figure 75 W target 120keV Energy Fluence Distribution.

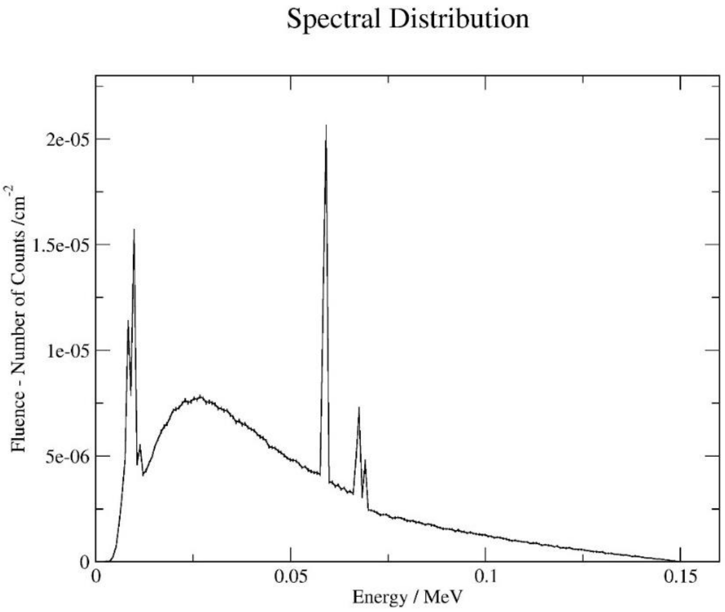

Figure 76 W target 150keV Spectral Distribution.

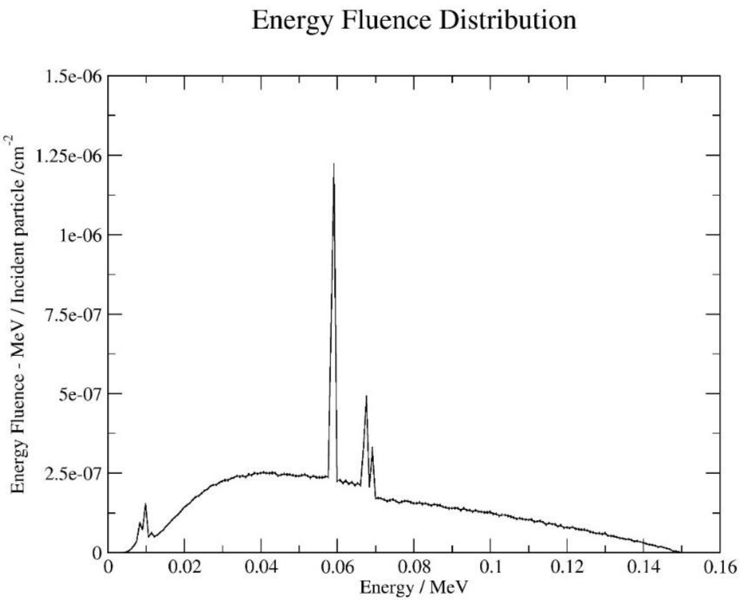

Figure 77 W target 150keV Energy Fluence Distribution.

The spectral distributions and energy fluence distributions for the energy range 30 - 150keV with a step of 30keV are shown in Figures 68-77. Appendix 1 has much more information on additional data in more depth, and the energy range is 30 - 150 keV with a 5 keV step.

As presented for the material W tungsten, only the $L_{a,b,c}$ = 0.012MeV [161] characteristics can be detected at 30keV and 60keV. The characteristics K_{a1} = 0.057MeV, K_{a2} = 0.059MeV, K_{b1} = 0.067MeV, and K_{b2} = 0.069MeV begin to appear in the spectral distribution as the energy increases at 90keV, 120keV, and 150keV, with the K_a characteristics being the leaders having more intense activity in the energy fluence distributions.

In most CT scanners the detectors are mostly being reached by photons of the K_a characteristics [161], in both cases for AU and W after 60keV, those materials can be used for x-rays tubes, performing CT examinations.

8.3 CT irradiation – Dosimetric map slices.

8.3.1 Abdomen phantom dosimetric maps.

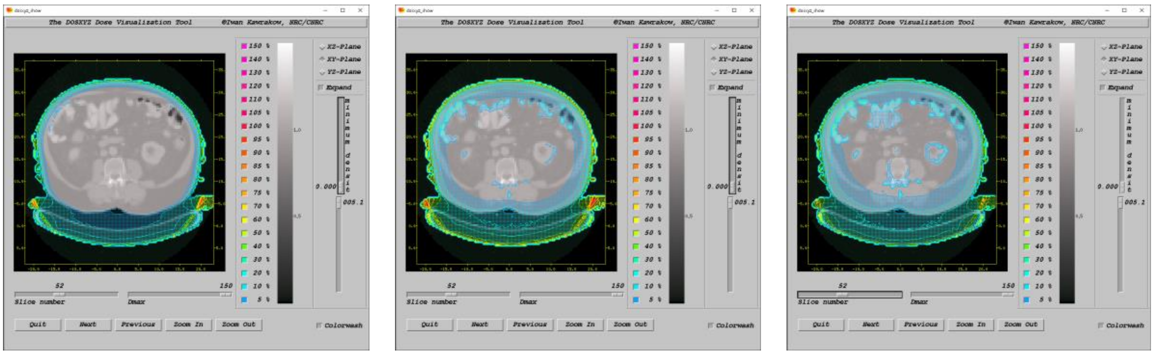

30keV 60keV 90keV

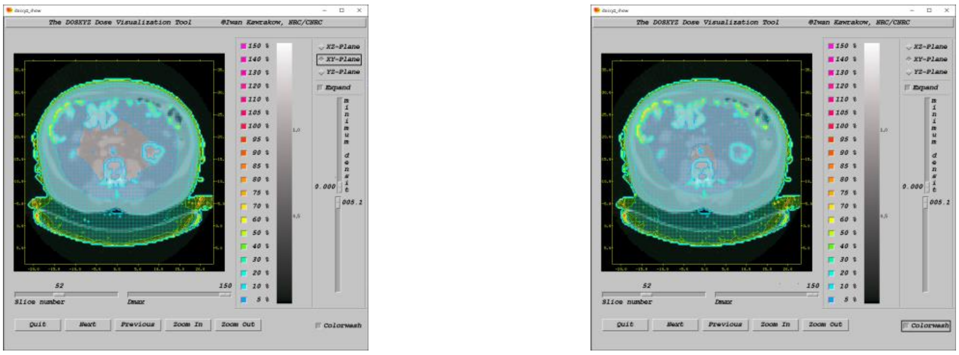

120keV 150keV

Figure 78 Abdomen AU target Beam - Dosimetric map30-150keV.

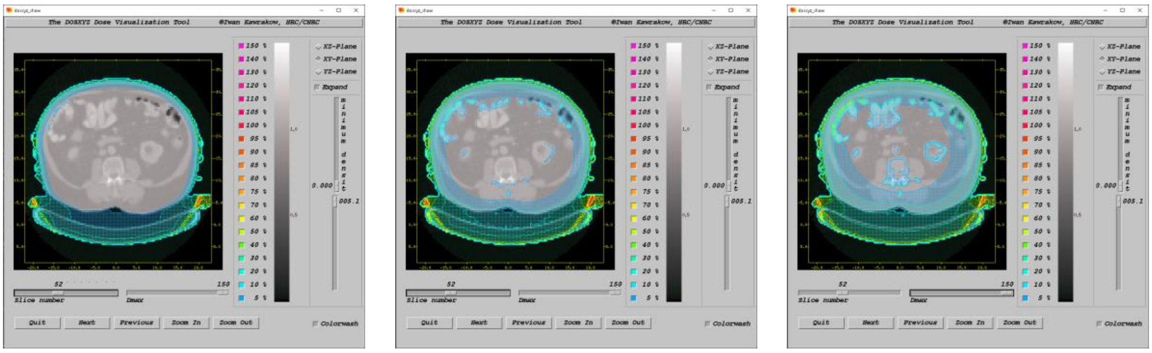

30keV 60keV 90keV

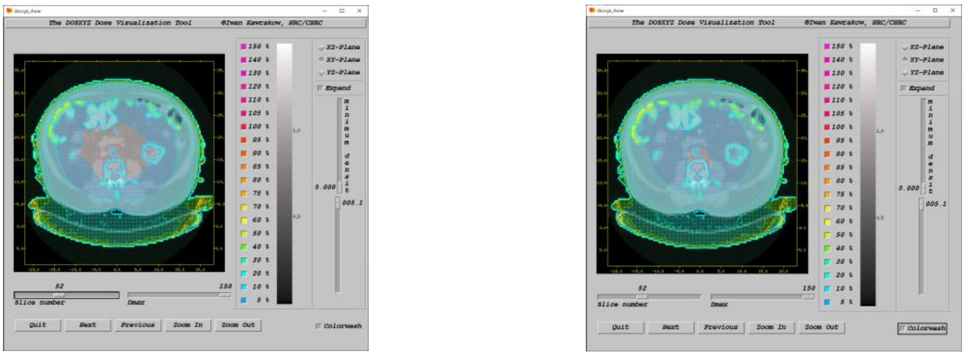

120keV 150keV

Figure 79 Abdomen W target Beam - Dosimetric map30-150keV.

8.3.2 Brain phantom dosimetric maps.

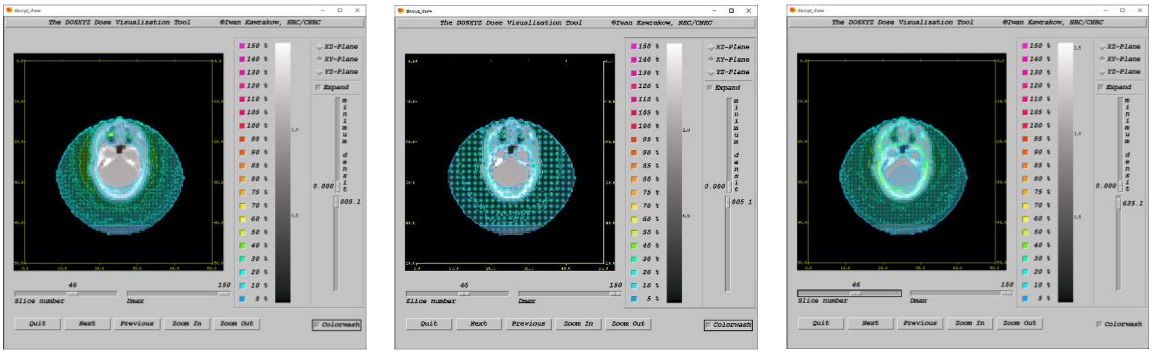

30keV 60keV 90keV

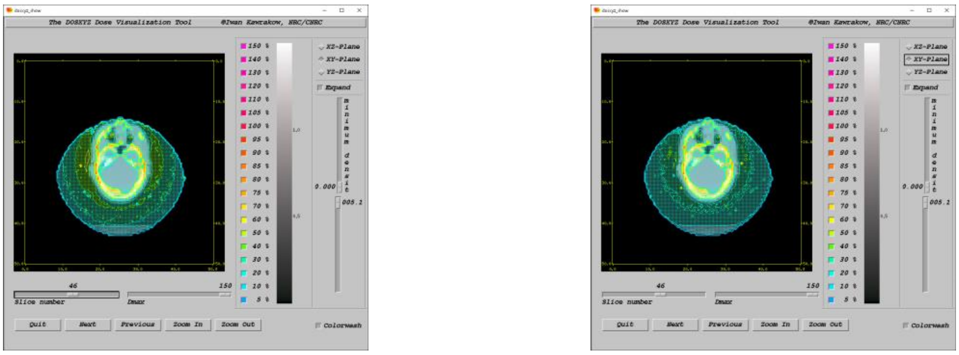

120keV 150keV

Figure 80 Brain AU target Beam - Dosimetric map30-150keV.

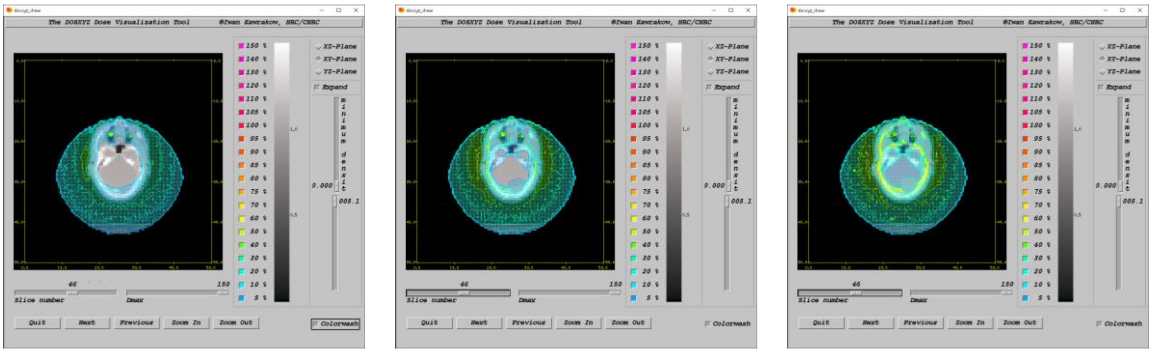

30keV 60keV 90keV

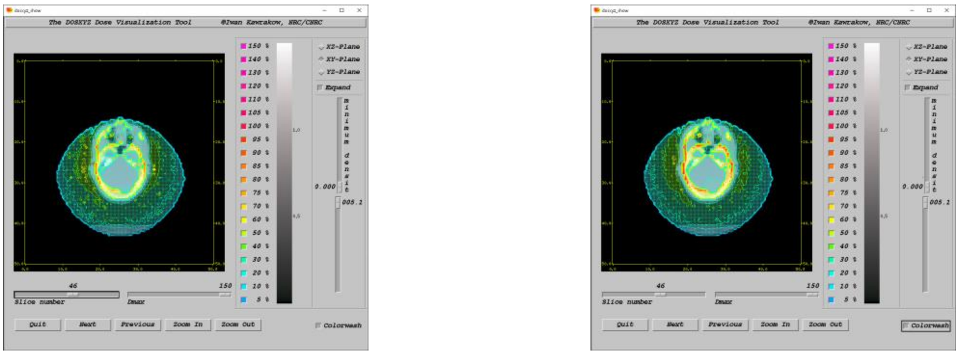

120keV 150keV

Figure 81 Brain W target Beam - Dosimetric map30-150keV.

8.3.3 Chest phantom dosimetric maps.

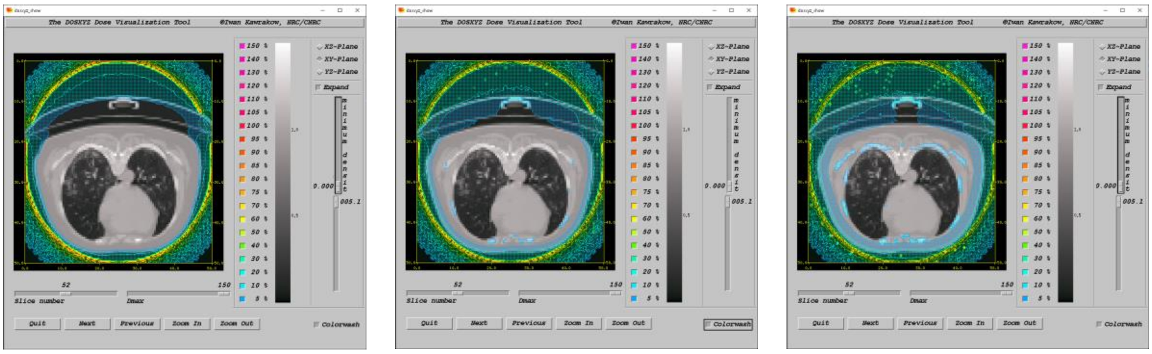

30keV 60keV 90keV

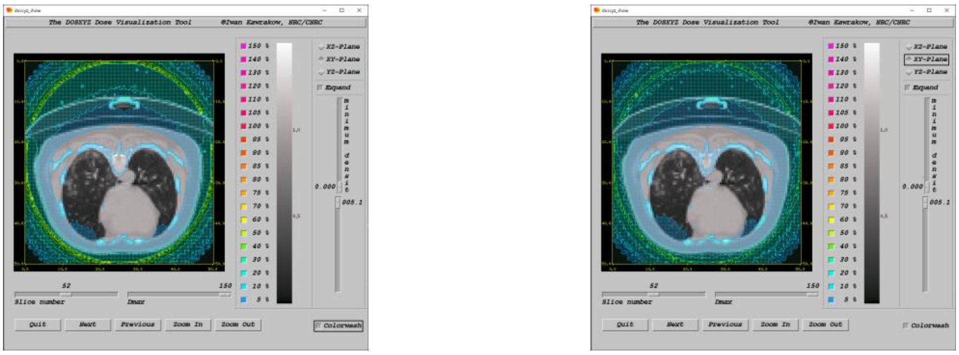

120keV 150keV

Figure 82Chest AU target Beam - Dosimetric map30-150keV.

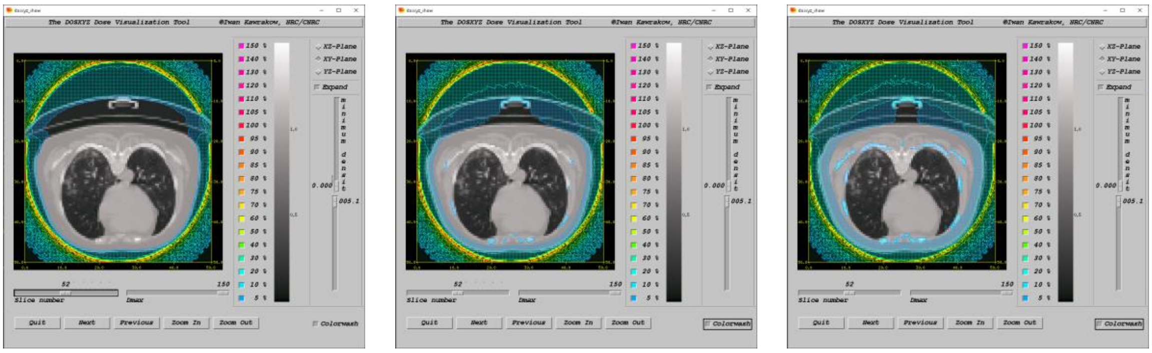

30keV 60keV 90keV

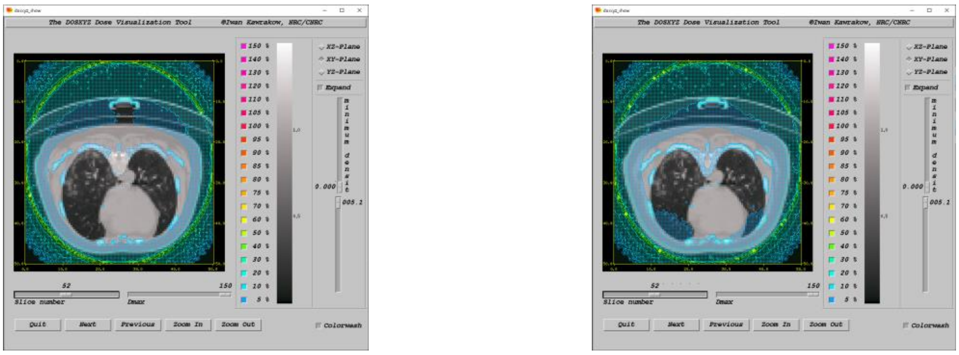

120keV 150keV

Figure 83 Chest W target Beam - Dosimetric map30-150keV

Figures 78-83 show the same phantom slice with a dosimetric map of the dosage distribution constructed. From 60keV and above, the distribution of the dosage begins to actually enter the phantom and disperse the dose even more inside the organs, for each case of phantom: abdomen, brain, and chest. As the dosimetric map shows, there are no significant changes between AU and W target materials.

In the instance of the abdominal phantom, figures 78 and 79 show that at 30 keV, there is no dose distribution within the phantom in the area near the spine, but the majority of the dose is spread towards the outside skin. Figures 80 and 81 show that the dosage starts spreading nearly immediately after the 30keV beams, but as the energy increases, the dose is increasingly spread toward the inner cranial bone layers.

In the final case, the chest phantom, it can be seen that at low energies of 30 and 60 keV, the scored dosage is distributed near the skin on the phantom, but as the energy increases to 90kev and beyond, the dose is distributed more evenly towards internal organs, such as the lungs and heart. Appendix 1 has many additional photos, including a comprehensive energies grid from 30-150keV with a step of 5keV, 25 examples, for each target material, AU and W, demonstrating the dosage distribution on the phantoms, and even more slices for each situation.

8.4 Organ dose profiles.

8.4.1 Abdomen

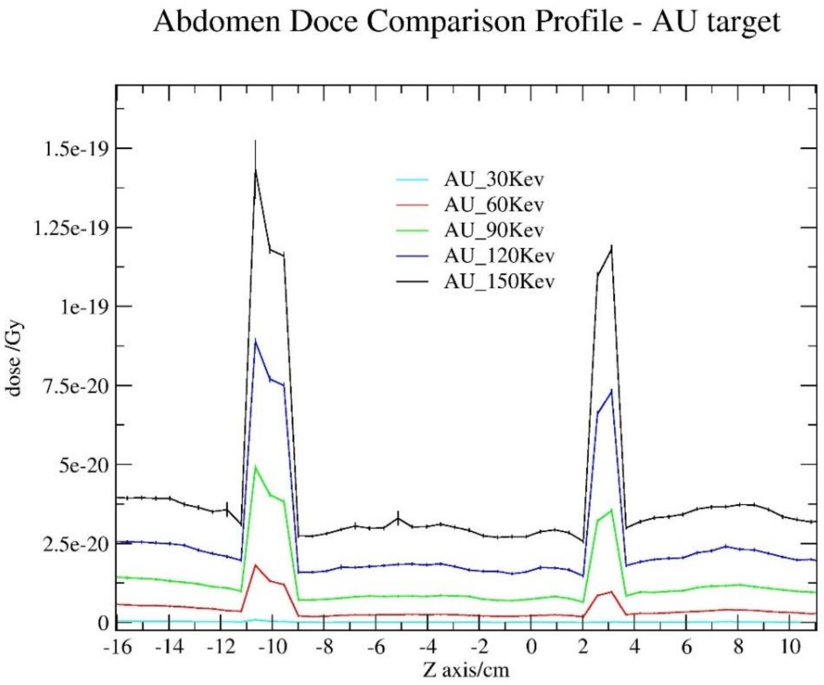

Figure 84 Abdomen Dose Comparison Profile - AU target.

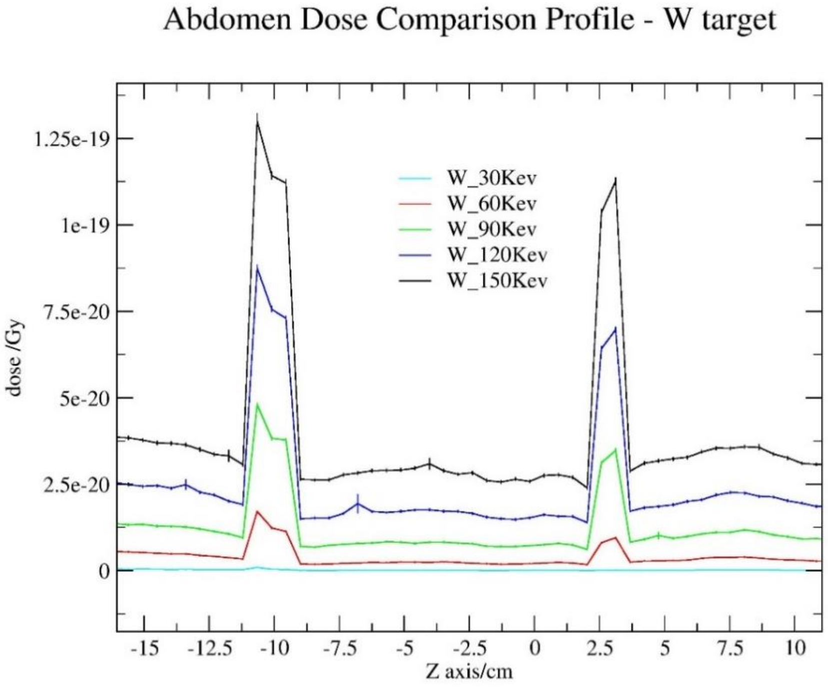

Figure 85 Abdomen Dose Comparison Profile - W target.

8.4.2 Brain

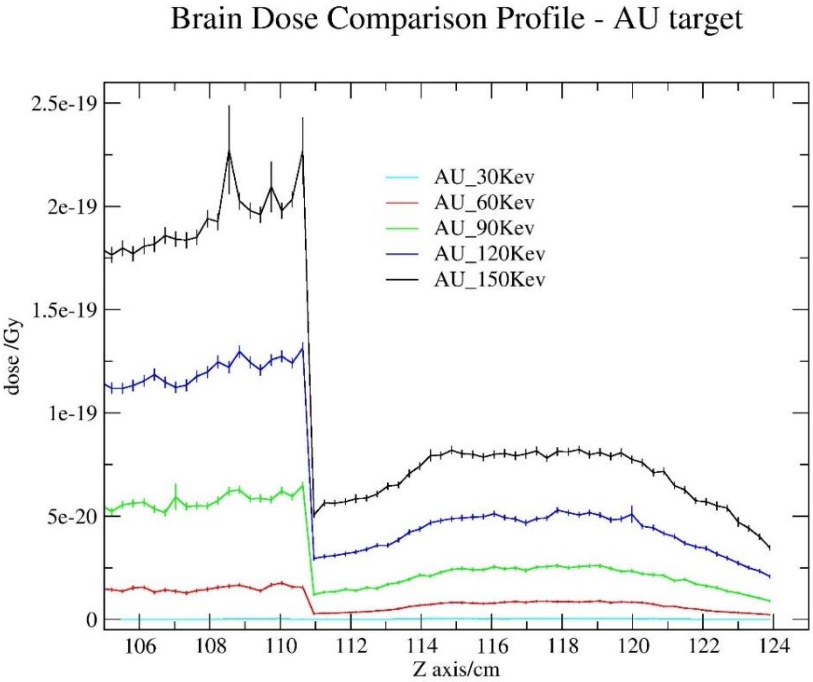

Figure 86 Brain Dose Comparison Profile - AU target.

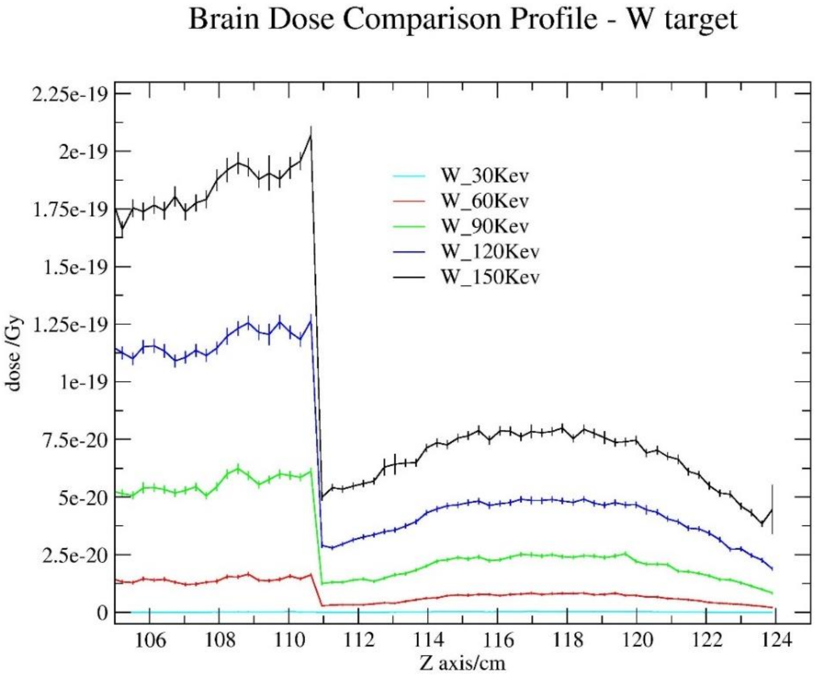

Figure 87 Brain Dose Comparison Profile - W target.

8.4.3 Heart

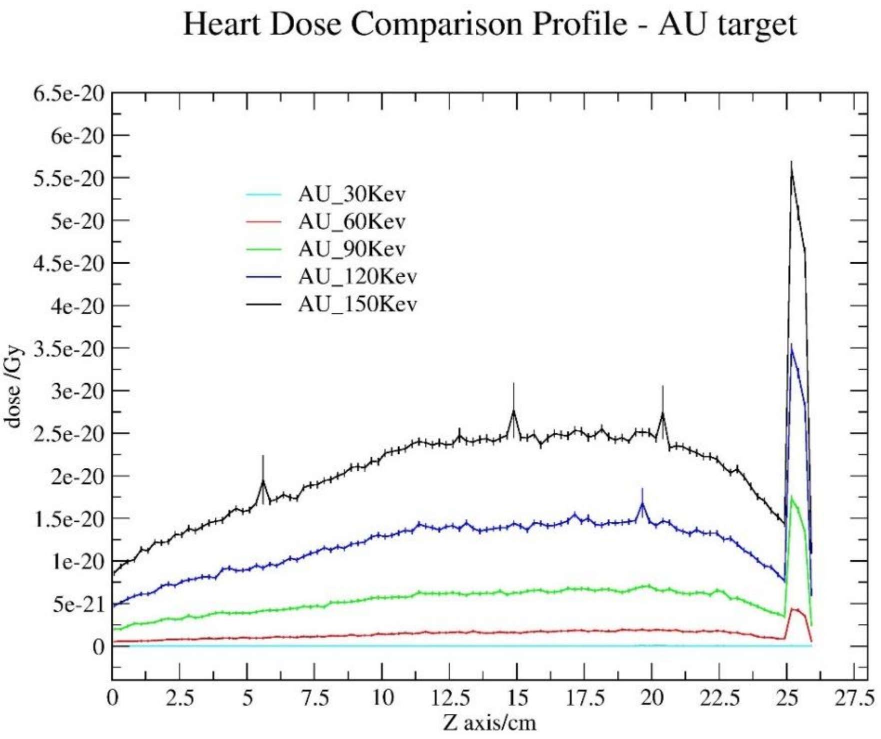

Figure 88Heart Dose Comparison Profile - AU target.

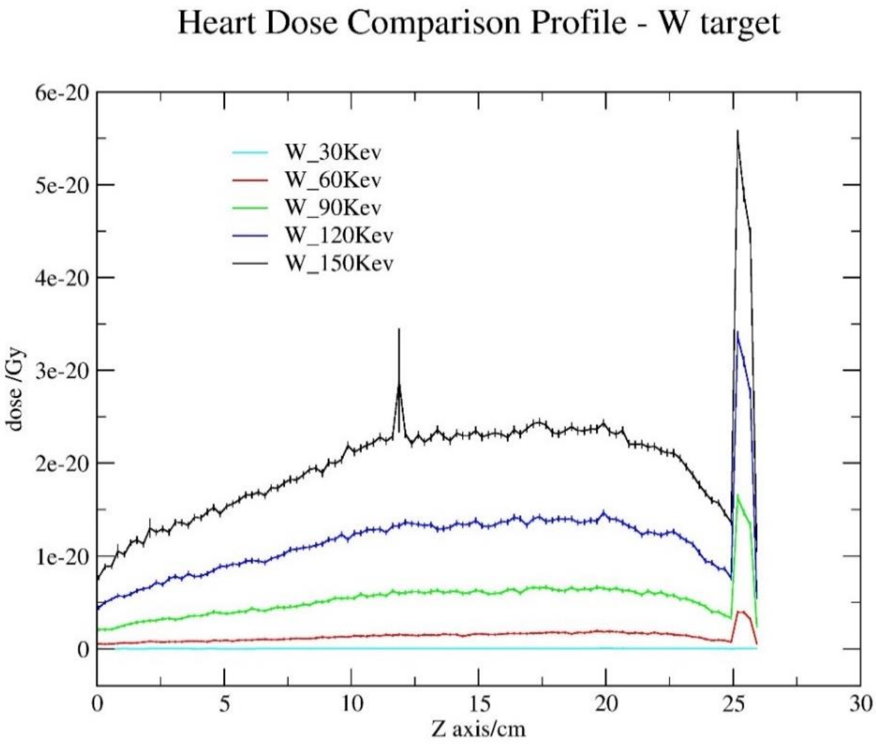

Figure 89 Heart Dose Comparison Profile - W target.

8.4.4 Lung

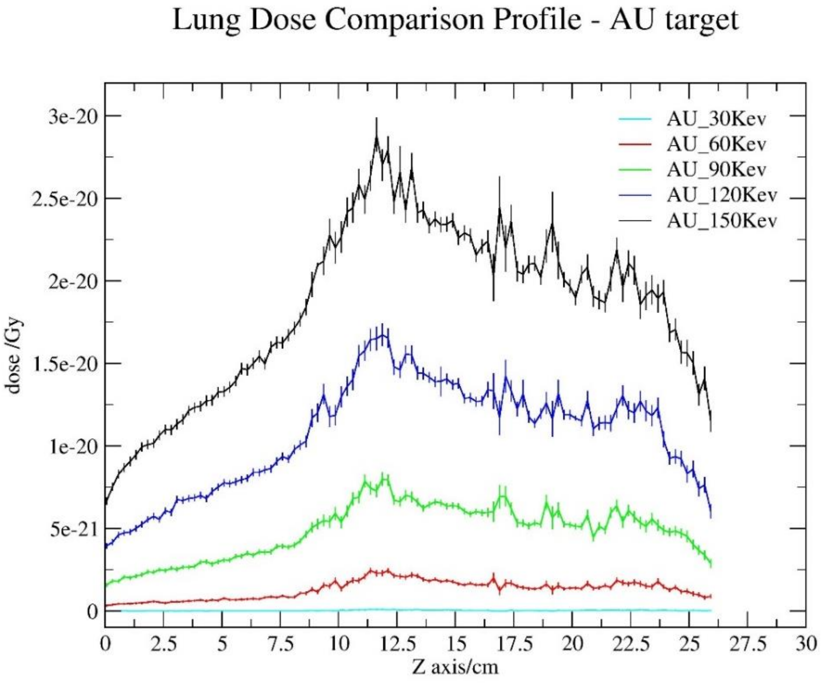

Figure 90 Lung Dose Comparison Profile - AU target.

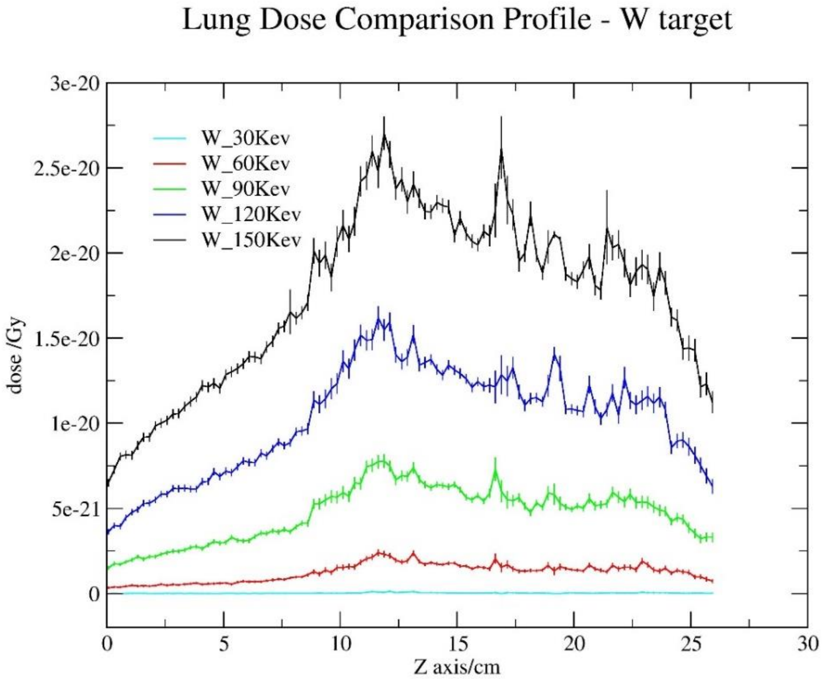

Figure 91 Lung Dose Comparison Profile - W target.

8.4.5 Skin

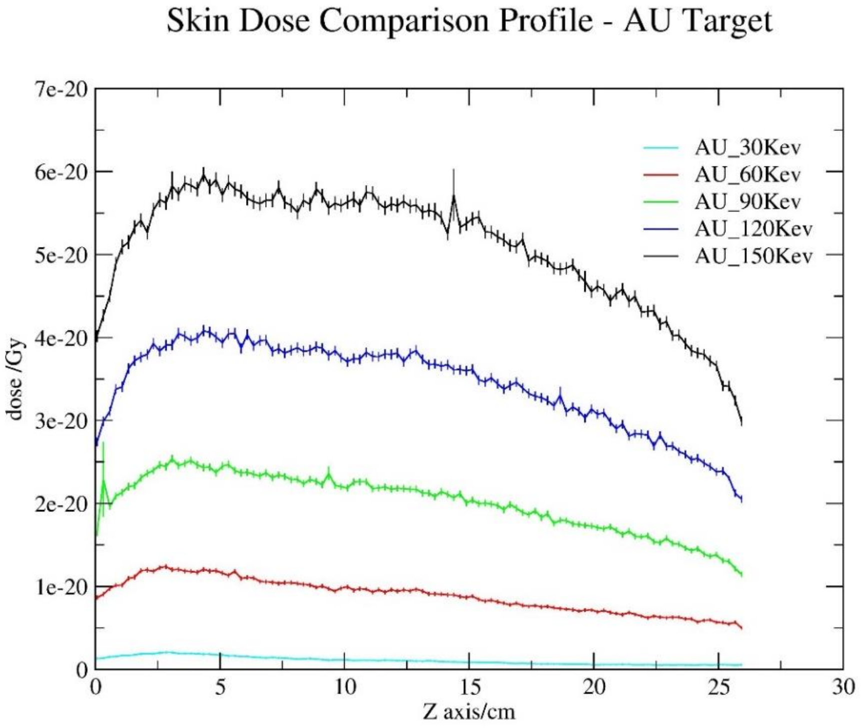

Figure 92 Skin Dose Comparison Profile - AU target.

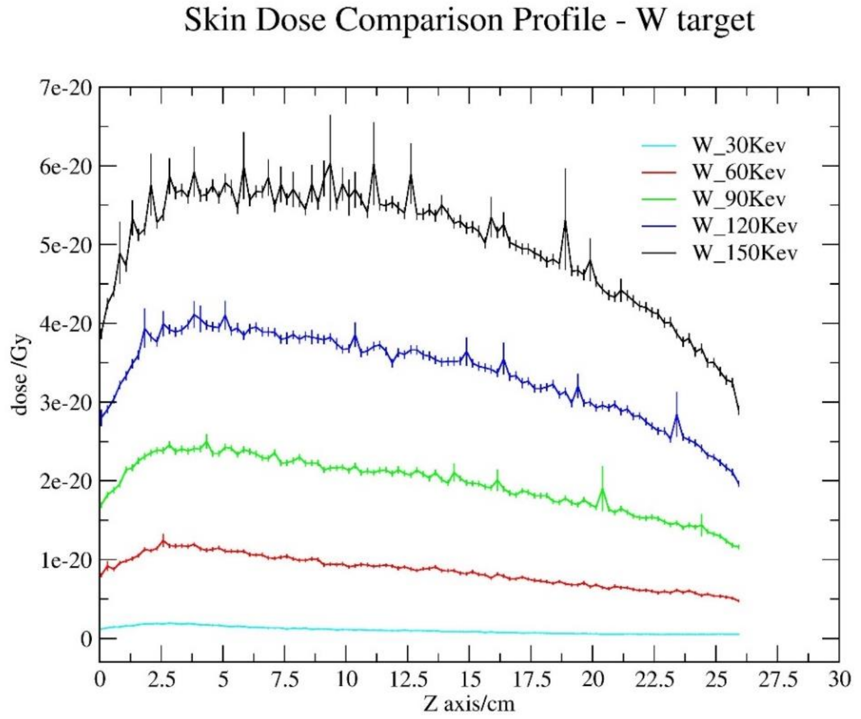

Figure 93 Skin Dose Comparison Profile - W target.

8.4.5 Spine

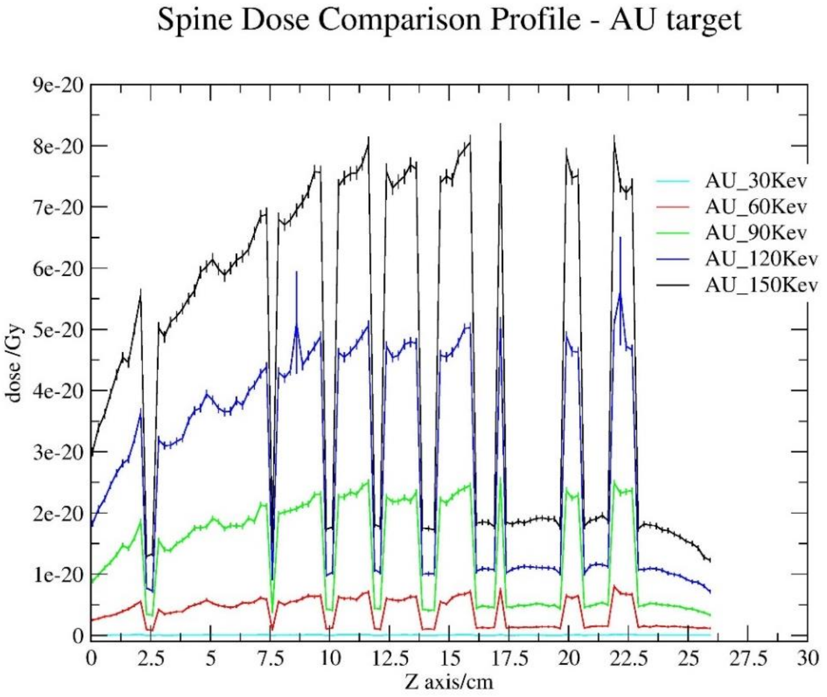

Figure 94 Spine Dose Comparison Profile - AU target.

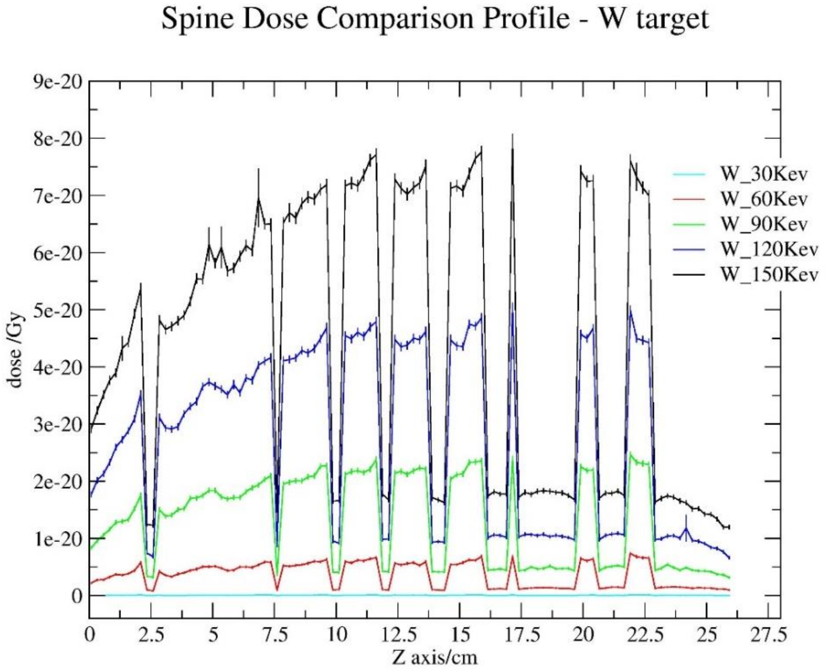

Figure 95 Spine Dose Comparison Profile - W target.

The organ dosage patterns from all three phantom simulations are shown in Figures 84-95. Starting from the top dosage profiles for organs like the abdomen, brain, heart, lung, skin, and spine may be shown two at a time, one for the AU instances and one for the W cases. The intricacy of each organ's geometry and position within the phantom has a major impact on the dosage distribution throughout the organ. From the beam's quality assurance, it was known that the fluence is not significant enough to pierce the phantoms in the instance of 30 keV, therefore there is very little dose scored, near to 0 in most organ cases, except the skin case. Moving up from 60 keV, the dosage begins to rise; in all situations, the scored values of the AU target profiles are somewhat slightly larger than the W ones. After irradiating all phantoms and presenting the dosage profiles, the comparison of various beams can be seen, not only in terms of spectrum and energy fluence distributions, but also in terms of dose.

8.5 AnyScan based SPECT-head Simulation.

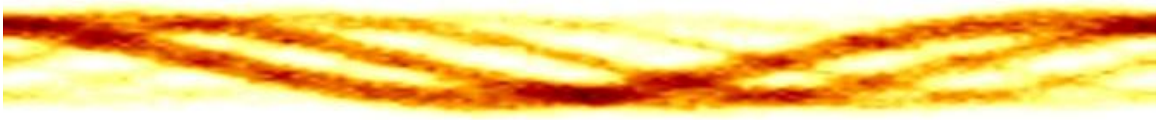

Figure 96 AnyScan NaI Crystal, Hot spheres Jaszczak Phantom Sinogram Visualization.

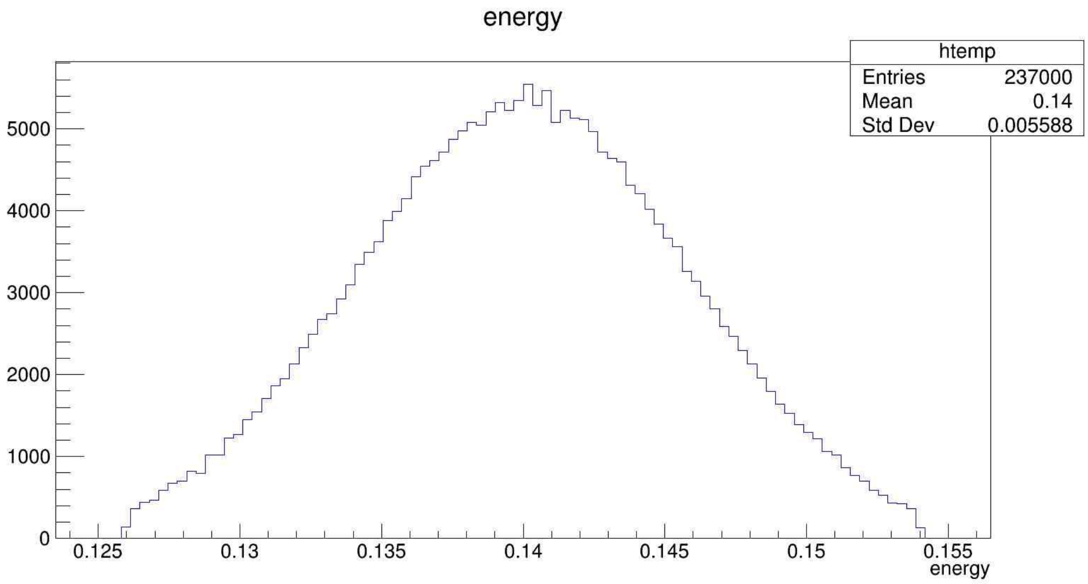

Figure 97 AnyScan NaI Crystal, Hot spheres Jaszczak Phantom - Singles Energy Distribution.

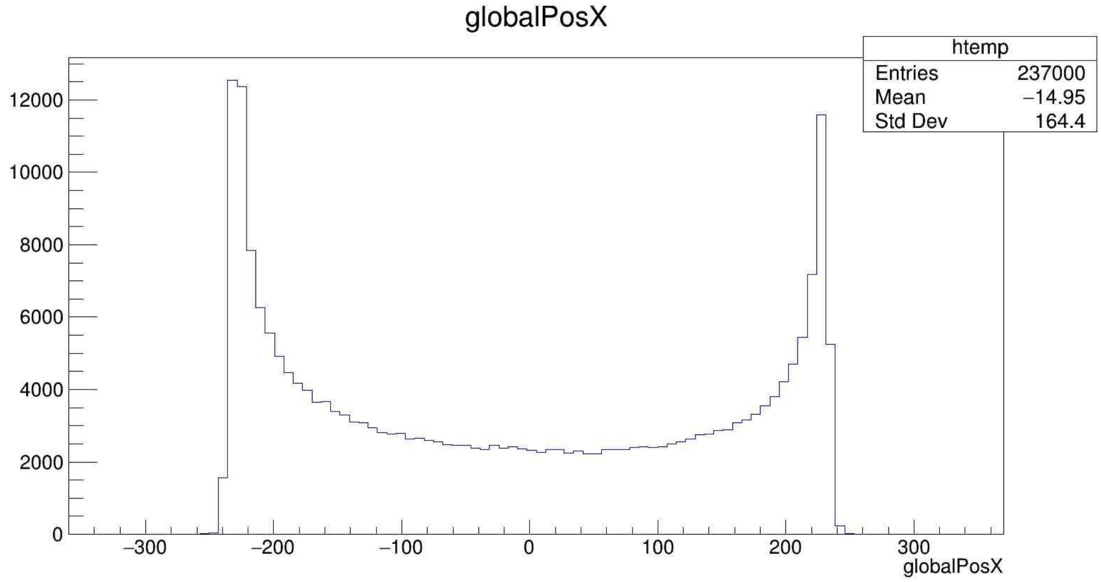

Figure 98 AnyScan NaI Crystal, Hot spheres Jaszczak Phantom - Singles Spatial Distribution Position X.

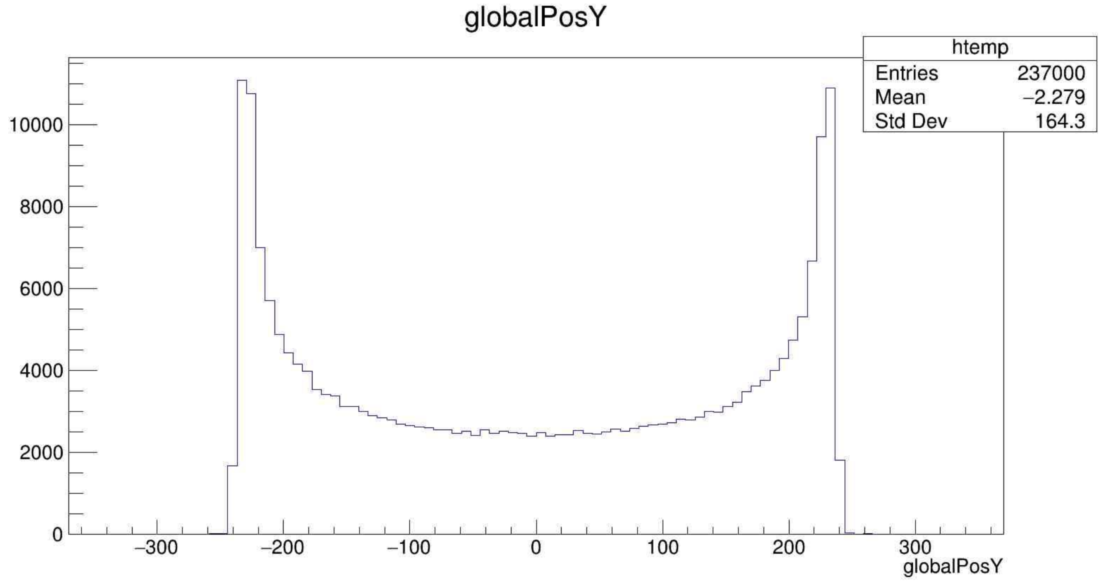

Figure 99 AnyScan NaI Crystal, Hot spheres Jaszczak Phantom - Singles Spatial Distribution Position Y.

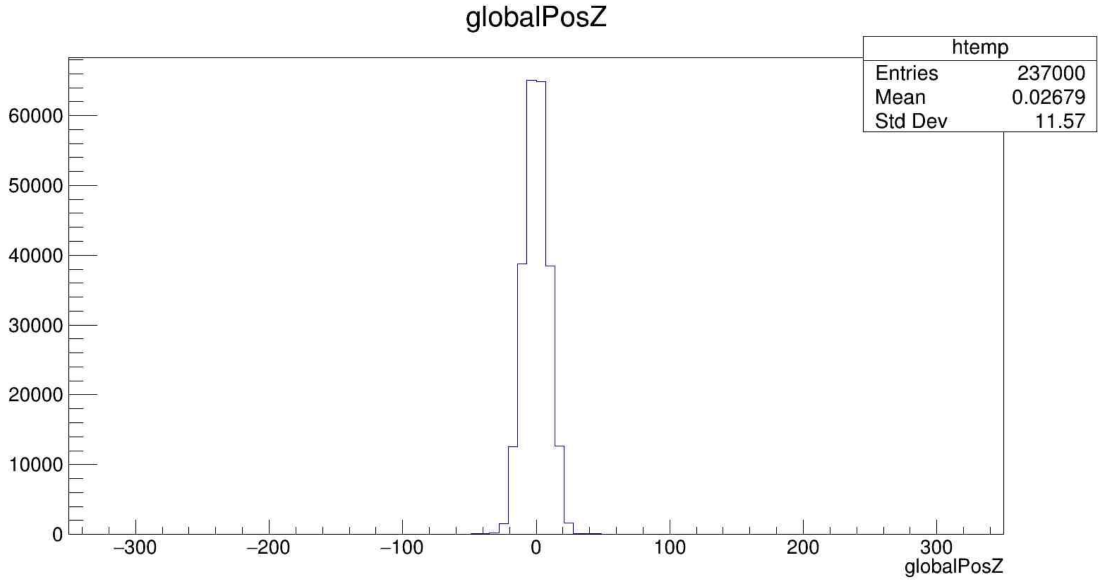

Figure 100 AnyScan NaI Crystal, Hot spheres Jaszczak Phantom - Singles Spatial Distribution Position Z.

Figure 96 shows the sinogram of the AnyScan-based SPECT-head simulation with the jaszczak phantom in hot spheres mode. Figure 97 shows the energy distribution of singles caught by the detector. It can be seen that the peak is around 140 keV, with the lowest point being 126 keV and the highest being 154 keV, indicating that the energy range is 140 keV ± 10% (126, 154), as specified in the GATE simulation.mac file. Figures 98-100 show the spatial distribution of singles detected.

At this point, it's worth noting that the PCs running native Ubuntu took roughly 72-76 hours to finish the simulation, however the system running Windows 10 and the WSL virtualization version of Ubuntu, took over 680 hours, making it nearly unworthy to run GATE simulations in that arrangement. Furthermore, there were relatively few changes in execution time between EGSnrc simulations, with the newest CPUs being somewhat quicker, regardless of the virtualization.

8.5.1 OSMAPOSL Comparison for optimal subset and iteration combination.

		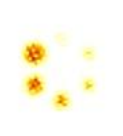
2Subsets, 2Iteration	2Subsets, 10Iteration	2Subsets, 100Iteration
	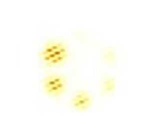	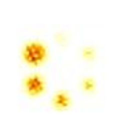
8Subsets, 2Iteration	8Subsets, 10Iteration	8Subsets, 100Iteration
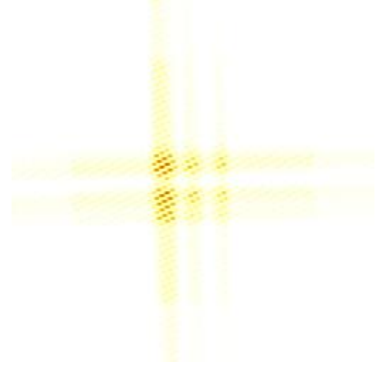		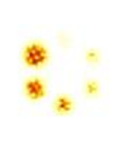
32Subsets, 2Iteration	32Subsets, 10Iteration	32Subsets, 100Iteration

Table 3 OSMAPOSL reconstructions for various subset and iteration options.

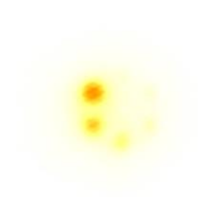	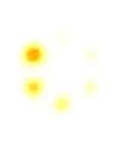	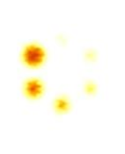
2Subsets, 2Iteration	2Subsets, 10Iteration	2Subsets, 100Iteration

	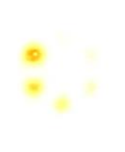	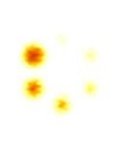
8Subsets, 2Iteration	8Subsets, 10Iteration	8Subsets, 100Iteration
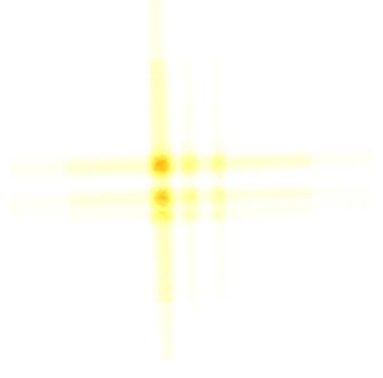	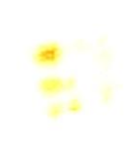	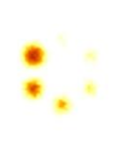
32Subsets, 2Iteration	32Subsets, 10Iteration	32Subsets, 100Iteration

Table 4 OSMAPOSL Volume Rendering for various subset and iteration options.

An analysis was carried out in order to determine which are the best available possibilities for subset and iteration combination when utilizing OSMAPOSL algorithm for SPECT image reconstruction. The results of image reconstruction, transverse view, with OSMAPOSL are presented in tables 3 and the results of the volume-rendering image are provided in table 4, with each scenario having a different number of subsets and iterations.

The number of subset was set to 2, 8, 32, and iteration to 2, 10, 100, yielding nine reconstructed images presented. After examining table 3 and table 4, the conclusion was that the optimal combination of subsets and iterations is the combination: 8 subsets, 100 iterations. The iterations being 100 is the option which cannot be denied that is the best one, but regarding the subset being 2 or 8 or 32 another parameter needs to be taken in to account. OSMAPOSL algorithm take advantage of geometrical symmetries and perform the reconstruction relatively quicker, as the number of subsets increases. But if there aren't so many symmetries, like the case with 32 subsets, then the algorithm performs poorer and wastes more and more time in order to converge. Furthermore, as demonstrated in the samples with the subset being set to 32, for the 2 and 10 iterations cases the reconstruction does not look so much as the end image but as the number of repetitions increases to 100, the algorithm converges to the same result as the other cases, with iterations set to 100.

Due to the big number of images produced there wasn’t enough space to present in the thesis the detailed investigation, for that purpose a great number of images are stored in Appendix 3. More data can be accessed as the investigation presented there is for subsets 1,2,4,8,16,32 and iterations to 1,2,5,10,100 with not only the transverse side but also the coronal and sagittal for each slice viewed.

8.5.2 Hot spheres Jaszczak phantom OSMAPOSL vs FBP Comparison.

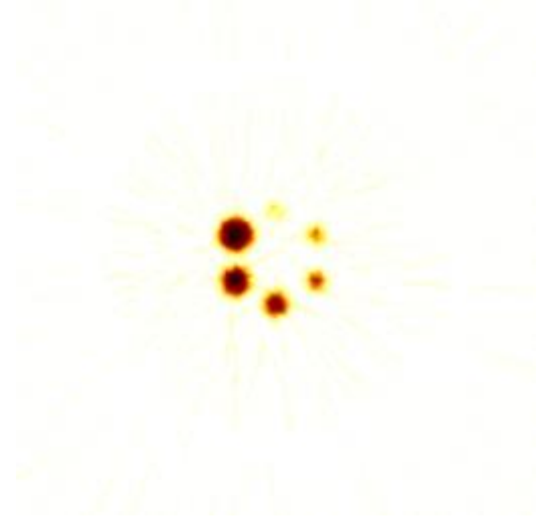	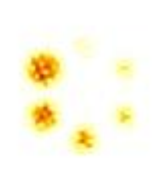
FBP	OSMAPOSL

	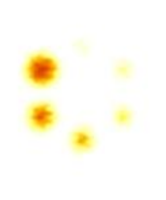
Volume Rendering - FBP	Volume Rendering - OSMAPOSL

Table 5 FBP - OSMAPOSL Jaszczak hot spheres phantom.

As it can be observed in table 5, side by side the results of the reconstruction with OSMAPOSL and FBP, along with the volume renderings of the reconstructions. As it can be seen, with the spheres being hot and the background cold, the FBP algorithm has a clearer reconstruction. Although OSMAPOSL reconstruction is very impressive for an iterative algorithm, without the usage of the algorithms full capabilities taking into consideration filtering, attenuation and other parameters cannot outperform FBP algorithm in 2D reconstruction. This run with the activity set up at 10 Bq/mm^3 took around 76 hours to finish, while the result it produced are quick decent.

8.5.3 COLD spheres Jaszczak phantom OSMAPOSL vs FBP Comparison.

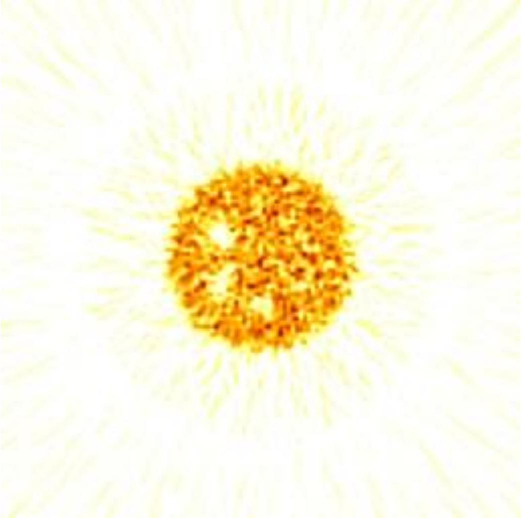	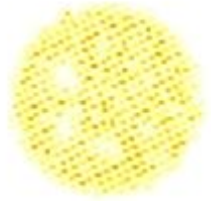
FBP	OSMAPOSL
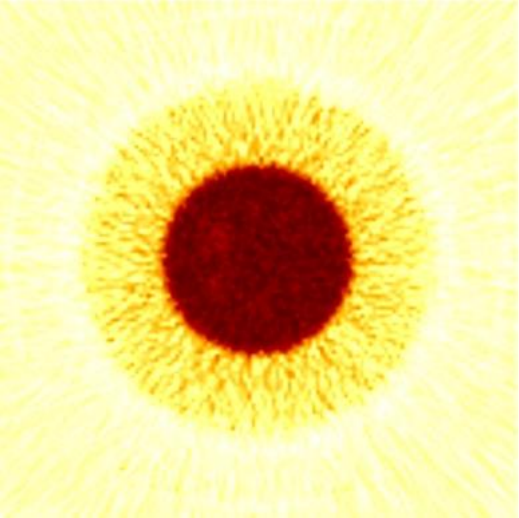	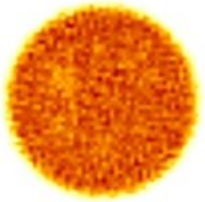
Volume Rendering FBP	Volume Rendering OSMAPOSL

Table 6 FBP - OSMAPOSL Jaszczak cold spheres phantom.

As it can be seen in Table 6, both algorithms did their best in this rather difficult scenario, with OSMAPOSL having slightly better results, in the opinion of the writer. Although volume rendering is useful in many cases and can enhance the quality of the reconstruction, in this particular case did not reveal any extra cold regions, but in addition was unable enhance the already revealed ones.

Both the OSMAPOSL and FBP reconstruction reveals the S6=38mm, S5=31.8mm and S4=25.4mm spheres to have cold background, while FBP has a quite better contrast, OSMAPOSL not clearly enough presents the S3=19.1 mm sphere too. This run took around 11 days to finish, the activity of the source being 1 Bq/mm^3 seems a small number but the cylindrical hot area in this case, is quite larger in relation to the spheres, making it much more expensive in terms of computational time.

8.5.4 Comparison for various Crystal substances for AnyScan S based SPECT-head.

BGO	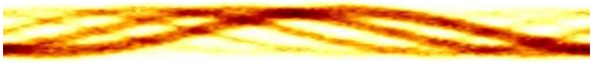
GSO	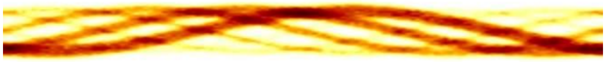
LSO	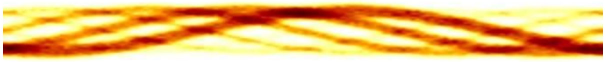
NaI	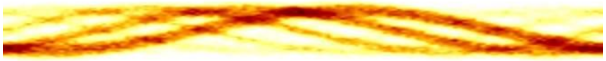

Table 7 Sinograms for different crystal substances.

BGO	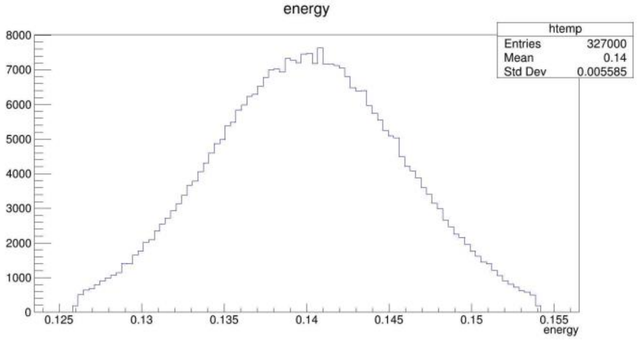

<table>
<tr><td>GSO</td><td>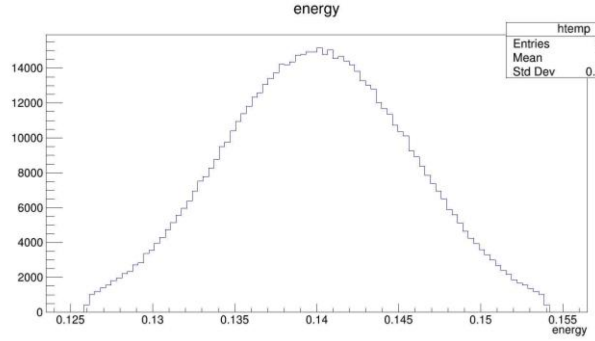
</td></tr>
<tr><td>LSO</td><td>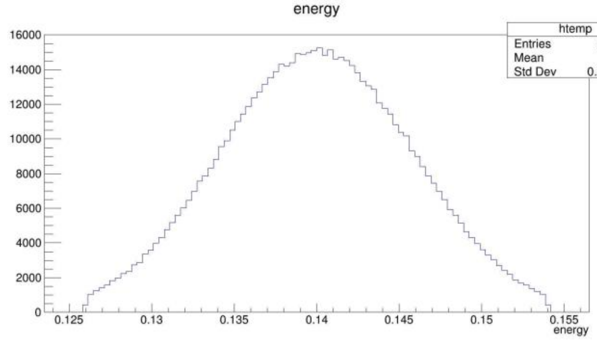
</td></tr>
<tr><td>NaI</td><td>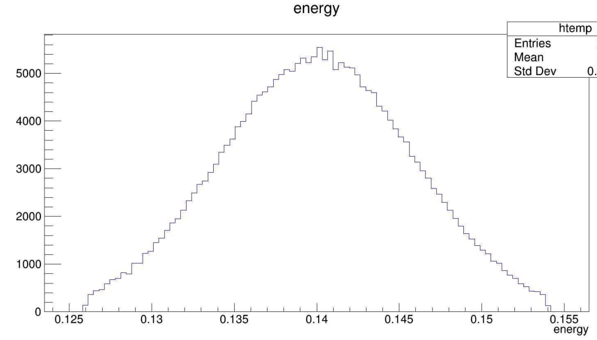
</td></tr>
</table>

Table 8 Singles - Energy distributions for different crystal substances.

<table>
<tr><td>BGO</td><td> </td><td> </td></tr>
</table>

GSO	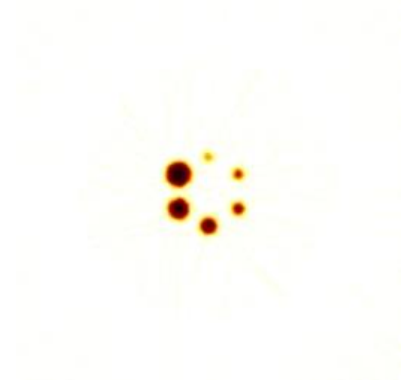	
LSO	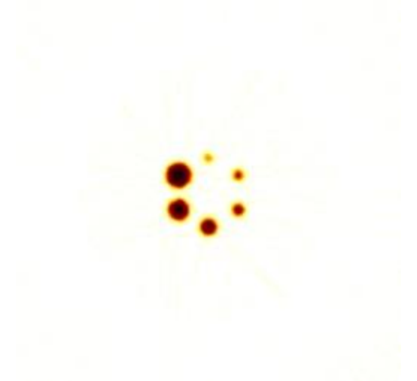	
NaI	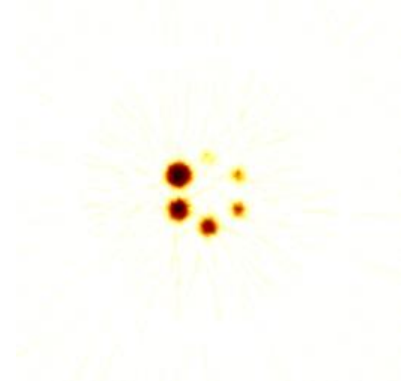	

Table 9 FBP reconstructions and volume renderings for different crystal substances.

BGO	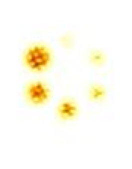	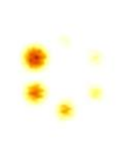

GSO		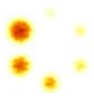
LSO	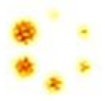	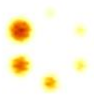
NaI	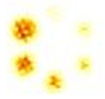	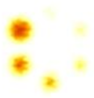

Table 10 OSMAPOSL reconstructions and volume renderings for different crystal substances.

At this point it is necessary to advice that besides the change in crystal material, nothing else has been changed on the code between simulations. The comparison begins with Table 7 where the sinograms of each case are presented. As observed the sinograms with BGO, LSO, GSO crystals are quite a bit brighter than the sinogram with the NaI crystal.

For the singles scored at each case, table 8 presents the energy distributions per case. As it can be seen, the BGO case had 327.000 hits, the LSO case had 669.637 hits, the GSO case had 666.000 hits and the NaI case had 237.000 hits. As it was predicted, the other crystals have more hits than the NaI case, which explains also, why the sinograms are brighter for the BGO, LSO and GSO cases.

Table 9 presents the FBP reconstructions and volume renderings for all cases. As presented, great interest in the cases of GSO and LSO as the S1=12.7mm sphere can actually be seen very clearly, in comparison with the other cases where it is not so clear.

Table 10 presents the OSMAPOSL reconstructions and volume renderings for all situations. Besides OSMAPOSL images being rather low in contrast, again the cases of GSO and LSO present better image quality and as it can be observed the S2=15.9mm sphere now is more visible.

Following the extensive comparison, the argument follows that by changing the crystal in a SPECT system from NaI to BGO, LSO, or GSO and without changing the activity of the radioisotope to a patient, the same examination can provide a superior quality image.

8.6 Custom Small Animal SPECT-head Simulation.

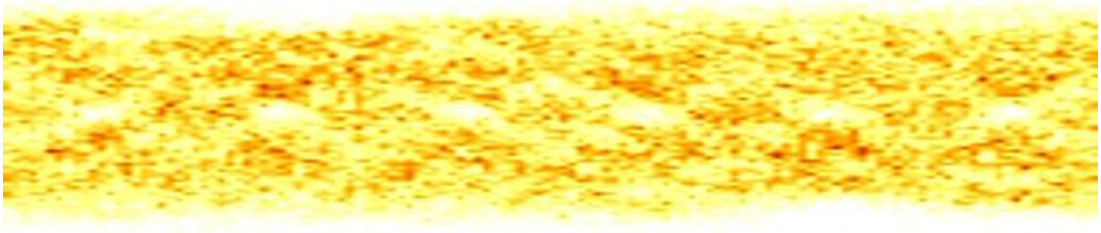

Figure 101 Custom Small Animal NaI Crystal, Hot rods Jaszczak Phantom Sinogram Visualization.

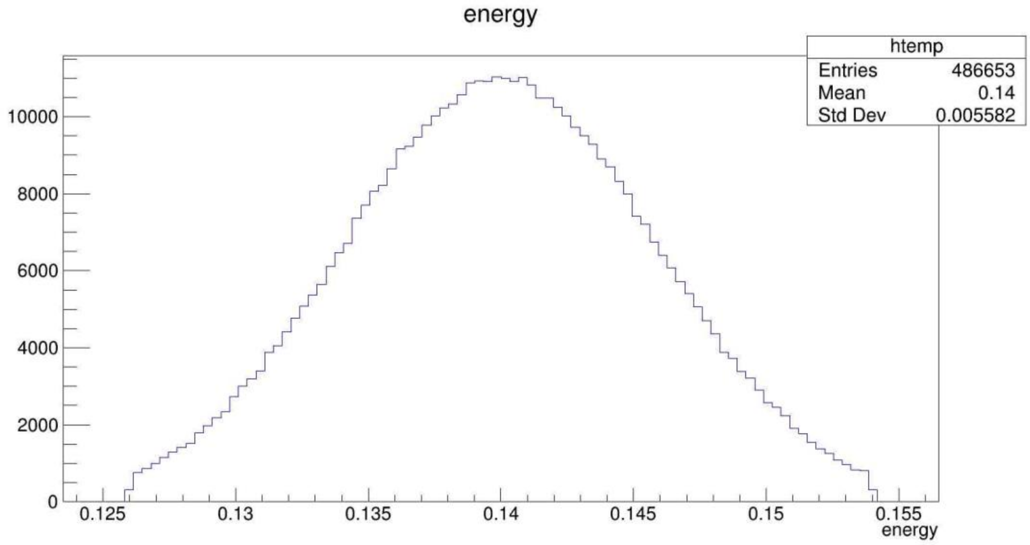

Figure 102Custom Small Animal NaI Crystal, Hot rods Jaszczak Phantom, Singles - Energy Distribution.

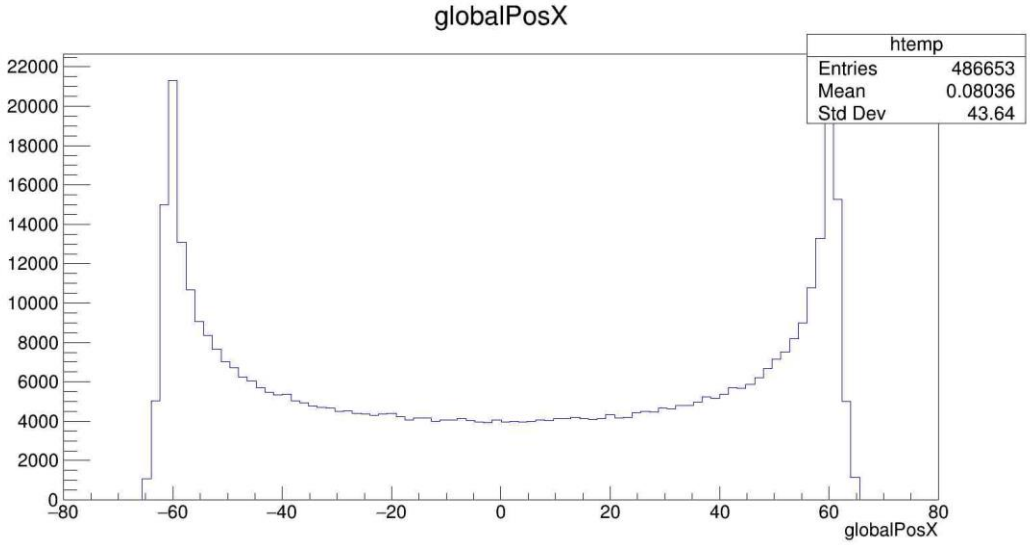

Figure 103 Custom Small Animal NaI Crystal, Hot rods Jaszczak Phantom, Singles - Spatial Distribution Position X.

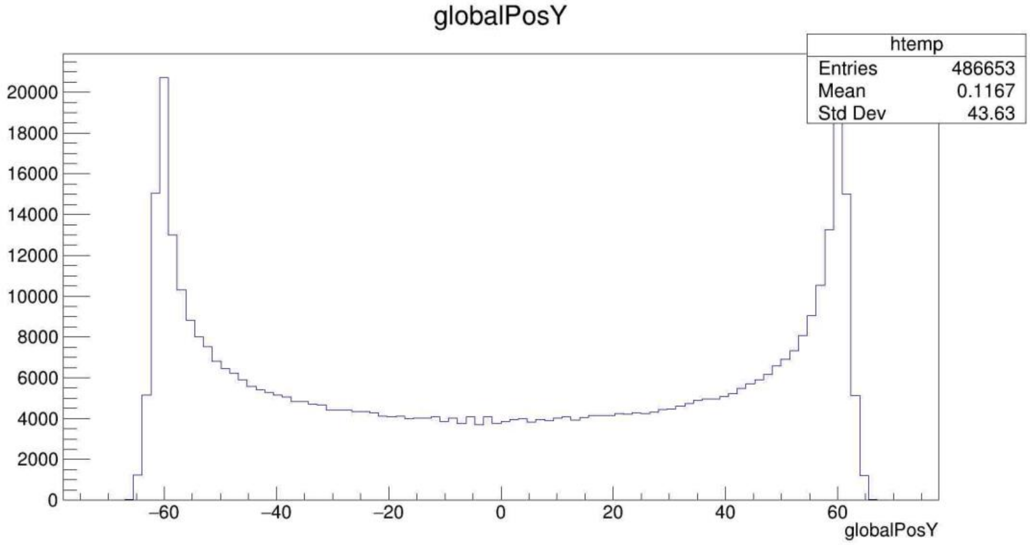

Figure 104 Custom Small Animal NaI Crystal, Hot rods Jaszczak Phantom, Singles - Spatial Distribution Position Y.

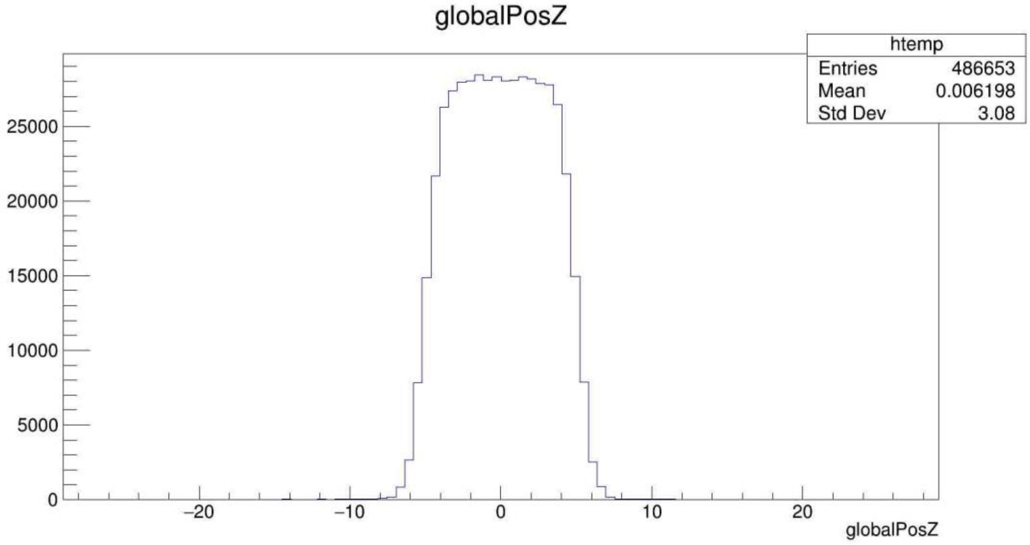

Figure 105 Custom Small Animal NaI Crystal, Hot rods Jaszczak Phantom, Singles - Spatial Distribution Position Z.

Figure 101 displays the sinogram of the customized small animal SPECT-head simulation with the Jaszczak phantom operating in hot rods mode. The singles scored by the detector have energy distribution shown in Figure 102. As can be observed, the energy range is 140 keV ± 10% (126, 154), as defined in the GATE configuration .mac file, with the peak being approximately 140 keV, and the lowest and highest points being 126 and 154 keV, respectively. Figures 103 to 105 depict, respectively, the spatial distribution of the singles scored by the SPECT-head in the x, y, and z directions.

It's important to note that the activity was adjusted to 1200 Bq/mm3 at this stage since the geometry of the custom-built small animal SPECT-head is considerably smaller than the AnyScan-based SPECT-head. The simulation time for the activity was around 74–76 hours.

8.6.1 OSMAPOSL Comparison for optimal subset and iteration combination.

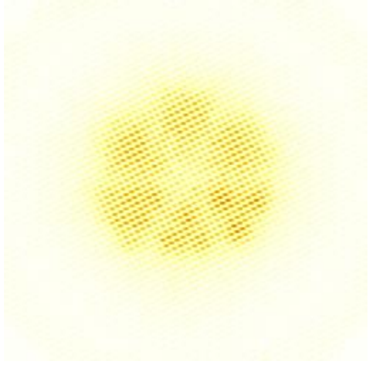	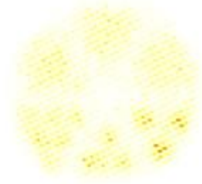	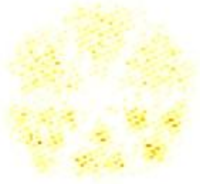
2Subsets, 2Iteration	2Subsets, 10Iteration	2Subsets, 100Iteration
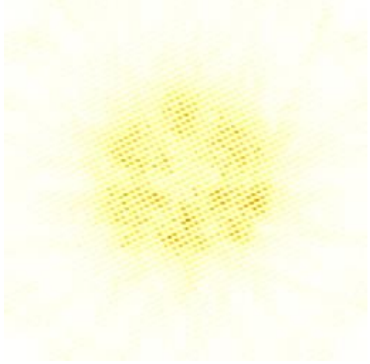	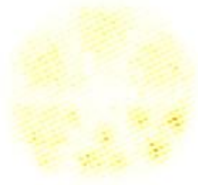	
8Subsets, 2Iteration	8Subsets, 10Iteration	8Subsets, 100Iteration
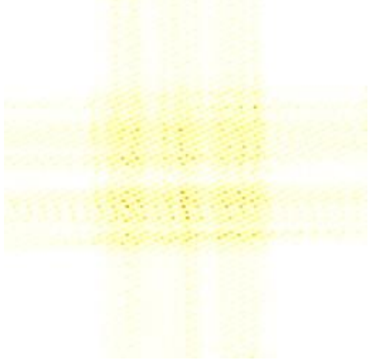		
32Subsets, 2Iteration	32Subsets, 10Iteration	32Subsets, 100Iteration

Table 11 OSMAPOSL reconstructions for various subset and iteration options.

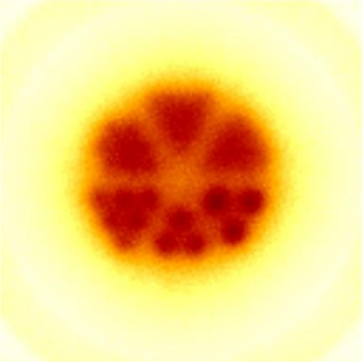	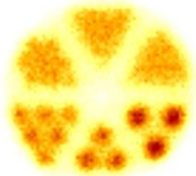	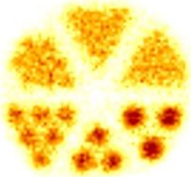
2Subsets, 2Iteration	2Subsets, 10Iteration	2Subsets, 100Iteration
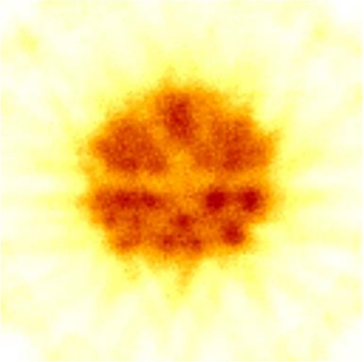	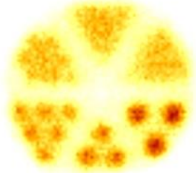	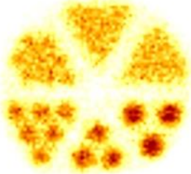
8Subsets, 2Iteration	8Subsets, 10Iteration	8Subsets, 100Iteration
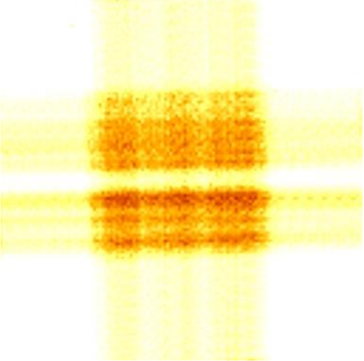	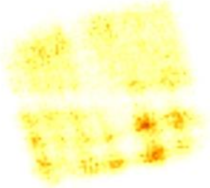	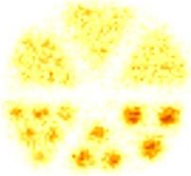
32Subsets, 2Iteration	32Subsets, 10Iteration	32Subsets, 100Iteration

Table 12 OSMAPOSL Volume renderings for various subset and iteration options.

When using the OSMAPOSL method for SPECT image reconstruction, similar to the AnyScan based SPECT-head, an analysis was done to establish which are the best options for subset and iteration combination. Each scenario had a varied number of subsets and iterations, and the results of the image reconstruction in transverse view with OSMAPOSL are shown in tables 11 and table 12, respectively. There were nine given reconstructed pictures as a result of the subset size being 2, 8, 32 and the iteration size being 2, 10, 100.

Having come to the same conclusion, as with the AnyScan based SPECT-head, that the combination of 8 subsets and 100 iterations is the best one after looking at tables 11 and 12.

Additional information may be acquired through the inquiry detailed in Appendix 3, which includes subsets 1,2,4,8,16,32 and iterations up to 1,2,5,10,100, with each slice's coronal and sagittal as well as transverse sides available for viewing.

8.6.2 Comparison of collimator's hole size for small animal SPECT.

4mm	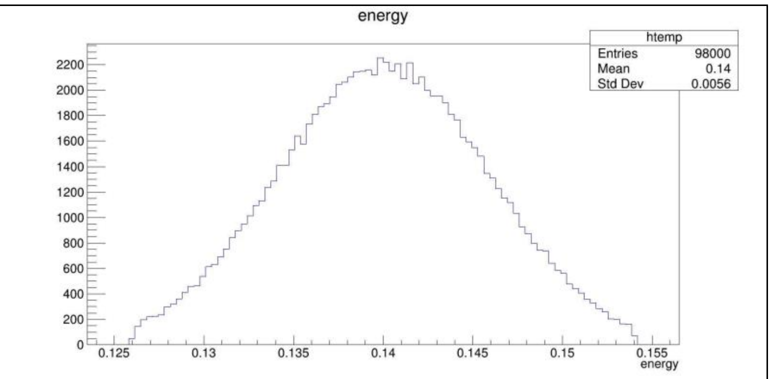
8mm	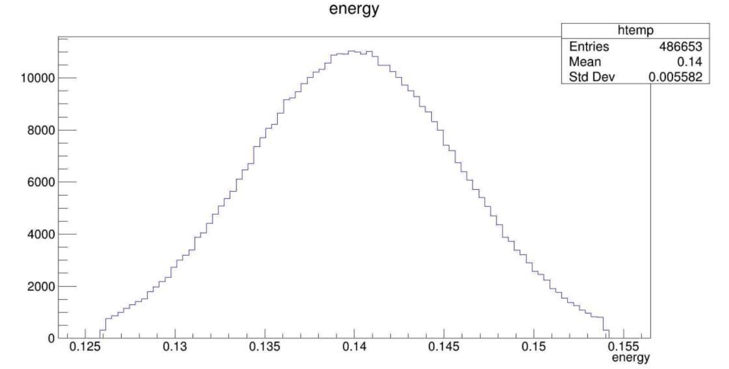
16mm	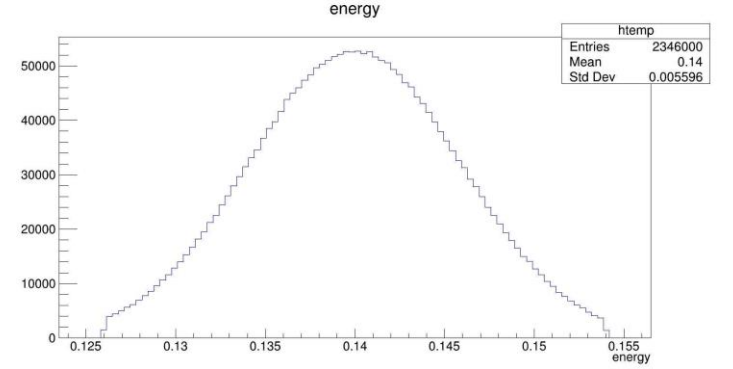

Table 13 Singles - Energy distribution for different diameters of collimator's hole sizes.

4mm	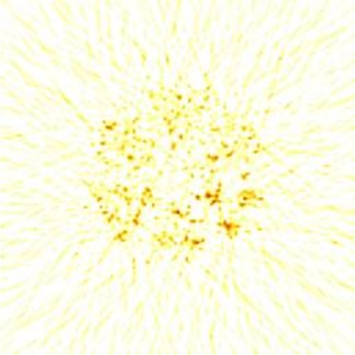	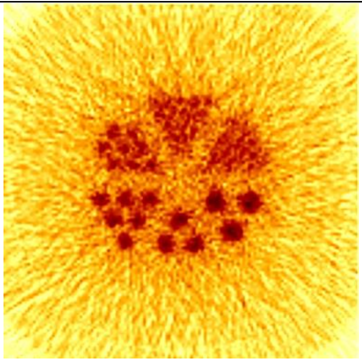
8mm	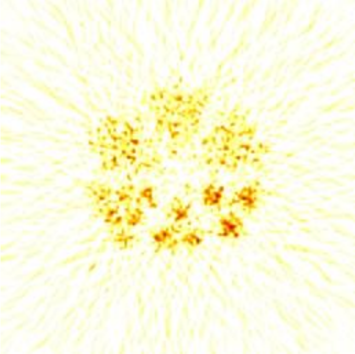	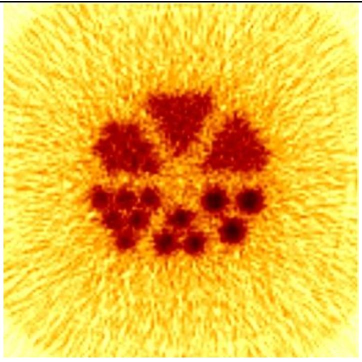
16mm	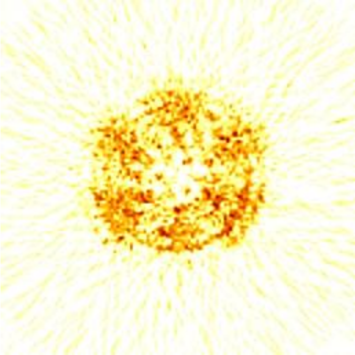	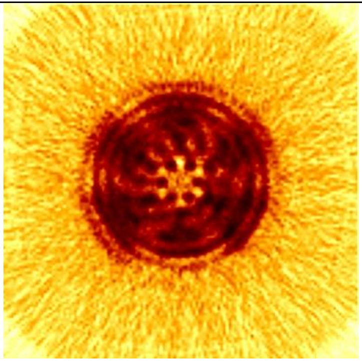

Table 14 FBP reconstructions and volume renderings for different diameters of collimator's hole sizes.

4mm		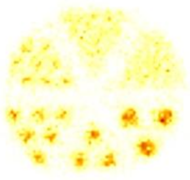

8mm	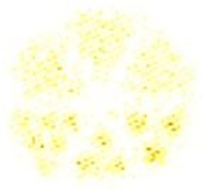	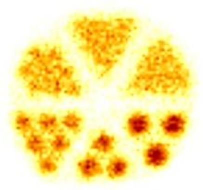
16mm	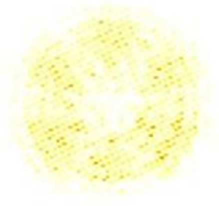	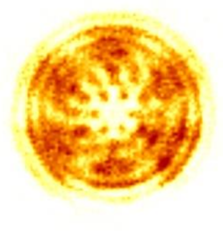

Table 15 OSMAPOSL reconstructions and volume renderings for different diameters of collimator's hole sizes.

At this stage, it is important to note that the only difference between simulations is the size of the collimators' holes; all other parameters stay the same. Beginning with Table 13, which shows the Energy Distribution of single photons scored by the detector, the 4mm hole size acquired 98000 hits, the 8mm hole size acquired 486653 hits, and the 16mm hole size acquired 2346000 hits.

Moving on to Table 14, which displays the reconstructions alongside the volume renderings. Although the cases with 16mm hole size received many hits, according to the energy distribution in Table 13, the reconstructed image is not clear at all, leaving the cases with 8mm and 4mm that return the phantom's cylindrical sources, being suitable for further investigation. Both cases, 4mm and 8mm sizes, are capable of identifying phantom cylinders with the radius of 1.2mm, 1mm, and 0.85mm.

When the number of hits is few, such as in a 4mm hole, volume rendering improves the image quality and can reveal that in the 4mm scenario, even if the 0.675mm cylinders are not clearly visible in the reconstruction, they can be seen in the volume rendering. Table 15 shows a similar phenomenon, with the OSMAPOSL reconstructions and volume renderings of the 4mm case being the best suited for that specific scanner, demonstrating that GATE with STIR may yield results for optimization parameters, as stated by Han Guy Kang et al [157]. In addition, it is important to say that in 2D mode, like the case of SPECT, FBP has better results than OSMAPOSL.

8.7 Conclusions

All the results were provided in this chapter. Two primary portions can be seen: the CT irradiation data has been shown in the first three sub-sections, and the SPECT approach data has been presented in the final two sub-sections.

First, an evaluation of the data from the CT experiments is being conducted. For the instances of interest, the spectrum and energy fluence distributions are shown, and some explanations of the beam's energy, x-ray properties, and other factors are explored. Further details were available regarding the irradiation when the dosimetric map slices were shown with the approach being completed by taking one last look at the comparison dose profiles for the following organs: abdomen, brain, heart, lung, skin, and spine, which are supplied for energies 30 keV to 150 keV with a step of 30 keV.

The possibilities of the GATE platform have been discussed in relation to the SPECT systems, both the AnyScan S-based system and the custom-made system for small animals. After the simulations, a comparison of the best subset and iteration combinations when employing the OSMAPOSL reconstruction method is being carried out for both SPECT-heads. The OSMAPOSL and FBP algorithms, provided by STIR, to reconstruct images from the GATE’s simulated projectional outputs.

Five simulations occurred in the case of the AnyScan-based SPECT-head, of which the first shows the reconstructions of hot spheres Jaszczak phantom, the second presenting the cold spheres Jaszczak phantom case, and the third shows the effects of changing the crystal material from NaI to BGO, LSO, or GSO on the reconstructed image. The FBP, OSMAPOSL reconstructions, and volume renderings are viewed for each of these situations.

The custom-made small animal SPECT-head completed three simulations with the size of the collimator's hole varying from 4, 8, 16 mm for each simulation, with the results being consistent with previous studies.

9. General Conclusions

The current research aimed to address questions regarding the modelling of CT and SPECT systems, from a dosimetric stand point, utilizing Monte Carlo open source software. On the one hand, there are particles that somehow interacting with the world around us and on the other hand, those interactions needed to be mathematically modelled and algorithmically calculated. Chapter A describes and introduction to the fundamentals of particle interaction with matter, dosimetric quantities and the principles of operation of both CT and SPECT systems are described. Additionally, it describes a practical approach of how to model such interactions with Monte Carlo techniques. Chapter B, depicts the research part of the dissertation which covers all the information regarding the software utilized, such as how to compile and install it, how to properly utilize it to meet the needs of the experimental scenario and finally how to further analyze the outputs to results. Furthermore, the results for each system as well as the approaches utilized were evaluated.

There were many challenges utilizing open source software and being able to perform simulations. The compilation and installation procedure for GATE, EGSnrc and STIR was a challenge, but Appendix 2 technical report was created as well as two lengthy video tutorials were built in order to overcome those challenges. Another issue was the small number of computational units, which in this case were 3 computers, two with native Ubuntu and another with Windows 10 utilizing WSL 2.0 virtualization in order to run Ubuntu. The outcome of that restriction lead to the creative thinking by the side of the researchers and enable them to utilize techniques like variance reduction in order to save major simulation and execution time. In addition, the access to commercial CT and SPECT systems was very difficult at the time being due to COVID-19 pandemic, the solution here was extensive bibliography research and collaboration with the other researchers, like the one with University of Thessaly. Also it is very time consuming testing new ideas and systems utilizing Monte Carlo, as each execution takes a long time to produce outcomes and for the result to be evaluated there is an extra time cost, this challenge was overcome with very good time development and monitoring in order not to waist a second.

The strategy for the CT approach was to utilize EGSnrc routines, BEAMnrc produced outputs .egsphsp files that were beam simulations and with DOSXYZnrc the irradiation from all angles, forming a circle around special personalized phantoms. The most significant questions answered was:

1. How to approach CT with EGSnrc.
2. How does someone evaluates CT beams?
3. When we say CT has low dosage, how low?
4. How much is the exposure of organs from a CT examination?
5. What is the energy range, relationship with the dose in organs?

The results of the CT experiments are being evaluated. The spectrum and energy fluence distributions for the cases of interest are displayed, and several hypotheses regarding the beam's energy, x-ray characteristics, and other elements are investigated. The approach was completed by taking one final look at the comparison dose profiles for the following organs: abdomen, brain, heart, lung, skin, and spine, which are supplied for energies from 30 keV to 150 keV with a step of 30 keV, providing additional information. Additional information and a detailed evaluation can be found in Appendix 1, where the data presented are from 30-150 keV with step 5keV.

The philosophy changed when approaching the SPECT system. Before, a beam was generated, evaluated and the beam irradiates the phantom. Due to the principle of operation the source in a SPECT examination is the patient so the irradiation comes from inside out. GATE helped building scenarios to simulate the orbiting and rotation of the SPECT-head, also the sources were able to be defined and the experiment beginning. Afterwards the sinogram and the .root output were collected from the GATE simulations and the .root file was utilized for the evaluation of the simulation and the projectional data were reconstructed with STIR. The most significant questions answered were:

1. How to approach a SPECT system with GATE?
2. How to reconstruct projectional data with STIR?
3. If the SPECT characteristics were optimized, what effect would that have in the reconstructed image?

The SPECT systems, including the AnyScan S-based and the custom-made for small animals, have been addressed about the GATE platform's potential. The optimal subset and iteration combinations for using the OSMAPOSL reconstruction approach are being compared after the simulations for both SPECT heads. STIR's OSMAPOSL and FBP algorithms are used to recreate visuals from the outputs of the GATE's simulated projections.

The AnyScan-based SPECT-head was subjected to five simulations, the first of which displays the reconstructions of the hot spheres Jaszczak phantom case, the second the cold spheres Jaszczak phantom case and the third the effects of switching the crystal material from NaI to BGO, LSO, or GSO on the reconstructed image. For each of these scenarios, the FBP, OSMAPOSL reconstructions, and volume renderings are seen. The results of three simulations using the specially designed small animal SPECT-head, with the collimator's hole sizes ranging from 4, 8, and 16 mm for each simulation, were in agreement with earlier research. Additional information can be found in Appendix 3 where more reconstructed images can be viewed.

The contribution of thousands of people who shared hundreds of lines of code and experience allowed this research to be completed. The code for every case used and further details about the execution are all included in Appendix 4.

10. Future work

Regarding the work that will be done in the near future, the objective is to develop x-ray tube simulation on mammography, dental radiology, commercial CT, and CBCT systems while extending the CT technique. The methods outlined in this study can be utilized to imitate the type of x-ray tubes used in modern airport security scanning. Another stage is to use GATE to replicate the head of a CT detector. In the near future, the SPECT technique will continue with computational phantom simulations, Specific Absorbed Fractions (SAF) calculation using GATE and EGSnrc, and the contribution of the results to the OpenDose database. Simulating PET systems using GATE is also a short-term objective.

On a different level, the investigation of Monte Carlo simulation codes is particularly fascinating; as an illustration, TOPAS is a fantastic tool for creating Linacs and modules for proton treatment. Both x-ray tube simulation and linac simulations are especially interested in a comparison between TOPAS and EGSnrc. Packages such as Geant4-dna and Topas-nBio will be at the forefront of research attention in the next years as they provide new capabilities for Monte Carlo simulations at the molecular - DNA level, so a good start is to start to know such tools today.

References

[1]. Wikipedia contributors. (2023). Medical imaging. *Wikipedia*. https://en.wikipedia.org/wiki/Medical_imaging.

[2]. *The Nobel Prize in Physics 1903*. (2023). NobelPrize.org. https://www.nobelprize.org/prizes/physics/1903/becquerel/facts/.

[3]. Nilsson, B., & Brahme, A. (2014). Interaction of Ionizing Radiation with Matter. In *Elsevier eBooks* (pp. 1–36). https://doi.org/10.1016/b978-0-444-53632-7.00920-5.

[4]. Nikjoo, H., Uehara, S., & Emfietzoglou, D. (2016). Interaction of Radiation with Matter. In *CRC Press eBooks*. https://doi.org/10.1201/b12109.

[5]. Binjola, A. (2019). Interaction of Radiation with Matter. In *Springer eBooks* (pp. 3–11). https://doi.org/10.1007/978-981-15-0073-2_1.

[6]. INTERNATIONAL ATOMIC ENERGY AGENCY. (2014). *Diagnostic Radiology Physics*. IAEA. https://www.iaea.org/publications/8841/diagnostic-radiology-physics.

[7]. Podgoršak, E. B. (2010). Radiation Physics for medical physicists. In *Biological and medical physics series*. https://doi.org/10.1007/978-3-642-00875-7.

[8]. *Excitation and ionization potential of an atom*. (2023). QS Study. https://qsstudy.com/excitation-and-ionization-potential-of-an-atom/.

[9]. Evans, R. D., & Beiser, A. (1956). *The Atomic Nucleus*. *Physics Today*, *9*(12), 33–34. https://doi.org/10.1063/1.3059850.

[10]. Prabhu, S., Naveen, D. K., Bangera, S., and Bhat, B. S. (2020). Production of X-RAYS using X-RAY Tube. *Journal of Physics*, *1712*(1), 012036. https://doi.org/10.1088/1742-6596/1712/1/012036.

[11]. Nikolopoulos, D., Giannakopoulos, P., and Kottou, S. (2015). *Ακτινοβολίες περιβάλλοντος και άνθρωπος*. Kallipos, Open Academic Editions.

[12]. Podgoršak, E. B. (2009). Interactions of Photons with Matter. In *Biological and medical physics series* (pp. 277–375). https://doi.org/10.1007/978-3-642-00875-7_7.

[13]. Çalişkan, B. and Çalışkan, A. C. (2018). Interaction with Matter of Ionizing Radiation and Radiation Damages (Radicals). In *InTech eBooks*. https://doi.org/10.5772/intechopen.74691.

[14]. Mayles, P., Nahum, A. and Rosenwald, J. (2007). Handbook of Radiotherapy Physics. In *CRC Press eBooks*. https://doi.org/10.1201/9781420012026.

[15]. Batool, S., Nisar, M., Mangini, F., Frezza, F., and Fazio, E. (2020). Scattering of Light from the Systemic Circulatory System. *Diagnostics*, *10*(12), 1026. https://doi.org/10.3390/diagnostics10121026.

[16]. Shultis, J. K., and Faw, R. (2016). Fundamentals of nuclear science and engineering. In *CRC Press eBooks*. https://doi.org/10.1201/9781315183183.

[17]. Manninen, A. (2014). CLINICAL APPLICATIONS OF RADIOPHOTOLUMINESCENCE (RPL) DOSIMETRY IN EVALUATION OF PATIENT RADIATION. *ResearchGate*. https://www.researchgate.net/publication/298709741_CLINICAL_APPLICATIONS_OF_RADIOPHOTOLUMINESCENCE_RPL_DOSIMETRY_IN_EVALUATION_OF_PATIENT_RADIATION_EXPOSURE_IN_RADIOLOGY_Determination_of_absorbed_and_effective_dose.

[18]. Podgoršak, E. B. (2016). Radiation Physics for medical physicists. In *Graduate texts in physics*. https://doi.org/10.1007/978-3-319-25382-4.

[19]. Tolstikhina, I. Y., Imai, M., Winckler, N. and Shevelko, V. P. (2018). Basic atomic interactions of accelerated heavy ions in matter. In *Springer series on atomic, optical, and plasma physics*. https://doi.org/10.1007/978-3-319-74992-1.

[20]. Mahuvava, C. and Du Plessis, F. (2015). Monte Carlo evaluation of the dose perturbation effect of hip prostheses for megavoltage photon radiotherapy. *Physica Medica*. https://doi.org/10.1016/j.ejmp.2015.07.108.

[21]. Lechner, A. (2018). Particle interactions with matter. *CERN Yellow Reports: School Proceedings*, *5*, 47. https://doi.org/10.23730/cyrsp-2018-005.47.

[22]. Berger, M. J. and Hubbell, J. (1987). *XCOM: Photon cross sections on a personal computer*. https://doi.org/10.2172/6016002.

[23]. Burhop, E. H. S. (1935). The Auger effect. *Proceedings of the Royal Society of London*, *148*(864), 272–284. https://doi.org/10.1098/rspa.1935.0018.

[24]. Attix, F. (1986). *Introduction to radiological physics and radiation dosimetry*. https://doi.org/10.1002/9783527617135.

[25]. Adlienė, D. (2018). Chapter 9 Nanomaterials and Nanotechnologies for Photon Radiation Enhanced Cancer Treatment. In *NATO science for peace and security series* (pp. 181–202). https://doi.org/10.1007/978-94-024-1544-5_9.

[26]. Cesáreo, R., Hanson, A., Gigante, G., Pedraza, L., & Mathaboally, S. (1992). Interaction of keV photons with matter and new applications. *Physics Reports*, *213*(3), 117–178. https://doi.org/10.1016/0370-1573(92)90086-f.

[27]. Suetens, P. (2017). *Fundamentals of medical imaging*. https://doi.org/10.1017/9781316671849.

[28]. Wingerter-Seez, I. (2014). Particle Physics instrumentation. *HAL (Le Centre Pour La Communication Scientifique Directe)*. https://doi.org/10.23730/cyrsp-2017-002.295.

[29]. Podgorsak, E. (2005). *Radiation oncology physics: A handbook for teachers and students*. http://inis.iaea.org/search/search.aspx?orig_q=RN:36071456.

[30]. Bell, D. and Jones, J. (2008). Kerma. *Radiopaedia.org*. https://doi.org/10.53347/rid-5104.

[31]. Bluemke, D. A. and Liu, S. (2012). Imaging in clinical trials. In *Elsevier eBooks* (pp. 597–617). https://doi.org/10.1016/b978-0-12-382167-6.00041-2.

[32]. Guo, E., Zeng, G., Kazantsev, D., Rockett, P., et. al. (2017). Synchrotron X-ray tomographic quantification of microstructural evolution in ice cream - a multi-phase soft solid. *RSC Advances*, *7*(25), 15561–15573. https://doi.org/10.1039/c7ra00642j.

[33]. Morigi, M. P., Casali, F., Bettuzzi, M., Brancaccio, R. and D'Errico, V. (2010). Application of X-ray Computed Tomography to Cultural Heritage diagnostics. *Applied Physics A*, *100*(3), 653–661. https://doi.org/10.1007/s00339-010-5648-6.

[34]. McCollough, C. H., Bushberg, J. T., Fletcher, J. G., and Eckel, L. J. (2015). Answers to common questions about the use and safety of CT scans. *Mayo Clinic Proceedings*, *90*(10), 1380–1392. https://doi.org/10.1016/j.mayocp.2015.07.011.

[35]. Seeram, E. (2015). *Computed tomography: physical principles, clinical applications, and quality control*. (4th ed. ed.) Elsevier.

[36]. Kastner, J. and Heinzl, C. (2019). X-Ray tomography. In *Springer eBooks* (pp. 1095–1166). https://doi.org/10.1007/978-3-319-26553-7_5.

[37]. Withers, P. J. and Preuss, M. (2012). Fatigue and damage in structural materials studied by X-Ray tomography. *Annual Review of Materials Research*, *42*(1), 81–103. https://doi.org/10.1146/annurev-matsci-070511-155111.

[38]. Lowe, T., Garwood, R. J., Simonsen, T. J., Bradley, R. S. and Withers, P. J. (2013). Metamorphosis revealed: time-lapse three-dimensional imaging inside a living chrysalis. *Journal of the Royal Society Interface*, *10*(84), 20130304. https://doi.org/10.1098/rsif.2013.0304.

[39]. Van Offenwert, S., Cnudde, V., and Bultreys, T. (2019). Pore-Scale visualization and quantification of transient solute transport using fast microcomputed tomography. *Water Resources Research*, *55*(11), 9279–9291. https://doi.org/10.1029/2019wr025880.

[40]. Proudhon, H., Moffat, A., Sinclair, I., and Buffière, J. (2012). Three-dimensional characterisation and modelling of small fatigue corner cracks in high strength Al-alloys. *Comptes Rendus Physique*, *13*(3), 316–327. https://doi.org/10.1016/j.crhy.2011.12.005.

[41]. Finegan, D. P., Scheel, M., Robinson, J. B., Tjaden, B., et al. (2015). In-operando high-speed tomography of lithium-ion batteries during thermal runaway. *Nature Communications*, *6*(1). https://doi.org/10.1038/ncomms7924.

[42]. Als-Nielsen, J. and McMorrow, D. F. (2011). *Elements of modern X-ray physics*. https://doi.org/10.1002/9781119998365.

[43]. Sullivan, Louis H. (1896). "The Tall Office Building Artistically Considered". Lippincott's Magazine (March 1896): 403-409, https://archive.org/details/tallofficebuildi00sull.

[44]. Withers, P. J., Bouman, C. A., Carmignato, S., Cnudde, V., et. al. (2021). X-ray computed tomography. *Nature Reviews Methods Primers*, *1*(1). https://doi.org/10.1038/s43586-021-00015-4.

[45]. Stock, S. R. (2019). MicroComputed Tomography. In *CRC Press eBooks*. https://doi.org/10.1201/9780429186745.

[46]. Cengiz, I. F., Oliveira, J. M. and Reis, R. L. (2018). Micro-CT – a digital 3D microstructural voyage into scaffolds: a systematic review of the reported methods and results. *Biomaterials Research*, *22*(1). https://doi.org/10.1186/s40824-018-0136-8.

[47]. Aamodt, A., Kvistad, K. A., Andersen, E. A., Lund-Larsen, J., et. al. (1999). Determination of the Hounsfield value for CT-based design of custom femoral stems. *The Journal of Bone and Joint Surgery*, *81-B*(1), 143–147. https://doi.org/10.1302/0301-620x.81b1.0810143.

[48]. INTERNATIONAL ATOMIC ENERGY AGENCY. (2015). *Nuclear Medicine Physics*. IAEA. https://www.iaea.org/publications/10368/nuclear-medicine-physics.

[49]. Ebert, M. A. and Carruthers, B. (2003). Dosimetric characteristics of a low-kV intra-operative x-ray source: Implications for use in a clinical trial for treatment of low-risk breast cancer. *Medical Physics*, *30*(9), 2424–2431. https://doi.org/10.1118/1.1595611.

[50]. Boone, J. M. and Seibert, J. A. (1997). An accurate method for computer-generating tungsten anode x-ray spectra from 30 to 140 kV. *Medical Physics*, *24*(11), 1661–1670. https://doi.org/10.1118/1.597953.

[51]. McNitt-Gray, M. F. (2002). AAPM/RSNA Physics tutorial for residents: Topics in CT. *Radiographics*, *22*(6), 1541–1553. https://doi.org/10.1148/rg.226025128.

[52]. Taylor, R. E. P., Yeğin, G. and Rogers, D. W. O. (2006). TU-EE-A1-04: Monte Carlo modelling of the Xoft AXXENT X-Ray source. *Medical Physics*, *33*(6Part17), 2205. https://doi.org/10.1118/1.2241589.

[53]. Wernick, and Aarsvold, J. N. (2004). Emission tomography the fundamentals of PET and SPECT / [edited by] Miles N. Wernick, John N. Aarsvold. Elsevier Academic Press.

[54]. Anger, H. O. (1958). Scintillation camera. *Review of Scientific Instruments*, *29*(1), 27–33. https://doi.org/10.1063/1.1715998.

[55]. Kuhl, D. and Edwards, R.Q. (1963). Image Separation Radioisotope Scanning. *Radiology*, *80*, 653-662.

[56]. Jaszczak, R. (2006). The early years of single photon emission computed tomography (SPECT): an anthology of selected reminiscences. *Physics in Medicine and Biology*, *51*(13), R99–R115. https://doi.org/10.1088/0031-9155/51/13/r07.

[57]. Hutton, B. F. (2013). The origins of SPECT and SPECT/CT. *European Journal of Nuclear Medicine and Molecular Imaging*, *41*(S1), 3–16. https://doi.org/10.1007/s00259-013-2606-5.

[58]. *Physics in Nuclear Medicine - 4th Edition*. (2012). https://shop.elsevier.com/books/physics-in-nuclear-medicine/cherry/978-1-4160-5198-5.

[59]. Hasegawa, B., Gingold, E. L., Reilly, S. M., Liew, S. C. and Cann, C. E. (1990). Description of a simultaneous emission-transmission CT system. *Proceedings of SPIE*. https://doi.org/10.1117/12.18783.

[60]. Ljungberg, M. and Pretorius, P. H. (2018). SPECT/CT: an update on technological developments and clinical applications. *British Journal of Radiology*, *91*(1081), 20160402. https://doi.org/10.1259/bjr.20160402.

[61]. Themes, U. (2021, May 16). *Nuclear Imaging—The gamma camera*. Radiology Key. https://radiologykey.com/nuclear-imaging-the-gamma-camera/.

[62]. Van Audenhaege, K., Van Holen, R., Vandenberghe, S., Vanhove, C., et. al. (2015). Review of SPECT collimator selection, optimization, and fabrication for clinical and preclinical imaging. *Medical Physics*, *42*(8), 4796–4813. https://doi.org/10.1118/1.4927061.

[63]. Van Der Have, F., Vastenhouw, B., Ramakers, R. M., Branderhorst, W., et. al. (2009). U-SPECT-II: an Ultra-High-Resolution device for molecular Small-Animal imaging. *The Journal of Nuclear Medicine*, *50*(4), 599–605. https://doi.org/10.2967/jnumed.108.056606.

[64]. Bruyant, P. P. (2002, October 1). *Analytic and iterative reconstruction algorithms in SPECT*. Journal of Nuclear Medicine. https://jnm.snmjournals.org/content/43/10/1343/tab-article-info.

[65]. Shan, T., Alessio, A. M. and Kinahan, P. E. (2010b). Image reconstruction for PET/CT scanners: past achievements and future challenges. *Imaging in Medicine*, *2*(5), 529–545. https://doi.org/10.2217/iim.10.49

[66]. Barrett, H. H. (1984). III The Radon Transform and Its Applications. In *Progress in Optics* (pp. 217–286). https://doi.org/10.1016/s0079-6638(08)70123-9.

[67]. Radon, J. (1917). Uber die Bestimmung von Funktionen durch ihre Integralwerte langs gewissez Mannigfaltigheiten, Ber. *Verh. Sachs. Akad. Wiss. Leipzig, Math Phys Klass*, *69*.

[68]. Kak, A. and Slaney, M. (1988) Principles of computerized tomographic imaging. IEEE, New York.

[69]. Matej, S., and Lewitt, R. (1996). Practical considerations for 3-D image reconstruction using spherically symmetric volume elements. *IEEE Transactions on Medical Imaging*, *15*(1), 68–78. https://doi.org/10.1109/42.481442.

[70]. Ravi, M., Sewa, A., Shashidhar, T. G. and Sanagapati, S. S. S. (2019). FPGA as a hardware accelerator for computation intensive maximum likelihood expectation maximization medical Image Reconstruction algorithm. *IEEE Access*, *7*, 111727–111735. https://doi.org/10.1109/access.2019.2932647.

[71]. Yavuz, M. and Fessler, J. A. (1998). Statistical image reconstruction methods for randoms-precorrected PET scans. *Medical Image Analysis*, *2*(4), 369–378. https://doi.org/10.1016/s1361-8415(98)80017-0.

[72]. Bouman, C. A. and Sauer, K. D. (1996). A unified approach to statistical tomography using coordinate descent optimization. *IEEE Transactions on Image Processing*, *5*(3), 480–492. https://doi.org/10.1109/83.491321.

[73]. Fisher, R. a. S. (1921). *014: On the "Probable Error" of a Coefficient of Correlation Deduced from a Small Sample.* https://digital.library.adelaide.edu.au/dspace/handle/2440/15169.

[74]. H. L. Van Trees, "Detection, Estimation and Modulation Theory (Part I)," Wiley, New York, 1968.

[75]. Dempster, A. P., Laird, N. M. and Rubin, D. B. (1977). Maximum Likelihood from Incomplete Data via the EM Algorithm. *Journal of the Royal Statistical Society. Series B (Methodological)*, *39*(1), 1–38. http://www.jstor.org/stable/2984875.

[76]. Axelsson, O. (1994). *Iterative solution methods*. https://doi.org/10.1017/cbo9780511624100.

[77]. Shepp, L. and Vardi, Y. (1982). Maximum likelihood reconstruction for emission tomography. *IEEE Transactions on Medical Imaging*, *1*(2), 113–122. https://doi.org/10.1109/tmi.1982.4307558.

[78]. Hudson, H. M. and Larkin, R. (1994). Accelerated image reconstruction using ordered subsets of projection data. *IEEE Transactions on Medical Imaging*, *13*(4), 601–609. https://doi.org/10.1109/42.363108.

[79]. Klein, J. S., Brant, W. E., Vinson, E. N. and Helms, C. A. (2018). *Brant and Helms' fundamentals of Diagnostic Radiology*.

[80]. Stears, J. G., Felmlee, J. P. and Gray, J. (1986). Half-value-layer increase owing to tungsten buildup in the x-ray tube: fact or fiction. *Radiology*, *160*(3), 837–838. https://doi.org/10.1148/radiology.160.3.3737925.

[81]. Crișan, G., Moldovean-Cioroianu, N. S., Timaru, D., Andrieș, G., et. al. (2022). Radiopharmaceuticals for PET and SPECT Imaging: A Literature Review over the Last Decade. *International Journal of Molecular Sciences*, *23*(9), 5023. https://doi.org/10.3390/ijms23095023.

[82]. Lecoq, P. (2016). Development of new scintillators for medical applications. *Nuclear Instruments and Methods in Physics Research Section A: Accelerators, Spectrometers, Detectors and Associated Equipment*, *809*, 130–139. https://doi.org/10.1016/j.nima.2015.08.041.

[83]. Metropolis, N. (1987). The beginning. *Los Alamos Science*, *15*, 125-130.

[84]. Metropolis, N., & Ulam, S. M. (1949). The Monte Carlo method. *Journal of the American Statistical Association*, *44*(247), 335–341. https://doi.org/10.1080/01621459.1949.10483310.

[85]. Attig, N., Binder, K., Grubm, H. and Kremer, K. (2004). Computational soft matter: from synthetic polymers to proteins. *ResearchGate*. https://www.researchgate.net/publication/250209318_Computational_Soft_Matter_From_Synthetic_Polymers_to_Proteins/citations.

[86]. Siewerdsen, J. H. and Jaffray, D. A. (2001). Cone-beam computed tomography with a flat-panel imager: Magnitude and effects of x-ray scatter. *Medical Physics*, *28*(2), 220–231. https://doi.org/10.1118/1.1339879.

[87]. *Introduction to Monte Carlo simulation*. (2008, December 1). IEEE Conference Publication | IEEE Xplore. https://ieeexplore.ieee.org/document/4736059/.

[88]. Kroese, D. P., Brereton, T., Taimre, T. and Botev, Z. I. (2014). Why the Monte Carlo method is so important today. *Wiley Interdisciplinary Reviews: Computational Statistics*, *6*(6), 386–392. https://doi.org/10.1002/wics.1314.

[89]. Zellner, M., Abbas, A. E., Budescu, D. V. and Galstyan, A. (2021). A survey of human judgement and quantitative forecasting methods. *Royal Society Open Science*, *8*(2). https://doi.org/10.1098/rsos.201187.

[90]. Haghighat, A. (2020). Monte Carlo methods for particle transport. In *CRC Press eBooks*. https://doi.org/10.1201/9780429198397.

[91]. Nickgould. (2020). Monte Carlo Tutorial: Calculating PI. Kaggle. https://www.kaggle.com/code/nickgould/monte-carlo-tutorial-calculating-pi.

[92]. Knuth, D. E. (1998). *The Art of Computer Programming Volumes 1-3 Boxed Set* (2nd ed.). USA: Addison-Wesley Longman Publishing Co., Inc.

[93]. Bär, H. and Bopp, P. (1988). M. H. Kalos and P. A. Whitlock:Monte Carlo Methods, Volume I:Basics, John Wiley and Sons, New York, Chichester, Brisbane, Toronto and Singapore 1986, Library of Congress QA298.K35 1986. 186 Seiten mit einem Index, *Berichte Der Bunsengesellschaft Für Physikalische Chemie*. https://doi.org/10.1002/bbpc.198800128.

[94]. Lehmer, D. H. (1951). Mathematical methods in large-scale computing units. *In Proceedings of the Second Symposium on Large Scale Digital Computing Machinery,* Harvard University Press. 141-146.

[95]. Marsaglia, G., Zaman, A., and Tsang, W. P. (1990). Toward a universal random number generator. *Statistics & Probability Letters*, *9*(1), 35–39. https://doi.org/10.1016/0167-7152(90)90092-l.

[96]. L'Ecuyer, P. (1990). Random numbers for simulation. *Communications of the ACM*, *33*(10), 85–97. https://doi.org/10.1145/84537.84555.

[97]. L'Ecuyer, P. (1999). Good parameters and implementations for combined multiple recursive random number generators. *Operations Research*, *47*(1), 159–164. https://doi.org/10.1287/opre.47.1.159.

[98]. Jordán, D., Algora, A. and Taín, J. L. (2016). An event generator for simulations of complex β-decay experiments. *Nuclear Instruments and Methods in Physics Research Section A: Accelerators, Spectrometers, Detectors and Associated Equipment*, *828*, 52–57. https://doi.org/10.1016/j.nima.2016.05.034.

[99]. Sparapani, R. (2004). Random Number Generation and Monte Carlo Methods (Second Edition). *Journal of Statistical Software*, *11*(Book Review 8). https://doi.org/10.18637/jss.v011.b08.

[100]. Morin, R. L. (2019). Monte Carlo Simulation in the Radiological Sciences. In *CRC Press eBooks*. https://doi.org/10.1201/9780429277085.

[101]. Burington, R. S. and May, D. C., Jr. (1954). Handbook of Probability and Statistics, with Tables. *Soil Science*, *77*(3). Retrieved from https://journals.lww.com/soilsci/fulltext/1954/03000/handbook_of_probability_and_statistics,_with.12.aspx.

[102]. Murphy, K. P. (2012). *Machine learning: a probabilistic perspective*. MIT press.

[103]. Lewis, E E, and Miller, W F. *Computational methods of neutron transport*. United States.https://www.amazon.com/Computational-Methods-Neutron-Transport-Hardcover/dp/B015X4FO76

[104]. Vassiliev, O. N. (2017). Monte Carlo methods for radiation transport. In *Biological and medical physics series*. https://doi.org/10.1007/978-3-319-44141-2.

[105]. *Enterprise Open Source and Linux | Ubuntu*. (2023). Ubuntu. https://ubuntu.com/.

[106]. *Oracle VM VirtualBox*. (2023). https://www.virtualbox.org/.

[107]. *Windows VM | WorkStation Pro | VMware*. (2023). VMware. https://www.vmware.com/products/workstation-pro.html.

[108]. Microsoft Contributors (2023). *Install WSL*. Microsoft Learn. https://learn.microsoft.com/en-us/windows/wsl/install.

[109]. Microsoft Store *GWSL*. (2023). Microsoft Apps. https://apps.microsoft.com/detail/gwsl/9NL6KD1H33V3?hl=en-us&gl=GR.

[110]. Bigelow, S. J. (2023). operating system (OS). *WhatIs.com*. https://www.techtarget.com/whatis/definition/operating-system-OS.

[111]. Wikipedia contributors. (2023, September 29). Bash (Unix shell). In *Wikipedia, The Free Encyclopedia*. Retrieved 09:46, October 10, 2023, from https://en.wikipedia.org/w/index.php?title=Bash_(Unix_shell)&oldid=1177761988.

[112]. Siever, E., Figgins, S., Love, R. and Robbins, A. (2009). Linux in a Nutshell. Retrieved from https://books.google.gr/books?id=YM28wAEACAAJ.

[113]. Kitware *CMAKE*. (2023). https://cmake.org/.

[114]. Schneider, C. A., Rasband, W. and Eliceiri, K. W. (2012). NIH Image to ImageJ: 25 years of image analysis. *Nature Methods*, *9*(7), 671–675. https://doi.org/10.1038/nmeth.2089.

[115]. *Kaggle: your machine learning and data science community*. (2023). https://www.kaggle.com/.

[116]. *Zenodo - Research. shared.* (2023). https://zenodo.org/.

[117]. Chatzisavvas, N., Priniotakis, G., Papoutsidakis, M., Nikolopoulos, D., Valais, I., and Karpetas G. (2021). Monte Carlo Computational software and methods in radiation dosimetry. *Annals of Emerging Technologies in Computing.*, *5*(3), 36–51. https://doi.org/10.33166/aetic.2021.03.004.

[118]. Šolc, J., Jakůbek, J., Marek, L., Oancea, C., et. al. (2022). Monte Carlo modelling of pixel clusters in Timepix detectors using the MCNP code. *Physica Medica*, *101*, 79–86. https://doi.org/10.1016/j.ejmp.2022.08.002.

[119]. Kawrakow I, Rogers DWO, Mainegra-Hing E, Tessier F, et. al. (2000). EGSnrc toolkit for Monte Carlo simulation of ionizing radiation transport, https://doi.org/10.4224/40001303.

[120]. Hoff, G., Streck, E. E., Lai, A., Fanti, V., et. al. (2021). Using Geant4 Monte Carlo toolkit to evaluate a low power X-ray tube generator configuration. *Applied Radiation and Isotopes*, *168*, 109487. https://doi.org/10.1016/j.apradiso.2020.109487.

[121]. Perl, J., Shin, J., Schümann, J., Faddegon, B. A., & Paganetti, H. (2012). TOPAS: An innovative proton Monte Carlo platform for research and clinical applications. *Medical Physics*, *39*(11), 6818–6837. https://doi.org/10.1118/1.4758060.

[122]. Sarrut, D., Arbor, N., Baudier, T., Borys, D., et. al. (2022). The OpenGATE ecosystem for Monte Carlo simulation in medical physics. *Physics in Medicine and Biology*, *67*(18), 184001. https://doi.org/10.1088/1361-6560/ac8c83.

[123]. Zain, J. A., Bardouni, T. E., Mohammed, M. and Hajjaji, O. E. (2019). Validation of GAMOS code based on Geant4 Monte Carlo for a 12 MV Saturne43 Linac. *Journal of King Saud University - Science*, *31*(4), 500–505. https://doi.org/10.1016/j.jksus.2018.07.003.

[124]. Li, J. (2020). MoNTe CarLO Investigation of the UK's first EPR nuclear reactor startup core using Serpent. *Energies*, *13*(19), 5168. https://doi.org/10.3390/en13195168.

[125]. Romano, P. K., Horelik, N., Herman, B., Nelson, A. G., Forget, B. and Smith, K. (2015). OpenMC: A state-of-the-art Monte Carlo code for research and development. *Annals of Nuclear Energy*, *82*, 90–97. https://doi.org/10.1016/j.anucene.2014.07.048.

[126]. Ford, R. L. and Nelson, W. R. *The EGS Code System: Computer Programs for the Monte Carlo Simulation of Electromagnetic Cascade Showers (Version 3)*. United States. https://doi.org/10.2172/1104725.

[127]. Nelson, W. R., Hirayama, H. and Rogers, D. W. (1985). *EGS4 code system* (No. SLAC-265). Stanford Linear Accelerator Center, Menlo Park, CA (USA).

[128]. Bielajew, A. F. and Rogers, D. W. O. (1986). Presta: The parameter reduced electron-step transport algorithm for electron monte carlo transport. *Nuclear Instruments and Methods in Physics Research Section B: Beam Interactions With Materials and Atoms*, *18*(1–6), 165–181. https://doi.org/10.1016/s0168-583x(86)80027-1.

[129]. Kawrakow, I. (1996). Electron transport: multiple and plural elastic scattering. *Nuclear Instruments and Methods in Physics Research Section B: Beam Interactions With Materials and Atoms*, *108*(1–2), 23–34. https://doi.org/10.1016/0168-583x(95)01046-7.

[130]. Bielajew, A. F. (1996). A hybrid multiple-scattering theory for electron-transport Monte Carlo calculations. *Nuclear Instruments and Methods in Physics Research Section B: Beam Interactions With Materials and Atoms*, *111*(3–4), 195–208. https://doi.org/10.1016/0168-583x(95)01337-7.

[131]. Hideo H., Yoshihito N., Bielajew, T., Wilderman, A. F. et. al. *The EGS5 Code System*. United States. https://doi.org/10.2172/877459.

[132]. Kawrakow, I. (2000). Accurate condensed history Monte Carlo simulation of electron transport. I. EGSnrc, the new EGS4 version. *Medical Physics*, *27*(3), 485–498. https://doi.org/10.1118/1.598917.

[133]. Chatzisavvas, N. (2020, October 15). *EGSNRCmp on Ubuntu 20.04 Installation tutorial* [Video]. YouTube. https://www.youtube.com/watch?v=t3OW-q9wR6M.

[134]. Nrc-Cnrc. (2023). *Installation overview*. GitHub. https://github.com/nrc-cnrc/EGSnrc/wiki/Installation-overview.

[135]. Almatani, T. (2021). Validation of a 10 MV photon beam Elekta Synergy linear accelerator using the BEAMnrc MC code. *Journal of King Saud University - Science*, *33*(4), 101406. https://doi.org/10.1016/j.jksus.2021.101406.

[136]. Mesbahi, A., and Zakariaee, S. S. (2013). Effect of anode angle on photon beam spectra and depth dose characteristics for X-RAD320 orthovoltage unit. *Reports of Practical Oncology & Radiotherapy*, *18*(3), 148–152. https://doi.org/10.1016/j.rpor.2012.12.001.

[137]. Chatzisavvas, N., Nikolopoulos, D., Priniotakis, G., Valais, I., Koustas, T., & Karpetas G. (2023b). Monte Carlo Simulation of Cone X-ray Beam and Dose Scoring on Voxel Phantom with Open Source Software EGSnrcmp. *Annals of Emerging Technologies in Computing.*, *7*(2), 23–34. https://doi.org/10.33166/aetic.2023.02.003.

[138]. Mainegra-Hing, E., & Kawrakow, I. (2006). Efficient x-ray tube simulations. *Medical Physics*, *33*(8), 2683–2690. https://doi.org/10.1118/1.2219331.

[139]. Ma C. M. and Rogers D. W. “BEAMDP Users Manual, Technical Report PIRS–0509c”, Ottawa, Canada, National Research Council of Canada, 2021.

[140]. Brinkert, T. (2015) Grace User’s Guide (for Grace-5.1.25). Semibyte Srls, Provincia di Prato.

[141]. Ma, C.M., Rogers, D. W. and Walters, B. (2010). DOSXYZnrc users manual. *NRC Report PIRS 794 (Rev B)*.

[142]. Jun M., Cheng G., Yixin W., Xingle A., et.al. (2020). COVID-19 CT Lung and Infection Segmentation Dataset (Verson 1.0) [Data set]. Zenodo. https://doi.org/10.5281/zenodo.3757476.

[143]. *Patient Contributed Image Repository (PCIR)*. (2023). http://www.pcir.org/index.html.

[144]. Bilic, P., Christ, P. F., Vorontsov, E., Chlebus, G., et. al. (2023). The Liver Tumor Segmentation Benchmark (LITS). *Medical Image Analysis*, *84*, 102680. https://doi.org/10.1016/j.media.2022.102680.

[145]. Kawrakow I. (2018). “The dose visualization tool dosxyz_show Technical Report”. *NRC Report PIRS 0624*.

[146]. McGowan H.C.E., Faddegon B.A. and Ma C.M. (2023). STATDOSE for 3D dose distributions, Technical Report. *NRC Report PIRS 0509f*.

[147]. Sarrut, D., Bardiès, M., Boussion, N., Freud, N., et. al. (2014). A review of the use and potential of the GATE Monte Carlo simulation code for radiation therapy and dosimetry applications. *Medical Physics*, *41*(6Part1), 064301. https://doi.org/10.1118/1.4871617.

[148]. Jan, S., Santin, G., Strul, D., Staelens, S., et. al. (2004). GATE: a simulation toolkit for PET and SPECT. *Physics in Medicine and Biology*, *49*(19), 4543–4561. https://doi.org/10.1088/0031-9155/49/19/007.

[149]. Didi, S., Moussa, A., Tayalati, Y. and Zerfaoui, M. (2015). Simulation of the 6 MV Elekta Synergy Platform linac photon beam using Geant4 Application for Tomographic Emission. *Journal of Medical Physics*, *40*(3), 136. https://doi.org/10.4103/0971-6203.165077.

[150]. Brun, R., and Rademakers, F. (1997). ROOT — An object oriented data analysis framework. *Nuclear Instruments and Methods in Physics Research Section A: Accelerators, Spectrometers, Detectors and Associated Equipment*, *389*(1–2), 81–86. https://doi.org/10.1016/s0168-9002(97)00048-x.

[151]. Allison, J., Amako, K., Apostolakis, J., Arce, P., et. al. (2016). Recent developments in Geant4. *Nuclear Instruments and Methods in Physics Research Section A: Accelerators, Spectrometers, Detectors and Associated Equipment*, *835*, 186–225. https://doi.org/10.1016/j.nima.2016.06.125.

[152]. Sandberg, I., Aminalragia-Giamini, S., Papadimitriou, C., Van Gijlswijk, R., et. al. (2022). First results and analysis from ESA next generation Radiation Monitor Unit

onboard EDRS-C. *IEEE Transactions on Nuclear Science*, *69*(7), 1549–1556. https://doi.org/10.1109/tns.2022.3160108.

[153]. Incerti, S., Kyriakou, I., Bernal, M. A., Bordage, M., et. al. (2018). Geant4-DNA example applications for track structure simulations in liquid water: A report from the Geant4-DNA Project. *Medical Physics*, *45*(8). https://doi.org/10.1002/mp.13048.

[154]. Chatzisavvas N. (2020). *Geant - Gatev9 on Ubuntu 20.04 installation tutorial* [Video]. YouTube. https://youtu.be/mwc8MNjP8pU.

[155]. Gate Contributors. GATE documentation. (2023). *OpenGate Collaboration*. *Retrieved from*: https://opengate.readthedocs.io/en/latest/index.html.

[156]. Islamian, J. P., Toossi, M. T. B., Momennezhad, M., Naseri, S. and Ljungberg, M. (2012). Simulation of a Quality Control Jaszczak Phantom with SIMIND Monte Carlo and Adding the Phantom as an Accessory to the Program. *DOAJ (DOAJ: Directory of Open Access Journals)*. https://doi.org/10.22038/ijmp.2012.319.

[157]. Kang, H., Tashima, H., Hong, S. and Yamaya, T. (2018). Optimization of a High Resolution Small Animal SPECT System using GATE and STIR Software. In *2018 IEEE Nuclear Science Symposium and Medical Imaging Conference Proceedings (NSS/MIC)* (pp. 1-3). https://doi.org/10.1109/NSSMIC.2018.8824511.

[158]. Efthimiou, N., Brown, R., Tsoumpas, C., Deidda, D., et. al. (2022). STIR: Software for Tomographic Image Reconstruction (rel_5.0.2). Zenodo. https://doi.org/10.5281/zenodo.6604468.

[159]. University College London Contributors. (2023). *GitHub - UCL/STIR: software for tomographic image reconstruction*. GitHub. https://github.com/UCL/STIR.

[160]. Loening, A. M. and Gambhir, S. S. (2003). AMIDE: a free software tool for multimodality medical image analysis. *Molecular Imaging*, *2*(3), 153535002003031. https://doi.org/10.1162/15353500200303133.

[161]. Thompson, A. and Vaughan, D., Center for X-ray Optics (Lawrence Berkeley National Laboratory), Center for X-ray optics, advanced light source, & Lawrence Berkeley National Laboratory. Advanced Light Source (2009). *X-ray Data Booklet*. Lawrence Berkeley National Laboratory, University of California.

Appendix1: CT simulation results

Appendix 1 consists of EGSNRC runs results. Due to the very big file of Appendix 1 it was cut down into 5 separate documents. Appendix1 has 4900 images and each file has the beam characteristic charts, the Dosimetric map Slices for all cases and energies and Dose profiles for 6 organs for each case and energy. Each file contains 5 energies for each case of the two target materials, so each file contains 980 images, at 300pdi image quality, each image. For all data are presented in a particular order:

a. BEAMnrc Graphs: Includes 25W target beams, 25AU target beams, and energies between 30keV – 150keV with step 5keV. 50Beams in total with each beam having 6 charts. So initially 50beams*6charts=300 images, have been generated.
b. Phantoms Dosimetric Map Slices: After the beams creation begins the irradiation with those 50Beams of the three phantoms, (Chest, Abdomen and Brain) created from anonymous personalized dicom images. For each case: 50beams*86slices per energy for all 3 cases =4300 images.
c. Dose Profiles: For 6 organs from all three cases. 50 beams * 6 organs = 300 images.

Appendix2: Compilation and Installation Technical Report

Technical Report for:

Installation of EGSNRCmp, GATE v9.0, STIR v4.0 extra commands

Installation environment UBUNTU 20.04.

1. Add repositories:

```
sudo add-apt-repository main

sudo add-apt-repository universe

sudo add-apt-repository restricted

sudo add-apt-repository multiverse
```

2. Install packages:

```
sudo apt update && sudo apt upgrade

sudo apt install linux-headers-$(uname -r) dkms

sudo apt install apt-transport-https binutils build-essential ca-certificates cmake cmake-curses-gui curl dpkg-dev emacs evince g++ gcc geany gedit gfortran gimp git gnome-tweaks grace graphviz-dev libavahi-compat-libdnssd-dev libboost-dev libcfitsio-dev libfftw3-dev libftgl-dev libglew-dev libglew1.5-dev libgsl0-dev libinsighttoolkit4-dev libkrb5-dev libldap2-dev libmotif-dev libmysqlclient-dev libncurses-dev libpcre3-dev libpng-dev libssl-dev libtbb-dev libtiff5-dev libvtk7-qt-dev libvtk7.1p libvtk7.1p-qt libx11-dev libxext-dev libxft-dev libxml2-dev libxmu-dev libxpm-dev make mayavi2 mpi-default-bin mpi-default-dev octave okular openjdk-11-jdk p7zip-full p7zip-rar python python-dev python-numpy python3-dev qpdfview qt5-default qt5-qmake qtbase5-dev qtbase5-dev-tools qtchooser rar socket software-properties-common swig tcsh ubuntu-restricted-extras unrar vlc vtk7 vtk7-doc vtk7-examples vtkdata wine winetricks xlibmesa-glu-dev
```

GATE Installation:

Video Tutorial made in University of West Attica:

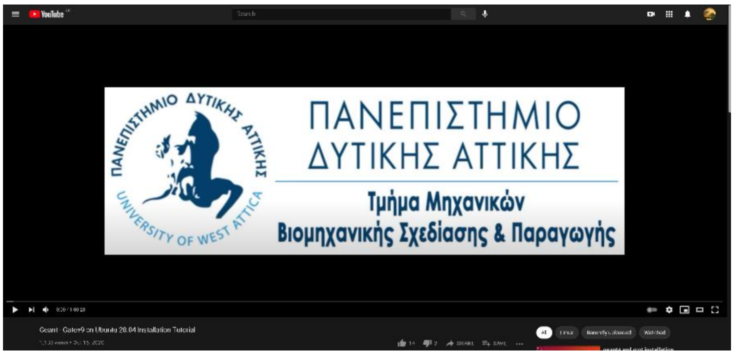
YouTube
Search
ΠΑΝΕΠΙΣΤΗΜΙΟ ΔΥΤΙΚΗΣ ΑΤΤΙΚΗΣ
UNIVERSITY OF WEST ATTICA
ΠΑΝΕΠΙΣΤΗΜΙΟ
ΔΥΤΙΚΗΣ ΑΤΤΙΚΗΣ
Τμήμα Μηχανικών
Βιομηχανικής Σχεδίασης & Παραγωγής
Geant - Gatev9 on Ubuntu 20.04 Installation Tutorial
SHARE
SAVE
All
Watched

YouTube url: : https://youtu.be/mwc8MNjP8pU

Programs and Versions:

GATE version 9.0

Geant4 version 10.06.p02

ROOT version 6.22.02

InsightToolkit version 5.1.1

Libtorch Version cxx11-abi-shared-with-deps-1.4.0+cpu

Lmf version 3

Ecat version 7

Kindly unzip all files and .tar.gz files to one directory GATE90 and send the files inside that.

Compilation process:

1.GEANT4:

```
cd where_your_folder_for GATE_is/GATEv9 (mostly /home/username make a folder called GATE90 – suggestion not mandatory)
```

```
mkdir geant4_10_06-build
```

```
mkdir geant4_10_06-install
```

```
cd geant4_10_06-build
```

```
cmake -DCMAKE_INSTALL_PREFIX= where_your_folder_for GATE_is/GATE90/geant4.10.06.p02-install where_your_folder_for GATE_is/GATE90/geant4.10.06.p02 -DGEANT4_INSTALL_DATA=ON -DGEANT4_USE_OPENGL_X11=ON -DGEANT4_USE_XM=ON -DGEANT4_USE_QT=ON
```

```
after make –j4 (for 4 threads)
```

```
make install
```

```
source /where_your_folder_for GATE_is /GATE90/geant4_10_06-install/bin/geant4.sh
```

2. ROOT:

```
cd /where_your_folder_for GATE_is /GATE90/
```

```
mkdir root-6.20.02-build
```

```
mkdir root-6.20.02-install
```

```
cd root-6.20.02-build
```

```
cmake -DCMAKE_INSTALL_PREFIX=/where_your_folder_for GATE_is /GATE90/root-6.20.02-install /where_your_folder_for GATE_is /GATE90/root-6.20.02
```

```
cmake –build . -- -j4
```

```
make install
```

```
source /where_your_folder_for GATE_is /GATE90/root-6.20.02-install/bin/thisroot.sh
```

3.ECAT7 fixes:

Before modify:

utils/matlist.c --> #include <stdlib.h> #include <stdio.h>

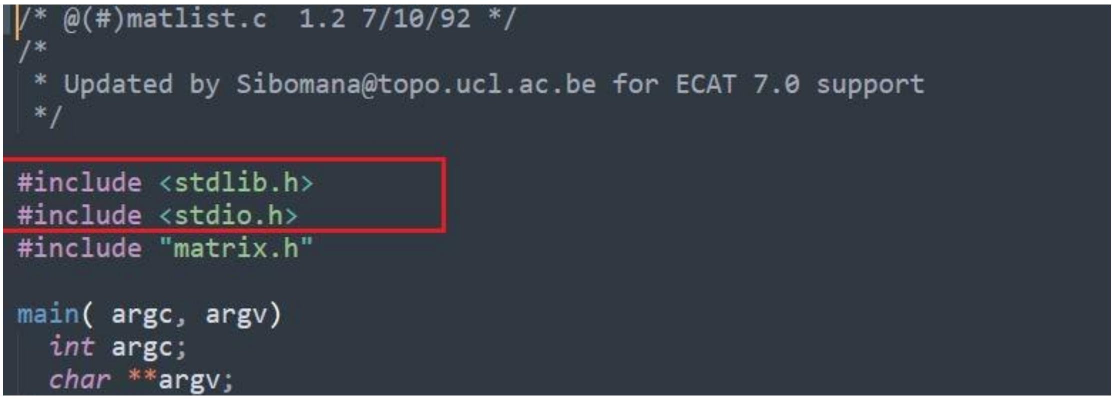

```
/* @(#)matlist.c  1.2 7/10/92 */
/*
 * Updated by Sibomana@topo.ucl.ac.be for ECAT 7.0 support
 */

#include <stdlib.h>
#include <stdio.h>
#include "matrix.h"

main( argc, argv)
  int argc;
  char **argv;
```

utils/show_header.c --> #include <math.h> #include <string.h> #include <stdlib.h> and at 189 line change: mh->dosage

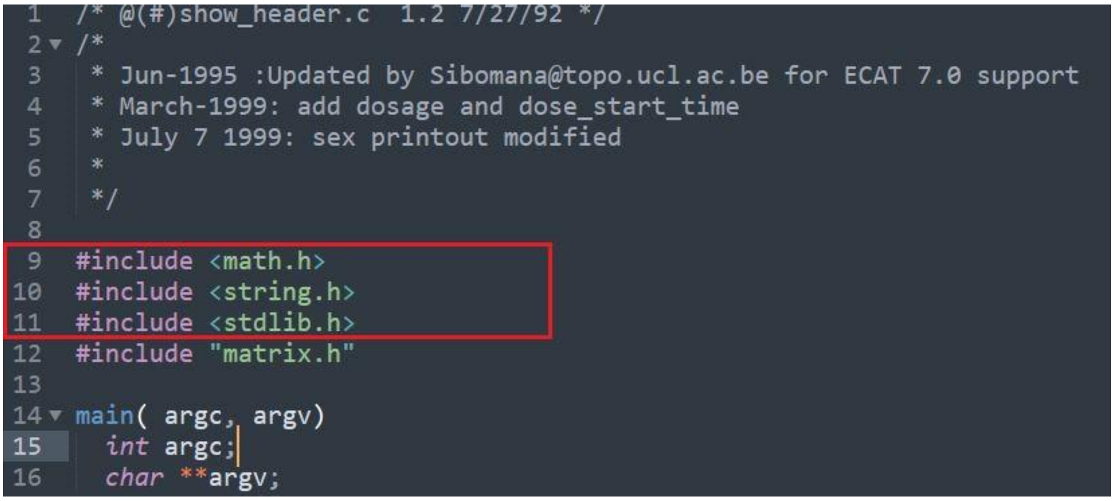

```
/* @(#)show_header.c  1.2 7/27/92 */
/*
 * Jun-1995 :Updated by Sibomana@topo.ucl.ac.be for ECAT 7.0 support
 * March-1999: add dosage and dose_start_time
 * July 7 1999: sex printout modified
 *
 */

#include <math.h>
#include <string.h>
#include <stdlib.h>
#include "matrix.h"

main( argc, argv)
  int argc;
  char **argv;
```

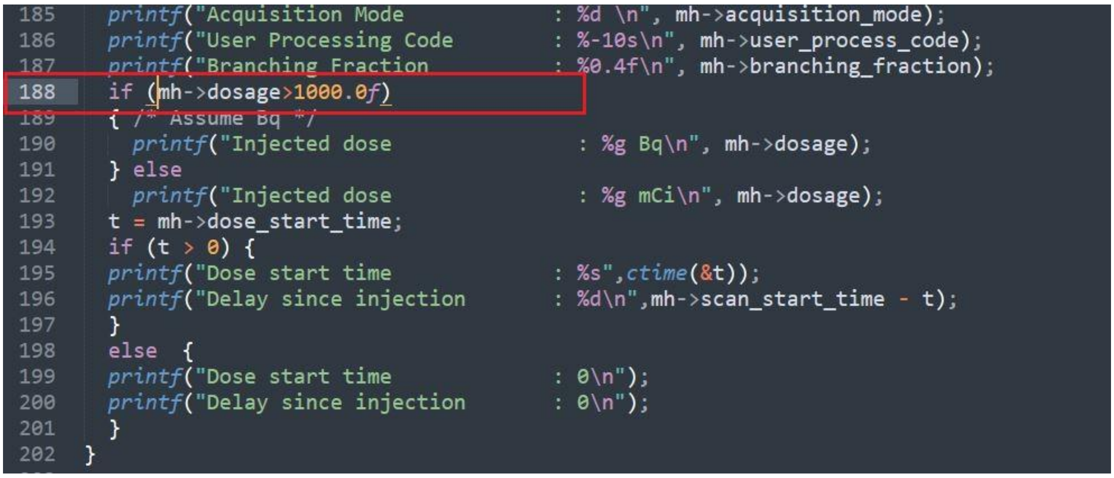

```
185    printf("Acquisition Mode             : %d \n", mh->acquisition_mode);
186    printf("User Processing Code         : %-10s\n", mh->user_process_code);
187    printf("Branching Fraction           : %0.4f\n", mh->branching_fraction);
188    if (mh->dosage>1000.0f)
189    { /* Assume Bq */
190      printf("Injected dose                : %g Bq\n", mh->dosage);
191    } else
192      printf("Injected dose                : %g mCi\n", mh->dosage);
193    t = mh->dose_start_time;
194    if (t > 0) {
195    printf("Dose start time              : %s",ctime(&t));
196    printf("Delay since injection        : %d\n",mh->scan_start_time - t);
197    }
198    else  {
199    printf("Dose start time              : 0\n");
200    printf("Delay since injection        : 0\n");
201    }
202  }
```

utils/applynorm.c --> #include <string.h> and line 87 #include <math.h>

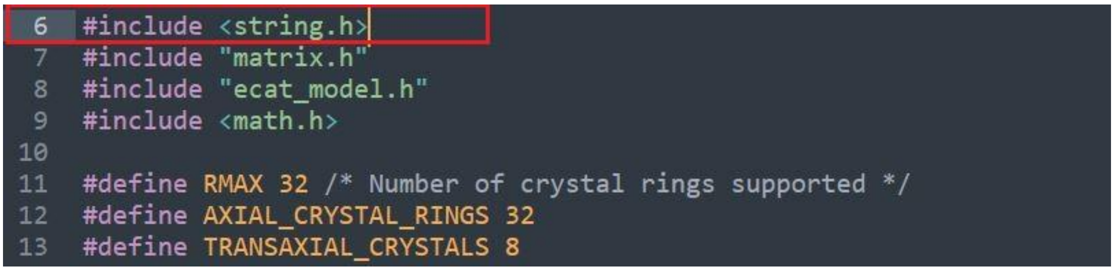

```
6   #include <string.h>
7   #include "matrix.h"
8   #include "ecat_model.h"
9   #include <math.h>
10
11  #define RMAX 32 /* Number of crystal rings supported */
12  #define AXIAL_CRYSTAL_RINGS 32
13  #define TRANSAXIAL_CRYSTALS 8
```

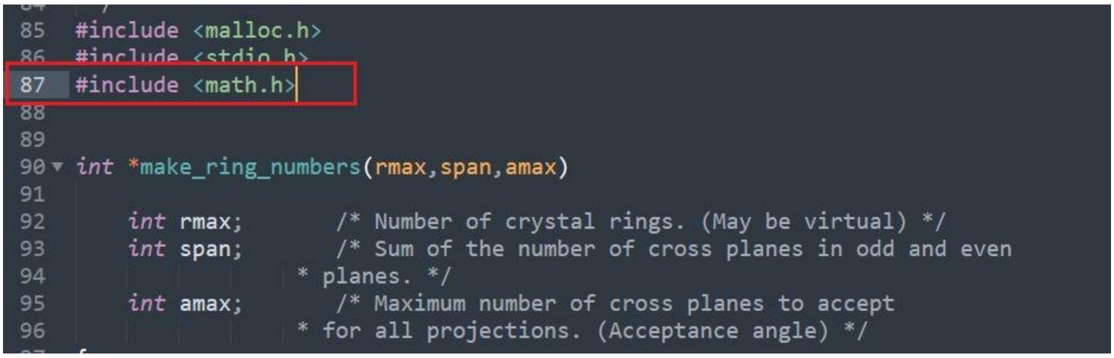

```
85  #include <malloc.h>
86  #include <stdio.h>
87  #include <math.h>
88
89
90  int *make_ring_numbers(rmax,span,amax)
91
92      int rmax;         /* Number of crystal rings. (May be virtual) */
93      int span;         /* Sum of the number of cross planes in odd and even
94                      * planes. */
95      int amax;         /* Maximum number of cross planes to accept
96                      * for all projections. (Acceptance angle) */
```

rts_cmd.c -->line 176 cfree => free

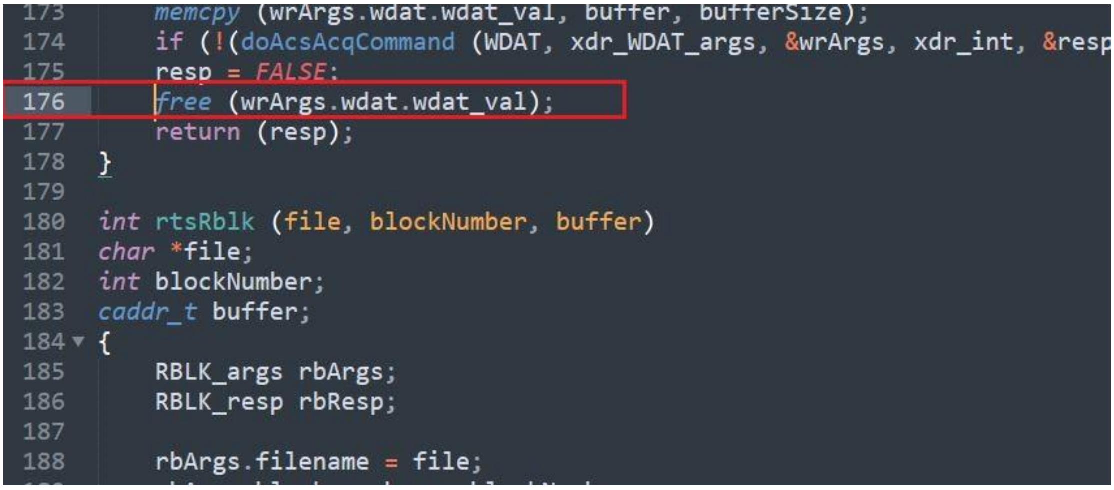

```
173         memcpy (wrArgs.wdat.wdat_val, buffer, bufferSize);
174         if (!(doAcsAcqCommand (WDAT, xdr_WDAT_args, &wrArgs, xdr_int, &resp
175         resp = FALSE;
176         free (wrArgs.wdat.wdat_val);
177         return (resp);
178     }
179
180     int rtsRblk (file, blockNumber, buffer)
181     char *file;
182     int blockNumber;
183     caddr_t buffer;
184     {
185         RBLK_args rbArgs;
186         RBLK_resp rbResp;
187
188         rbArgs.filename = file;
```

```
cp Makefile.unix Makefile

make

mkdir include

cp *.h /where_your_folder_for GATE_is /GATE90 /ecat7/include/

mkdir lib

cp libecat.a lib/

cd utils

cp Makefile.unix Makefile

make -f Makefile LIBS=-lm
```

4.LMF_3 fixes:

make changes to files where you see *gets -> gets

src/correctUnknownField.c

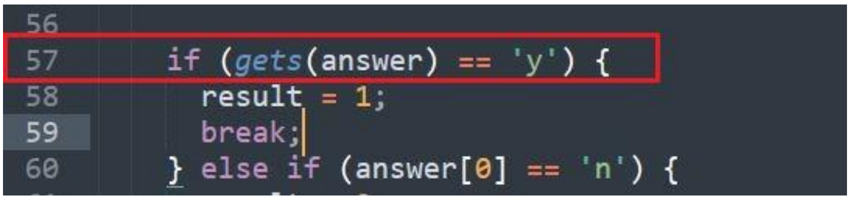

```

    if (gets(answer) == 'y') {
      result = 1;
      break;
    } else if (answer[0] == 'n') {
```

src/newFieldInCchFile.c

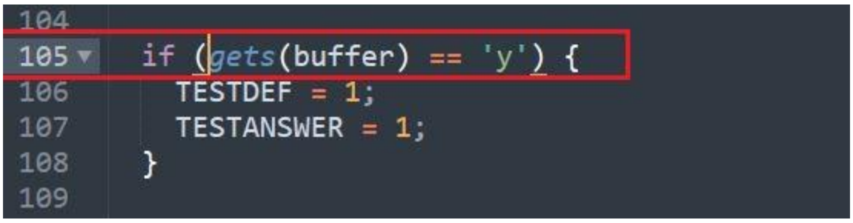

```

  if (gets(buffer) == 'y') {
    TESTDEF = 1;
    TESTANSWER = 1;
  }

```

src/fileNameManager.c

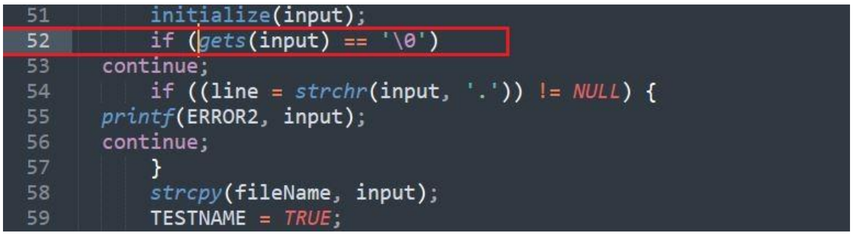

```
        initialize(input);
        if (gets(input) == '\0')
    continue;
        if ((line = strchr(input, '.')) != NULL) {
    printf(ERROR2, input);
    continue;
        }
        strcpy(fileName, input);
        TESTNAME = TRUE;
```

src/editLMF_cchInfo.c

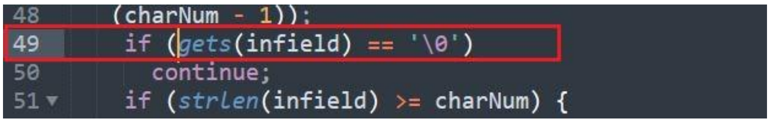

```
    (charNum - 1));
     if (gets(infield) == '\0')
       continue;
     if (strlen(infield) >= charNum) {
```

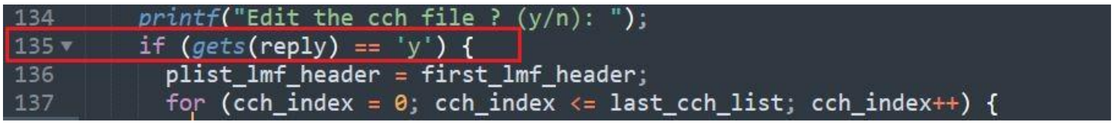

```
    printf("Edit the cch file ? (y/n): ");
    if (gets(reply) == 'y') {
      plist_lmf_header = first_lmf_header;
      for (cch_index = 0; cch_index <= last_cch_list; cch_index++) {
```

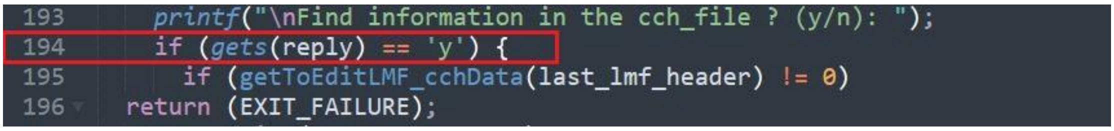

```
    printf("\nFind information in the cch_file ? (y/n): ");
    if (gets(reply) == 'y') {
      if (getToEditLMF_cchData(last_lmf_header) != 0)
return (EXIT_FAILURE);
```

src/testField.c

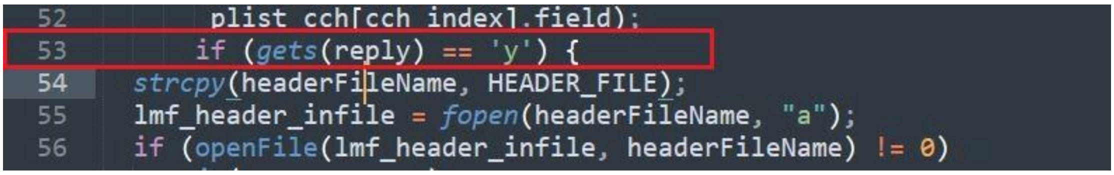

```
          plist_cch[cch_index].field);
        if (gets(reply) == 'y') {
strcpy(headerFileName, HEADER_FILE);
lmf_header_infile = fopen(headerFileName, "a");
if (openFile(lmf_header_infile, headerFileName) != 0)
```

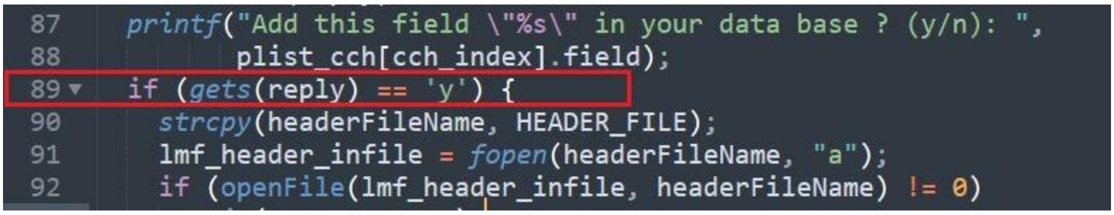

```
printf("Add this field \"%s\" in your data base ? (y/n): ",
        plist_cch[cch_index].field);
if (gets(reply) == 'y') {
  strcpy(headerFileName, HEADER_FILE);
  lmf_header_infile = fopen(headerFileName, "a");
  if (openFile(lmf_header_infile, headerFileName) != 0)
```

./configure

make clean

make

5. ITK

Go inside the ITK folder with the source code

mkdir build

mkdir bin

cd build

ccmake -DITK_USE_REVIEW=ON ..

"press c to generate once first generation is complete then press t and turn on Module_RTK=ON, then press g "

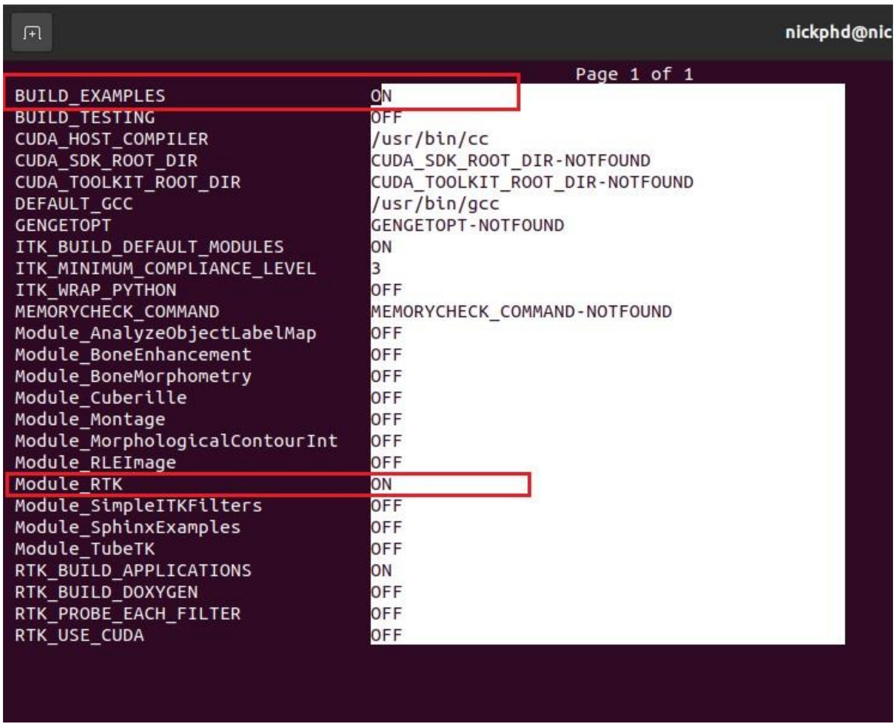

```
                                               Page 1 of 1
BUILD_EXAMPLES                  ON
BUILD_TESTING                   OFF
CUDA_HOST_COMPILER              /usr/bin/cc
CUDA_SDK_ROOT_DIR               CUDA_SDK_ROOT_DIR-NOTFOUND
CUDA_TOOLKIT_ROOT_DIR           CUDA_TOOLKIT_ROOT_DIR-NOTFOUND
DEFAULT_GCC                     /usr/bin/gcc
GENGETOPT                       GENGETOPT-NOTFOUND
ITK_BUILD_DEFAULT_MODULES       ON
ITK_MINIMUM_COMPLIANCE_LEVEL    3
ITK_WRAP_PYTHON                 OFF
MEMORYCHECK_COMMAND             MEMORYCHECK_COMMAND-NOTFOUND
Module_AnalyzeObjectLabelMap    OFF
Module_BoneEnhancement          OFF
Module_BoneMorphometry          OFF
Module_Cuberille                OFF
Module_Montage                  OFF
Module_MorphologicalContourInt  OFF
Module_RLEImage                 OFF
Module_RTK                      ON
Module_SimpleITKFilters         OFF
Module_SphinxExamples           OFF
Module_TubeTK                   OFF
RTK_BUILD_APPLICATIONS          ON
RTK_BUILD_DOXYGEN               OFF
RTK_PROBE_EACH_FILTER           OFF
RTK_USE_CUDA                    OFF
```

press t and specify the INSTALL_PREFIX to the forlder /where_your_folder_for GATE_is /GATE90/PATH_TO_ITK/bin

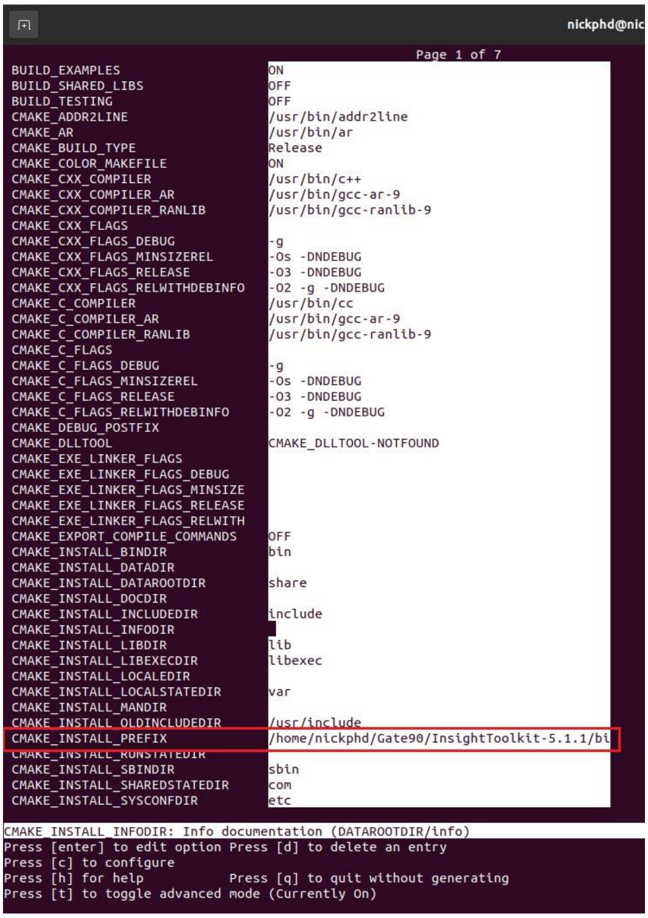

```
                                               Page 1 of 7
BUILD_EXAMPLES                   ON
BUILD_SHARED_LIBS                OFF
BUILD_TESTING                    OFF
CMAKE_ADDR2LINE                  /usr/bin/addr2line
CMAKE_AR                         /usr/bin/ar
CMAKE_BUILD_TYPE                 Release
CMAKE_COLOR_MAKEFILE             ON
CMAKE_CXX_COMPILER               /usr/bin/c++
CMAKE_CXX_COMPILER_AR            /usr/bin/gcc-ar-9
CMAKE_CXX_COMPILER_RANLIB        /usr/bin/gcc-ranlib-9
CMAKE_CXX_FLAGS
CMAKE_CXX_FLAGS_DEBUG            -g
CMAKE_CXX_FLAGS_MINSIZEREL       -Os -DNDEBUG
CMAKE_CXX_FLAGS_RELEASE          -O3 -DNDEBUG
CMAKE_CXX_FLAGS_RELWITHDEBINFO   -O2 -g -DNDEBUG
CMAKE_C_COMPILER                 /usr/bin/cc
CMAKE_C_COMPILER_AR              /usr/bin/gcc-ar-9
CMAKE_C_COMPILER_RANLIB          /usr/bin/gcc-ranlib-9
CMAKE_C_FLAGS
CMAKE_C_FLAGS_DEBUG              -g
CMAKE_C_FLAGS_MINSIZEREL         -Os -DNDEBUG
CMAKE_C_FLAGS_RELEASE            -O3 -DNDEBUG
CMAKE_C_FLAGS_RELWITHDEBINFO     -O2 -g -DNDEBUG
CMAKE_DEBUG_POSTFIX
CMAKE_DLLTOOL                    CMAKE_DLLTOOL-NOTFOUND
CMAKE_EXE_LINKER_FLAGS
CMAKE_EXE_LINKER_FLAGS_DEBUG
CMAKE_EXE_LINKER_FLAGS_MINSIZE
CMAKE_EXE_LINKER_FLAGS_RELEASE
CMAKE_EXE_LINKER_FLAGS_RELWITH
CMAKE_EXPORT_COMPILE_COMMANDS    OFF
CMAKE_INSTALL_BINDIR             bin
CMAKE_INSTALL_DATADIR
CMAKE_INSTALL_DATAROOTDIR        share
CMAKE_INSTALL_DOCDIR
CMAKE_INSTALL_INCLUDEDIR         include
CMAKE_INSTALL_INFODIR
CMAKE_INSTALL_LIBDIR             lib
CMAKE_INSTALL_LIBEXECDIR         libexec
CMAKE_INSTALL_LOCALEDIR
CMAKE_INSTALL_LOCALSTATEDIR      var
CMAKE_INSTALL_MANDIR
CMAKE_INSTALL_OLDINCLUDEDIR      /usr/include
CMAKE_INSTALL_PREFIX             /home/nickphd/Gate90/InsightToolkit-5.1.1/bi
CMAKE_INSTALL_RUNSTATEDIR
CMAKE_INSTALL_SBINDIR            sbin
CMAKE_INSTALL_SHAREDSTATEDIR     com
CMAKE_INSTALL_SYSCONFDIR         etc

CMAKE_INSTALL_INFODIR: Info documentation (DATAROOTDIR/info)
Press [enter] to edit option Press [d] to delete an entry
Press [c] to configure
Press [h] for help           Press [q] to quit without generating
Press [t] to toggle advanced mode (Currently On)
```

make –j4

```
make install
```

6. Libtorch

You only have to unzip the files and in the cmake panel you need to:

specify the path to libtorch/share/cmake/Torch

specify the path to libtorch/share/cmake/Caffe2/public

7. GATE

```
mkdir GATE_90-build
```

```
mkdir GATE_90-install
```

```
cd GATE_90-build
```

```
ccmake ../GATE_90
```

turn on the libraries as RTK

correct the installation path

turn on ecat7 and specify the path to ecat7 inside ccmake panel

turn on lmf_3_0 and specify the path to lmf_3_0 inside ccmake panel

specify the path to libtorch/share/cmake/Torch

specify the path to libtorch/share/cmake/Caffe2/public

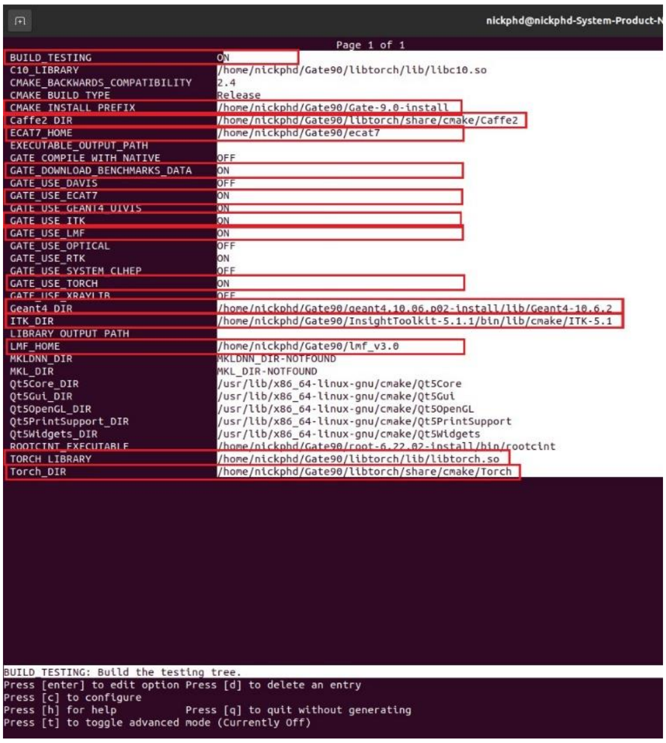

```
                                   Page 1 of 1
 BUILD_TESTING                    ON
 C10_LIBRARY                      /home/nickphd/Gate90/libtorch/lib/libc10.so
 CMAKE_BACKWARDS_COMPATIBILITY    2.4
 CMAKE_BUILD_TYPE                 Release
 CMAKE_INSTALL_PREFIX             /home/nickphd/Gate90/Gate-9.0-install
 Caffe2_DIR                       /home/nickphd/Gate90/libtorch/share/cmake/Caffe2
 ECAT7_HOME                       /home/nickphd/Gate90/ecat7
 EXECUTABLE_OUTPUT_PATH
 GATE_COMPILE_WITH_NATIVE         OFF
 GATE_DOWNLOAD_BENCHMARKS_DATA    ON
 GATE_USE_DAVIS                   OFF
 GATE_USE_ECAT7                   ON
 GATE_USE_GEANT4_UIVIS            ON
 GATE_USE_ITK                     ON
 GATE_USE_LMF                     ON
 GATE_USE_OPTICAL                 OFF
 GATE_USE_RTK                     ON
 GATE_USE_SYSTEM_CLHEP            OFF
 GATE_USE_TORCH                   ON
 GATE_USE_XRAYLIB                 OFF
 Geant4_DIR                       /home/nickphd/Gate90/geant4.10.06.p02-install/lib/Geant4-10.6.2
 ITK_DIR                          /home/nickphd/Gate90/InsightToolkit-5.1.1/bin/lib/cmake/ITK-5.1
 LIBRARY_OUTPUT_PATH
 LMF_HOME                         /home/nickphd/Gate90/lmf_v3.0
 MKLDNN_DIR                       MKLDNN_DIR-NOTFOUND
 MKL_DIR                          MKL_DIR-NOTFOUND
 Qt5Core_DIR                      /usr/lib/x86_64-linux-gnu/cmake/Qt5Core
 Qt5Gui_DIR                       /usr/lib/x86_64-linux-gnu/cmake/Qt5Gui
 Qt5OpenGL_DIR                    /usr/lib/x86_64-linux-gnu/cmake/Qt5OpenGL
 Qt5PrintSupport_DIR              /usr/lib/x86_64-linux-gnu/cmake/Qt5PrintSupport
 Qt5Widgets_DIR                   /usr/lib/x86_64-linux-gnu/cmake/Qt5Widgets
 ROOTCINT_EXECUTABLE              /home/nickphd/Gate90/root-6.22.02-install/bin/rootcint
 TORCH_LIBRARY                    /home/nickphd/Gate90/libtorch/lib/libtorch.so
 Torch_DIR                        /home/nickphd/Gate90/libtorch/share/cmake/Torch

BUILD_TESTING: Build the testing tree.
Press [enter] to edit option Press [d] to delete an entry
Press [c] to configure
Press [h] for help           Press [q] to quit without generating
Press [t] to toggle advanced mode (Currently Off)
```

```
make –j4

make install

export PATH=/home/nickphd/GATE82/GATE_v8_2-install/bin:$PATH
```

7.1 compile jobsplitter and filemerger

```
cd /where_your_folder_for GATE_is /GATE90/GATE_90/cluster_tools/jobsplitter

make

cp /where_your_folder_for GATE_is /GATE90/GATE_90/cluster_tools/jobsplitter/gjs
/where_your_folder_for GATE_is /GATE90/GATE_90-install/bin


cd /where_your_folder_for GATE_is /GATE90/GATE_90/cluster_tools/filemerger

make

cp /where_your_folder_forGATE_is/GATE90/GATE_90/cluster_tools/filemerger/gjm
/where_your_folder_for GATE_is /GATE90/GATE_90-install/bin
```

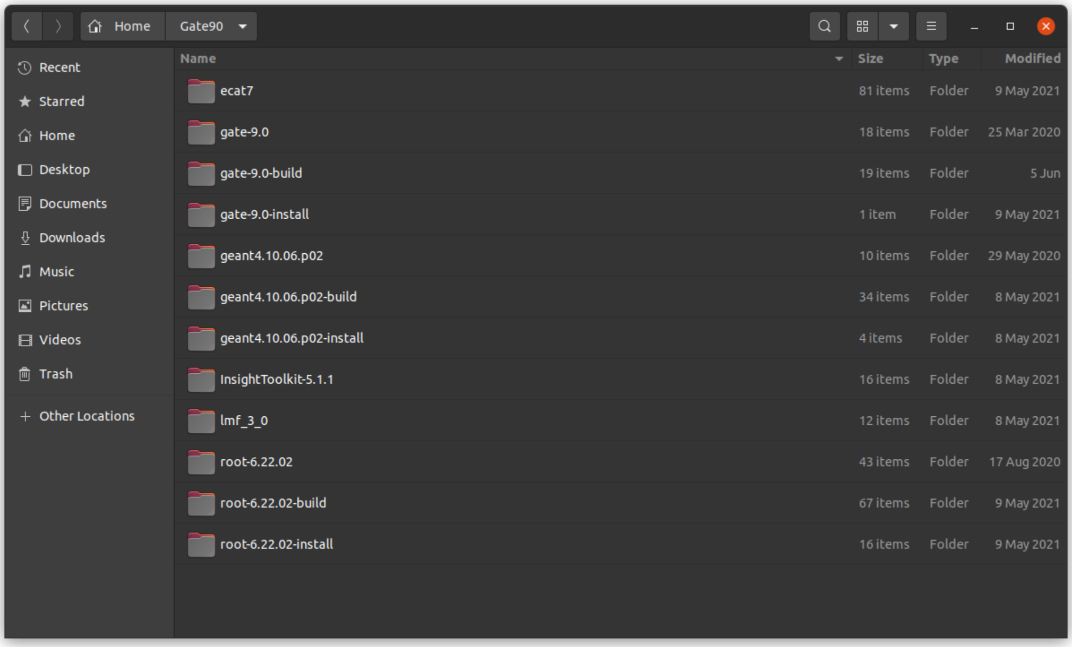

Name	Size	Type	Modified
ecat7	81 items	Folder	9 May 2021
gate-9.0	18 items	Folder	25 Mar 2020
gate-9.0-build	19 items	Folder	5 Jun
gate-9.0-install	1 item	Folder	9 May 2021
geant4.10.06.p02	10 items	Folder	29 May 2020
geant4.10.06.p02-build	34 items	Folder	8 May 2021
geant4.10.06.p02-install	4 items	Folder	8 May 2021
InsightToolkit-5.1.1	16 items	Folder	8 May 2021
lmf_3_0	12 items	Folder	8 May 2021
root-6.22.02	43 items	Folder	17 Aug 2020
root-6.22.02-build	67 items	Folder	9 May 2021
root-6.22.02-install	16 items	Folder	9 May 2021

All files without the prefix –build or –install are the extraction of the source code from the packages, ecat7, lmf3, GATE, geant4, root, InsightToolkit.

In order to run GATE you need to source some files:

```
#Geant

source /where_your_folder_forGATE_is/GATE90/geant4.10.06.p02-install/bin/geant4.sh
```

```
#ROOT

source /where_your_folder_forGATE_is/GATE90/root-6.22.02-install/bin/thisroot.sh

#GATE 9.0

export PATH=$PATH:/where_your_folder_forGATE_is/GATE90/GATE-9.0-install/bin
```

Afterwards you can run GATE on your terminal.

EGSNRCmp Installation:

Video Tutorial made in University of West Attica:

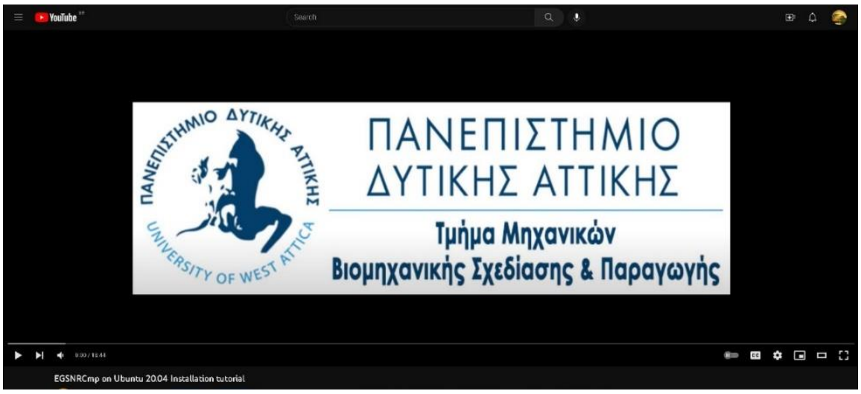
YouTube
Search
ΠΑΝΕΠΙΣΤΗΜΙΟ ΔΥΤΙΚΗΣ ΑΤΤΙΚΗΣ
UNIVERSITY OF WEST ATTICA
ΠΑΝΕΠΙΣΤΗΜΙΟ
ΔΥΤΙΚΗΣ ΑΤΤΙΚΗΣ
Τμήμα Μηχανικών
Βιομηχανικής Σχεδίασης & Παραγωγής
EGSNRCmp on Ubuntu 20.04 Installation tutorial

YouTube url: https://youtu.be/t3OW-q9wR6M

Test compilers and prerequisite software:

```
gfortran --version

gcc --version

g++ --version

make --version

echo 'puts [info patchlevel]; exit 0' | wish

grace -version

xmgrace
```

Clone the github repository from github inside the folder that you want to put EGSnrc installation folder.

```
git clone https://github.com/nrc-cnrc/EGSnrc.git

cd EGSnrc/

export HEN_HOUSE="" EGS_HOME="" EGS_CONFIG=""
export QTDIR=/usr/lib/qt5/

export QT_SELECT=qt5

./HEN_HOUSE/scripts/configure
```

After configuration kindly press 3 to compile all

After put inside .bashrc file the following:

```
export EGS_HOME=WHERE_YOUR_EGS_directory_IS/EGSnrc/egs_home/

export EGS_CONFIG= WHERE_YOUR_EGS_directory_IS/EGSnrc/HEN_HOUSE/specs/linux.conf

source WHERE_YOUR_EGS_directory_IS/EGSnrc/HEN_HOUSE/scripts/egsnrc_bashrc_additions
```

after compilation, compile guis

```
cd $HEN_HOUSE

cd egs++/view/

make clean

make

cd $HEN_HOUSE

cd gui/

make clean

make
```

STIR Installation:

Download the STIR-stir_rel_4.0.0.zip from the github page.
https://github.com/UCL/STIR/releases/tag/stir_rel_4.0.0

Make a folder TOOLS

Inside unzip the STIR_rel_4.0.0

If you want to use ecat7 for the STIR kindly follow the instructions for STIR with Ecat7, change:

files : src/IO/stir_ecat7.cxx

src/include/stir/listmode/CListRecordECAT962.h src/include/stir/listmode/CListRecordECAT962.h

https://github.com/UCL/STIR/pull/581/commits/46f347b604e0e11a60af42a4519411b9c11065e3

make a ecat7_stir directory inside TOOLS folder (same folder as STIR-bin and STIR-rel_4.0.0 follow the instructions about ecat7 for GATE but compile using :

```
make -f Makefile.unix CC="gcc -fPIC"

cd utils/

make -f Makefile.unix CC="gcc -fPIC" LIBS=-lm
```

On the same directory make a folder STIR-bin and inside the STIR-bin make a Release directory.

```
mkdir STIR-bin

cd STIR-bin

mkdir Release

cd Release

ccmake ../../STIR
```

inside the ccmake put ON BUILD_SWIG_PYTHON, BUILD_TESTING, define root directory, leave ITK4.13

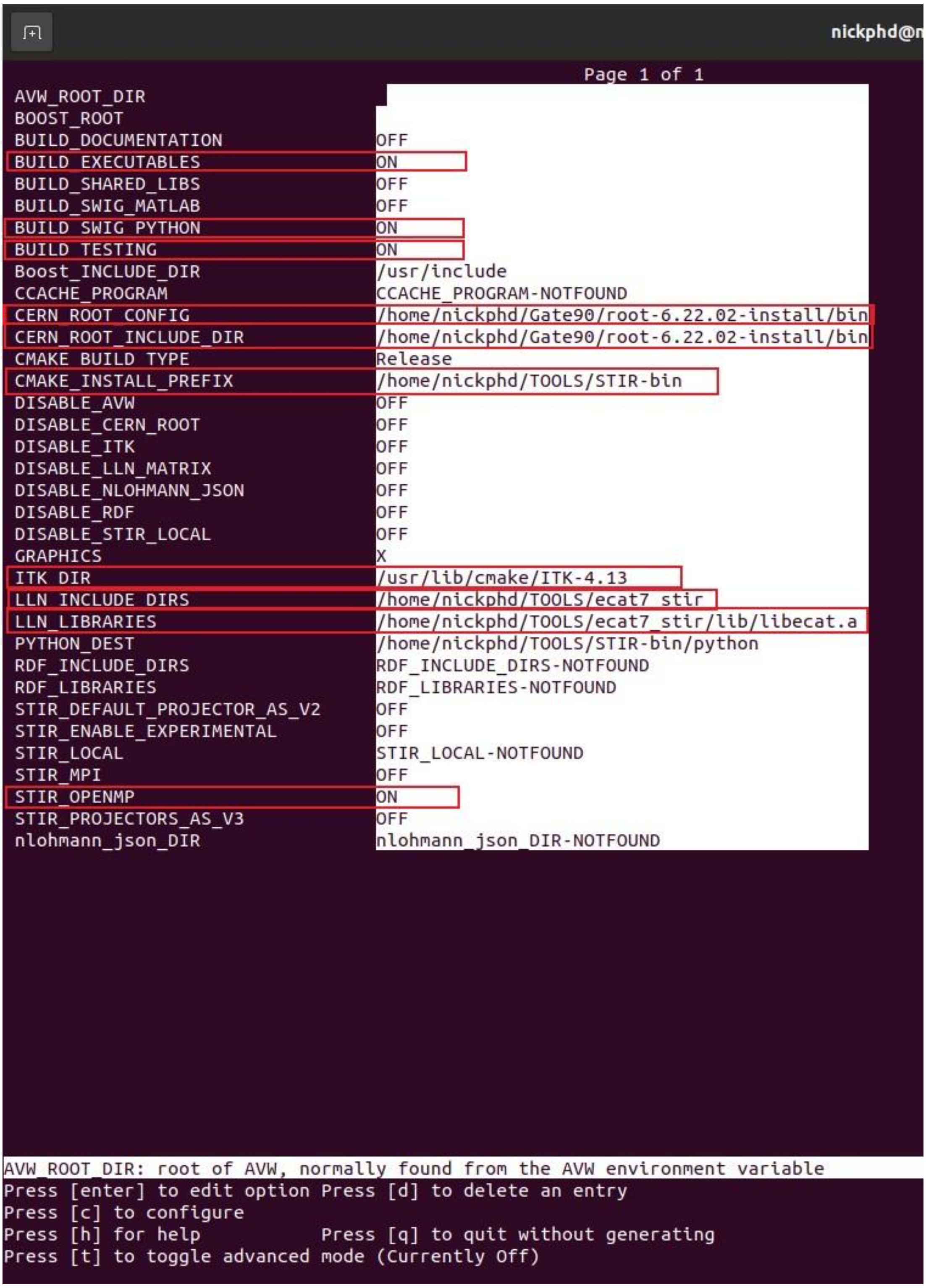

```
                                                     Page 1 of 1
 AVW_ROOT_DIR
 BOOST_ROOT
 BUILD_DOCUMENTATION              OFF
 BUILD EXECUTABLES                ON
 BUILD_SHARED_LIBS                OFF
 BUILD_SWIG_MATLAB                OFF
 BUILD SWIG PYTHON                ON
 BUILD TESTING                    ON
 Boost_INCLUDE_DIR                /usr/include
 CCACHE_PROGRAM                   CCACHE_PROGRAM-NOTFOUND
 CERN ROOT CONFIG                 /home/nickphd/Gate90/root-6.22.02-install/bin
 CERN_ROOT_INCLUDE_DIR            /home/nickphd/Gate90/root-6.22.02-install/bin
 CMAKE BUILD TYPE                 Release
 CMAKE_INSTALL_PREFIX             /home/nickphd/TOOLS/STIR-bin
 DISABLE_AVW                      OFF
 DISABLE_CERN_ROOT                OFF
 DISABLE_ITK                      OFF
 DISABLE_LLN_MATRIX               OFF
 DISABLE_NLOHMANN_JSON            OFF
 DISABLE_RDF                      OFF
 DISABLE_STIR_LOCAL               OFF
 GRAPHICS                         X
 ITK DIR                          /usr/lib/cmake/ITK-4.13
 LLN INCLUDE DIRS                 /home/nickphd/TOOLS/ecat7 stir
 LLN_LIBRARIES                    /home/nickphd/TOOLS/ecat7_stir/lib/libecat.a
 PYTHON_DEST                      /home/nickphd/TOOLS/STIR-bin/python
 RDF_INCLUDE_DIRS                 RDF_INCLUDE_DIRS-NOTFOUND
 RDF_LIBRARIES                    RDF_LIBRARIES-NOTFOUND
 STIR_DEFAULT_PROJECTOR_AS_V2     OFF
 STIR_ENABLE_EXPERIMENTAL         OFF
 STIR_LOCAL                       STIR_LOCAL-NOTFOUND
 STIR_MPI                         OFF
 STIR_OPENMP                      ON
 STIR_PROJECTORS_AS_V3            OFF
 nlohmann_json_DIR                nlohmann_json_DIR-NOTFOUND

AVW_ROOT_DIR: root of AVW, normally found from the AVW environment variable
Press [enter] to edit option Press [d] to delete an entry
Press [c] to configure
Press [h] for help           Press [q] to quit without generating
Press [t] to toggle advanced mode (Currently Off)
```

In order to pass all test, you must source ROOT:

#ROOT

source /where_your_folder_forGATE_is/GATE90/root-6.22.02-install/bin/thisroot.sh

Compile with:

make -j4

```
make test
```

```
make install
```

After the installation update the .bashrc file as follows:

```
#STIR

export PATH=$PATH:PATH_TO_STIR_FOLDER/TOOLS/STIR-bin/bin

export LD_LIBRARY_PATH=$LD_LIBRARY_PATH: PATH_TO_STIR_FOLDER
/TOOLS/STIR-bin/lib
```

Appendix3: SPECT-heads simulations Results.

Appendix 3 consists of GATE-STIR runs results. Due to the size of the file, Appendix3 has its own external file. It includes 5 runs for the AnyScan SPECT study and simulation and 3 runs for the SmallAnimal SPECT study. For each SPECT Head study for the first run an investigation is taking place to determine the best iterations {1,2,5,10,100} and subsets {1,2,4,8,16,32} settings for the OSMAPOSL reconstruction algorithm. For the first run in each case, 30 reconstructions OSMAPOSL and 1 reconstruction with FBP are being carried out. For the other cases, 1 plus 1 reconstructions for OSMAPOSL and FBP are being carried out respectively. For each GATE run the Singles detected - Spatial Distributions in XYZ axis, the Singles - Energy Distribution and the Sinogram detected by the head detector are being viewed. Therefore, all 8 simulation have 31*2 + 6*2 = 74 reconstructions. Each reconstruction contains 3 images of view slices for transverse, sagittal and coronal views, plus 1 more image containing the Volume Rendering image slice. Altogether, the Appendix contains 74*4 + 8*5 = 336 images.

Appendix4: Source Code.

Appendix 4 contains all the code routines of the BEAMnrc, DOSXYZnrc, GATE Simulations and STIR reconstruction that were utilized in order to produce the results presented in this thesis. Due to the size of the file, Appendix4 has its own external file.

Author's Curriculum Vitae

NIKOLAOS N. CHATZISAVVAS

Born 19/06/1990|Greek and Russian Nationality |Male |

CONTACT INFO

Address: Athens, Greece.
Tel.: 0030 697 66 17 192
email: nikolaos.chatzisavvas@gmail.com

EDUCATION

University of West Attica

PhD Candidate

Department of Industrial Design & Production – School of Engineering, FEB 2020-Present

Technological Education Institute of Athens

Master of Science

Department of Electronic Engineering, 2013-2016 **Grade 8.3**

Technological Education Institute of Piraeus

Bachelor of Engineering

Electronic Computer Systems Engineer, 2008-2013 **Grade 7.55**

CURRENT STATUS

Current research activities involve the following fields:

(a) Monte Carlo modelling of *dosimetry* via (b1) custom codes, (b2) EGSnrcmp, (b3) GATE and (b4) TOPAS

(b) Monte Carlo modelling of *Radiotherapy Medical Accelerators* with BEAMnrc and TOPAS

(c) x-ray and optical measurements for the *evaluation* of new medical imaging scintillators in SPECT.

(d) Optimization and evaluation of Monte Carlo scenarios for further experimentation in the fields of brachytherapy and proton therapy.

PUBLICATIONS

7 full papers in International **peer-reviewed Journals**

11 publications in Conference Proceedings

In specific, the publications are as follows:

(a) Papers

1. D.Nikolopoulos, S. Kottou, **N. Chatzisavvas**, X Argyriou, E. Vlamakis, P Yannakopoulos, A Louizi,“A GATE Simulation Study of the Siemens Biograph DUO PET/CT System, Open Journal of Radiology, 2013.

2. Simone D’Incecco , Piero Di Carlo , Eleonora Aru'o , **Nikolaos Chatzisavvas**, Ermioni Petraki , Georgios Priniotakis , Ioannis Voyiatzis, Panayiotis H. Yannakopoulos and Dimitrios Nikolopoulos, Fractal Dimension Analysis Applied to Soil CO2 Fluxes in Campotosto’s Seismic Area, Central Italy, MDPI geosciences 2020.

3. Simone D’Incecco, Ermioni Petraki, **Nikolaos Chatzisavvas**, Demetrios Cantzos, Panayiotis Yannakopoulos, Georgios Priniotakis and Dimitrios Nikolopoulos, CO2 and radon emissions as precursors of seismic activity, Bulletin of Russian academy of natural sciences, 2020.

4. Nikolaos Chatzisavvas, Georgios Priniotakis, Michael Papoutsidakis, Dimitrios Nikolopoulos, Ioannis Valais and Georgios Karpetas, Monte Carlo Computational Software and Methods in Radiation Dosimetry, Annals of Emerging Technologies in Computing (AETiC), 2021.

5. Nikolaos Chatzisavvas, Thanasis Koustas, Georgios Karpetas, Ioannis Valais, Georgios Priniotakis, Dimitrios Nikolopoulos, Simulating Medical Imaging x-ray tubes with various parameters using BEAMnrc Monte Carlo Software, Open Journal of Radiology, 2022.

6. Nikolaos Chatzisavvas, Dimitrios Nikolopoulos, Georgios Priniotakis, Thanasis Koustas, Georgios Karpetas, Ioannis Valais, Generating CT x-rays and score dosimetric quantities on DICOM-based phantom utilizing Open Source Monte Carlo Software, International Journal of Computer Engineering and Sciences Research, 2022.

7. Nikolaos Chatzisavvas, Dimitrios Nikolopoulos, Georgios Priniotakis, Ioannis Valais, Thanasis Koustas, Georgios Karpetas, Monte Carlo Simulation of Cone x-ray Beam and Dose Scoring on Voxel Phantom with Open Source Software EGSnrcmp, Annals of Emerging Technologies in Computing (AETiC), 2023.

(b) Conference proceedings

8. N. Chatzisavvas, T. Sevvos, E. Vlamakis, A. A. Fotopoulos, X. Argyriou, X. Tsantilas, D. Nikolopoulos, P.H. Yannakopoulos, S. Kottou, A. Louizi, Impact of detector's thickness on imaging characteristics of the Siemens Biograph DUO PET/CT with GATE, eRA-7 International Scientific Conference, Technological Education Institute of Piraeus, Greece, 2012 September 28.

9. T. Sevvos, A. A. Fotopoulos, E. Vlamakis, X. Argyriou, **N. Chatzisavvas**, A. Efdaimon, K. Vagennas, P.H. Yannakopoulos, I. Valais, I. Kandarakis, D. Nikolopoulos, Monte Carlo comparison study of the radiation absorption of scintillators for use in Diagnostic Radiology and Nuclear Medicine Applications, eRA-7 International Scientific Conference, Technological Education Institute of Piraeus, Greece, 2012 September 28.

10. E. Vlamakis, X. Argyriou, T. Sevvos, A. A. Fotopoulos, **N. Chatzisavvas** P.H. Yannakopoulos, N. Kalyvas, I. Valais, I. Kandarakis, D. Nikolopoulos, Semi-empirical Monte Carlo optical-gain modeling of Nuclear Imaging scintillators, eRA-7 International Scientific Conference, Technological Education Institute of Piraeus, Greece, 2012 September 28,.

11. A. A. Fotopoulos, E. Petraki, E. Vlamakis, X. Argyriou, T. Sevvos, **N. Chatzisavvas**, A. Zisos, C. Nomicos, A. Louizi, J. Stonham, P.H. Yannakopoulos, D. Nikolopoulos , Similarities in the self-organised critical characteristics between soil radon and MHz electromagnetic disturbances during a very seismic period in Greece, eRA-7 International Scientific Conference, Technological Education Institute of Piraeus, Greece, 2012 September 28.

12. A. A. Fotopoulos, E. Petraki, E. Vlamakis, X. Argyriou, T. Sevvos, **N. Chatzisavvas**, A. Zisos, C. Nomicos, A. Louizi, J. Stonham, P.H. Yannakopoulos, D. Nikolopoulos Environmental monitoring of soil radon in a very tectonic area in South West Greece, eRA-7 International Scientific Conference, Technological Education Institute of Piraeus, Greece, 2012 September 28.

13. T. Sevvos, X. Argyriou, **N. Chatzisavvas**, N. Temenos, Y. Chaldeos, S. Filtisakos, N. Gorgolis, S. Potozi, E. Petraki, D. Koulougliotis, S. Kottou, P. Yannakopoulos, D. Nikolopoulos, A. Zisos Study of the response of open CR-39 detector to radon and progeny by Monte Carlo simulation with SRIM, eRA-8 International Scientific Conference, Technological Education Institute of Piraeus, Greece, 2013.

14. X. Argyriou, T. Sevvos, **N. Chatzisavvas**, N. Temenos, Y. Chaldeos, S. Filtisakos, N. Gorgolis, S. Potozi, E. Petraki, D. Koulougliotis, S. Kottou, P. Yannakopoulos, D. Nikolopoulos, A.Zisos, Long-term estimation of radon's equilibrium factor and radon progeny unattached fraction with SSNTDs through measurements and Monte-Carlo modeling, eRA-8 International Scientific Conference, Technological Education Institute of Piraeus, Greece, 2013.

15. D. Nikolopoulos, E. Petraki, D. Koulougliotis, S. Kottou, A.Louizi, P. Yannakopoulos, E. Vogiannis, S. Filtisakos, N. Gorgolis, X. Argyriou, T. Sevvos, N. Temenos, Y. Chaldeos, S. Potozi, G. Kefalas, R. S. Lorilla, **N. Chatzisavvas**, A. Zisos, Human radiation risk of due to radon and progeny: results from extended active measurements in Attica (Greece), eRA-8 International Scientific Conference, Technological Education Institute of Piraeus, Greece, 2013.

16. D. Nikolopoulos, E. Petraki, T. Sevvos, Y. Chaldeos, X. Argyriou, S. Filtisakos, N. Gorgolis, N. Temenos, G. Kefalas, R. S. Lorilla, S. Potozi, **N. Chatzisavvas**, D. Koulougliotis, S. Kottou, A.Louizi, P. Yannakopoulos, A. Zisos, Factors affecting indoor radon and progeny concentration variations in Attica (Greece), eRA-8 International Scientific Conference, Technological Education Institute of Piraeus, Greece, 2013.

17. N. Chatzisavvas, D. Nikolopoulos, I. Valais, N. Kalyvas, X. Argyriou, T. Sevvos, S. Kottou, P. Yannakopoulos, I. Kandarakis, GATE simulation of the Biograph 2 PET/CT scanner, eRA-8 International Scientific Conference, Technological Education Institute of Piraeus, Greece, 2013.

18. Nikolaos Chatzisavvas, Thanasis Koustas, Georgios Karpetas, Ioannis Valais, Georgios Priniotakis, Dimitrios Nikolopoulos, Investigation of x-ray tube target material, anode angle and filter at 120keV and 30keV using Monte Carlo, (poster) 1st Panhellenic Congress of Medical Physics, Athens, 23-25 September, 2022.

THESIS

Master's: Online Domestic Appliances Recycling Center, 2016, TEI of Athens, Greece

Bachelor: Study of Medical Imaging Applications through GATE/Geant4. 2013, TEI of Piraeus, Greece

LANGUAGES

English

Russian (native)

Greek (native)

HONORS & AWARDS

1. ***2nd Place in IEEE Region 8(Europe, Africa & M. East) Student Branches' website contest***

December 2011

2. ***Scholarship Award for distinguishing in studies and ethics in the Department of Electronic Computer Systems Engineering from Greek State Scholarships Foundation***
Period 2009 - 2010

3. Scholarship Award for distinguishing in studies and ethics in the Department of Electronic Computer Systems Engineering from Greek State Scholarships Foundation
Period 2010 – 2011

EXPERIENCE

1. *Software Developer* at Department of Physics, Chemistry and Material Science Sept. 2009 – Aug. 2010, **Develop a *Monte Carlo Approach in Photon Scattering in C language*, application of *EGSnrCMP* platform and *GATE***.

2. *Assistant Project Manager* at Department of Physics, Chemistry and Material Science Dec. 2009 – March 2010 Project "IndrAQ entitled A Multidisciplinary study of air quality with emphasis indoors",

3. *IEEE Student Branch TEI Piraeus*, **Founding member,** March 2011 – January 2012

4. *IEEE Student Branch TEI Piraeus*, **Research & Development Committee,** 2011 – 2013

5. **“**i - ΤΕΝΠ ΥΠΗΡΕΣΙΕΣ ΠΛΗΡΟΦΟΡΙΚΗΣ - ΕΡΓΑΣΤΗΡΙΟ ΕΛΕΥΘΕΡΩΝ ΣΠΟΥΔΩΝ”, **June 2012 – January 2013 KendoUI, Orchard CMS and PHP.**

6. ‘Self Employed’, **Jan 2014 – Jan 2018**

7. ‘Seaside Tankers’, Shipbroker **Feb 2018 – July 2019**

8. ‘Ankronet Mike’, Junior Developer **December 2019 – July 2020**

9. ‘Self Employed’, **Aug 2020 – Oct 2023**

Skills

1. Monte Carlo with EGSnrc - GATE

Monte Carlo modelling with EGSnrc toolkit and GATE/Geant4 application.

2. Matlab

3. Java

Spring Boot

4. Linux

Arch, Debian, Ubuntu, Fedora, Centos etc.

Source code building and bash shell scripting.

5.PHP

Laravel Framework.

6. Web Design

HTML5-CSS3-Javascript with KendoUI, Bootstrap

7. C/C++

Algorithms and C/C++ experience with GEANT4

8. Microsoft Office

Many projects and a lot of experience with Office since Bachelor and Masters years.

9. Web Development

.Net C# developing.

Java and Python frameworks.

MySQL – MongoDB – PostgreSQL

10. Python

Django

<u>HOBIES</u>

Martial Arts

Chess